

ABSTRACT

Title of Dissertation: ISOTHERMAL MECHANICAL AND THERMO-MECHANICAL DURABILITY CHARACTERIZATION OF SELECTED PB-FREE SOLDERS

Qian Zhang, Doctor of Philosophy, 2004

Dissertation directed by: Professor Abhijit Dasgupta

Department of Mechanical Engineering

Due to the hazards of Pb in the environment and its effect on humans and marketing competition from Japanese electronics manufacturers, the conversion to Pb-free solders in the electronics industry appears imminent. As major mechanical, thermal, and electrical interconnects between the component and the PWB, solder joints are crucial for the reliability of the most electronic packages. There is an urgent need for constitutive properties, mechanical durability and thermo-mechanical durability of Pb-free solders.

A partitioned constitutive model consisting of elastic, plastic, primary creep and secondary creep models is obtained for the Sn_{3.9}Ag_{0.6}Cu solder and the baseline Sn₃₇Pb solder from comprehensive monotonic and creep tests conducted on Thermo-Mechanical-Microscale (TMM) setup. The comparison between two solders shows that Sn_{3.9}Ag_{0.6}Cu has much better creep resistance than Sn₃₇Pb at the low and medium stresses.

The isothermal mechanical durability of three NEMI recommended Pb-free solders, Sn3.9Ag0.6Cu, Sn3.5Ag, Sn0.7Cu, is tested on the TMM setup under low creep and high creep test conditions. The damage propagation rate is also analyzed from the test data. The generic Energy-Partitioning (E-P) durability model is obtained for three Pb-free solders by using the incremental analytic model developed for TMM tests. The scatter of the test results from the prediction by these E-P durability model constants is small.

The thermo-mechanical durability of the Pb-free Sn3.8Ag0.7Cu solder is investigated by a systematic approach combining comprehensive thermal cycling tests and finite element modeling. The effects of mixed solder systems, device types, and underfill are addressed in the tests. Thermal cycling results show that Sn3.8Ag0.7Cu marginally outperforms SnPb for four different components under the studied test condition. The extensive detailed three-dimensional viscoplastic FE stress and damage analysis is conducted for five different thermal cycling tests of both Sn3.8Ag0.7Cu and Sn37Pb solders. Power law thermo-mechanical durability models of both Sn3.8Ag0.7Cu and Sn3Pb are obtained from thermal cycling test data and stress and damage analysis. The energy-partitioning durability models of two solders are also obtained. It is found that the slopes of the plastic and creep curves in the E-P damage model of Pb-free solders for thermal cycling are steeper than those for mechanical cycling and those of Sn37Pb solders.

ISOTHERMAL MECHANICAL AND THERMO-MECHANICAL DURABILITY
CHARACTERIZATION OF SELECTED PB-FREE SOLDERS

by

Qian Zhang

Dissertation submitted to the faculty of the Graduate School of the
University of Maryland, College Park in partial fulfillment
of the requirements for the degree of
Doctor of Philosophy
2004

Advisory Committee:

Professor Abhijit Dasgupta, Chair and Advisor
Dr. Bongtae Han
Dr. Patrick McCluskey
Dr. Jungho Kim
Dr. Norman Wereley

©COPYRIGHT by

QIAN ZHANG

2004

DEDICATION

To my mother and father, who give me the freedom to pursue the knowledge and provide any support I need, to my dear upcoming baby, and to my lovely wife, who stands with me in all circumstances during this period.

ACKNOWLEDGEMENTS

I would like to thank Mr. Nelson and Mr. Rafanelli from Raytheon System Company for sponsoring the Pb-free project and providing the test data.

I would like to acknowledge the professors and staff of Mechanical Engineering Department and CALCE Electronic Products and Systems Center who supported me in the project.

I also would like to thank my labmates, Joe, Dan, and Gayatric. My acknowledgement is also given to other CALCE students, Yunqi, Haiyu, Yuri, Kaushik..., for their valuable discussion and knowledge.

I would like to thank the students from the German exchange program, Marco, Mike, Paul, for their help in the project.

In particular, I would like to acknowledge my dissertation committee: Dr. Han, Dr. McCluskey, Dr. Kim, and Dr. Wereley for evaluating my dissertation and providing the valuable suggestions.

Most of all, I would like to thank my advisor, Dr. Abhijit Dasgupta, for his valuable guidance and support. I deeply appreciate his patience, understanding, encouragement, spending time in the discussion and explanation.

TABLE OF CONTENTS

1	Introduction.....	1
1.1	Background and Motivation	2
1.1.1	Why Pb-free?	3
1.1.2	Pb-free Solder Selection	8
1.1.3	Technical Challenges for Ob-free Electronic Packaging.....	15
1.1.4	Data Needs for Pb-free Solders.....	22
1.2	Problem Statement and Objectives	23
1.3	Literature Review.....	25
1.3.1	Constitutive Properties.....	25
1.3.2	Mechanical Cycling Durability.....	39
1.3.3	Thermal Cycling Durability.....	45
1.4	Test System.....	61
1.4.1	Test Specimen.....	62
1.4.2	Test Setup.....	65
1.4.3	High Temperature Testing Module.....	67
1.4.4	Load-train Compliance Calibration	68
1.4.5	Test Setup Modifications	69
2	Constitutive Properties.....	72
2.1	Pb-free Solder Microstructure.....	72
2.2	Constitutive Behavior	76
2.2.1	Typical Experimental Results	77
2.2.2	Choice of Constitutive Models	79
2.2.3	Analytic Model of TMM Tests.....	82
2.2.4	Model Simulation to TMM Tests	88
2.2.5	Test Matrix.....	89
2.2.6	Elastic Model	90
2.2.7	Steady-state Creep Model.....	91
2.2.8	Transient Creep model.....	100
2.2.9	Plastic Model	101
3	Isothermal Mechanical Durability	103
3.1	Characterization of Durability Properties	104
3.1.1	Durability Modeling.....	104
3.1.2	Durability Testing Approach and Test Matrices.....	107
3.2	Experimental Results and Analysis	111
3.2.1	Power Law Durability.....	111
3.2.2	Damage propagation Rate Analysis.....	129
3.2.3	Post-test Microstructural Observations.....	134
3.3	Energy Partitioning Damage Model	140
3.3.1	Approach.....	140
3.3.2	E-P Damage Models of Pb-free Solders	148

4	Thermo-Mechanical Durability	151
4.1	Thermal Cycling Test	153
4.1.1	Test Vehicle	154
4.1.2	Board Assembly.....	156
4.1.3	Test Vehicle Characterization.....	157
4.1.4	Reliability Testing.....	165
4.2	Thermal Cycling Results and Discussion	165
4.3	Failure Analysis	171
4.3.1	Pure SnAgCu System.....	171
4.3.2	Pure SnPb System.....	175
4.3.3	Mixed Technology	175
4.4	Stress and Damage Modeling	177
4.4.1	Finite Element Modeling and Stress Analysis.....	179
4.4.2	FE Analysis Results and Discussion.....	188
4.4.3	Thermo-Mechanical Durability Models	196
5	Summary, Contributions and Suggestions for Future Work.....	212
5.1	Summary of Results.....	212
5.2	Contributions of the Dissertation.....	214
5.3	Suggestions for Future Work.....	217
6	Appendices.....	221
	Appendix A: TMM Modification Drawings.....	221
	Appendix B: VB Program of Incremental analytic model of TMM Tests	222
	Appendix C: A Microstrutural Steady-State Creep Model for Pb-free Solders	235
	Appendix D: Test Data and Durability Parameters of Sn37Pb at 98°C	240
	Appendix E: Ansys Input Files	241
	Appendix E1: Ansys Input File for Parametric Modeling.....	242
	Appendix E2: Ansys Input File for Thermal Profile	248
	Appendix E3: Ansys Input File for Post Processing.....	251
	Appendix F: Weibull Plots.....	253
7	Reference	255

LIST OF TABLES

Table 1.1: NCMS solder selection criteria.....	13
Table 1.2: NCMS selected solder alloys.....	14
Table 1.3: Comparison between Sb37Pb and Sb3.5Ag0.7Cu solder alloys [SOLDERTEC, 1999]	15
Table 1.4: Elastic-plastic model of Sn3.5Ag [Wiese, et al. 2002a].....	31
Table 1.5: Elastic-plastic model of Sn4Ag0.5Cu [Wiese, et al. 2002a]	32
Table 1.6: Plastic model parameters of two Pb-free solder alloys.....	32
Table 1.7: Creep models of seven Pb-free solder alloys.....	35
Table 1.8: Anand model constants for some Pb-free solder alloys.....	39
Table 1.9: Strain range partitioning model constants of some Pb-free solder alloys [Kariya, et al., 2001]	41
Table 1.10: Parameters for crack propagation model [Wiese, et al., 2001b].....	43
Table 1.11: Thermal cycling test matrix from the IDEALS projects	46
Table 1.12: Summary of thermal cycling tests on lead contamination [Amagai, et al., 2002, Nurmi and Ristolainen, 2002, Patwardhan, et al., 2002, Roubaud, et al., 2002]	56
Table 1.13: Summary of thermal cycling tests from literature	59
Table 1.14: Reliability of two solder interconnections for Flip Chip on FR-4 boards with underfill [Schubert, 2002a]	60
Table 2.1: Test matrix for TMM monotonic and creep tests.	90
Table 2.2: Comparison of the steady-state creep model constants between Sn37Pb and Sn3.9Ag0.6Cu solders	96
Table 2.3: Model constants of the primary creep of Sn37Pb and Sn3.9Ag0.6Cu solders	101
Table 2.4: Plastic model constants for Sn37Pb and Sn3.9Ag0.6Cu solders.....	102
Table 3.1: Summary of cyclic test statistics and load level for Sn3.9Ag0.6Cu solder...	113
Table 3.2: Power-law durability parameters for Sn3.9Ag0.6Cu	114
Table 3.3: Summary of cyclic test statistics and load level for Sn3.5Ag solder.....	117
Table 3.4: Power-law durability parameters for Sn3.5Ag	118
Table 3.5: Summary of cyclic test statistics and load level for Sn0.7Cu solder.....	120
Table 3.6: Power-law durability parameters for Sn0.7Cu	121
Table 3.7: Power-law durability data from this study and the literature	129

Table 3.8: Summary of damage propagation rate analysis for three Pb-free solder alloys	134
Table 3.9: Shear modulus for three Pb-free solders.....	145
Table 3.10: Plastic model constants for three Pb-free solders.....	146
Table 3.11: Secondary creep model constants for Sn3.9Ag0.6Cu and Sn3.5Ag.....	146
Table 3.12: Energy-partitioning model constants for three Pb-free solders.....	150
Table 3.13: Energy-partitioning model constants for Sn3.9Ag0.6Cu: with and without primary creep.....	150
Table 4.1: Device characteristics.....	155
Table 4.2: PWB characteristics.....	156
Table 4.3: Board assembly configuration.....	156
Table 4.4: X-ray solder defect summary.....	157
Table 4.5: Measured geometry for fleXBGA144, TABGA96, and μ BGA46 joints.....	163
Table 4.6: Measured effective CTE of components and PWB.....	164
Table 4.7: Thermal cycling test results.....	167
Table 4.8: Weibull analysis results.....	167
Table 4.9: Summary of temperature profiles.....	180
Table 4.10: Temperature-dependent elastic and plastic properties of the solder.....	186
Table 4.11: Plastic model constants for Sn37Pb and Sn3.9Ag0.6Cu solders.....	187
Table 4.12: Steady-state creep model constants for Sn37Pb and Sn3.9Ag0.6Cu solders	188
Table 4.13: Coffin-Manson type durability parameters for two solders.....	200
Table 4.14: Comparison of the ratio $\Delta W_{pl}/\Delta W_{cr}$ between Sn3.8Ag0.7Cu and Sn37Pb solders.....	202
Table 4.15: Thermo-mechanical Energy-Partitioning model constants for Sn3.8Ag0.7Cu and Sn37Pb.....	203
Table 4.16: Summary of characteristic life, acceleration factor and life cycle durability under the laptop use environment.....	211
Table 6.1: Material parameters in the micromechanical model of a Tin matrix containing both Ag_3Sn and Cu_5Sn_6 dispersoids.....	238
Table 6.2: Summary of cyclic test count and load level for Sn37Pb solder.....	241
Table 6.3: Power-law durability parameters for Sn37Pb.....	241

LIST OF FIGURES

Figure 1.1: Pb-free products: Panasonic MJ-30 mini-disk player (left) and Nortel Meridian desk telephone (right).....	7
Figure 1.2: the melting points of Pb-free solder alloys.....	11
Figure 1.3: Optical micrograph of a SnAgCu solder joint.....	18
Figure 1.4: Tin whisker found on “matte” tin plating in a Dual-in Line package (DIP) lead [www.nist.gov].....	21
Figure 1.5: Temperature-dependent Young’s modulus of some solders [Wiese, et al. 2001a]	29
Figure 1.6: Comparison of plastic properties of the Sn3.5Ag and Sn40Pb solders [Darveaux and Banerji, 1992, Darveaux, et al. 1995]	30
Figure 1.7: Tri-linear elastic-plastic approximation [Wiese, et al. 2002a]	31
Figure 1.8: A typical constant-load creep test result of the Sn37Pb solder	34
Figure 1.9: Typical strain profiles and hysteresis curve [Kariya, et al., 2001].....	41
Figure 1.10: Coffin-Manson plots for Sn-3.5Ag-xBi solders [Kariya and Otsuka, 1998].....	42
Figure 1.11: Test grip configurations [Park and Lee 2002].....	44
Figure 1.12: Fatigue life versus displacement range for Sn3.5Ag0.75Cu for different test grip configurations [Park and Lee 2002]	44
Figure 1.13: Work-based isothermal mechanical durability curve comparison of four solders at room temperature (3.3E-2 1/s strain rate).....	45
Figure 1.14: Shear strength variation with cycles for 1206 resistor for solder-board-paste medium combination. SPA=Sn36Pb1Ag SP=Sn37Pb 96SC=Sn3.8Ag0.7Cu 96SCX= Sn3.8Ag0.7Cu plus 0.4%X [IDEALS, 1999a, 1999b, 1999c; Stam and Davitt, 2001]	47
Figure 1.15: Thermal cycling fatigue life comparison of the Pb-free solders for chip resistor 1206 [Soldertec, 1999].....	48
Figure 1.16: Thermal cycling fatigue life comparison of the Pb-free solders for LCCC44 [Soldertec, 1999].....	48
Figure 1.17: Thermal cycling fatigue life comparison of the Pb-free solders for LCCC20 [Gayle, et al., 2001; Whitten, 2000].....	50
Figure 1.18: Acceleration factor comparison for Sn37Pb and Sn4Ag0.5Cu alloys (TC1 and TC3 thermal cycling, fleXBGA package) [Syed, 2001b].....	50
Figure 1.19: Durability of reflowed Sn3.8Ag0.7Cu solder joints [Boeing 2002]	53
Figure 1.20: Optical micrographs of the cross sections of four tested solder joints on Cu UBM after thermal cycling from 0°C to 100°C [Frear, et al., 2001].....	53

Figure 1.21: Thermal fatigue life versus thermal strain for four solder alloys [Frear, et al., 2001]	54
Figure 1.22: Reliability comparison of four solders in two different test conditions (0/100 °C and –40/125 °C temperature ranges) [Gayle, 2001]	60
Figure 1.23: Reliability comparison of Sn4Ag1Cu with Sn37Pb solder interconnections for two different packages [Syed, 2001b]	60
Figure 1.24: Thermal cycling durability curve comparison of four solders with creep work density as failure criterion [NCMS, 1997]	61
Figure 1.25: TMM specimen schematic	62
Figure 1.26: Optical micrograph of a Sn3.9Ag0.6Cu solder specimen	64
Figure 1.27: TMM test frame [Haswell, 2001]	65
Figure 1.28: TMM grip schematic [Haswell, 2001]	66
Figure 1.29: Heating module schematic [Haswell, 2001]	68
Figure 1.30: TMM apparatus with horizontal fixture	70
Figure 1.31: TMM experimental system	71
Figure 1.32: Test result variation for same cyclic test condition: Sn0.7Cu	71
Figure 2.1: Microstructure of Sn3.8Ag0.7Cu solders [Schubert et. al. 2002a]	73
Figure 2.2: ESEM micrograph with backscatter of Sn3.9Ag0.6Cu TMM solder joint	73
Figure 2.3: ESEM micrograph with backscatter of Sn3.5Ag TMM solder joint	74
Figure 2.4: Optical micrographs of TMM solder joints	74
Figure 2.5: Optical micrographs of Sn0.7Cu TMM solder joint	75
Figure 2.6: Optical micrographs of Sn3.5Ag TMM solder joints before and after 100 hours aging at 132°C	76
Figure 2.7: Optical micrographs of Sn0.7Cu TMM solder joints before and after 100 hours aging at 136°C	76
Figure 2.8: Typical monotonic stress-strain test results	78
Figure 2.9: Strain-time data from presented stress-strain test	78
Figure 2.10: Typical constant load test results	79
Figure 2.11: Schematic of analytical model of TMM tests	83
Figure 2.12: Schematic of solder joint dimensions	83
Figure 2.13: Schematic of incremental analysis process	84
Figure 2.14: Monotonic test simulation. Sn3.9Ag0.6Cu, 125°C, 1.1×10^{-1} 1/s strain rate	86
Figure 2.15: Monotonic test simulation. Sn3.9Ag0.6Cu, 125°C, 4.4×10^{-4} 1/s strain rate	87

Figure 2.16: Comparison of model simulation to monotonic test data for Sn3.9Ag0.6Cu solder.....	89
Figure 2.17: Comparison of model simulation to monotonic test data for Sn37Pb solder.....	89
Figure 2.18: Schematic of a log-log plot of the shear secondary creep strain rate vs. the shear stress	93
Figure 2.19: Steady-state creep data for Sn37Pb solder	93
Figure 2.20: Steady-state creep data for Sn3.9Ag0.6Cu solder.....	94
Figure 2.21: Normalized steady-state creep data for Sn37Pb solder.....	94
Figure 2.22: Normalized steady-state creep data for Sn3.9Ag0.6Cu solder.....	95
Figure 2.23: Comparison of the steady-state creep.....	96
Figure 2.24: Schematic of proposed steady-state creep mechanisms of Pb-free solders..	98
Figure 2.25: Comparison of three steady state creep models of SnAgCu solder	98
Figure 2.26: Comparison of three steady state creep models of SnPb solder.....	99
Figure 2.27: Transient creep shear strain vs. time for Sn3.9Ag0.6Cu solder.....	100
Figure 2.28: Plastic shear strain-stress curves for Sn37Pb and Sn3.9Ag0.6Cu solders .	102
Figure 3.1: Cyclic durability test matrix	108
Figure 3.2: Effects of percentage of load drop on the durability model (Sn3.5Ag solder test results for regime 1)	109
Figure 3.3: 25°C, 3.3E-2 1/s strain rate cyclic fatigue data, Sn3.9Ag0.6Cu solder	114
Figure 3.4: 125°C, 4.4E-4 1/s strain rate cyclic fatigue data, Sn3.9Ag0.6Cu solder	114
Figure 3.5: Comparison of regime 1 and regime 2 results: Sn3.9Ag0.6Cu solder, work-based (ΔW) and inelastic strain range-based (ISR) damage relation.....	115
Figure 3.6: 25°C, 2.9E-2 1/s strain rate cyclic fatigue data, Sn3.5Ag solder	117
Figure 3.7: 128°C, 4.5E-4 1/s strain rate cyclic fatigue data, Sn3.5Ag solder	118
Figure 3.8: Comparison of regime 1 and regime 2 results: Sn3.5Ag solder, work-based (ΔW) and inelastic strain range-based (ISR) damage relation.....	119
Figure 3.9: 25°C, 3.6E-2 1/s strain rate cyclic fatigue data, Sn0.7Cu solder	121
Figure 3.10: 132°C, 4.9E-4 1/s strain rate cyclic fatigue data, Sn0.7Cu solder	121
Figure 3.11: Comparison of regime 1 and regime 2 results: Sn3.5Ag solder, work-based (ΔW) and inelastic strain range-based (ISR) damage relation.....	122
Figure 3.12: Work-based damage relation comparison of four solder alloys at room temperature	125
Figure 3.13: ISR-based damage relation comparison of four solder alloys at room temperature	126

Figure 3.14: Work-based damage relation comparison of four solder alloys at high temperature	126
Figure 3.15: ISR-based damage relation comparison of four solder alloys at high temperature	127
Figure 3.16: Work-based damage relation comparison of four solder alloys at same homologous temperature (0.75)	128
Figure 3.17: ISR-based damage relation comparison of four solder alloys at same homologous temperature (0.75)	128
Figure 3.18: Load drop versus cycles from a TMM test of Sn3.5Ag solder	130
Figure 3.19: Damage propagation rate at 25°C, 3.3E-2 1/s strain rate	131
Figure 3.20: Damage propagation rate at 125°C, 4.4E-4 1/s strain rate	131
Figure 3.21: Damage propagation rate at 25°C, 2.9E-2 1/s strain rate	132
Figure 3.22: Damage propagation rate at 128°C, 4.5E-4 1/s strain rate	132
Figure 3.23: Damage propagation rate at 25°C, 3.6E-2 1/s strain rate: Sn0.7Cu	133
Figure 3.24: Damage propagation rate at 132°C, 4.9E-4 1/s strain rate: Sn0.7Cu	133
Figure 3.25: Post-test ESEM micrograph of Sn3.5Ag solder joint (low creep conditions, 25°C, 2.0% inelastic strain range control, 2.6E-2 1/s shear strain rate, 80% total load drop)	135
Figure 3.26: Post-test ESEM micrograph of Sn3.9Ag0.6Cu solder joint (high creep cyclic conditions, 125°C, 7.9% inelastic strain range control, 4.5E-4 s ⁻¹ shear strain rate, 55% total load drop)	136
Figure 3.27: Post-test ESEM micrograph of Sn3.9Ag0.6Cu solder joint (high creep cyclic conditions, 125°C, 7.9% inelastic strain range control, 4.5E-4 s ⁻¹ shear strain rate, 55% total load drop)	136
Figure 3.28: Post-test ESEM micrograph of Sn0.7Cu solder joint (high creep cyclic conditions, 132°C, 2.8% inelastic strain range control, 4.7E-4 1/s shear strain rate, 80% total load drop)	137
Figure 3.29: Post-test ESEM micrograph of Sn0.7Cu solder joint (high creep cyclic conditions, 132°C, 8.5% inelastic strain range control, 5.2E-4 1/s shear strain rate, 80% total load drop)	137
Figure 3.30: Post-test ESEM micrograph of Sn3.9Ag0.6Cu (low creep cyclic conditions, 25°C, 1.0% inelastic strain range control, 3.2E-2 s ⁻¹ shear strain rate, 53% total load drop)	138
Figure 3.31: Post-test ESEM micrograph of Sn3.5Ag solder joint (low creep cyclic conditions, 25°C, 2.6% inelastic strain range control, 3.1E-2 s ⁻¹ shear strain rate, 80% total load drop)	139

Figure 3.32: Post-test ESEM micrograph of Sn0.7Cu solder joint (low creep cyclic conditions, 25°C, 4.7% inelastic strain range control, 3.9E-2 s ⁻¹ shear strain rate, 80% total load drop).....	139
Figure 3.33: Post-test ESEM micrograph of Sn3.5Ag solder joint (low creep cyclic conditions, 25°C, 4.7% inelastic strain range control, 3.2E-2 s ⁻¹ shear strain rate, 80% total load drop).....	140
Figure 3.34: Overall approach for mechanical durability analysis.....	143
Figure 3.35: Comparison of the hysteresis loops from experiments and simulation for Sn3.9Ag0.6Cu solder.....	147
Figure 3.36: Comparison of the hysteresis loops from experiments and simulation for Sn3.5Ag solder.....	148
Figure 3.37: Comparison of the hysteresis loops from experiments and simulation for Sn0.7Cu solder.....	148
Figure 3.38: Comparison of the durability predicted by energy-partitioning model with measured test results for Sn3.9Ag0.6Cu, Sn3.5Ag and Sn0.7Cu solders.....	150
Figure 4.1: Test vehicle schematic.....	155
Figure 4.2: Optical micrographs of SnAgCu solder joints; (a) PBGA352, (b) fleXBGA144, (c) TABGA96, (d) μBGA46, (e) μBGA48.....	158
Figure 4.3: Optical micrographs of four solder systems of TABGA 96 component (label: Solder ball/paste).....	160
Figure 4.4: Optical micrograph of pure SnAgCu PBGA352 solder joint after etching..	161
Figure 4.5: Optical micrograph of pure SnAgCu PBGA352 solder joint after etching..	161
Figure 4.6: Optical micrograph of SnAgCu/SnPb solder joint of μBGA48 device after etching.....	161
Figure 4.7: Dimensions of solder joint and copper pads for PBGA352 joint.....	162
Figure 4.8: Schematic geometry for solder joints of the fleXBGA144, TABGA96, and μBGA46.....	162
Figure 4.9: Typical TMA CTE test results for PBGA352 package.....	164
Figure 4.10: Temperature profile.....	165
Figure 4.11: Effects of mixed technology and component type on characteristic life of the solder joints.....	169
Figure 4.12: Weibull plot of fleXBGA144 components.....	170
Figure 4.13: Optical micrographs of four kinds of components after micro sectioning.	173
Figure 4.14: Optical micrographs of μBGA46 with extremely early failure.....	174
Figure 4.15: Optical micrographs of PBGA352 solder joint.....	174
Figure 4.16: Optical micrographs of TABGA96 solder joint with voids.....	174

Figure 4.17: Optical micrographs of PBGA352 solder joint	175
Figure 4.18: Optical micrographs of TABGA96 solder joint.....	176
Figure 4.19: Optical micrographs of PBGA352 solder joints.....	176
Figure 4.20: Overall approach for thermomechanical durability analysis.....	178
Figure 4.21: Schematic of thermal profile	180
Figure 4.22: Finite element model of fleXBGA144 package.....	182
Figure 4.23: Finite element model of TABGA96 package.....	182
Figure 4.24: Finite element model showing boundary conditions.....	183
Figure 4.25: Variation of equivalent creep strain range per cycle with mesh density; creep strain is averaged in the local neighborhood of the critical region in the critical solder joint	184
Figure 4.26: Finite element meshing of the solder ball array for fleXBGA144	184
Figure 4.27: Equivalent stress-strain hysteresis loops for fleXBGA1 package subjected to our thermal cycling	185
Figure 4.28: Total work density contour of fleXBGA1 package at -125°C before dwell: Sn3.8Ag0.7Cu solder	189
Figure 4.29: Total work density contours of fleXBGA2 package at 100°C before dwell: Sn3.8Ag0.7Cu solder	189
Figure 4.30: Total work density contours of TABGA package at -125°C before dwell: Sn3.8Ag0.7Cu solder	190
Figure 4.31: Comparison between thermal cycle tests and FE simulation of fleXBGA1: Sn3.8Ag0.7Cu solder	191
Figure 4.32: Comparison between thermal cycle tests and FE simulation of TABGA96: Sn3.8Ag0.7Cu solder	191
Figure 4.33: Half layer used to assess average stress, strain and energy: TABGA96, Sn3.8Ag0.7Cu, -125°C before dwell	192
Figure 4.34: Normal stress contour plot of the whole layer of the critical solder joint: TABGA96, Sn3.8Ag0.7Cu, -125°C before dwell	193
Figure 4.35: Hysteresis loops of Sn3.8Ag0.7Cu and Sn37Pb solders: TABGA96	194
Figure 4.36: Comparison of hysteresis loops for fleXBGA1 and TABGA96 packages: Sn3.8Ag0.7Cu solder	195
Figure 4.37: Effect of thermal profile on hysteresis loop of SAC for fleXBGA2.....	196
Figure 4.38: Coffin-Manson type durability model for Sn3.8Ag0.7Cu solder.....	199
Figure 4.39: Coffin-Manson type durability model for Sn37Pb solder	199
Figure 4.40: Comparison of Coffin-Manson type durability model between Sn3.8Ag0.7Cu solder and Sn37Pb solder	200

Figure 4.41: Comparison of Energy-Partitioning model between Sn3.8Ag0.7Cu and Sn37Pb solders.....	204
Figure 4.42: Comparison of the predicted thermo-mechanical durability by energy-partitioning model and thermal cycling test results for Sn3.8Ag0.7Cu and Sn37Pb	205
Figure 4.43: Comparison of the prediction results of previous E-P durability model for Sn37Pb: before scaling and after scaling	206
Figure 4.44: Comparison of Energy-Partitioning damage model of SnAgCu solder between mechanical cycling and thermal cycling	208
Figure 4.45: Stress contour plots of fleXBGA1 package at -55°C before dwell.....	208
Figure 4.46: Comparison of the prediction results of the E-P durability model from mechanical cycling tests of Sn3.9Ag0.6Cu: before scaling and after scaling	209
Figure 4.47: Thermal profile of typical laptop life cycle environment [Darveaux, et al., 1995]	211
Figure 6.1: Mechanical drawing of fixture frame.....	221
Figure 6.2: Mechanical drawing of frame foot.....	222
Figure 6.3: Comparison of the steady-state creep strain rate between pure tin and Sn3.9Ag0.6Cu solder	239
Figure 6.4: Comparison of the steady-state creep strain rate between test data and results from the micromechanical model	239
Figure 6.5: The reference strain rate $\dot{\epsilon}_0$ used in the micromechanical model.....	240
Figure 6.6: Schematic of proposed steady-state creep mechanisms of Pb-free solders..	240
Figure 6.7: 98°C, 4.6E-4 1/s strain rate cyclic fatigue data, Sn37Pb solder.....	241
Figure 6.8: 3-P Weibull plots for fleXBGA144 package	253
Figure 6.9: 3-P Weibull plots for TABGA96 package	253
Figure 6.10: 3-P Weibull plots for PBGA352 package	254
Figure 6.11: 2-P Weibull plots for μ BGA46 package	254

1 Introduction

Leaded solders have been used for a few thousand years since Egyptian started to use them. Tin-Lead Solders with different compositions also have been used in the electronics industry for more than fifty years because they have many advantages. They are inexpensive compared with other alloys and have good process characteristics (such as low melting points, eutectic characteristics, fine microstructure, high strength and ductility). They also possess good electronic, mechanical, thermal properties such as high electrical conductivity, good fatigue resistance, joint integrity, and high thermal conductivity. All these characteristics make eutectic or near eutectic SnPb alloys well suited for electronic applications. As a result, SnPb solders are extensively used as board finish, lead finish, solder bump, solder ball and die attach in component and PCB manufacturing. As the electronics industry transition to surface mount technology and advanced electronic packaging such as flip-chip, CSP, and BGA, the role of solder joints becomes more and more important.

However, in early nineteenth-century, lead poisoning was diagnosed in paint pigment workers in USA and France. Since then, the use of lead has been gradually banned worldwide in plumbing, paints, and gasoline through the enactment of various legislations. Research into a Pb-free replacement for the current standard eutectic (and near-eutectic) SnPb solder family has also been underway for almost fifteen years since legislation for banning lead was proposed in the U.S in 1989 [Environmental Concepts, 1997]. Although the legislative push was dropped under strong pressure from the

electronics industry because of its small lead consumption (about 1.5%~2.5% of worldwide consumption, by some estimates), industrial and research activities related to Pb-free solders have recently increased due to the legislation in the European Union brought on by environmental and health concerns, and due to market competition in Asia. The European Commission's (EC) draft directives, Waste Electrical and Electronic Equipment (WEEE) and Restriction of Hazardous Substances (ROHS), have sanctioned the ban of lead in electronics by July 2006 (WEEE) in European Union countries. Furthermore, several Japanese electronics manufacturers have successfully created a market differentiation based on "green" products that use Pb-free solders. The resulting rush among the component supply chain to move to components with Pb-free terminations is pressuring all OEMs (Original Equipment Manufacturers) to eliminate Pb-based solders, including those OEMs that are exempted from WEEE and ROHS (e.g. military, aerospace, high-temperature users, etc). The conversion to Pb-free solders in the electronics industry now appears imminent, with many manufacturers targeting a transition well ahead of the EU legislative deadlines.

1.1 Background and Motivation

A Pb-free electronic product or component is defined as the product or component which is assembled without the intentional use of lead in the raw materials or the manufacturing process. A certain level of incidental lead impurities is accepted in Pb-free products. The Joint Electron Device Engineering Council (JEDEC) has approved a definition for Pb-free products as "solid-state devices that contain no more than 0.2% by weight of elemental lead." [JEDEC, 2002] The National Electronics Manufacturing Initiative

(NEMI) used a similar definition for Pb-free products, which have no lead intentionally added, and joints that have less than 0.2% lead by weight [NEMI, 2002].

The change to Pb-free solder materials and processes has a profound influence in the electronics industry. This section discusses the background of the Pb-free conversion, the Pb-free solder selection, technical challenges for Pb-free electronics, and data needs for Pb-free solders. The motivation of this dissertation is also drawn from the discussion.

1.1.1 Why Pb-free?

Why does the electronics industry want to move to Pb-free soldering in order to eliminate the use of Pb? There are three major drivers: hazards of Pb in the environment and its effects on human health, legislative requirements, and market competition.

1.1.1.1 Environmental and human health

The hazards of Pb in the environment and its effect on humans are generally accepted. Lead is regarded as one of the top seventeen chemicals posing the greatest threat to human health [Hwang, 1994]. Medical studies have shown that lead can damage the kidneys, liver, blood, and central nervous system once absorbed in the body. It is also known that young children absorb lead more easily than adults.

Lead can be ingested in the human body by eating, drinking and inhaling. Under normal conditions and typical applications in the electronics industry, lead cannot vaporize to form fumes. Thus the risk of lead ingestion can be eliminated by some precautions for

workers and operators in contact with lead in working environment. Some examples of these precautions include wearing a facemask during maintenance and solder dross removal at wave solder pot, prohibiting smoking in areas with lead, and cleaning their hands before eating, drinking, and smoking.

The real risk of Pb in the electronics industry does not come from the production environment but from the disposal of electronic products containing lead, such as home appliances, TVs, computers, etc. Consumer electronics constitutes 40% of lead found in landfills [Woodrow, 2002]. The major concern in regard to the presence of lead in landfills is the potential for lead to leach and contaminate the underground water, and subsequently go into the drinking water [WEEE, 2001].

1.1.1.2 Legislation

The use of Pb in plumbing, paint, gasoline, and other common applications has been banned for many years in USA and Europe. In the USA, such bans were established in 1991 via Congressional legislation. But electronic products have been exempted from all such legislation in the USA and elsewhere since the electronics industry represents a very small percentage of total lead consumption but a significant and increasing percentage of the GNP [Robins, 2000]. There are now a series of initiatives worldwide that outline targets for electronic equipment re-use and recycling. In such initiatives, the use of hazardous materials such as lead is often limited in order to improve the ease of recycling.

The most important such international actions are the directives on Waste from Electronic and Electrical Equipment (WEEE) and Reduction of Hazardous Substances (RHS) proposed within the European Union (EU). The WEEE and RHS Directives have been published in the Official Journal of the European Communities on 13th February 2003 and came into force on that date. These directives aim to:

- prevent waste of electronic and electrical equipment
- promote re-use, recycling and recovery of such waste
- minimize risks and impact to the environment associated with treatment and disposal of end-of-life electronic and electrical equipment

As part of these objectives, it is expected that the use of hazardous materials will be phased out:

“Member states shall ensure that the use of lead, mercury, cadmium, hexavalent chromium, PBB and PBDEs in electrical and electronic equipment is substituted on 1 July 2006.” [WEEE, 2001]

Currently only certain product categories are targeted; IT, telecom, consumer appliances, medical, lighting, monitoring and control instruments, automatic dispensers and toys. Automotive applications are exempted from the directive implicitly by omission of this category from the listing of types of equipment covered by the regulations. Other specific exemptions are included in one of the annexes of the document.

The WEEE and RHS directives are significant because they would affect a market that consists of fifteen member states, four associated states, and an unknown number of

future EU members. The provisions of the directives will govern not only products produced in the EU, but also those sold in the EU regardless of origin.

Motivated by the increasing electronic product consumption and its physical limitations, Japan has passed seven laws and acts for collecting and recycling waste products including household appliances and electronic products to the producers of these products. While these regulations do not explicitly ban the use of lead, it does mandate the recovery of lead contained in specified consumer electronics, and is an indirect incentive to Japanese manufacturers to completely avoid the use of lead.

Although there is no federal legislation yet in the US, there are a number of State electronics recycling initiatives to consider. In addition, the U.S. Environmental Protection Agency (EPA) has recently proposed stricter community reporting requirements for all industries that use lead compounds. Usage reporting thresholds of release and off-site transfer of Pb and Pb compounds have been reduced to 100 pounds from 25,000 pounds for manufacturers and processors and from 10,000 pounds for users.

1.1.1.3 Marketing Competition

Besides legislative pressures, many electronics manufacturers have found it wise to take a very proactive stance on the Pb-free issue. Labeling of their products as being more “green” is an advantage to product marketing when concern for environmental damage due to industrial activity is rising among the general consumers. Market forces may become a major driver in the conversion to Pb-free soldering for the electronics industry.

Japanese electronic companies are ahead of their US and European competitors in the plan to eliminate Pb and release of Pb-free products. Many companies, including Hitachi, NEC, Toshiba, Matsushita, and Sony, have announced plans for conversion to Pb-free assembly during 2000-2001. A few Pb-free products have already been introduced in Japan. The most frequently cited example is a mini-disk player produced by Panasonic, as shown in Figure 1.1 (left). This product allowed Panasonic to increase its market share from 4.7% to 15 %. Although this product is not completely Pb-free, it was assembled using a Sn/Ag/Bi solder alloy instead of SnPb, and most of components have Pb-free lead finishes. In addition, NEC became the first company in the world to begin use of a new solder material that does not include any lead in PC motherboards in 1999.



Figure 1.1: Pb-free products: Panasonic MJ-30 mini-disk player (left) and Nortel Meridian desk telephone (right)

Mainly driven by the WEEE/RHS directives, European electronic companies, including Nortel, Nokia, Siemens, and Ericsson have internal programs for the development of Pb-free solder processes. They have defined their Pb-free component and process specifications. There are few actual Pb-free products announced by European companies. One such product was Nortel Meridian desk telephone, as shown in Figure 1.1 (right). This phone was assembled using SnCu solder screened on an organic solder preservative (OSP)-Cu PCB. More recently Ericsson Microelectronics has launched the

world's first Pb-free solderable, surface mount DC/DC power module. Many European institutes and industrial organizations such as International Tin Research Institute (ITRI) are also conducting extensive research on possible issues to convert to Pb-free soldering.

Pb-free activity in the US has been mainly sponsored by automotive electronics suppliers such as Ford Visteon and Delphi-Delco electronics. Their interest is also driven by the desire to increase the operating temperature of their products. But SnPb solder has weak reliability at high temperature which motivated their search for Pb-free high temperature solders. Under the pressures of the pending EU legislations and market competition from Japan, many US manufacturers, including Intel, AMD, Motorola, and TI, have made commitment of support for elimination of Pb from electronic products. In addition, a few industry organizations and consortia are very active in Pb-free soldering development. The IPC and NEMI have organized various conferences and initiated a few development projects on Pb-free conversion. The National Center for Manufacturing Sciences (NCMS) has conducted the studies on Pb-free solder Alternatives and High temperature Pb-free Solders. The High Density Packaging Users Group (HDPUG) has initiated a consortia project with European and US manufacturers.

1.1.2 Pb-free Solder Selection

In order to eliminate the use of Pb in electronic products, the replacement of traditional SnPb solder has to be recognized. When considering a new Pb-free solder alloy we should check if it would meets the following requirements [NCMS, 1998]:

- melting temperature and melting range (Liquidus/Solidus temperatures) close to that of SnPb (183 °C)
- good solderability (particularly wettability)
- good electrical and thermal properties (electrical conductivity, heat capacity, thermal conductivity)
- good mechanical properties (strength, ductility, creep resistance, and thermomechanical fatigue resistance)
- thermal expansion coefficient
- corrosion resistance
- acceptable and consistent manufacturability (both at the component level and board level)
- no toxic materials
- low alloy cost
- acceptable repairability/reworkability

Until now no drop-in replacement has been found to meet all requirements in such an optimal way as SnPb solder, based on the conclusion of NCMS Pb-free solder project in 1998 [NCMS, 1998]. In addition, the quality of formed solder joints is determined by factors other than the solder alloy itself, for example, solder flux, reflow profile, metallurgical reaction between solder alloys and copper, etc. Hence, a systematic study of process parameters (especially reflow profile for Pb-free solders) has to be conducted to define acceptable process windows for high yields and reliability. The development of a good Pb-free solder alloy, which has all the desired properties and allows robust assembling, is really a comprehensive and challenging task.

A lot of extensive research has been carried out on the Pb-free solder alloys since 90's last century. More recently, manufacturers that have begun to develop Pb-free assembly processes have worked independently, and as a result a number of replacement Pb-free solder alloys have been developed and patented. The issue of intellectual property is an additional factor in the selection process.

A limited number of elements can be found as the replacement for lead when we consider the soldering process requirements. Numerous elements with desired properties were eliminated either because they are in limited supply (e.g. Germanium) or because they are toxic (e.g. Antimony and Cadmium). The elements that can be used in Pb-free solder alloys are listed as follows:

- Tin (Sn): abundant, very low toxicity, stable in alloy form, easily workable, 232 °C melting point. Tin has been used as the base element in most Pb-free solder alloys.
- Silver (Ag): limited availability, low human toxicity but potentially harmful to aquatic animals and plants, oxide is conductive, easily workable, excellent grain refiner, 962 °C melting point.
- Copper (Cu): very abundant, inexpensive, very low toxicity, easily workable, 1084 °C melting point.
- Bismuth (Bi): abundant, low toxicity, low ductility and difficult to work, 272 °C melting point.
- Zinc (Zn): readily available, inexpensive, low toxicity, easily oxidized, 420 °C melting point.

- Indium (In): Limited availability, low toxicity, very ductile, 157 °C melting point.

Tin is the only element that can form the base metal for any Pb-free solder alloy since other elements with low melting point (e.g. Bi, In) are in limited supply. The solder alloys that tin and the above elements (except In) form have the melting points in the range of 139 °C (Sn/Bi) to 227 °C (Sn/Cu), as shown in Figure 1.2. Thus a variety of alternative solder alloys can be obtained for different applications.

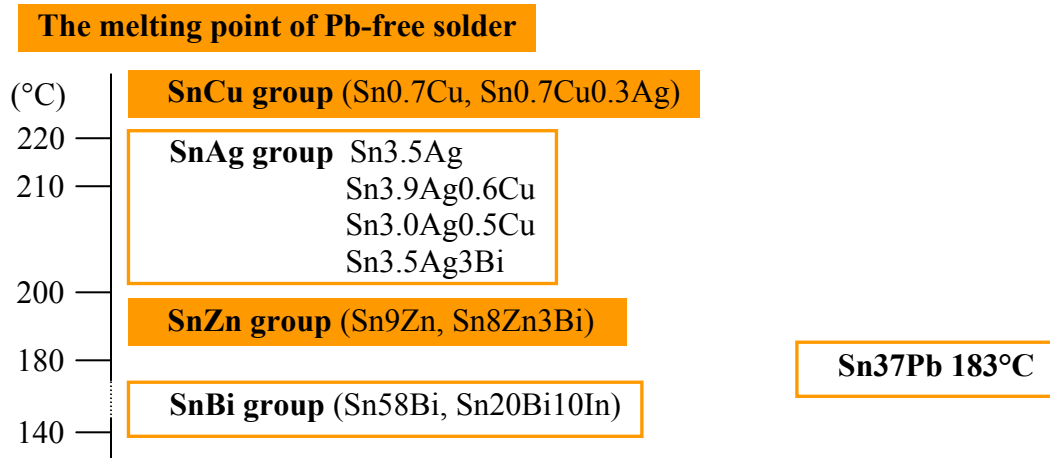


Figure 1.2: the melting points of Pb-free solder alloys

The NCMS in the US and the IDEALS project in Europe have conducted independent extensive evaluation of solder alloys based on the above elements. The extensive compilation of data on solder materials was released by the NCMS in 1998 after a four-year \$19 million collaborative program. This consortium of 11 industrial corporations, academic institutions and national laboratories evaluated 79 solder alloys, including material properties, economics and toxicity. They down selected to seven promising candidate replacements and subsequently conducted manufacturing evaluations of compatible surface finishes and extensive reliability evaluations.

The NCMS used some major properties of solder alloys as selection criteria, which is shown in Table 1.1 [NCMS, 1998]. The primary criterion was a liquidus temperature below 225°C and a pasty range smaller than 30 °C (The pasty range is the range between solidus and liquidus temperature of solder alloys. Eutectic solder alloys have no pasty range). Selected alloys also have good wettability and mechanical properties. All NCMS selected Pb-free solder alloys and eutectic SnPb solder alloy are shown in Table 1.2. The NCMS reported that none of the materials on the list can truly be drop-in replacements for eutectic SnPb alloy. But some Pb-free solders have many characteristics that are better than the Sn/Pb solder. Sn0.7Cu wasn't recommended due to the high melting point (227°C) and Sn2.8Ag20In was also not recommended due to the limited availability.

The electronics industry feels that it would be of significant benefit to industry to focus on one standard alloy for replacing lead in solder. The NEMI, made up of over 50 electronics equipment manufacturers, suppliers, associations, government agencies and universities, recommended a “standardized” Pb-free solder alternative to the industry in 2000. For reflow applications (which represent at least 70% of all board assembly production), the NEMI group was recommending the use of Sn3.9Ag0.6Cu [NEMI, 2000]. For wave solder production (which requires larger amounts of solder), the NEMI was recommending Sn0.7Cu or Sn3.5Ag — as alternatives. The Japan Electronic Industry Development Association (JEIDA) also recommended Sn3Ag0.5Cu either for reflow or wave solder applications from point of view of cost and performance. Sn3.5Ag and Sn0.7Cu with a very small amount of other elements were also recommended for

wave solder production. In Europe, SnAgCu solder alloy was also preferred as the replacement of the SnPb solder by most of electronic manufacturers in European Pb-free Technology Roadmap compiled by SOLDERTEC based at the ITRI [SOLDERTEC, 1999]. Although the preferred SnAgCu composition is a little different in the three major trade areas (US, Europe and Japan), the selection of a Pb-free solder alloy is converging to SnAgCu (also called SAC alloy).

<i>Properties</i>	<i>Definitions</i>	<i>Limits</i>
Liquidus Temperature	Temperature at which solder alloy is completely molten.	< 225°C
Pasty Range	Difference between solidus and liquidus temperatures. Represents the temperature range where the alloy is part solid and part liquid	< 30°C
Wettability	A wetting balance test assesses the force resulting when a copper wire is wetted by molten solder. A large force indicates a good wetting, as does a short time to attain a wetting force of zero, and a short time to attain the two-thirds of the maximum wetting force.	F _{max} > 300μN t ₀ < 0.6s t _{2/3} < 1s
Area of Coverage	Assesses the coverage of the solder on Cu after a typical DIP test.	> 85%
Drossing	Assesses the amount of oxide formed in air on the surface of molten solder after a fixed time at soldering temperature.	Qualitative scale
Thermomechanical Fatigue (TMF-1)	Cycles-to-failure for a given percent failed based on a specific solder joint/board configuration, as compared to the eutectic Sn/Pb.	> 75%
Coeff. of Thermal Expansion (CTE)	Differences in thermal expansion behavior between alloys might create differences in thermal stresses.	< 29 ppm/°C
Creep	Stress required at room temperature to cause failure in 10,000 minutes	> 500 psi
Elongation	Total percent elongation of material under uniaxial tension at room temperature.	> 10%

Table 1.1: NCMS solder selection criteria

<i>Selected Pb-free Alloys</i>			
Composition	Solidus/Liquidus Temperature (°C)	Alloy Type	Companies Evaluating or using
Sn37Pb	183	Eutectic (Standard)	
Sn3.5Ag	221	Eutectic	Siemens
Sn0.7Cu	227	Eutectic	Nortel
Sn58Bi	139	Eutectic	Matsushita
Sn3Ag0.5Cu	217	Non-eutectic	Siemens, Nortel, Nokia
Sn3Ag2Bi	220	Non-eutectic	Fijitsu
Sn2.6Ag0.8Cu0.5Sb	211	Non-eutectic	Sony (+ GE)
Sn3.4Ag4.8Bi	210	Non-eutectic	Matsushita
Sn2.8Ag20In	187	Non-eutectic	
Sn3.5Ag0.5Cu1Zn	221	Non-eutectic	NEC

Table 1.2: NCMS selected solder alloys

Table 1.3 lists the property comparison of Sn37Pn and Sn3.5Ag0.7Cu solder alloys. Compared with Sn37Pb solder, SnAgCu has higher melting point, which consequently results in higher process temperature. SnAgCu also has higher tensile strength, Young's Modulus and greater creep resistance, but higher cost than SnPb solder. These characteristics result in higher stress levels in the interconnects of SnAgCu assemblies. However, in board-level reliability tests using surface-mount and chip components, SnAgCu appeared to perform better than the SnPb solder in most test conditions due to its high creep resistance and mechanical strength.

Property	Sn37Pb	Sn3.5Ag0.7Cu
Melting Point, °C	183	217
Reflow Temperature, °C	220	260
Solderability Performance	Good	ok
Creep, Fatigue Performance	ok	ok
Toxicity	High	Low
Recyclability	High	High
Relative Abundance	Good	ok
Cost, \$/cc	0.05	0.14
Tensile Strength, psi	3900	5730
Electromigration	ok	Excellent
Ductility	Good	Good
Young's Modulus, Mpsi	4.5	7.4

Table 1.3: Comparison between Sn37Pb and Sn3.5Ag0.7Cu solder alloys [SOLDERTEC, 1999]

1.1.3 Technical Challenges for Pb-free Electronic Packaging

As shown in Table 1.3, Pb-free solders have very different properties from SnPb solder, which is the consequence of different composition and microstructures. Due to these differences, many issues are emerging as the industry is changing to Pb-free solders.

These issues can be broken into three categories:

- Compatibility: metallurgical compatibility with current component and board finishes; selection of thermal profiles, solder fluxes; compatibility of packaging materials due to higher process temperature, etc.

- Reliability: performance of Pb-free solders in thermomechanical fatigue, mechanical fatigue, electromigration, and so on; new reliability issues for Pb-free solders such as Sn whisker and Sn transformation.
- Management: cost of converting manufacturing processes; schedule of changing to Pb-free processes.

1.1.3.1 Compatibility

There is no drop-in replacement for SnPb solder. A number of alternative Pb-free solder systems are possible during the transition period before industry organizations throughout the world agree on a single alloy or a limited set of replacement alloys. Different customers may choose different Pb-free solder systems based on their own needs and external events. It is difficult for component or board manufacturers to support multiple solder systems or develop a packaging solution compatible with various solder alloys.

A. Component and Board Finishes

The PCB and component finishes are critical for achieving good solder joints as they facilitate soldering process during the printed circuit board (PCB) assembly. Solder dipping is employed to make Sn37Pb plating for through-hole components with large lead spacing while electroplating process is used for fine-pitch surface-mounted components. The Hot Air Soldering Level (HASL) process for creating Sn37Pb solder board finishes, has been extensively adopted in PCB manufacturing for many years. With the movement to Pb-free electronics, the electronics industry has been exploring a number of new options to eliminate Pb in these processes. Some possible options include

organic solderability preservative (OSP), Ni/Au (ENIG), Ni/Pd/Au, pure Sn, Sn/Bi, and Sn/Cu. The assessment of these finishes has been under way by some industry consortia including NEMI, ITRI, and the Printed Wiring Board Manufacturing Technology Center (PMTEC). There is no superior finish to be identified among them. Each option has its own disadvantages: Ni/Au and Ni/Pd/Au are expensive; pure Sn has the possibility to grow tin whisker; there are manufacturing difficulties for Sn/Bi and Sn/Cu. Further effort will be required to overcome all these drawbacks by collaborative work between solder manufacturers, board fabricators, and component manufacturers.

B. Assembly Issues

A variety of components are assembled onto printed wiring boards either through waving or through reflowing soldering process. The higher melting temperature of most of the promising Pb-free solders results in an increase in the board assembly processing temperature. For example, the most preferred replacement SnAgCu for the reflow process has a melting point of 217°C, which is 34°C higher than Sn37Pb. The melting temperature is even higher because of the variation in solder composition from its eutectic point. If the reflow time is maintained, the higher peak temperature can mean higher heat-up and cool-down rates and greater thermal damage in the components. The higher process temperatures and ramp rates increase the vulnerability to moisture-driven “popcorning” failures in plastic encapsulated components [Hayward, 2000]. The components highly susceptible to thermal damage, such as electrolytic capacitors and wooden components, have to be substituted with more robust alternatives due to the increased temperature.

Pb lowers the surface and interfacial energies of the solder so that SnPb solder has excellent wettability and solderability to copper solder pads [Zeng and Tu, 2002]. Thus Pb-free solders normally have inferior wettability and solderability. Consequently, a weaker interface is formed between the Pb-free solders and the Cu pad. With the combination of the higher assembly temperature, the higher strength and less stress relaxation of most of the Pb-free solders, increased failures at interfaces is anticipated for the Pb-free solders. In addition, different intermetallic compounds are created as new alloy elements, such as Ag and Bi, are introduced in the Pb-free solders. A well-known example is the large Ag_3Sn compounds with plate-like morphology, which are found in many SnAgCu and SnAg solder joints, as shown in Figure 1.3. It is not clear if these intermetallic compounds affect the reliability of the solder joints. It is necessary to conduct comprehensive studies on the soldering process of Pb-free solders and the intermetallic formation both at interfaces and in the bulk solder, during this process.

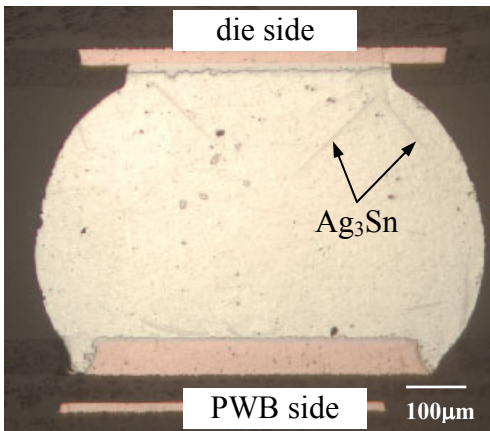


Figure 1.3: Optical micrograph of a SnAgCu solder joint

It is inevitable that the electronics industry will take several years to complete the transition to Pb-free solder assemblies. During this period, leaded packages with SnPb solder finishes may continue to be used with Pb-free solders or vice versa, thus creating

“mixed-technology” assemblies. The dissolution of Pb from the finishes or the presence of Bi in the solder creates a low melting region. It has been reported for double-sided through-hole joints that the fillet can pivot away from the land as the solder joint solidifies, referred as “fillet-lifting” problem [IDEALS, 1999a, 1999b, 1999c]. However, as the larger contributor of Pb consumption, Ball Grid Array (BGA) typed packages have similar compatibility problems. When a SnPb solder ball is assembled with a Pb-free solder paste or a Pb-free solder ball is assembled with a SnPb solder paste, the lower melting SnPb solder will alloy with the Tin-rich Pb-free solder, forming a non-eutectic alloy of indeterminate composition. The alloy may freeze before the higher melting Pb-free solder would have melted. This “cold” solder joint may have low fatigue resistance although no comprehensive proof has been reported yet. Another issue for mixed-technology solder joints is the migration of Pb from the SnPb solder to the Pb-free solder during the reflow process, or during thermal aging or thermal cycling. Recent research shows conflicting results on the effects of Pb contamination on the solder joint fatigue [Amagai, et al., 2002, Nurmi and Ristolainen, 2002, Patwardhan, et al., 2002, Roubaud, et al., 2002]. This issue will be addressed again in the next section and in Chapter 4.

1.1.3.2 Reliability

Pb-free solders have significantly different microstructure and composition than SnPb solder, thus resulting in different mechanical, electrical, and thermal properties. The effect of these different properties on the reliability of electronic products is a critical issue. Equivalent or better reliability of the Pb-free solder is critical to convince the electronics industry to make this transition.

A. Fatigue

Recent research, including this study, demonstrate that many Pb-free solder alloys have larger strength and creep resistance than SnPb solder [Frear, et al., 2001, Huang, 2002, Schubert, et al., 2002b, Wiese, et al., 2001a]. The increase in the strength and creep resistance should results in more fatigue-resisted solder joints. But the higher strength and creep resistance also give rise to higher level of stresses in both the solder joint and the interfaces between the joint and the lead or the substrate/die pads. The quality of the interfaces will play a more critical role in solder joint reliability as the Pb-free solders form weaker interfaces with the pad or lead metals. Solder joints are deployed in numerous application environments where the solder joints experience various loading conditions (vibration, bending, thermal cycling, shock, etc.). The solder materials behave elastically, plastically, and viscoplastically in those environments. There is an urgent need to characterize mechanical properties and durability of Pb-free solder alloys over a sufficiently large range of environmental stresses before we can understand their reliability performance. As this thesis focuses on viscoplastic constitutive behavior and creep-fatigue durability of Pb-free solders, more details on this issue are presented in the subsequent literature review in section 1.3.

B. Sn Whiskers

Pure tin plating is emerging as an economical replacement for SnPb plating as the electronics industry moves to Pb-free soldering. But pure tin plating results in renewed concern over failures due to Tin whiskers, which was reported as early as the 1940s [Levine, 2002]. Tin whiskers are electrically conductive, single crystal structures that can

grow to more than 10 mm in length (typically 1 mm or less) and to 10 μm in diameter (typically 1-3 μm) from surfaces that use tin (especially electroplated tin) as a final finish. Figure 1.4 shows an example of tin whisker. Whiskers can grow spontaneously in almost any application environment: dry or humid, with or without an applied electric field, air pressure or vacuum, etc. Failures in electronic systems can occur as tin whiskers grow to bridge circuit elements maintained at different electrical potentials. Although the growth mechanism of tin whiskers has been studied for many years, there is no single, widely accepted explanation established. Tin whisker growth is generally believed to be primarily due to stresses in the tin plating [Cunningham, 1990]. These stresses can be from many sources including: residual stresses within the tin plating, intermetallic formation, externally applied compressive stresses due to bending or stretching, stress concentration at scratches or nicks, and thermal expansion mismatches. Without an in depth understanding of the growth mechanism, it has not been possible to develop an industry-accepted test to determine the propensity of tin whiskers to grow on a finished surface. Thus the change to the pure tin plating has to be made with considerable caution.

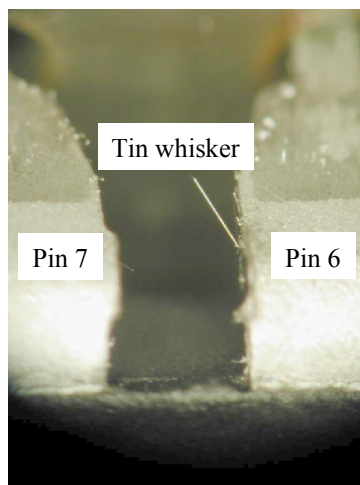


Figure 1.4: Tin whisker found on “matte” tin plating in a Dual-in Line package (DIP) lead [www.nist.gov]

C. Electromigration

As an electrical interconnection, the solder joint is subjected to higher stress resulting from both thermal and electrical effects. Driven by high temperature and high current density, Pb tends to migrate to form a Pb-rich phase at the anode (one of two interfaces between the solder and the pads) of SnPb solder joint [Brandenburg and Yeh, 1998, Gan, 2003]. The electromigration can result in the formation of voids at the interface wherever current crowding exists. Finally, the solder joint fails as the void propagates along the whole interface. Generally, the atomic diffusivity is proportional to the melting point of the solder. It is expected that Pb-free solders will have slower electromigration rates than SnPb eutectic solder. But as a result of decreasing joint sizes and die sizes, the current density carried by solder joints is increasing. Combined with high stress and the increased tendency of void formation in Pb-free solders, electromigration is still an important issue.

1.1.4 Data Needs for Pb-free Solders

There are extensive databases of mechanical properties, durability properties (for both mechanical and thermal cycling), and micromechanical characteristics for Sn-Pb solders. But similar databases are not readily yet available for Pb-free solders. NEMI has recognized a list of database needs for industrial applications and fundamental studies of Pb-free solders [NEMI, 2001]:

- solder materials characterization (temperature dependent properties - CTE and viscoplastic deformations for both bulk solder and solder joint)

- solder durability characterization (isothermal mechanical cycling at different load levels, different temperatures and different strain rates; and thermal cycling with different test conditions)
- failure mechanisms of Pb-free solder joints under accelerated temperature cycling (ATC) (the failure sites, the failure modes, and the microstructural evolution)
- solder-metallization interactions (intermetallic compounds characterization, intermetallics growth with time and temperature, effect of intermetallic layer on the durability of the solder joints, and data on the wetting/solderability and surface tension)
- micro-scale characterization (the microstructure evolution during reflow, aging, testing and field environments, micromechanical characterization and deformation characterization)

An adequate database of various properties of Pb-free solders is needed to design robust electronics for both mechanical and thermal environmental stresses. These properties need to be assessed for Pb-free solders, to enable successful elimination of lead from electronics. These material properties are critical for design and virtual qualification of electronic products with Pb-free interconnects, because current product development processes rely heavily on modeling and simulation.

1.2 Problem Statement and Objectives

Because of the urgent need for constitutive and durability properties of Pb-free solders, the primary objective of this study is to characterize the viscoplastic constitutive

properties and to assess the isothermal mechanical durability and cyclic thermo-mechanical durability of SnAgCu, SnAg and SnCu solders. Mechanical constitutive behavior, which describes the deformation of a material in response to an applied load, is a function of stress history and temperature, as well as other secondary factors such as the manufacturing process, aging and annealing histories, and specimen size. Durability is defined here as a material property which quantifies the ability of a material to withstand damage accumulated during cyclic loading. Durability in this study is investigated under isothermal mechanical cycling and temperature cycling.

Although a few accelerated thermal cycling tests and isothermal mechanical cycling tests for Pb-free assemblies have been conducted, systematic post-processing to derive unified durability models from these tests for Pb-free solder materials, has not been reported in the literature. The term “unified” is used here to indicate that these durability models are valid for wide range of combinations of cyclic mechanical and thermal loading conditions. In this study, not only accelerated tests are reported, but also a systematic approach combining experimental and analytical tools is presented, the generic unified models are used to explain the differences observed between thermal cycling and mechanical cycling durability behavior of SnPb and Pb-free solders. To derive the durability model constants for Pb-free solder materials, eutectic SnPb solder is also characterized, to provide a benchmark for comparison.

1.3 Literature Review

This work focuses on the characterization of isothermal mechanical durability and thermo-mechanical durability of selected Pb-free solder alloys. In order to assess the durability, viscoplastic constitutive properties of the solder alloys also need to be characterized. Studies related to constitutive and durability properties of relevant solder alloys are reviewed in this section.

1.3.1 Constitutive Properties

Although the Pb-free solders considered in this study only include three NEMI recommended solders: Sn3.9Ag0.6Cu, Sn3.5Ag and Sn0.7Cu, in the interest of completeness, the solder materials reviewed in this section include alloys of polycrystalline Sn with one or more other metals such as Pb, Ag, Cu, Bi, In, Zn, and Sb. Pb, Ag, Bi, In, Zn, and Sb form large embedded islands and lamellar inclusions, while Ag and Cu form intermetallic compounds distributed in the form of particulate and needle-like inclusions. These solder materials respond viscoplastically to mechanical loading. In other words, there are multiple competing inelastic deformation mechanisms, each with a different characteristic time scale. Some, like dislocation slip, occur over very short (almost instantaneous) time scales. Others, like dislocation glide/climb, grain-boundary sliding, dislocation pipe diffusion (self diffusion along dislocation cores), grain-boundary diffusion, and intragranular diffusion, occur over much longer time scales and have an Arrhenius dependence on temperature. The fact that most solders are above 0.5 homologous temperature during operation, makes the contribution of each of these rate-dependent mechanisms significant. This multiplicity of deformation mechanisms

manifests itself as a combination of recoverable (elastic) deformations as well as irrecoverable (inelastic), nonlinear rate-dependent deformations.

The constitutive models used by the mechanics community for modeling and simulation of mechanical deformations in viscoplastic materials can be broadly grouped into two families: partitioned and unified models. The partitioned constitutive modeling approach partitions the inelastic deformations conceptually into two main groups [Haswell, 2001]. Deformations occurring over very short time scales (eg. due to dislocation slip) are idealized as “instantaneous,” and hence insensitive to the loading rate. These deformations are termed “plastic” in this discussion. The remaining deformations (those occurring over longer time-scales) are termed “creep.” Creep deformation is often further sub-divided into transient (primary) and steady state (secondary) categories, based on whether the strain rate varies with time or not at a constant stress level. Thus, in this approach, the total strain (ε) can be constructed as a linear combination from three separate deformation mechanisms: rate-independent elastic strain, ε_{el} , rate-independent plastic strain, ε_{pl} , rate-dependent primary creep strain, ε_{pcr} , and rate-dependent secondary creep strain, ε_{scr} :

$$\varepsilon(t) = \varepsilon_{el} + \varepsilon_{pl} + \varepsilon_{pcr}(t) + \varepsilon_{scr}(t) \quad (1.1)$$

The unified constitutive modeling approach still differentiates between elastic and inelastic strain, but integrates creep and plastic deformations into a single inelastic term which is expressed in terms of internal state variables [Anand, 1982].

The test results reported in the literature for solder material properties typically display large variabilities and discrepancies across different studies. As an example, the steady state shear strain rates for SnPb eutectic solder at 75°C reported by various researchers span several orders of magnitude [Haswell, 2001]. These discrepancies result from a variety of factors such as: differences in specimen design; differences in alloying compositions; differences in specimen preparation techniques; differences in test methods and stress states generated during testing. The primary issue in specimen design is the characteristic length scale of the specimen. Most solder joints in electronic packages are small enough to be comparable to the microstructural length scale of the polycrystalline solder materials. Large bulk specimens provide results quite different from those observed in small solder joints. Thus test specimens for material property characterization (both constitutive and durability properties) should be carefully designed to represent the length scale of real solder joints.

Small changes in alloying composition around the eutectic region can also create significant differences in the behavior of many Pb-free solders as many of the second phase materials form intermetallics with the Sn matrix. For example, in ternary SnAgCu alloys, if the Ag and Cu are less than the eutectic amount, small nanoscale precipitates of intermetallic (Cu_6Sn_5 , and Ag_3Sn) are found uniformly dispersed in the grain boundaries of the Sn matrix. These solder compositions are likely to be reasonably ductile and have relatively high fatigue ductility. However, if the second phase amounts exceed the eutectic composition by a small amount, then fairly large, nonuniform, intermetallic

precipitates are found in the bulk of the Sn matrix, resulting in significant embrittlement and loss of fatigue ductility.

The fabrication process used for solder test specimens is also extremely important as it affects both constitutive and durability behavior. Parameters such as reflow profile affect the void content, average grain size, intermetallic amount and concentrations, and void content. Parameters such as flux choice and surface cleanliness can affect the wetting and interfacial strength. Parameters such as choice of plating on the metal terminations can affect local intermetallic compositions, and hence interfacial strength. Choice of test method involves deciding what type of loading to use (e.g. cyclic temperature changes, or cyclic mechanical loading or combinations), and what stress state to use (e.g. tensile, shear, combination). The test method therefore also adds to the variability of the test results.

1.3.1.1 Partitioned Constitutive Model

In this section, the literature on elastic modulus measurement is discussed first, followed by those for plastic and creep constitutive constants.

A. Elastic Properties (Young's Modulus)

Weise and co-authors have summarized the data reported in the literature for temperature-dependent Young's moduli of SnAg and SnAgCu solders, as shown in Figure 1.5 [Wiese, et al. 2001a]. The relation $G = E / (2(1 + \nu))$ has been used to estimate the Young's modulus from the shear modulus in the case of shear tests. It is noted that

Pb-free solders generally have larger Young's modulus than the SnPb solders, although there are discrepancies among data reported by different authors (tensile test, DMA or ultrasonic pulse). The primary reason for the discrepancies is the difference in the strain rates used by the different investigators during the mechanical testing. Because of the contributions from creep deformation, slow strain rates always produce an apparently lower modulus. Thus solders with high creep rates must be tested at higher loading rates for measuring elastic properties. The fact that most Pb-free solders are far more creep resistant than Sn37Pb solder, could be contributing to the fact that their measured elastic stiffness is apparently high at any given temperature and loading rate. Ultrasonic methods measure the Young's modulus at very high strain rates so that these results have the smallest effect from creep deformation.

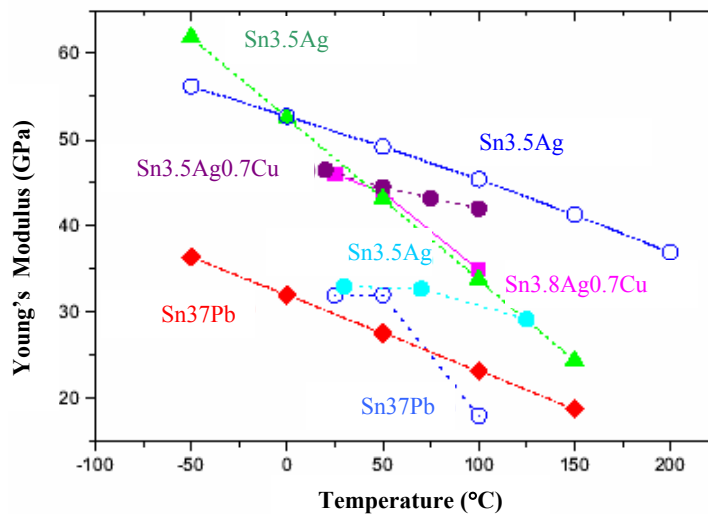


Figure 1.5: Temperature-dependent Young's modulus of some solders [Wiese, et al. 2001a]

B. Plastic Behavior

As discussed earlier, “instantaneous” inelastic deformations beyond the yield point are treated here as rate-independent “plastic” deformation. Such plastic behavior is usually described by a power law relationship [Darveaux, et al., 1995]:

$$\sigma = C_{pl} \varepsilon_{pl}^n \quad (1.2)$$

where σ is the equivalent stress, ε_{pl} is the equivalent plastic strain, C_{pl} and n are the strength coefficient and the hardening exponent, respectively. There is very little plastic data for Pb-free solders reported in the literature. The plastic properties of the eutectic Sn3.5Ag solder were measured by Darveaux [Darveaux and Banerji, 1992, Darveaux, et al. 1995]. As shown in Figure 1.6, at low temperature, Sn3.5Ag solder has larger plastic deformation than eutectic SnPb solder at the same stress level. At high temperature, the plastic strain of the Sn3.5Ag solder is smaller than that of the SnPb solder at stresses beyond 13MPa.

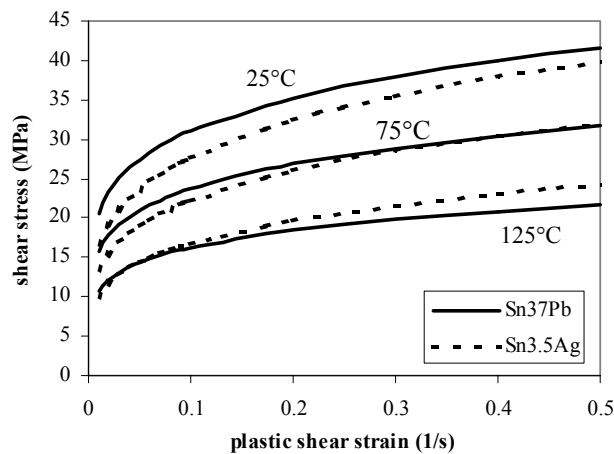


Figure 1.6: Comparison of plastic properties of the Sn3.5Ag and Sn40Pb solders [Darveaux and Banerji, 1992, Darveaux, et al. 1995]

By fitting simulation results to experimental data, a tri-linear approximation of elastic-plastic behavior was obtained for Sn3.5Ag and Sn4Ag0.5Cu solders [Wiese, et al. 2002a]. This formulation is characterized by five parameters (ϵ_1 , ϵ_2 , σ_1 , σ_2 , σ_3), as shown in Figure 1.7. The first line represents the elastic behavior, the second line describes the initial plasticity and the third one refers to saturated plasticity. The parameters for two Pb-free solders at different conditions are given in Table 1.4 and Table 1.5.

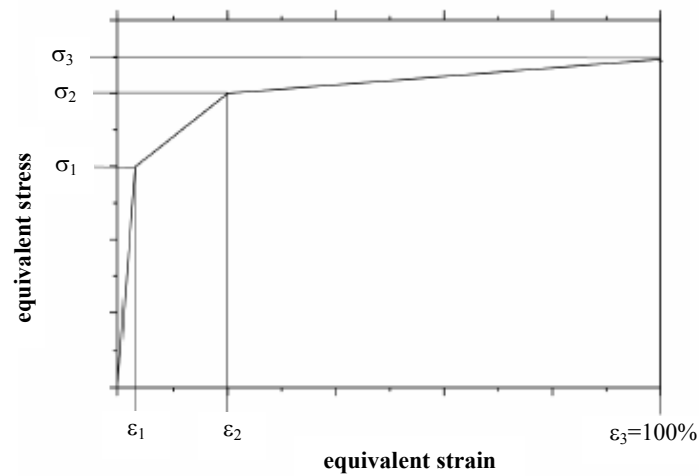


Figure 1.7: Tri-linear elastic-plastic approximation [Wiese, et al. 2002a]

Sn3.5Ag T(K)	ϵ_1	ϵ_2	σ_1 (MPa)	σ_2 (MPa)	σ_3 (MPa)
as cast					
278	1e-3	4e-3	41	64	700
323	1e-3	4e-3	38	57.4	400
after temperature storage					
278	Under investigation				
323	Under investigation				

Table 1.4: Elastic-plastic model of Sn3.5Ag [Wiese, et al. 2002a]

SnAgCu T(K)	ϵ_1	ϵ_2	σ_1 (MPa)	σ_2 (MPa)	σ_3 (MPa)
as cast					
278	1.4e-3	4e-3	57.4	80	2500
323	1.4e-3	4e-3	53.2	72	1900
Stored at T=150°C for 1500 h					
278	6e-4	1.5e-3	24.6	36	2100
323	6e-4	1.5e-3	22.8	32	1500

Table 1.5: Elastic-plastic model of Sn4Ag0.5Cu [Wiese, et al. 2002a]

Haswell and Dasgupta measured the constitutive properties of the Sn3.9Ag0.6Cu solder using a thermo-mechanical-microstructural (TMM) test system, developed by them [Haswell and Dasgupta, 2001a]. Iosipescu type specimens were tested in pure shear condition. The constitutive properties of the Sn3.5Ag solder were also characterized by Lee and Han [Lee and Han, 2002]. A modified single lap shear test configuration was employed in their study. The plastic model parameters from these studies are summarized in Table 1.6. Since their parameters are obtained from shear tests, the following standard von Mises relations are employed [Meyers and Chawla, 1984] to compare the results in terms of the effective strains and stresses:

$$\sigma = \sqrt{3}\tau \quad (1.4a)$$

$$\epsilon = \frac{1}{\sqrt{3}}\gamma \quad (1.4b)$$

where σ and ϵ are effective stress and strain, respectively.

Solder	C_{pl}	n
Sn3.9Ag0.6Cu (Haswell and Dasgupta)	141.8 – 0.307 T(K)	0.651 – 0.0015 T(K)
Sn3.5Ag (Lee and Han)	286.0 – 0.579 T(K)	0.000203T(K) – 0.03998

Table 1.6: Plastic model parameters of two Pb-free solder alloys

C. Creep Behavior

Creep is the most common and important micromechanical inelastic deformation mechanism in solder joints because the solder is above half of its melting point at operating temperatures. A typical constant-load creep deformation curve is composed of primary, secondary, and tertiary creep sections, as shown schematically in Figure 1.8.

The secondary (also termed steady state) creep is generally expressed by three major types of relationships:

$$\frac{d\varepsilon_{scr}}{dt} = A\sigma^n \exp\left(-\frac{Q}{RT}\right) \quad (1.3a)$$

$$\frac{d\varepsilon_{scr}}{dt} = A[\sinh(\alpha\sigma)]^n \exp\left(-\frac{Q}{RT}\right) \quad (1.3b)$$

$$\frac{d\varepsilon_{scr}}{dt} = A(\sigma^n / T) \exp\left(-\frac{Q}{RT}\right) \quad (1.3c)$$

where σ is the applied equivalent stress, ε_{scr} is the equivalent strain, R is the universal gas constant ($= 8.31451 \text{ m}^2 \text{ kg/s}^2 \text{ K mol}$), T is the temperature in K, Q is an activation energy in J/mol, A and n are model constants. Equation (1.3a) is the Weertman's secondary creep law [Tribula and Morris, 1990], which is used for steady state creep mechanism over a wide range of temperature and stress. Equation (1.3b) is Garofalo, or sinh, creep law [Darveaux, et al., 1993], which can represent two different creep mechanisms at different stress levels. Equation (1.3c) is Dorn's creep law [Kahyap and Murty, 1981], which considers the temperature dependence of the hardening mechanism.

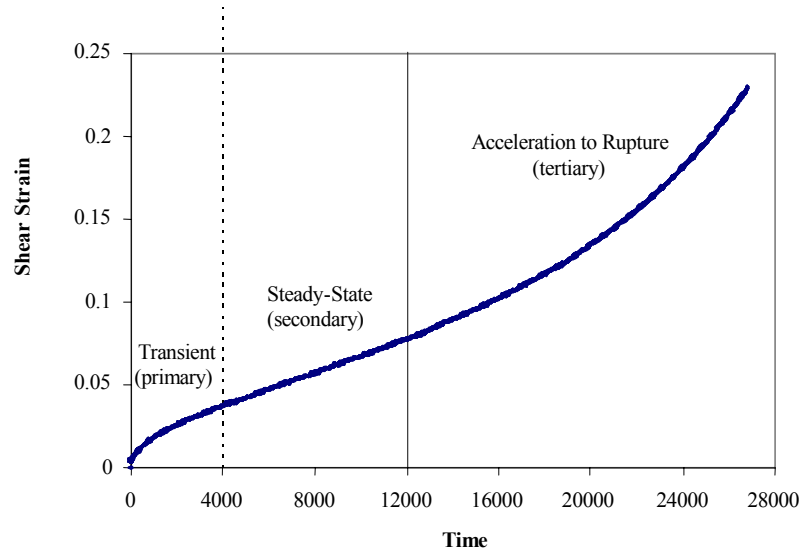


Figure 1.8: A typical constant-load creep test result of the Sn37Pb solder

Available data for seven Pb-free solder alloys are summarized in Table 1.7 for Equation (1.3a). In a few instances, Equation (1.3b) is used, as evidenced by the presence of α . Since some creep model constants reported in the literature are obtained from shear tests and some from tensile tests, the following standard von Mises relations are employed [Meyers and Chawla, 1984] to compare the results in terms of the effective strains and stresses:

$$\sigma = \sqrt{3}\tau \quad (1.4a)$$

$$\varepsilon = \frac{1}{\sqrt{3}}\gamma \quad (1.4b)$$

where σ and ε are effective stress and strain, respectively. Based on Equations (1.4a) and (1.4b), model constants are modified by the following conversion relations:

$$A = \frac{1}{\sqrt{3}} A_{shear} \quad (3.5a)$$

$$\alpha = \frac{1}{\sqrt{3}} \alpha_{shear} \quad (3.5b)$$

In addition, $f(T)$ in Table 1.7 means that the constant A is a function of temperature.

Test specimens used in these studies can be divided into two groups: bulk, cast, dog-bone shaped specimens and small solder joint type specimens. Tests conducted on the bulk specimens include those by Frear [Frear, et al., 2001], Mavoori [Mavoori, et al., 1997], Schubert [Schubert, et al., 2002a, 2002b], Neu [Neu, et al., 2001], Liang [Liang, et al., 1997], Raeder [Raeder, et al., 1994], Mei, [Mei and Morris, 1992], and Goldstein [Goldstein, et al. 1994a, 1994b]. There are four different solder joint type specimens: double lap shear [Darveaux, et al. 1995], single lap shear [Wiese, et al., 2001a], Iosipescu [Haswell and Dasgupta, 2001a], and modified single lap shear [Lee and Han, 2002]. The test ranges of the steady state strain rates are different among all tests, which span from 10^{-11} s^{-1} to 10^{-2} s^{-1} . The temperature ranges from -55°C to 180°C in all tests.

Solder Group	A (1/s)	α (1/MPa)	n	Q (kJ/mol)	Ref
SnAg	5.37×10^{-5}	0.0527	6.05	61.2	Frear 2001 Sn3.5Ag (1.3a)
	1.42×10^5		5.5	72.4	Darveaux 1995 Sn3.5Ag (1.3b)
	1.5×10^{-3}		11.3	79.5	Mavoori 1997 Sn3.5Ag (1.3a)
	5×10^{-6}	0.11535	4.75	57.2	Schubert 2002b Sn3.5Ag (1.3b)
			11	79.8	Wiese 2001a Sn3.5Ag (1.3a)
			9.6	94.0	Neu 2001 Sn4Ag (1.3a)
			1.0×10^{-2}		
SnCu	1.41×10^{-8}		8.1	79.4	Liang 1997 Sn1Cu (1.3a)
SnAgCu	1.5×10^{-5}	0.1878	3.69	36	Frear 2001 Sn3.8Ag0.7Cu (1.3a)
	2×10^{-21}		3.07	52.6	Schubert 2002a Sn3.8Ag0.7Cu (1.3b)
	2.44×10^{-12}		18	83.1	Wiese 2001a Sn3.8Ag0.7Cu (1.3a)
	7.15×10^{31}		8.36	59.8	Pao 1994 Sn4Cu0.5Ag (1.3a)
			f(t)	32.9	32.9
SnCuSbAg	1.75		8.91	82	Pao 1994 (1.3a) Sn2Cu0.8Sb0.2Ag
SnAgCuSb	1.45×10^{-12}		14.0	95.0	Neu 2001 (1.3a) Sn2.5Ag0.8Cu0.5Sb
SnBi	f(T)		3.1	59.8	Raeder 1994 Sn58Bi (1.3a)
	f(T)		4	70.5	Mei 1992a Sn58Bi (1.3a)
	f(T)		3.2	62.7	Goldstein Sn58Bi 1994a (1.3a)
SnIn	f(T)		3.3	70.5	Goldstein Sn52In 1994b (1.3a)
	f(T)		2.8-3.7	95.5	Mei Sn52In 1992b (1.3a)
SnZn	0.0217		5.7	65.2	Mavoori Sn9Zn 1997 (1.3a)

Table 1.7: Creep models of seven Pb-free solder alloys

Most Pb-free solders in this table (except Sn58Bi ,and Sn52In) consist of pure Sn grains and dispersed intermetallic. The steady state creep activation energy could, therefore, be

equal to or higher than pure Sn. The steady state creep of pure Sn is controlled by dislocation pipe diffusion process as σ/E is larger than 5×10^{-5} [Igoshev 2000]. The activation energy of such a process is close to 39.6-44.4 kJ/mol for pure Sn. Observation of Table 1.7 shows that activation energies of five Pb-free solders (SnAg, SnCu, SnAgCu, SnCuSbAg, Castin, and SnZn) are larger than 39.6-44.4 kJ/mol except the data of Sn_{3.8}Ag_{0.7}Cu from Frear [Frear, et al., 2001] and Sn_{3.9}Ag_{0.6}Cu from Haswell [Haswell and Dasgupta, 2001a]. It is also noticed that there is a large scatter in these published data. For example, the activation energy varies from 32.9 to 83.1 kJ/mol for SnAgCu solder alloy and stress exponent value also changes from 3.07 to 18. As for Sn₅₈Bi and Sn₅₂In solders, their activation energies are higher than that of dislocation pipe diffusion for pure Sn, and their stress exponent values are relatively smaller than those of the other five Pb-free solders.

1.3.1.2 Unified Constitutive Model

Both rate-independent plastic and rate-dependent creep deformations are combined as a rate-dependent inelastic deformation in unified constitutive models. By introducing an internal evolution variable for the physical material state, unified constitutive model relate steady state inelastic strain rate, $\frac{d\varepsilon_p}{dt}$, to stress, temperature and material properties as follows [Anand, 1982],:

$$\frac{d\varepsilon_p}{dt} = A \exp\left(-\frac{Q}{RT}\right) \left[\sinh\left(\alpha \frac{\sigma}{s}\right)\right]^{\frac{1}{m}} \quad (1.6)$$

where A , Q , R , σ and T are same parameters as those in equation (1.3b), except that s is an internal scalar variable, with dimensions of stress, called the deformation resistance

and m is the strain rate sensitivity of stress. An evolution equation for s has been proposed by Anand [Anand, 1982], which can be written as

$$\dot{s} = \left\{ h_0 \left| 1 - \frac{s}{s^*} \right|^a \operatorname{sign}\left(1 - \frac{s}{s^*}\right) \right\} \frac{d\varepsilon_p}{dt} \quad (1.7)$$

where s^* is the value of the internal variable at the saturation stress σ^* , h_0 is the hardening constant, a is the strain rate sensitivity of hardening. σ^* can be written as

$$\sigma^* = cs^* \quad (1.8a)$$

where

$$s^* = \hat{s} \left[\frac{1}{A} \frac{d\varepsilon_p}{dt} \exp\left(\frac{Q}{RT}\right) \right]^n \quad (1.8b)$$

and

$$c = \frac{1}{\alpha} \sinh^{-1} \left[\left\{ \frac{1}{A} \frac{d\varepsilon_p}{dt} \exp\left(\frac{Q}{RT}\right) \right\}^m \right] \quad (1.8c)$$

In these equations, \hat{s} is the coefficient for deformation resistance saturation value and n is the deformation resistance exponent. Combining Equations (1.8a)-(1.8c), the saturation stress σ^* can be described with the following relation:

$$\sigma^* = \frac{\hat{s}}{\alpha} \left[\frac{1}{A} \frac{d\varepsilon_p}{dt} \exp\left(\frac{Q}{RT}\right) \right]^n \sinh^{-1} \left[\left\{ \frac{1}{A} \frac{d\varepsilon_p}{dt} \exp\left(\frac{Q}{RT}\right) \right\}^m \right] \quad (1.9)$$

Based on Equation (1.9), the material constants: Q , A , \hat{s} , α , n and m can be fitted to the strain rate vs. the saturation stress data from a set of experiments. In addition, the stress can be written as:

$$\sigma = cs \quad (1.10)$$

So that equation (1.8b) can be rewritten as the following:

$$\frac{d\sigma}{d\varepsilon_p} = ch_0 \left(1 - \frac{\sigma}{\sigma^*}\right)^a \quad (1.11)$$

where h_0 and a can be determined by curve fitting experimental data.

Anand's model has been used to describe the constitutive behavior of traditional SnPb solders [Wilde, et al., 2000, Cheng, et al., 2000, Darveaux 2000, Wang, et al., 2001]. Very little data are available for Pb-free solders. Amagai and coauthors have presented the model constants for both Sn3.5Ag0.75Cu and Sn1.0Ag3.5Cu solders from their experiments using bulk solder specimens [Amagai, et al. 2002]. Wang and coauthors derived the viscoplastic Anand model constants based on Darveaux's tests [Darveaux and Banerji, 1992, Darveaux, et al. 1995] for Sn3.5Ag solders [Wang, et al., 2001]. Lee and Han have tested Sn3.5Ag Pb-free solders using single-lap shear specimens and obtained the Anand model constants [Lee and Han, 2002]. All model constants are summarized in Table 1.8. One set of constants for the Sn40Pb solders are also included for comparison.

Another unified creep-plasticity model employed to describe the constitutive behavior of Pb-free solders is the McDowell model [McDowell, 1992]. This model includes two isotropic hardening and two saturation stresses instead of one hardening and one saturation stress in Anand's model. Neu and coauthors have obtained the model constants for Sn4Ag and Castin (Sn2.5Ag0.8Cu0.5Sb) Pb-free solder alloys, based on tests conducted on bulk as-cast specimens, using a servohydraulic uniaxial test frame [Neu, et al., 2001]. Uniaxial strain rate jump tests along with isothermal cyclic tests were performed on Sn4Ag and Castin (Sn2.5Ag0.8Cu0.5Sb) Pb-free solder alloys.

Material Constants	Sn40Pb (Wang)	Sn3.5Ag (Wang)	Sn3.5Ag (Lee)	Sn3.5Ag0.75Cu (Amagai)	Sn1.0Ag0.5Cu (Amagai)
A (s^{-1})	1.49×10^7	2.23×10^4	22452	4.61×10^6	2.42×10^7
Q/R ($^{\circ}K$)	10830	8900	12270	8400	8400
α	11	6	19	0.038	0.043
M	0.303	0.182	0.5607	0.162	0.168
$\hat{\sigma}$ (MPa)	80.42	73.81	43.03	1.04	1.005
N	0.0231	0.018	0.0266	0.0046	8.10×10^{-4}
h_0 (MPa)	2640.75	3321.15	3327	3090	3162
A	1.34	1.82	1.2830	1.56	1.59

Table 1.8: Anand model constants for some Pb-free solder alloys

1.3.2 Mechanical Cycling Durability

Isothermal mechanical cycling durability is important for solders, because electronic assemblies are subjected to cyclic mechanical loading such as vibration and cyclic bending or twisting. Compared with thermal cycling tests, mechanical cycling tests are inexpensive and easier to conduct in the laboratory. There are reasonable amounts of data in the literature for mechanical cycling durability of SnPb solders [Cuttingco et al., 1990, Haswell, 2001, Solomon et al., 1989, Vaynman et al., 1993]. However, the experimental data are sparse for Pb-free solders. In 1995, Mavoori tested Sn3.5Ag and Sn9Zn solders using bulk, cast, dogbone-shaped specimens [Mavoori and Chin, 1995]. Mechanical cycling tests were conducted with total strain control on a servo-hydraulic machine. All tests were conducted at room temperature, at a frequency of 0.5 Hz, with no dwells at the extremes of the cycle. The results show that both Sn3.5Ag and Sn9Zn solders survived longer than Sn37Pb eutectic solder for the total strain range investigated (0.2-2%). Subsequent analysis of their data shows that the fatigue curves of both Pb-free solders have larger slopes than that of Sn37Pb solder. More recent mechanical cycling

test results have been reported for Pb-free solders by Kariya, et al., who conducted tensile mechanical cycling tests on bulk, cast, dogbone-shaped specimens made from Sn3.5Ag, Sn3.5Ag1Cu, Sn3.5Ag2Bi and Sn3.5Ag5Bi Pb-free solders using a servo-valve-controlled electro-hydraulic machine [Kariya, et al., 2001]. Four types of symmetrical (fast-fast and slow-slow) and asymmetrical (slow-fast and fast-slow) saw-tooth strain profiles are used in their tests, as shown in Figure 1.9. They found that the fatigue lives of four solders were dramatically reduced under slow-fast mode due to nucleation of creep cavities and intergranular failure during the slow tensile load step.

It was also found that the addition of Bismuth considerably decreases the fatigue life of Sn3.5Ag solder. They also presented the constants of the strain range-partitioning (SRA) model for four Pb-free solders. The strain range partitioning model is described by the following equation:

$$\frac{1}{N_f} = \left(\frac{\Delta\varepsilon_{pp}}{A_{pp}}\right)^{n_{pp}} + \left(\frac{\Delta\varepsilon_{cc}}{A_{cc}}\right)^{n_{cc}} + \left(\frac{\Delta\varepsilon_{cp}}{A_{cp}}\right)^{n_{cp}} + \left(\frac{\Delta\varepsilon_{pc}}{A_{pc}}\right)^{n_{pc}} \quad (1.12)$$

where N_f is the cycles to failure, $\Delta\varepsilon_{pp}$, $\Delta\varepsilon_{cc}$, $\Delta\varepsilon_{cp}$ and $\Delta\varepsilon_{pc}$ are the partitioned strain ranges for four types of cycles: plasticity reversed by the plasticity (pp), creep reversed by creep (cc), creep reversed by the plasticity (cp), and the plasticity reversed by creep (pc), respectively. In the Equation (3.12), n_{pp} , n_{cc} , n_{cp} , and n_{pc} are the reciprocals of the slopes of Coffin-Manson plots for the four types of partitioned strain ranges and A_{pp} , A_{cc} , A_{cp} , and A_{pc} are related to the intercepts of these plots. Constants of the SRA model for four solder alloys are listed in Table 1.9.

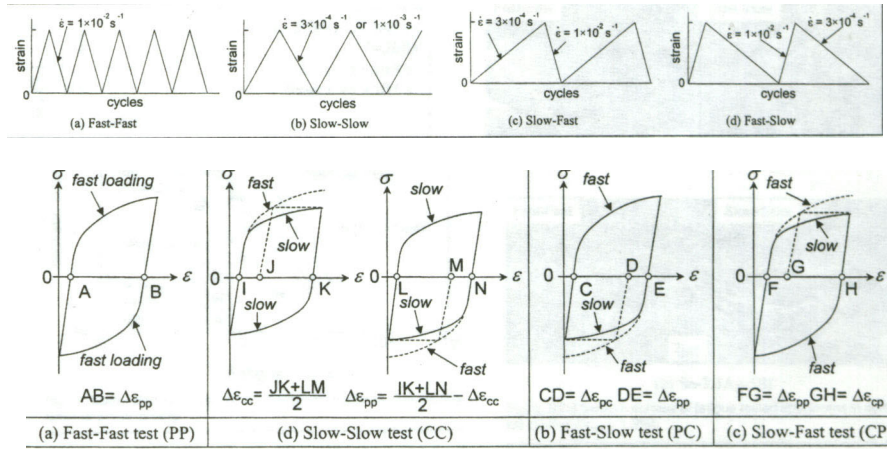


Figure 1.9: Typical strain profiles and hysteresis curve [Kariya, et al., 2001]

Model Constants	Sn3.5Ag	Sn3.5Ag1Cu	Sn3.5Ag2Bi	Sn3.5Ag5Bi
n_{pp}	1.92	1.82	1.85	2.50
A_{pp}	1.06	1.47	0.51	0.1
n_{cc}	1.56	1.22	2.27	2.44
A_{cc}	0.24	7.46	0.24	0.03
n_{cp}	1.67	0.71	1.41	1.03
A_{cp}	1.92	140.2	0.74	0.63
n_{pc}	0.98	0.65	2.43	0.88
A_{pc}	4.76	565.6	0.04	4.39

Table 1.9: Strain range partitioning model constants of some Pb-free solder alloys [Kariya, et al., 2001]

The effect of Bismuth on the mechanical durability of Sn3.5Ag solders was also investigated by Kariya and Otsuka [Kariya and Otsuka, 1998]. Bulk, chill-cast specimens of Sn3.5Ag and Sn3.5Ag-Bi (2, 5, 10%) solders were tested on a electromechanical testing machine. Tensile tests were carried out at room temperature and at a strain rate of 0.05 1/s. Coffin-Manson plots for all solders are shown in Figure 1.10. The durability dramatically decreases as Bismuth content increases in the Sn3.5Ag solder. They concluded that there are two reasons: (1) the decrease of ductility due to an increase of bismuth content; (2) coarse and plate-like Ag_3Sn intermetallic particles. It is

also noted in Figure 1.10 that fatigue curves of Sn3.5Ag and Sn3.5Ag-Bi (2, 5, 10%) solders have steeper slopes than that of the Sn37Pb solder.

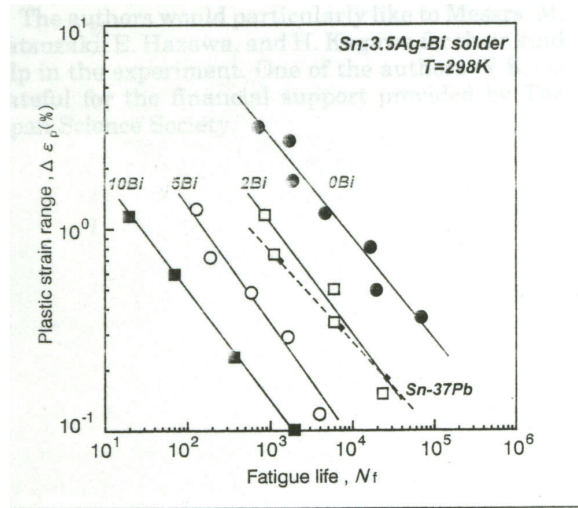


Figure 1.10: Coffin-Manson plots for Sn-3.5Ag-xBi solders [Kariya and Otsuka, 1998]

Flip chip specimens have been used to characterize the mechanical durability of several Pb-free solders [Wiese, et al., 2001b, Park and Lee, 2002], developed a micro-mechanical test apparatus with very high resolution of force and displacement. Their tester is so small that it can be used inside the SEM. The specimens were loaded in pure shear condition. The crack propagation of the Sn4Ag0.5Cu solder and the Sn37Pb solder was monitored by SEM during mechanical cycling tests at room temperature. The strain range was from 0.3% to 4% and the test frequency ranged from 0.0004 to 10Hz. Power law relations were used to correlate the crack growth rate da/dN (m/cycle) with the plastic work density ΔW_{pl} (Nm/m³) or the accumulated inelastic strain ϵ_{acc} in the following equations:

$$\frac{da}{dN} = \alpha_1 (\Delta W_{pl})^{\beta_1} \quad (1.13)$$

$$\frac{da}{dN} = \alpha_2 (\varepsilon_{acc})^{\beta_2}$$

Model parameters for both Sn4Ag0.5Cu and the Sn37Pb are listed in Table 1.10. Their results show that the exponent of either work-based or strain-based model for the Sn4Ag0.5Cu solder, the slope of the crack propagation rate versus $\Delta W_{pl}/\varepsilon_{acc}$ curve, is larger than that for the Sn37Pb solder.

Solder	α_1	β_1	α_2	β_2
Sn4Ag0.5Cu	2.5×10^{-8}	1.8	5×10^{-7}	2
Sn37Pb	8×10^{-7}	1	2×10^{-7}	1

Table 1.10: Parameters for crack propagation model [Wiese, et al., 2001b]

A similar tester was used by Park and Lee to characterize the durability of Sn3.5Ag0.75Cu solder [Park and Lee 2002]. Five different load states were employed to investigate the effect of the loading conditions (from tensile to pure shear), as shown in Figure 1.11. Their test results are shown in Figure 1.12. It is seen in the figure that fatigue life increases as phase angle increases. It is also noted that the slope of fatigue curve in terms of displacement range changes with the phase angle and the fatigue curve of pure shear condition (the phase angle = 90°C) has the flattest slope among all test conditions.

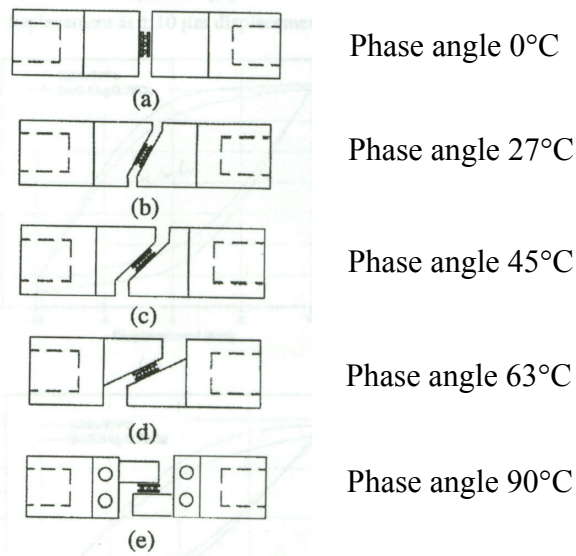


Figure 1.11: Test grip configurations [Park and Lee 2002]

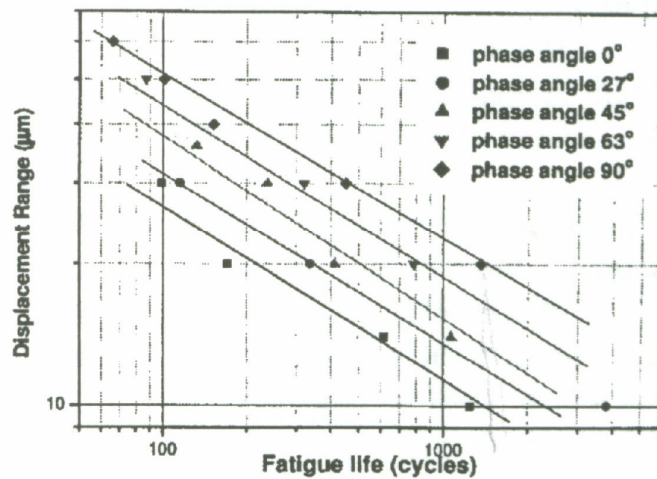


Figure 1.12: Fatigue life versus displacement range for Sn3.5Ag0.75Cu for different test grip configurations [Park and Lee 2002]

An important outcome of our present study is that under isothermal mechanical cycling, fatigue curves for Pb-free solders have a bigger slope than that for Sn37Pb, as shown in Figure 1.13. This observation is directly opposite of that for thermal cycling. A possible explanation for this phenomenon can come from different creep and plastic damage mechanisms between Sn37Pb and Pb-free solders. So one of the major objectives of this study is to explain this discrepancy by comparing generic energy-partitioning damage

models for thermal cycling durability and isothermal mechanical durability of both Sn37Pb and Pb-free solders.

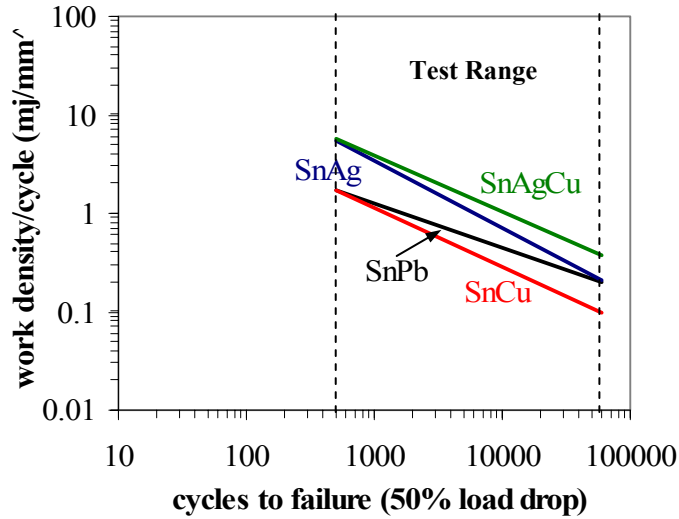


Figure 1.13: Work-based isothermal mechanical durability curve comparison of four solders at room temperature (3.3E-2 1/s strain rate)

1.3.3 Thermal Cycling Durability

The literature on thermal cycling durability of Pb-free solder joints has been rapidly increasing in recent years. Thermal cycling durability of solder joints is affected by a variety of factors such as package type, solder alloy composition, board/component finishes, reflow profile, cycle profile and so on. In this section, major focus is on reviewing the available literature on thermal cycling durability of the leading Pb-free solder joints for selected package styles. Related concerns such as the effects of board/component finish and reflow profile are discussed whenever it has been reported in the relevant papers.

In the search for a viable alternative to the SnPb solder alloy, extensive durability tests have been (and are being) conducted by a number of industry groups and consortia [IDEALS, NCMS, NEMI, JEIDA, IPC]. A broad range of components have been tested under different loading conditions. An European consortium called IDEALS (Improved Design Life and Environmentally Aware Manufacturing of Electronics Assemblies by Pb-free Soldering) [IDEALS, 1999a, 1999b, 1999c; Stam and Davitt, 2001] conducted a three-year study, where six kinds of accelerated durability tests were performed on SMT assemblies consisting of component such as chip resistors and MQFP 100 on FR4 assemblies. These tests included four air-to-air thermal cycle profiles, one liquid-to-liquid thermal cycle profile, and one power cycle profile, as shown in Table 1.11.

Test Type	T _{min} (°C)	T _{max} (°C)	No. Cycles	Cycle Time
Single chamber gas	-20	100	2000	1 hour cycle, ~20 minute dwells
Single chamber gas	-20	125	3500	2 hour cycle, asymptotic heating and cooling curves
Twin chamber gas/gas	-20	100	4000	1 hour cycle, rapid transfer, 30 minute dwells
Twin chamber gas/gas	-40	125	3000	1 hour cycle, rapid transfer, 30 minute dwells
Twin bath liquid/liquid	-20	125	3000	7 minute cycle, rapid transfer, 3 minute dwells
Power cycling	+25	110	5000	~20 minute cycle, asymptotic heating and cooling, 10 min. dwell @ 110°C. Temperatures for joints.

Table 1.11: Thermal cycling test matrix from the IDEALS projects

The Pb-free solders tested were Sn3.8Ag0.7Cu and Sn3.8Ag0.7CuX, where X is a proprietary elemental addition. Five kinds of component finishes and five kinds of board finishes were used for both reflow and wave soldering processes, respectively. In terms of thermo-mechanical test results, they concluded that the cyclic thermomechanical durability of the Pb-free assemblies is comparable to SnPb solder assemblies. It was also

found that the board/component finishes have significant effects on the durability of Pb-free assemblies, as shown in Figure 1.14.

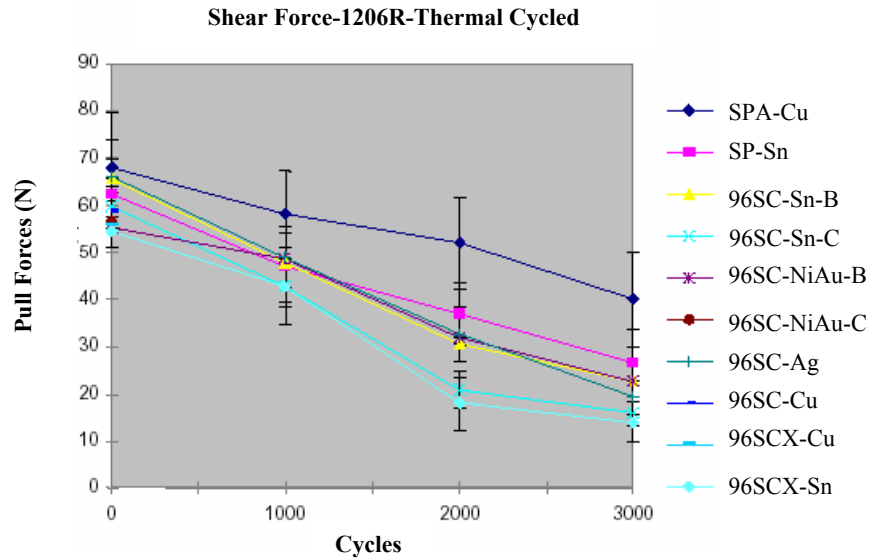


Figure 1.14: Shear strength variation with cycles for 1206 resistor for solder-board-paste medium combination. SPA=Sn36Pb1Ag SP=Sn37Pb 96SC=Sn3.8Ag0.7Cu 96SCX= Sn3.8Ag0.7Cu plus 0.4%X [IDEALS, 1999a, 1999b, 1999c; Stam and Davitt, 2001]

NCMS (National Center for Manufacturing Sciences) is an industry consortium actively conducting Pb-free solder research in USA. Two multi-year projects were conducted to investigate Pb-free solders for both general purpose and high temperature applications [Soldertec, 1999, Gayle, et al., 2001; Syed, 2001a; Syed, 2001b; Whitten, 2000]. In the first project, SMT test vehicles were assembled by reflow soldering LCCC44, 1206 resistors, QFP132, and PLCC84 on FR4 printed wiring boards. Test assemblies were thermally cycled according to two thermal profiles: (i) -55~+125°C with 20 min dwells and 11°C/min ramp rate; and (ii) 0~100°C with 5 min dwell and 10 min transition. The tested solder alloys included Pb-free solders such as Sn3.5Ag, Sn3Ag2Bi, Sn3.4Ag4.8Bi, Sn57Bi, Sn2.8Ag20In, Sn2.6Ag0.8Cu0.5Sb, Sn3.5Ag0.5Cu1Zn, and Sn37Pb as a control solder. Figure 1.15 and Figure 1.16 show their thermal cycling results. The results varied

with solder type, component style and loading magnitude. Sn57Bi outperformed all other solders for LCCC packages subjected to profile I. The Sn3.4Ag4.8Bi solder has the best durability in thermal profile II for 1206 chip resistor. It is also noticed that the scatter in the failure data of all solders increases as the test environment becomes more severe. This may be a result of multiple failure mechanisms, such as fatigue within the bulk of the solder and interfacial failures in the intermetallic (e.g. due to poor wetting).

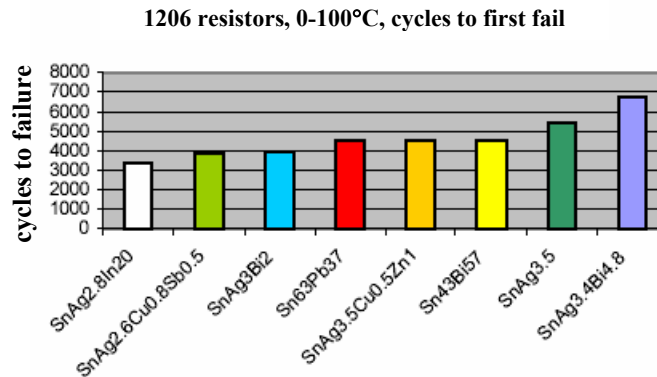


Figure 1.15: Thermal cycling fatigue life comparison of the Pb-free solders for chip resistor 1206 [Soldertec, 1999]

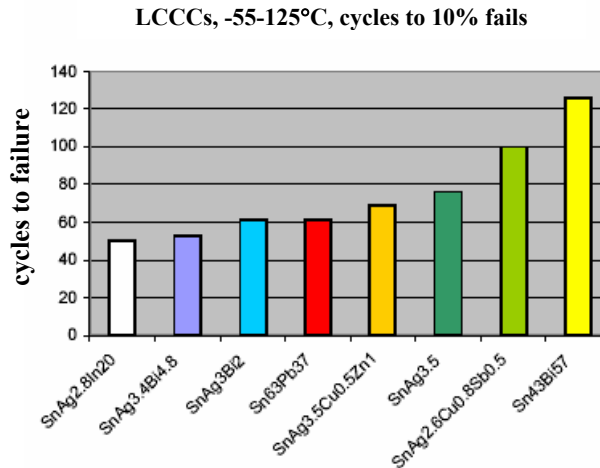


Figure 1.16: Thermal cycling fatigue life comparison of the Pb-free solders for LCCC44 [Soldertec, 1999]

The purpose of the second project was to identify Pb-free solders for high temperature application (up to 160°C). There were two stages in this project. In the preliminary stage, thirteen Pb-free solder alloys were screened by thermal cycling tests of the following profile: -55~160°C, ramp rate of 10°C. The tested solders were Sn3.5Ag, Sn4.7Ag1.7Cu, Sn4Ag1Cu, Sn4Ag0.5Cu, Sn4.7Ag1.7Cu0.5Co, Sn2.5Ag0.8Cu0.5Sb, Sn4.6Ag1.6Cu1Sb1Bi, Sn3.3Ag1Cu3.3Bi, Sn3.3Ag4.8Bi, Sn3.5Ag1.5In, Sn3.5Ag0.5Cu1Zn, Sn0.7Cu, Sn0.7Cu1In, and the control Sn37Pb solder. The test boards were built up with different types of SMT components (TSOP32, PLCC68, UTQFP80, QFP120, QFP160, PBGA256, LCCC20, CR0805 and CR1206), assembled on FR4 PWBs. The fatigue life comparison among all tested solders is shown in Figure 1.17 for LCCC20. It is seen that Sn37Pb solder outperformed all Pb-free solders in this very severe test environment. The (compared to Sn3.5Ag) varies from around 0.5 to more than 2 for all the alloys tested. Based on the thermal cycling test results, the following seven alloys appeared to be the best performers and were selected for further study in the second stage: Sn3.5Ag, Sn4Ag1Cu, Sn4Ag0.5Cu, Sn3.3Ag1Cu3.3Bi, Sn2.5Ag0.8Cu0.5Sb, Sn4.6Ag1.6Cu1Sb1Bi, Sn3.3Ag1Cu3.3Bi, Sn3.5Ag1.5In. Two types of ball grid array (BGA) packages using these seven solders were tested under two separate test profiles: TC1: -40~+125°C, ramp time of 10 min., dwell time of 10 min., single zone chamber cycling; TC3: 0~+100°C, ramp time of 10 min., dwell time of 5 min., single zone chamber cycling.

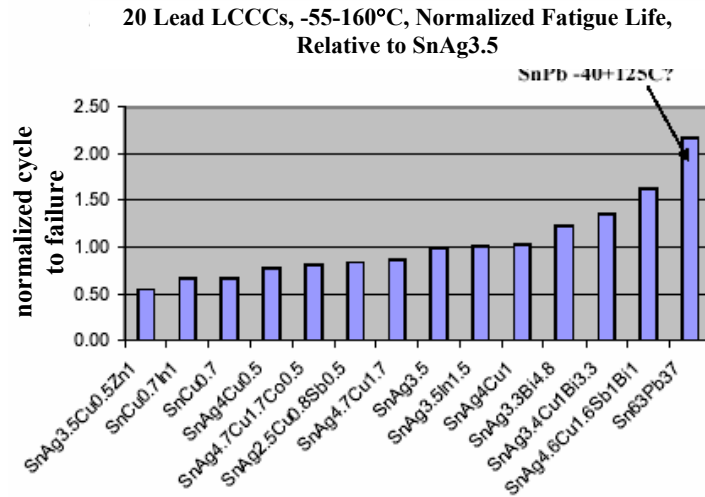


Figure 1.17: Thermal cycling fatigue life comparison of the Pb-free solders for LCCC20 [Gayle, et al., 2001; Whitten, 2000]

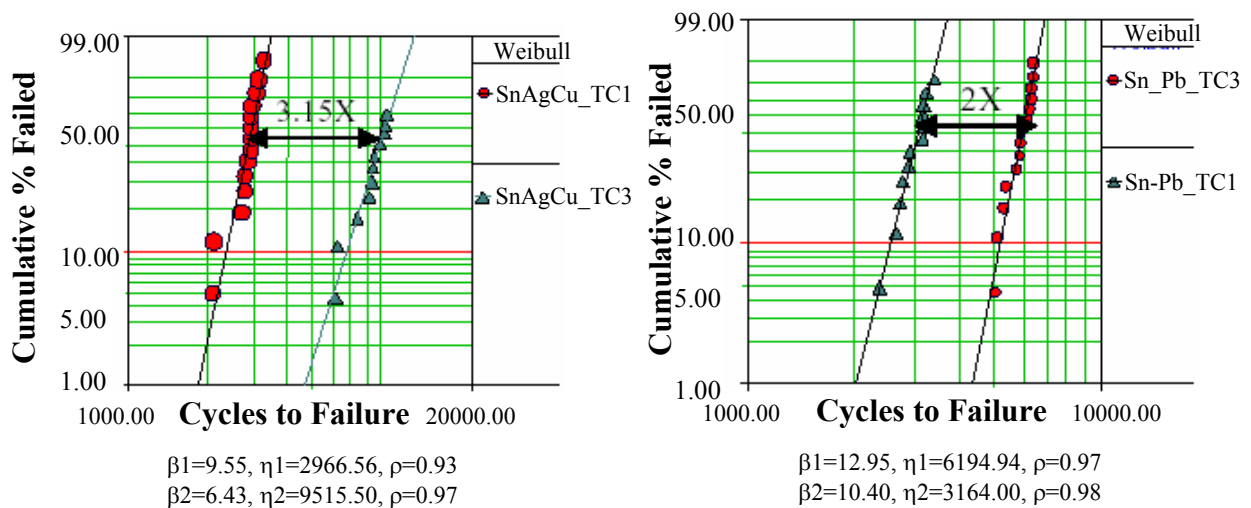


Figure 1.18: Acceleration factor comparison for Sn37Pb and Sn4Ag0.5Cu alloys (TC1 and TC3 thermal cycling, fleXBGA package) [Syed, 2001b]

The BGA packages tested were PBGA256 and fleXBGA144. An interesting result is shown in Figure 1.18. The Pb-free Sn4Ag0.5Cu solder shows higher acceleration factor than eutectic Sn37Pb solder over a large temperature range, implying the possibility of higher durability at field conditions for the Pb-free solders, even if they fail first under accelerated testing. Their results also suggest that the slightly different composition in

the Pb-free SnAgCu solders has no significant influence on the thermal cycling durability (for the range of variation examined).

There has also been significant amount of independent research efforts on the thermal cycling durability of the Pb-free solders, conducted by many electronics companies such as Motorola, Boeing, HP, National Semiconductor, IBM, Sony, FUJITSU, TI, ChipPAC, Flip Chip, and so on.

Boeing has performed extensive studies on the durability of the Pb-free Sn3.8Ag0.7Cu solder for reflow application and Sn0.7Cu solder for wave application [Boeing, 2002, Woodrow, 2002]. The effects of three kinds of board finishes (immersion silver, Ni/Au, and OSP) were also evaluated during these tests. The test assemblies were built by reflowing forty 1206 chip resistors and wave-soldering forty 1206 chip resistors on FR4 boards with different finishes. The test vehicles were then thermally cycled as per the following profile: -55~+125°C with dwell time of 15 minutes at each temperature extreme and a ramp rate of 7°C per minute. Their test data for reflowed Sn3.8Ag0.7Cu solder joints are shown in Figure 1.19. The Pb-free Sn3.8Ag0.7Cu solder joints began to fail much earlier than the Sn37Pb solder joints for all three finishes. The author suggested that it was due to the large coefficient of thermal expansion (CTE) mismatch between ceramic resistors and FR4 boards. It was also found that the board finish does have significant effects on the durability of the Pb-free solder joints. In the wave soldered test specimens, the Pb-free Sn0.7Cu solder joints failed at about the same

number of cycles as the Sn37Pb control specimens. They recommended that the Sn0.7Cu solder is a suitable alternative for Sn37Pb in wave soldering applications.

Motorola has also reported numerous studies on Pb-free solders [Frear, et al., 2001, Guo, et al., 2001, Jonnalagadda, et al., 2001, Levis and Mawer, 2000, Lin, et al., 2001, Zhang, et al., 2001]. Three Pb-free solders (Sn0.7Cu, Sn3.5Ag, Sn3.8Ag0.7Cu) were evaluated for flip-chip assemblies on FR4 substrates, by extensive thermal cycling tests. Two thermal cycling profiles were used: $-40\sim+125^{\circ}\text{C}$ and $0\sim+100^{\circ}\text{C}$, both at the frequency of 1 cycle/hour. A variety of under-bump metallurgies (UBM) (TiW/Cu, electrolytic nickel, and electroless Ni-P/Au) were also selected to investigate their effects on the durability of the Pb-free solder bumps. The optical micrographs of failed solder joints are shown in Figure 1.20. It is seen that cracks propagate near the solder/intermetallic interface for all the alloys except Sn0.7Cu, which deforms by grain sliding and fails further in the interior of the joint. The thermal fatigue data, as shown in Figure 1.21, shows that Sn0.7Cu solder is the best performer among Sn37Pb solder and the Pb-free solders, for the selected thermal cycle, due to its ability to sustain large deformations. This deformability occurs because of the relatively low yield strength and relatively high steady state creep rate. The authors also report that the short fatigue life for Sn3.8Ag0.7Cu and Sn3.5Ag solders was due to the failure mode of crack initiation and propagation at the intermetallics and intermetallic/solder interface.

Although eutectic SnPb solder has the same low shear strength and high steady state creep rate, its fatigue life was shortened by heterogeneous coarsening. The dashed parallel straight lines were added by the authors of this study, implying that the slope of

the fatigue curves are the same for all three solders. However, they do not present any experimental data to support this hypothesis. It seems that thermomechanical fatigue phenomenon in this environment is very complex and more investigation is needed.

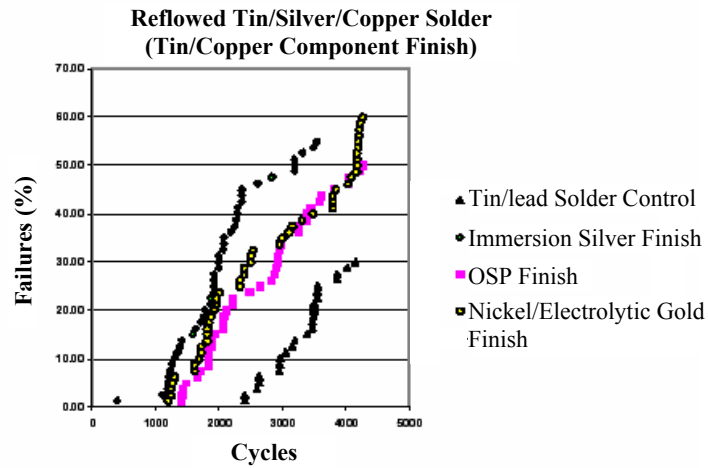


Figure 1.19: Durability of reflowed Sn3.8Ag0.7Cu solder joints [Boeing 2002]

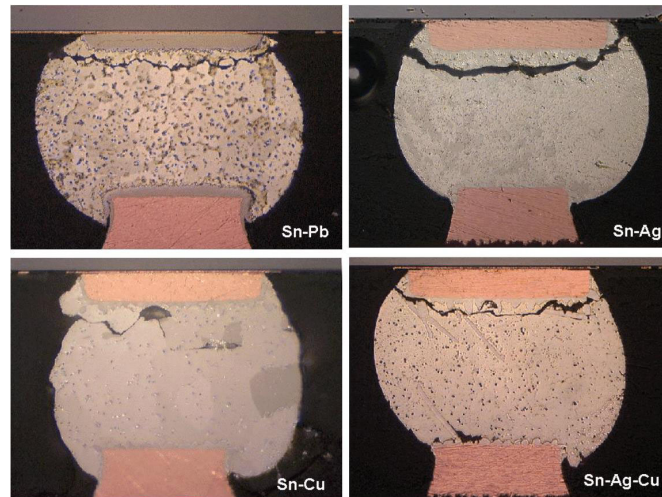


Figure 1.20: Optical micrographs of the cross sections of four tested solder joints on Cu UBM after thermal cycling from 0°C to 100°C [Frear, et al., 2001]

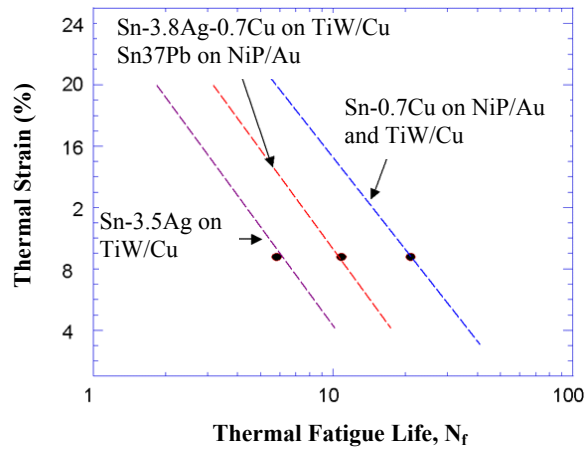


Figure 1.21: Thermal fatigue life versus thermal strain for four solder alloys [Frear, et al., 2001]

The thermo-mechanical fatigue durability of Pb-free solder joints in PGBA packages was also evaluated in Motorola [Jonnalagadda, et al., 2001, Levis and Mawer, 2000]. Jonnalagadda, et al., conducted liquid-liquid thermal shock testing from -55°C to 125°C on PBGA196 packages with Sn37Pb solder balls, assembled with Pb-free solder pastes (Sn3.4Ag4.8Bi, Sn3Ag0.7Cu, and Sn3.8Ag0.7Cu). The two SnAgCu solder pastes exhibited higher failure rates than that of Sn37Pb solder paste, even though all the solder assemblies exceeded typical requirements for portable electronic products. Another study was performed by Levis and Mawer to evaluate thermal fatigue durability of four kinds of solder joints formed by assembling Sn3.5Ag and Sn36Pb2Ag solder balls with Sn37Pb and Sn3.8Ag0.7Cu solder pastes. A 324 PBGA package was used for this study. Assembled boards were tested using two thermal cycling conditions: $-40\sim+125^{\circ}\text{C}$ with 15 min ramp and 15 min dwell; $-50\sim+150^{\circ}\text{C}$ with 24 min ramp and 15 min dwell. They found that PBGAs with Pb-free solder balls have longer thermal fatigue life than those with eutectic Sn37Pb in their test conditions.

Lead contamination is a major concern in thermal cycling fatigue of Pb-free solders joints because it is inevitable during the transition period from traditional lead-based solder technology to Pb-free technology. Several researchers have explored this issue using thermal cycling tests [Amagai, et al., 2002, Nurmi and Ristolainen, 2002, Patwardhan, et al., 2002, Prasad, et al., 2002, Roubaud, et al., 2002, Seelig and Suraski, 2001]. Lead contamination is now known to cause severe fillet lifting on wave-soldered through-hole joints, as discussed in the IDEALS project and in Suraski's work. Table 1.12 summarizes the thermal cycling tests of the four studies listed above. These tests focused on the thermo-mechanical fatigue of the SMT components with SnPb, Pb-free, and mixed SnPb/Pb-free solder joints. Their results appear conflicting. Nurmi and Ristolainen found that solder joints made with Sn37Pb solder balls and Pb-free solder pastes have better thermal fatigue resistance than solder joints made with Pb-free solder balls and Pb-free solder pastes (see Table 1.12 for testing details) [Nurmi and Ristolainen, 2002]. But the results from Roubaud, et al. indicate that Pb-free solder joints made with Pb-free solder balls and pastes have superior thermal fatigue resistance compared to joints made with eutectic SnPb solder balls and either SnPb or Pb-free pastes, for the thermal cycle investigated (see Table 1.12 for testing details) [Roubaud, et al., 2002].

Author	Solder Ball/Bump	Solder Paste	Package	TC Profile
Amagai, et al.	Sn36Pb2Ag Sn1Ag0.5Cu	Sn37Pb Sn3.5Ag0.75Cu	CSP151	-40~+125°C Dwell: 10 min. Ramp: 5 min.
Nurmi and Ristolainen	Sn37Pb Sn3.8Ag0.7Cu	Sn37Pb Sn3.8Ag0.7Cu	BGA151	-40~+125°C Dwell: 14 min. Ramp: 1 min.
Patwardhan, et al.	SnPb SnAgCu	SnPb Sn3.6Ag0.7Cu	WLCSP	-25~+125°C Dwell: 9 min. Ramp: 1 min.
Roubaud, et al.	Sn37Pb Sn3.5Ag Sn0.75Cu Sn4Ag0.5Cu Sn2.5Ag1Bi0.5Cu	Sn37Pb Sn4Ag0.5Cu	PBGA μBGA CSP MQFP	-40~+125°C Dwell: 15 min. Ramp: 15 min. 0~+100°C Dwell: 10 min. Ramp: 10 min.

Table 1.12: Summary of thermal cycling tests on lead contamination [Amagai, et al., 2002, Nurmi and Ristolainen, 2002, Patwardhan, et al., 2002, Roubaud, et al., 2002]

In addition, the effects of lead contamination also appear to have a complex dependence on the pad plating materials used. Amagai, et al., found that Cu plating is preferable for SnPb solders but Au/Ni plating is preferable for Pb-free solders. Their study also concludes that the thermal fatigue life of solder joints is reduced by the use of Pb-free pastes with SnPb solder balls. Most researchers now agree that the comparison of the thermal cycling fatigue durability of Pb-free solder joints to that of SnPb joints depends on the thermal cycling conditions, package type, and plating materials (including lead-contamination) [Prasad, et al., 2002; Roubaud, et al., 2002].

Additional Pb-free thermal cycling tests in the literature that has not been discussed in the previous section are summarized in Table 1.13. These studies indicate that SnAgCu is the most commonly studied Pb-free solder under thermal cycling conditions because many industrial consortia recommend this solder. Researchers from Japan are also

interested in SnAgCu solder alloy with small amount of Bi additions. CSP and Flip-Chip packages were extensively tested because they represent the future trends in packaging. Furthermore, these package styles impose the most severe mismatch stresses in the solder joints. The results from these tests are similar to those discussed in previous paragraphs.

In summary, the reliability of most Pb-free solder interconnects is better than that of Sn37Pb interconnects when the loading levels are not very high (e.g. for benign test conditions such as low peak temperature and small cyclic temperature range, and for packages with compliant leads and low CTE mismatches); but this difference decreases as the loading level increases. In fact, under extremely high loading (e.g. for severe test conditions and stiff interconnects with large CTE mismatch), Sn37Pb interconnects have actually outperformed some Pb-free interconnects [Woodrow, 2002, Suhling, 2003]. Sample data for a flip-chip die on FR4 shown in Table 1.14 [Schubert, 2002a], and for a flexBGA shown in Figure 1.22 [Gayle, 2001], illustrate this trend for two different thermal cycling environments. Similarly, Figure 1.23 [Syed, 2001b] illustrates this trend for two different packages subjected to the same thermal cycling environment. In this case, the flexBGA interconnects experience higher loading than the PBGA interconnects, because of higher CTE mismatch. The data in Figure 1.23 and Figure 1.24 are part of a large experimental study conducted by a NCMS taskforce on a variety of surface mount assemblies [NCMS, 1997]. As part of this NCMS study, the authors conducted viscoplastic finite element simulation of several of the component styles tested, to present the failure data in terms of creep work dissipated in the critical solder joints. The results presented in Figure 1.24 (obtained from FEA analysis of failed LCCC44 packages),

clearly demonstrate the difference in the slopes of the fatigue curves for Sn37Pb solder and Pb-free solders. The important consequences of this observation are that (1) the ranking between the durability of these different solders is load-dependent; and (2) Pb-free solders will have higher acceleration factors than Sn37Pb solder, when conducting accelerated thermal cycling durability tests.

Author	Solder Ball/Bump	Solder Paste	Package	TC Profile	Results
<i>Akamatsu, et al.</i>	Sn37Pb Sn58Bi	Sn37Pb Sn3Ag0.5Cu	BGA672	-25~+125°C -40~+125°C Dwell: 9 min. Ramp: 1 min.	SnBi/SnAgCu balls have better thermal cycling durability than SnPb balls
<i>Balkan, et al.</i>	Sn37Pb SnAgCu	Sn37Pb SnAgCu	Flip-Chip with underfills	-40~+125°C Dwell: 15 min. Ramp: 15 min.	SnAgCu bumps passed 1000 thermal cycles
<i>Farooq, et al.</i>	Sn37Pb Sn3.8Ag0.7Cu Sn5Sb Pb10Sn	Sn37Pb Sn3.8Ag0.7Cu	CBGA625	0~+100°C 2 cycles/hour	SnAgCu and SnSb systems have much longer lifetimes than Sn37Pb and Pb10Sn systems
<i>Grossmann, et al.</i>		Sn9Zn Sn3.8Ag0.7Cu Sn3.5Ag Sn2.6Ag0.8Cu0.5Sb	LCCC24	-20~+120°C Dwell: 30 min.(L), 10 min.(H) Ramp: 40 min.	Pb-free solder joints degrade faster than SnPbAg in terms of crack length
<i>Hirano, et al.</i>	Sn3.5Ag0.75Cu Sn2.5Ag0.5Cu1Bi Sn7.8Zn3Bi Sn37Pb	Sn3.5Ag0.75Cu Sn2.5Ag0.5Cu1Bi Sn7.8Zn3Bi Sn37Pb	CSP196	-25~+125°C 2 cycles/hour	Double-sided placement and board finish have a great influence on durability of Pb-free solders
<i>Hou, et al.</i>	Sn3.5Ag0.7Cu Sn37Pb	Sn3.5Ag0.7Cu Sn37Pb	Flip-Chip with underfill	-40~+125°C Liquid-Liquid Thermal Shock	Compared to SnPb, thermal shock durability of SnAgCu is reduced
<i>Kim, et al.</i>	SnAgCu Sn37Pb	SnAgCu Sn37Pb	WLCSP98	-40~+125°C Dwell: 15 min. Ramp: 15 min.	The Weibull life SnAgCu is 18% higher than that of SnPb
<i>Schubert, et al. 2002b</i>	Sn3.5Ag Sn4Ag0.5Cu Sn37Pb	Sn3.5Ag Sn4Ag0.5Cu Sn37Pb	Flip-Chip with underfill	-55~+125°C -55~+150°C Dwell: 10 min. 2 cycles/hour	Pb-free solders perform worse than SnPb in thermal cycling tests
<i>Shohji, et al.</i>	Sn3.5Ag Sn3.5Ag0.76Cu Sn1.9Ag0.5Cu7.6Bi Sn37Pb	Sn3.5Ag Sn3.5Ag0.76Cu Sn1.9Ag0.5Cu7.6Bi Sn37Pb	Flip-Chip	0~+100°C 3 cycles/hour	Pb-free solders have equivalent thermal fatigue lives to SnPb solders
<i>Wojciechowski, et al.</i>	Sn4Ag0.5Cu	Sn4Ag0.5Cu	LFPGA PSGA	-65~+150°C JESD22-A104	Pb-free solders passed 500 cycles qualification
<i>Xie, et al.</i>	Sn3.9Ag0.6Cu	Sn3.9Ag0.6Cu	CSP8~308 QFP208	-40~+85°C 0~+100°C -55~+125°C 0~+55°C	All Pb-free packages met consumer product spec. but only a few met telecomm spec.
<i>Zama, et al.</i>	Sn3.5Ag0.5Cu SnPb	Sn3.5Ag0.5Cu SnPb	Flip-Chip with underfill	-55~+125°C Liquid-Liquid Thermal Shock	SnAgCu failed more earlier than SnPb

Table 1.13: Summary of thermal cycling tests from literature

Test Conditions	Sn37Pb	Sn4Ag0.5Cu
-55 °C to 125 °C	2299	1929
-55 °C to 150 °C	1864	1237

Table 1.14: Reliability of two solder interconnections for Flip Chip on FR-4 boards with underfill [Schubert, 2002a]

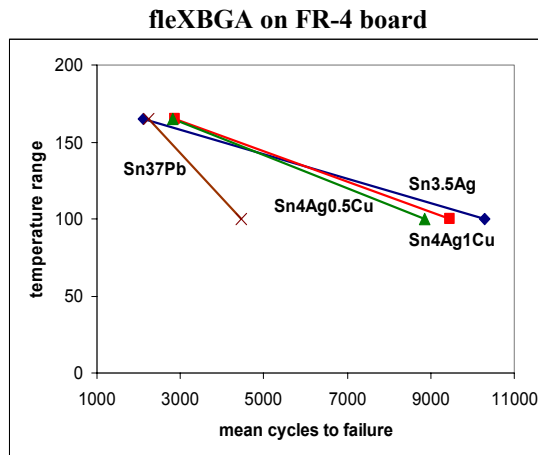


Figure 1.22: Reliability comparison of four solders in two different test conditions (0/100 °C and -40/125 °C temperature ranges) [Gayle, 2001]

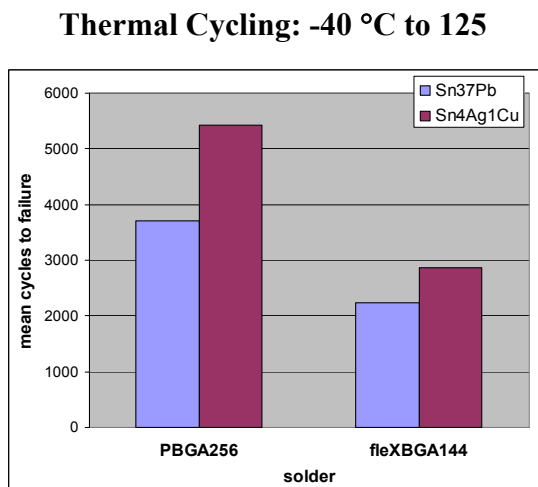


Figure 1.23: Reliability comparison of Sn4Ag1Cu with Sn37Pb solder interconnections for two different packages [Syed, 2001b]

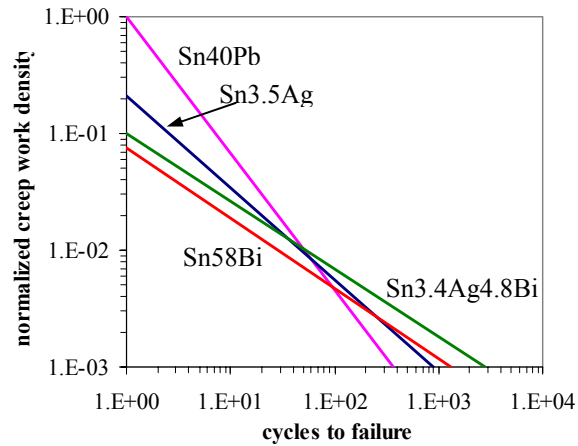


Figure 1.24: Thermal cycling durability curve comparison of four solders with creep work density as failure criterion [NCMS, 1997]

1.4 Test System

The experiments in this study are conducted on a custom test setup, Thermo-Mechanical-Microscale (TMM) setup, designed by Haswell for isothermal mechanical testing of solder materials [Haswell and Dasgupta, 1999, 2000, 2001, Haswell, 2001]. This setup is designed to conduct monotonic tests for constitutive properties as well as for cyclic durability tests, at different temperatures. The important feature of the setup is that it is designed to test specimen that is small enough to represent the length-scale effects that are expected to dominate in real solder joint in modern packaging architectures (e.g., CSPs, flip chips, etc.). Since the solder specimen is too small to be held in the test machine, it is soldered to two copper platens that provide the gripping area. This setup was modified during this study for more effective operation, as described in Section 1.4.2. The test system is briefly reviewed in this section and the details can be found in elsewhere [Haswell, 2001]. The modification during this study on the test setup is also discussed.

1.4.1 Test Specimen

The tests developed for this work use a simple, notched shear specimen similar to that proposed by Iosipescu [1967], which produces a very uniform stress field in the specimen gage zone [Reinikainen et al., 1997]. As shown in Figure 1.25, the TMM specimen consists of a thin layer of solder connected to two copper platens. The solder joint is typically 0.17-0.20 mm wide, 3.0 mm long and approximately 1mm thick. The specimen is originally 1.5mm thick and reduced to an approximate 1mm thickness using a standard grinding and polishing process.

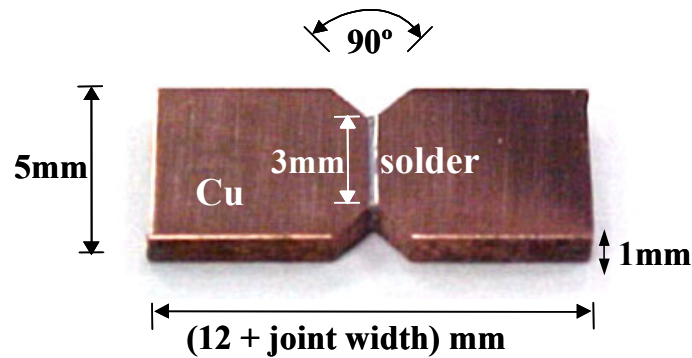


Figure 1.25: TMM specimen schematic

A manual soldering method using solder wire has been developed to produce high quality specimens with very low void content. Two major considerations in the development of the soldering method are good wetting of the solder to the copper and precise alignment of the two copper platens that are soldered together. The method is also designed to mimic a reflow process typically found in a mass-production assembly line, which includes a relatively slow preheat and comparatively fast melt and cool-down cycles. Before the soldering step, soldering surfaces of the copper platens were first polished using 1200 grit sandpaper, in order to produce a flat, uniform wetting surface. Then the wetting surfaces are cleaned twice by RMA flux and alcohol. After the cleaning, two

copper platens are placed in the alignment fixture and the solder joint height is established by inserting a shim spacer with a thickness of 180 μ m between two platens. After removal of the spacer, the two platens are checked visually for flatness and alignment in the fixture. A drop of RMA flux is placed over the gap between the platens, and the entire assembly is placed on a pre-heat plate with the temperature higher than the activation temperature of the solder flux. If the solder wire is not flux cored, then it is dipped in RMA flux before application. After the flux evaporates (or activates), the entire assembly is moved to the other hot plate with the temperature 40°C higher than the melting point of the solder. Then a length of solder wire is applied to the platen gap, and held there until the solder wire fully melts and the liquid solder fills the gap (it usually takes 30~45 seconds). At last, the entire assembly is moved on a steel heat sink to solidify the solder joint.

After the soldering and initial inspection, specimens are placed in a holding fixture and then grounded and polished in a group of six using the standard procedure. There are two reasons for this step: to reduce the specimen thickness from 1.5mm to 1mm, and to polish the joint surface to reveal the solder microstructure. Specimens are then conditioned at approximate 80% of absolute melting temperature (or 0.8 homologous temperature; e.g. 100°C for Sn63Pb37 eutectic solder) for 100 hours on the hot plate in order to stabilize the solder microstructure and to relax any residual stresses that remain from the reflow or polishing processes. Although the specimen is wrapped with high-temperature Kapton tape to reduce oxidation during aging, the surface is slightly polished again after aging in

order to obtain high quality micrographs. The result from the above process is a very uniform solder joint with rare voids, as shown in Figure 1.26.

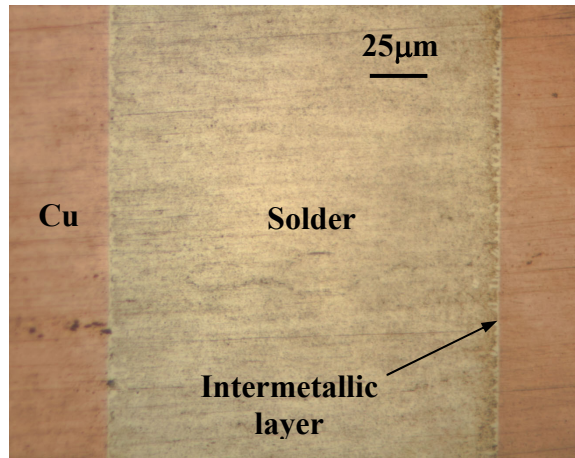


Figure 1.26: Optical micrograph of a Sn3.9Ag0.6Cu solder specimen

Test specimens are fully characterized before performing test. Geometric parameters such as joint height, specimen thickness and joint length are measured using digital micrometers. The microstructural features (e.g. average intermetallic particle size in Pb-free specimens), intermetallic layer thickness at soldered interfaces; and surface void content are characterized using an inverted metallographic optical microscope or a scanning electron microscope (SEM). There are two reasons for the microstructural observation: to obtain the understanding of the microstructural characteristics of Pb-free solder joints; to eliminate the specimens with any evidence of weak interfacial bonds, unusual microstructural formations (e.g. a very thick intermetallic layer), irregular joint geometries, and high void content. The detailed discussion about the microstructural characteristics of Pb-free solder specimens is presented in Section 2.1.

1.4.2 Test Setup

The TMM test setup designed by Haswell [Haswell, 2001] is shown in Figure 1.27. The frame is made from stainless steel, and is machined with a high precision using both conventional milling and wire electro-discharge machining (EDM). A solid-state lead-zirconate-titanate (PZT) piezoelectric stack actuator, installed in the integrated actuator collar, applies displacements to the specimen grips over a range of $90\mu\text{m}$ through a flexible link, a low-friction, Frelon™-lined linear bushing and a connecting shaft. The use of the flexible link and the linear bushing protects the actuator from the off-axis and bending loads generated by the shear loading during specimen installing and testing as the PZT ceramic material is extremely venerable to these kinds of loads. The bushing also maintains the axial alignment of the grip that might rotate due to bending moments generated by the shear loading.

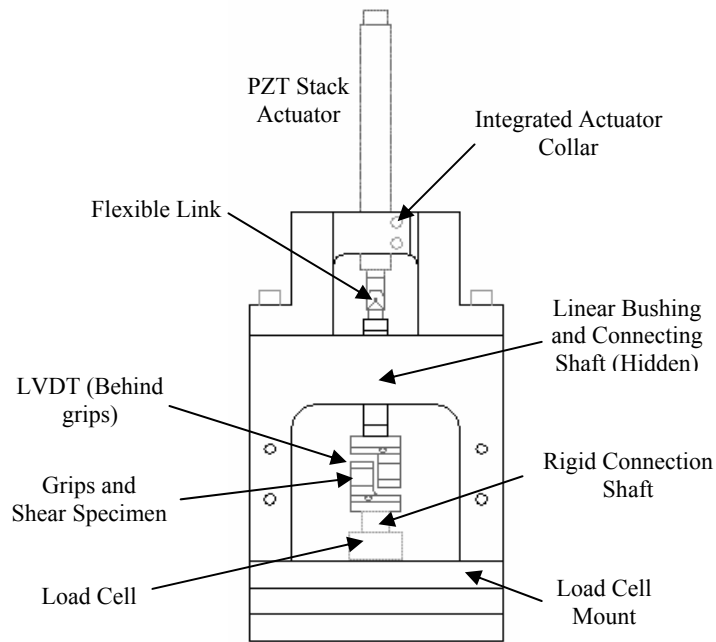


Figure 1.27: TMM test frame [Haswell, 2001]

The applied deformation is measured and controlled using a linear variable differential transformer (LVDT) spanning across the specimen grips. The resolution of the LVDT (and therefore the positioning resolution of the actuator) is determined by the resolution of the data acquisition system. A data acquisition card with a 16-bit digital-to-analog and analog-to-digital converter is used to collect test data as well as provide a control signal to the PZT actuator. With this I/O system, the effective positional resolution is approximately ± 10 nm. The force in the system is measured by a 445N capacity miniature tension/compression load cell with the effective resolution of 0.1N.

The test specimen is installed in the specimen grips with two set screws. The detailed grip schematic is shown in Figure 1.28. The specimen is sandwiched between two insulating blocks. Each copper platen is also held between one grip and a steel wedge, and the specimen is displaced in-plane so that the solder joint is deformed in pure shear. With tightening two set screws by a high torque, the specimen is held very securely during the test, which ensures correct load and displacement measurements.

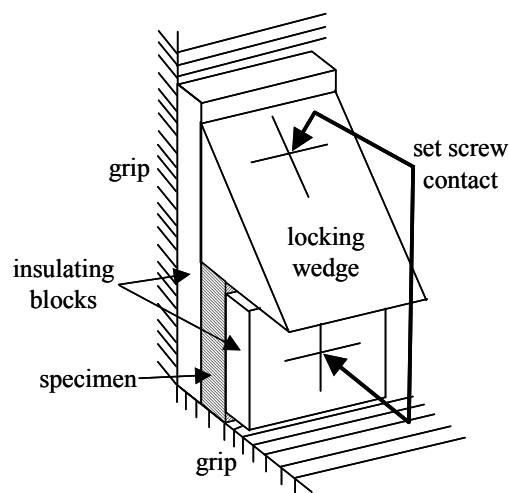


Figure 1.28: TMM grip schematic [Haswell, 2001]

1.4.3 High Temperature Testing Module

A high temperature testing module was developed by Haswell [Haswell, 2001] to heat a specimen to a specified temperature, so that TMM tests may be conducted at elevated temperatures. The heating module schematic is shown in Figure 1.29. The high temperature testing module consists of a pressure regulator, a high-wattage in-line air heater, a Type T thermocouple, a generic proportional-integral-derivative (PID) process controller, nozzles and pipes. Compressed, filtered air at ambient is regulated to approximately 4psi and then split into two streams. One stream flows through the air heater. The heater is regulated by the PID process controller in closed-loop control while feedback to the controller is provided by the thermocouple attached on the test specimen using a thermally conductive paste. Through a narrow nozzle, the heated air then blows across the exposed face of the specimen and heat the solder joint to the elevated temperature. The other stream of regulated air at ambient temperature is supplied to four nozzles, which then blow cooling air to the LVDT, load cell and the flexible link leading to the actuator. Combined with various heat shields used to deflect hot air away from sensitive components (i.e. LVDT, load cell and actuator), the cooling system ensures that the temperature of sensitive components does not exceed the allowable specifications. Some of the features of the heating system mentioned here can be seen in Figure 1.31.

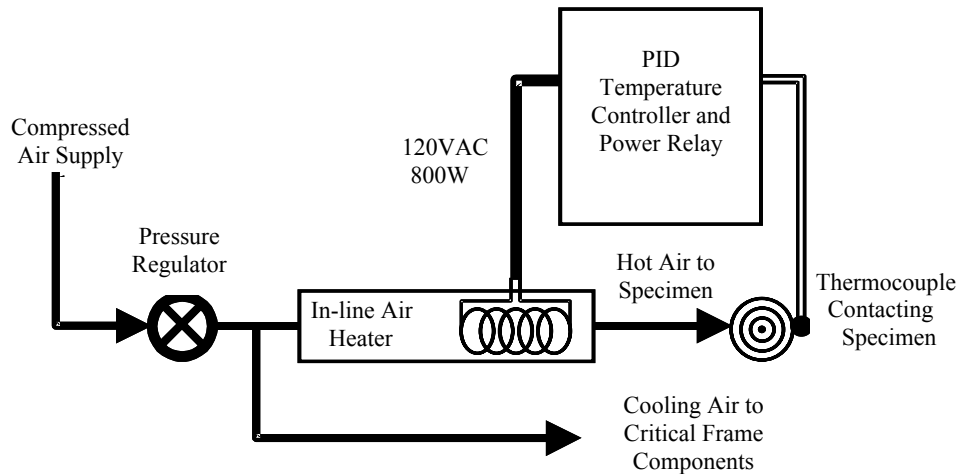


Figure 1.29: Heating module schematic [Haswell, 2001]

1.4.4 Load-train Compliance Calibration

In order to assess the deformations of the solder joint, the stiffness of the grip and copper platen assembly has to be calibrated as the LVDT measures the total deformation of the solder joint and the load-train. The load-train compliance calibration was performed by Haswell [Haswell, 2001]. First, the deformations of the solder joint and surrounding material were directly measured using a digital image correlation technique (DIC) at different load levels. At the same time, the total displacement of the grips and specimen was measured by the LVDT sensor during the calibration. Combining these data with the recorded loads produced a grip assembly compliance measurement of $0.045 \mu\text{m}/\text{N}$. Due to the significance of the load train compliance, an alternative method was also used to evaluate this value. In the second method, a series of cyclic tests is conducted under total deformation (i.e. total strain) control with different values of the load train compliance, distributed around the previous data point of $0.045 \mu\text{m}/\text{N}$, assumed for each test. Since the control algorithm adjusts the input displacement according to the load

train compliance value specified, only the test with a correctly assumed value actually showed results with no change in total deformation. The load train compliance value determined from these tests was $0.043\mu\text{m}/\text{N}$. The average value between the two test methods of $0.044\mu\text{m}/\text{N}$ is used in future testing.

1.4.5 Test Setup Modifications

The calibration of the TMM apparatus and the specimen installation procedure have significant impact on the accuracy and reproducibility of the test results. Tolerances, deviations from the nominal positions and unintentional misalignment of the specimen, should be reduced to a minimum. After the calibration, it should be possible to install the specimen without imposing any stress on the specimen. The calibration and TMM testing in the original setup were conducted in a vertical orientation. Some disadvantages of this approach were found during the course of testing. In order to improve the calibration and test handling, a fixture for the whole TMM apparatus and a calibration procedure are developed as part of this study. For better visualization, the modified setup fixture is shown in Figure 1.30. The fixture drawings can be found in Appendix A.

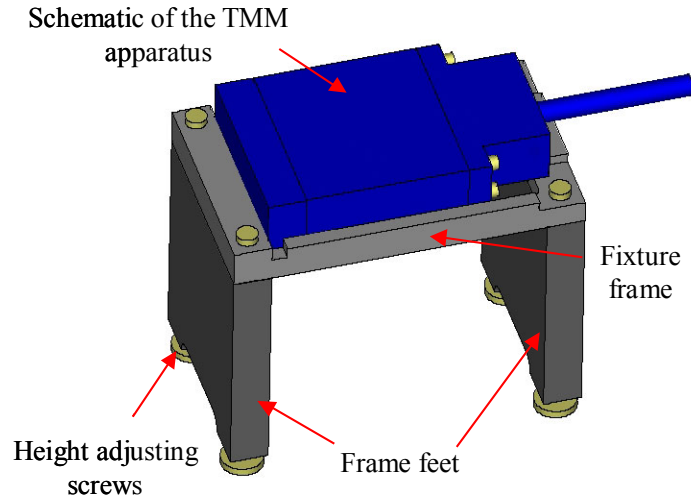


Figure 1.30: TMM apparatus with horizontal fixture

In this fixture, the TMM is reoriented 90° into a horizontal position. During the calibration a master specimen is installed and tightened. This master specimen is made from stainless steel and facilitates the task of aligning the grips in the torsional and the axial directions. The dimensions of this master specimen are the nominal dimensions of a testing specimen. The calibration can not be done very well in an upright position of the TMM apparatus, because the weight of the upper grip and the actuator would apply an unacceptable force on the load cell. Furthermore, in the horizontal position it is possible to install the testing specimens under the control of the EMZ-microscope to improve the accuracy of the installation and alignment. The fixture is designed for easy and secure handling of the TMM apparatus. This is necessary, because the setup must be moved from the testing position on the table to the measuring place under the microscope. And for the high temperature tests the TMM apparatus has to be in a lifted position, so that the cooling nozzles can be installed from the backside of the TMM. A photograph of the modified complete system is shown in Figure 1.31.

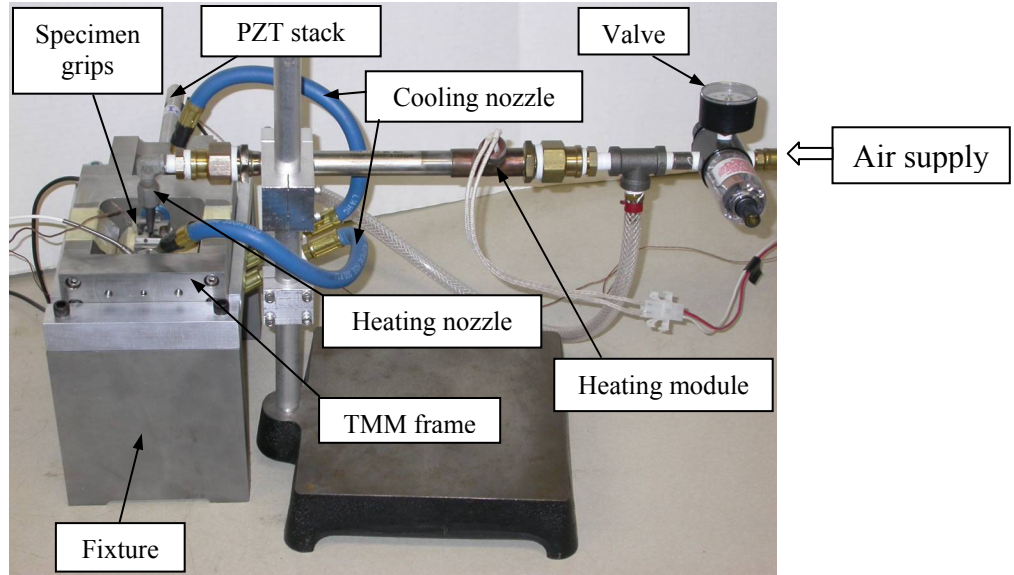


Figure 1.31: TMM experimental system

TMM cyclic tests of the Sn0.7Cu solder were carried out on the modified TMM system. As shown in Figure 1.32, test data do not show a wide range of variation and tests are more reproducible and more consistent than previous experiments.

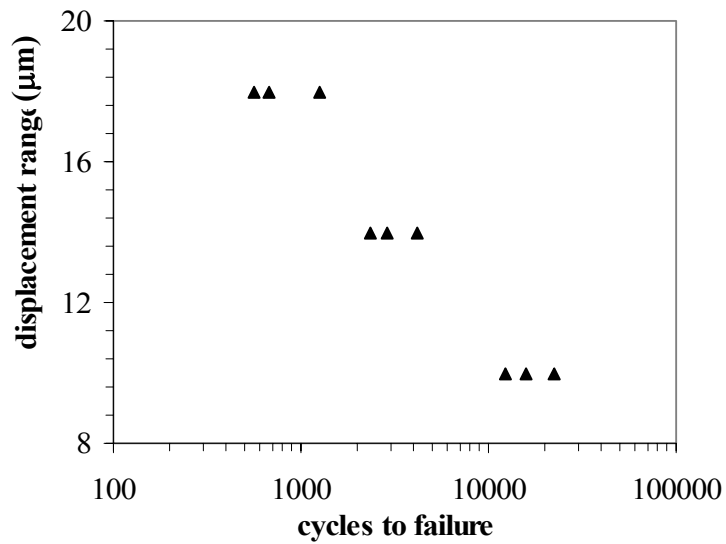


Figure 1.32: Test result variation for same cyclic test condition: Sn0.7Cu

2 Constitutive Properties

Mechanical constitutive behavior describes the deformation of a material in response to an applied load. In order to evaluate isothermal mechanical durability and thermo-mechanical durability of Pb-free solders, their constitutive properties need to be characterized. Since the microstructure of Pb-free solders is important to understand various deformation mechanisms (e.g. plastic and creep), the microstructural observations of Pb-free solders are first presented in this Chapter, followed by constitutive properties of Sn37Pb and Pb-free solder alloys obtained on the TMM setup.

2.1 Pb-free Solder Microstructure

The elastic, plastic and creep behaviors of the solder materials are directly related to their microstructure. Durability of the solder joints is affected by the solder microstructure and the microstructure change during the cyclic tests as the cumulative creep and plastic deformations lead to aging and failure of the solder joints. In this section, the microstructure of Pb-free solder joints is qualitatively discussed.

It is well known that the Sn37Pb solder is composed of two phases, large lead-rich soft particulates, in what can be essentially considered to be a tin-rich matrix [Schubert et. al. 2002a], as shown in Figure 2.1. But the microstructure of Pb-free solders is very different. Most Pb-free solders consist of a large amount of Sn with the addition of small amount Ag, Cu, Zn, or Bi. Some researchers pointed out that the microstructure of the SnAgCu solder consists of essentially pure Sn matrix with elongated intermetallic Ag_3Sn

and tiny round intermetallic Cu_6Sn_5 particles dispersed [Xiao et. al. 2000], as shown in Figure 2.1. Figure 2.2 shows the typical microstructure of a Sn3.9Ag0.6Cu TMM solder joint. Our specimen has very similar microstructure to that found in Figure 2.1 but the An_3Sn and Cu_6Sn_5 intermetallic particles are much smaller than those in Figure 2.1. In addition, intermetallic An_3Sn particles are very small and not elongated needle type. The difference is possibly the consequence of a faster cooling rate after soldering because the soldered TMM specimen was placed on a steel heat sink to cool it down. The Sn3.5Ag TMM solder joint has almost same microstructure as the Sn3.9Ag0.6Cu solder except that only the Ag_3Sn intermetallic particles can be found in the bulk solder, as shown in Figure 2.3. Similarly, the Sn0.7Cu TMM solder joint is composed of the Sn grain matrix with Cu_6Sn_5 intermetallic particles distributed on the grain boundaries.

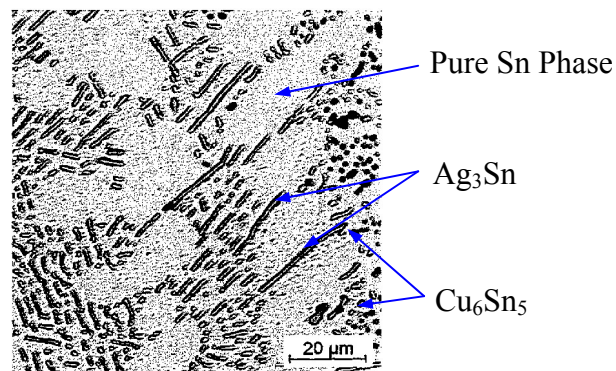


Figure 2.1: Microstructure of Sn3.8Ag0.7Cu solders [Schubert et. al. 2002a]

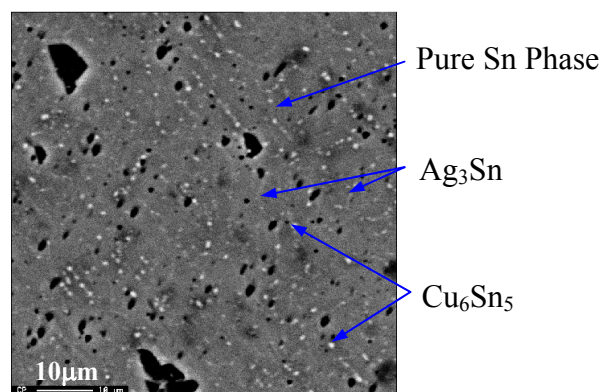


Figure 2.2: ESEM micrograph with backscatter of Sn3.9Ag0.6Cu TMM solder joint

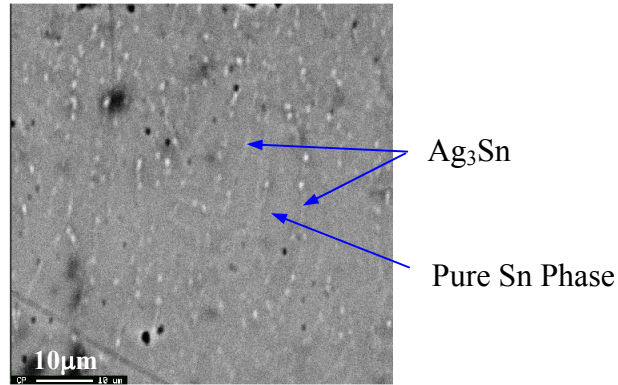
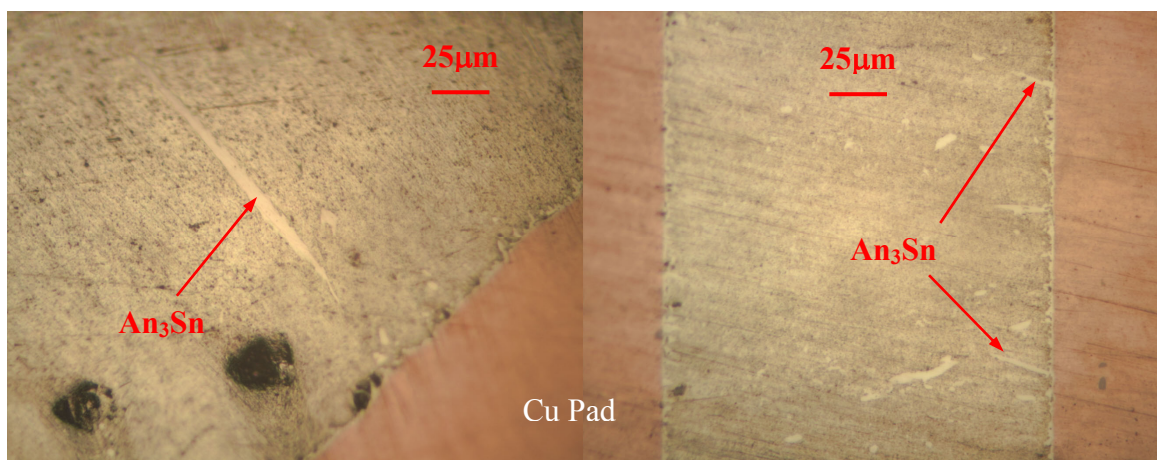


Figure 2.3: ESEM micrograph with backscatter of Sn3.5Ag TMM solder joint

Large Ag_3Sn needles and plates are also found in some specimens of Sn3.9Ag0.6Cu and Sn3.5Ag, as shown in Figure 2.4. These plates grow either from the intermetallic layer (Figure 2.4b) or in the extra solder of solder joint corners (Figure 2.4a). Liquid solder at the intermetallic layer solidifies before the bulk solder in the middle. Thus the Ag_3Sn phases have longer time to grow in the middle. Similarly, the extra solder in the corners solidifies at last and large Ag_3Sn needles and plates can be formed. However, the TMM specimens were carefully fabricated to prevent too much solder in the corners. Large Cu_6Sn_5 intermetallic particles are mostly found in Sn0.7Cu TMM solder joints, as shown in Figure 2.5. They are located in the interior of the bulk solder joint.



(a) Sn3.9Ag0.6Cu

(b) Sn3.5Ag

Figure 2.4: Optical micrographs of TMM solder joints

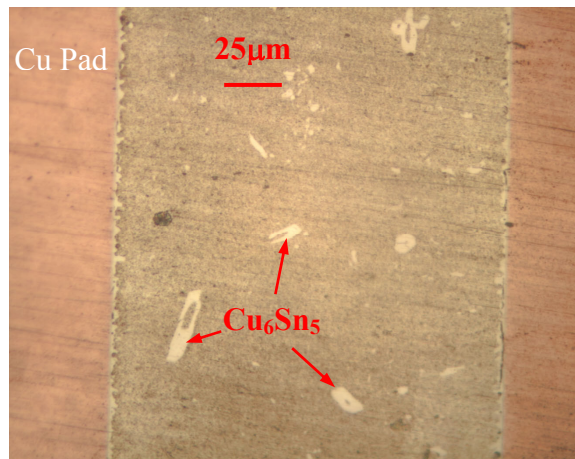


Figure 2.5: Optical micrographs of Sn0.7Cu TMM solder joint

Another microstructural feature that has an important effect on mechanical behavior of solder joints is the intermetallic layer at the interface with the metallized pad. The intermetallic layer of the Sn37Pb solder joint consists of a layer of Cu_6Sn_5 phase and a layer of very thin Cu_3Sn phase which grows when solder joints are aged at high temperature for a long period. The intermetallic layer of the Sn3.9Ag0.6Cu or Sn3.5Ag solder joint is composed of two distinct phases: scalloped Cu_6Sn_5 phase and elongated Ag_3Sn phase, as shown in Figure 2.6. The initial morphology of the intermetallic is uneven and discontinuous. After 100 hours aging at 132°C , the intermetallic layer becomes thicker, more uniform and continuous because a smooth grain structure is preferred in order to decrease the surface energy. The average thickness of the intermetallic layer is around $3\sim 5\mu\text{m}$ after aging. The intermetallic layer of the Sn0.7Cu solder joint consists of two layers: Cu_6Sn_5 layer and thin Cu_3Sn layer underneath, as shown in Figure 2.7. The morphology of the intermetallic layer has similar change to that of Sn3.5Ag solder after aging and its thickness increases to $3\sim 5\mu\text{m}$ as well.

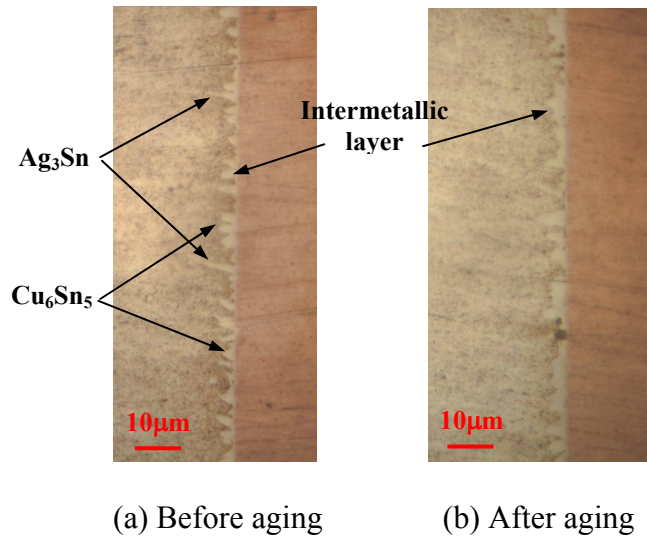


Figure 2.6: Optical micrographs of Sn3.5Ag TMM solder joints before and after 100 hours aging at 132°C

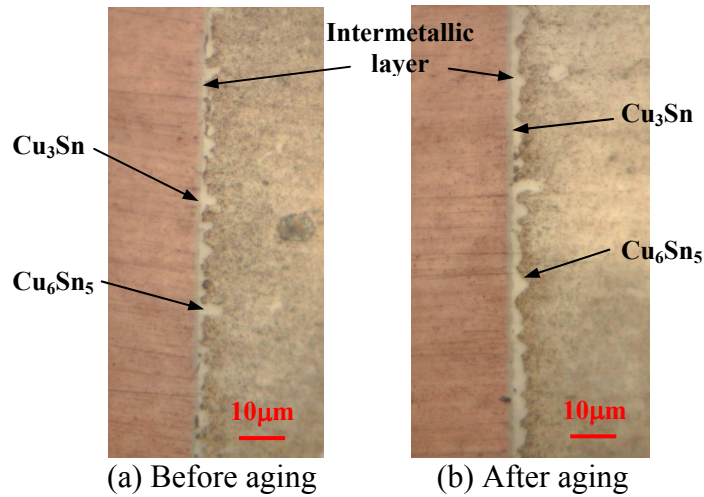


Figure 2.7: Optical micrographs of Sn0.7Cu TMM solder joints before and after 100 hours aging at 136°C

2.2 Constitutive Behavior

Constitutive behavior of Sn37Pb and Pb-free solder alloys is discussed now in this section. Typical monotonic and creep test results are first presented, followed by a one-dimensional incremental analytical model of TMM tests, and then constitutive properties of Sn37Pb and Pb-free solder alloys.

2.2.1 Typical Experimental Results

In order to obtain constitutive properties of solder materials, two sets of TMM tests, monotonic tests and constant stress tests (or creep tests), are conducted on the TMM setup. The monotonic tests are used to obtain elastic-plastic stress-strain curves while the constant stress tests are used to obtain creep curves. Typical experimental results are presented now.

2.2.1.1 Monotonic Tests

In the monotonic tests, displacement is applied on the test specimen at the constant displacement rate $\dot{\delta}$ ($\mu\text{m/s}$) until the displacement increment $\delta_{\text{inc}}(\mu\text{m})$ is reached. Then a unloading process occurs and another increment is applied. This continues until the total displacement $\delta_{\text{tot}}(\mu\text{m})$ is reached.

The results from a Sn3.9Ag0.6Cu specimen are shown in Figure 2.8, as a typical example of a monotonic stress-strain test. A total displacement of $65\mu\text{m}$ is applied in increments of $18\mu\text{m}$, at a constant displacement rate of $1\mu\text{m/s}$. The test temperature is 125°C (398K). The resultant strain rate is determined from the steady-state portions of the strain-time curve. Figure 2.9 yields a shear strain rate of $5.4\text{E-}3\text{s}^{-1}$. Under these conditions (the given strain rate and constant temperature) the observed flow shear stress is 15.9MPa . This strain rate is an average value across the LVDT mounting points, and thus includes deformations in the solder specimen, in the copper platens and in part of the grips. Since the solder yields, but the remainder of the materials do not, the actual strain rate in the solder does not remain constant, although the average strain rate across the

LVDT mounting points is held constant. New studies are underway to improve this shortcoming [Lee and Han, 2002, Kwon, Lee and Han 2003].

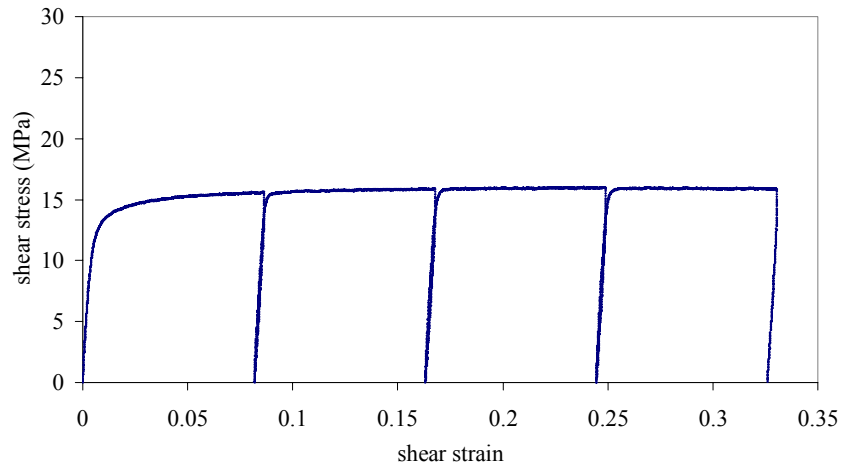


Figure 2.8: Typical monotonic stress-strain test results

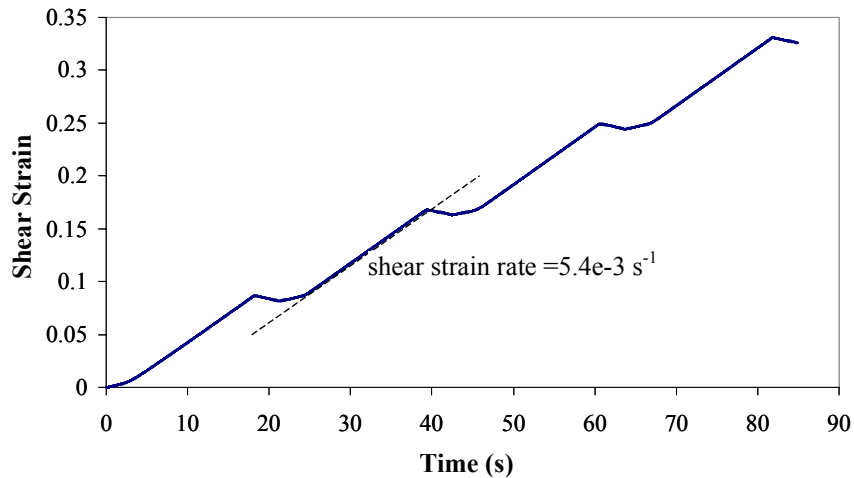


Figure 2.9: Strain-time data from presented stress-strain test

2.2.1.2 Constant Stress Tests

It is desirable to conduct tests at a constant load level, in order to determine the creep constitutive properties of the test material. In the constant stress tests, displacement is applied at a displacement rate of $20\mu\text{m/s}$ until a predetermined constant load is reached. The loading process is regulated by a controller. Then the controller maintains a constant

load on the specimen, while recording the change in displacement up to a predetermined total displacement.

The results from a SnPb eutectic specimen are presented in Figure 2.10, as a typical constant-load creep test data collected using the TMM system. In this test, a constant load of 23N (equivalent to a shear stress of 7.4 MPa) is applied over a displacement interval of 40mm, at a constant temperature of 25°C (298K). Distinct regions of primary, secondary and tertiary creep behavior are apparent in the figure. Based on the measured solder joint height, the average secondary, steady state shear strain rate measured from these data is $5.0E-6s^{-1}$.

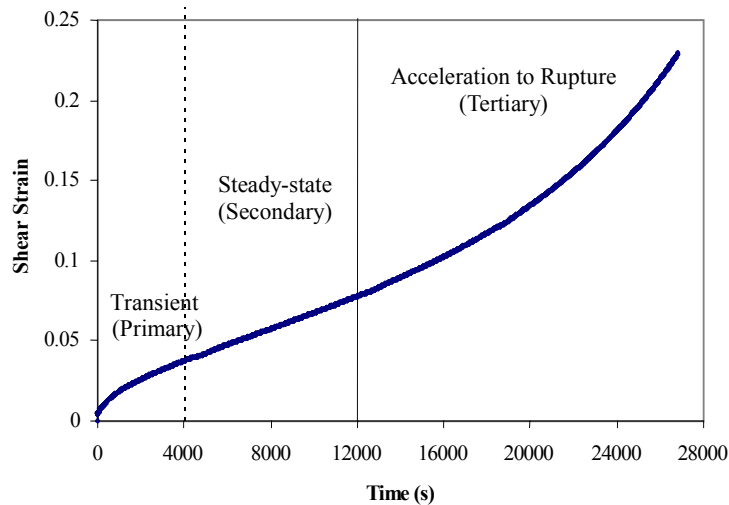


Figure 2.10: Typical constant load test results

2.2.2 Choice of Constitutive Models

Since partitioned plastic and creep energies are needed to develop Energy-Partitioning durability models of Pb-free solders, a partitioned constitutive model is desirable in this study. Considering the viscoplastic deformation characteristics of solder alloys under

complex loading in electronic components, the constitutive model of solder alloys is developed considering four major modes of solder deformation. The total shear strain, γ , is composed of time independent elastic strain, γ_{el} , time independent plastic strain, γ_{pl} , rate dependent primary creep strain, γ_{pcr} , and rate dependent secondary creep strain, γ_{scr} :

$$\gamma = \gamma_{el} + \gamma_{pl} + \gamma_{pcr} + \gamma_{scr} \quad (2.1)$$

These four modes of deformation represent the most important deformation which solder alloys experience in electronic applications.

Elastic deformations of materials result from both expansion (compression) and distortion of the molecular bonds as a external force is applied. They are fully recoverable, compared with non-recoverable inelastic deformations (plastic and creep deformations). In most engineering applications, the elastic behavior of metals is described by a simple linear relationship between applied stress and strain, i.e. Hooke's law. The linear coefficient relating stress and strain, the Young's modulus E (or the shear modulus G for the shear stress and strain), is usually temperature-dependent.

Plastic deformations occur over very short (almost instantaneous) time scales as the applied stress is beyond the yield stress. They are irreversible and due to dislocation slip mechanism. Rate-independent plasticity is typically modeled using the power law expression:

$$\tau = C_{pl} \gamma_{pl}^n \quad (2.2)$$

where τ is the shear stress; C_{pl} and n are the temperature-dependent material constants.

Rate-dependent creep deformations result from multiple microstructural mechanisms, which occur over much longer time scales and have an Arrhenius dependence on temperature. These mechanisms include dislocation glide/climb, grain-boundary sliding, dislocation pipe diffusion (self diffusion along dislocation cores), grain-boundary diffusion, and intragranular diffusion. At different stress level and temperature, different mechanism is dominated in the solder alloy. A detailed discussion on these mechanisms is presented in Section 2.2.7. In this study, the primary creep behavior of solders is modeled using the following general exponential model:

$$\frac{\gamma_{pcr-sat} - \gamma_{pcr}}{\gamma_{pcr-sat}} = \exp(-A_{pcr}t) \quad (2.3a)$$

$$A_{pcr} = C_1 \tau^{n_1} \exp\left(-\frac{C_2}{T}\right) \quad (2.3b)$$

where $\gamma_{pcr-sat}$ is the saturated primary creep, C_1 , n_1 , and C_2 are the material constants. The secondary shear creep strain rate is described by the Garofalo creep law:

$$\frac{d\gamma_{scr}}{dt} = A' [\sinh(\alpha\tau)]^{n'} \exp\left(-\frac{Q}{RT}\right) \quad (2.4)$$

where R is the universal gas constant ($= 8.31 \text{ m}^2 \text{ kg/s}^2\text{K mol}$), T is the absolute temperature in K, Q is an activation energy in J/mol, α is related to the stress level at which the power law dependence breaks down, and A' and n' are the material constants.

In summary, the total shear strain, γ , is expressed as the following equation:

$$\gamma = \frac{\tau}{G} + (\tau / C_{pl})^{1/n} + \gamma_{pcr-sat} (1 - \exp(-A_{pcr}t)) + A' (\sinh(\alpha\tau))^{n'} \exp\left(-\frac{Q}{RT}\right)t \quad (2.5)$$

2.2.3 Analytic Model of TMM Tests

As discussed in section 2.1, stress and strain are uniform in most of solder joint in TMM testing. Since the experimental data from the TMM experiments can only provide single-valued information on the average shear stress and shear strain in the solder joint, a simplified one-dimensional incremental stress model was developed to simulate the TMM tests, as shown in Figure 2.11. This analytic model was employed for obtaining constitutive properties and durability models of Pb-free solders from TMM test results in this section and in the next two chapters. The total deformation of the system consists of deformations of grips, copper pads and the solder joint. As shown in Figure 2.11, copper pads and grips deform elastically as the test loads are in the elastic region for coppers and steels, but the solder joint deforms elastically, plastically, and viscoplastically. Thus, two spring elements represent the deformations of lower and upper grips and copper pads while the combination of a spring element, plastic element and dashpot element represents the total deformation of the solder joint. A one-dimensional analytic simulation of the TMM setup is accomplished by marching at small time intervals along the specified loading profile (monotonic, creep, and cyclic) and calculating incremental changes in elastic-plastic and creep response of the material. The continuous, real-world deformation response is modeled as combination of a rate-independent (i.e. instantaneous) elastic-plastic response increment, followed by a proportional creep relaxation increment.

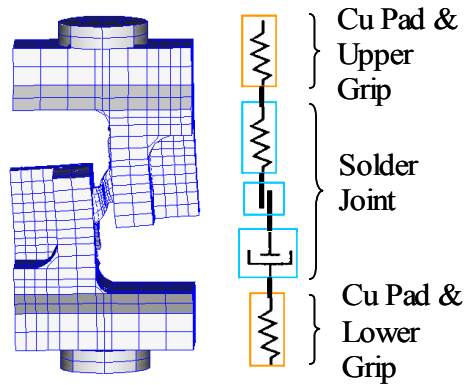


Figure 2.11: Schematic of analytical model of TMM tests

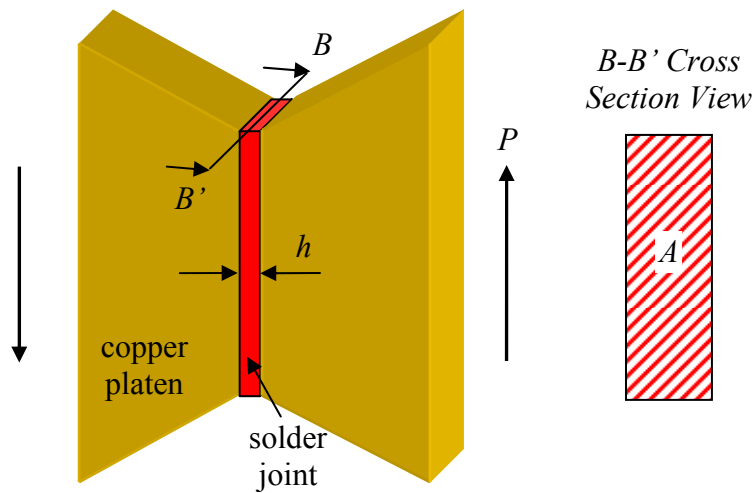


Figure 2.12: Schematic of solder joint dimensions

The information input to the 1-D analytical model is relatively simple in contrast to the Finite Element model. As shown in Figure 2.12, the height, h , and the cross-sectional area, A , of the solder joint are required. In addition, it is necessary to input the information on the test conditions: displacement ramp rate, displacement increment amplitude, and temperature for monotonic tests; temperature and load level for creep tests; constant test temperature, displacement amplitude, dwell times, displacement ramp rate and the number of cycles to be simulated for cyclic tests. Constitutive properties are required for the solder material, including elastic shear modulus as well as plasticity,

primary and secondary creep properties appropriate for the chosen constitutive models. The load train compliance is a constant value under all circumstances. Finally, appropriate analytical parameters must be specified: a time-stepping increment and the interval at which results are output to the file. In cyclic analyses, for example, a sufficiently small time increment is one-thousandth of the total cycle time.

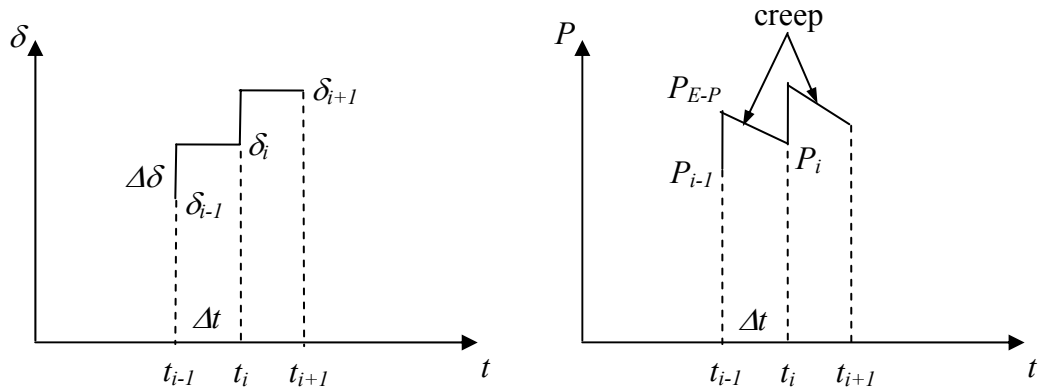


Figure 2.13: Schematic of incremental analysis process

The actual process steps for a displacement-controlled analysis are shown as follows. First, the time and total position are incremented:

$$\begin{aligned} t_i &= t_{i-1} + \Delta t \\ \delta_i &= \delta_{i-1} \pm \dot{\delta} \cdot \Delta t \end{aligned} \quad (2.6)$$

where t_i is the accumulated analysis time, Δt is the time-stepping increment, δ_i is the accumulated total displacement, $\dot{\delta}$ is the displacement ramp rate and the subscript $i-1$ indicates the value of each variable (time or displacement) calculated from the previous increment. Then, the process implements solder joint elastic-plastic and creep deformations in a piece-wise fashion, as shown in Figure 2.13. In the first substep, instant elastic-plastic response, P_{E-P} , is calculated by:

$$P_{E-P} = P_{i-1} + \frac{\Delta\delta}{\left(\frac{h}{AG} + C_{LT}\right)} \quad (2.7)$$

where $\Delta\delta$ is the displacement increment used in last step, h is the solder joint height, A is the solder joint cross-sectional area, C_{LT} is the load train compliance, and G is calculated as:

$$G = \begin{cases} G_{el}, & \tau_{i-1} < \tau_0 \\ 1/(1/G_{el} + nC_{pl}\tau_{i-1}^{n-1}), & \tau_{i-1} > \tau_0 \end{cases} \quad (2.8)$$

where G_{el} is the elastic shear modulus for monotonic and creep tests but the cyclic elastic shear modulus for cyclic tests, τ_0 is the yield stress; and C_{pl} and n are the material constant in power law plastic model shown in Equation (2.2), respectively. As the shear stress is beyond the yield stress, G is calculated as the tangential shear modulus of the shear stress versus strain curve.

In the second substep, the incremental strain consists of only incremental elastic strain and incremental creep strain. In other words, creep strains and elastic strains are exchanged during relaxation. Based on the elastic-plastic load, the creep strain increment $\Delta\gamma_{cr}$ is determined by:

$$\Delta\gamma_{cr} = (\dot{\gamma}_{pcr} + \dot{\gamma}_{scr})\Delta t \quad (2.9)$$

where the primary and secondary creep strain rates, $\dot{\gamma}_{pcr}$ and $\dot{\gamma}_{scr}$, is determined by the corresponding creep constitutive laws shown in Equations (2.3) and (2.4). Since creep strains and elastic strains are exchanged during the creep substep, the load is updated by:

$$P_i = P_{E-P} - \frac{\Delta\gamma_{cr}h}{\left(\frac{h}{AG_{el}} + C_{LT}\right)} \quad (2.10)$$

The final stress and strain are determined by:

$$\gamma_i = \frac{\delta_i - P_i C_{LT}}{h} \quad (2.11)$$

$$\tau_i = \frac{P_i}{A}$$

Equations 2.6 through 2.11 are repeated as required by the specified loading parameters.

The analytical model was accomplished by a Visual Basic program, which can be found in Appendix B.

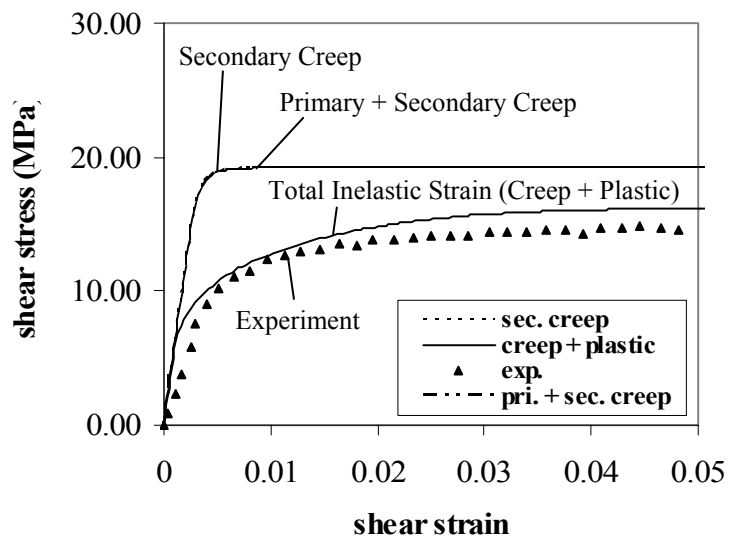


Figure 2.14: Monotonic test simulation. Sn3.9Ag0.6Cu, 125°C, 1.1×10^{-1} 1/s strain rate

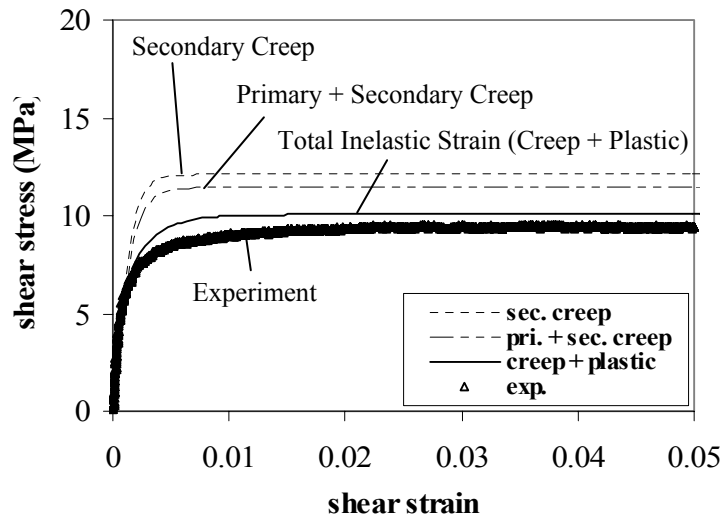


Figure 2.15: Monotonic test simulation. Sn3.9Ag0.6Cu, 125°C, 4.4×10^{-4} 1/s strain rate

Shown in Figure 2.14 and Figure 2.15 are simulation results for the Sn3.9Ag0.6Cu solder at 125°C with strain rates of 1.1×10^{-1} 1/s and 4.4×10^{-4} 1/s, respectively. The primary and secondary creep strains and rate-independent plastic strain add to give the total inelastic strain. In the relatively high strain rate test, the primary creep strain and secondary creep strain are not as significant as the plastic strain. However, in the low strain rate test, all three strains have important effects on the stress strain behavior of the solder alloy. It is also noted that the primary creep strain becomes important as the secondary creep strain significantly contributes in the total inelastic strain.

Through the simplified one-dimensional model, partitioned elastic, plastic and creep deformations are calculated for monotonic, creep and cyclic tests. This model can be used to obtain constitutive properties of solder alloys from monotonic and creep TMM test results, which is to be discussed in the following sections. In addition, for cyclic

tests, various cyclic damage parameters, e.g. deformation range, total and inelastic strain ranges, partitioned plastic and creep energy density are calculated per cycle by corresponding subroutines in the program. These parameters are necessary to derive a generic durability model, e.g. energy-partitioning damage model. A corresponding approach is discussed in next chapter.

2.2.4 Model Simulation to TMM Tests

The measured elastic, plastic, transient creep and steady-state creep constants (to be discussed in Section 2.2.6 through 2.2.9) are all included on the 1-D analytic model. As a verification exercise, monotonic tests are conducted at several different strain rates and temperatures, to allow different contributions from the elastic, plastic and creep deformation mechanisms. These tests are then simulated. Several simulations of monotonic tests for Sn3.9Ag0.9Cu and Sn37Pb are shown in Figure 2.17 and Figure 2.16, respectively, at different loading rates and different temperatures. Within the range of the measured data, there is a reasonable good agreement with the simulations results, in particular those for Sn3.9Ag0.9Cu at different temperatures and loading rates. It is also found that the model of the Sn37Pb solder overestimates the flow stress at high strain rates. This is mostly due to overestimation of strain hardening and the possibility of some anomalies in the particular tests.

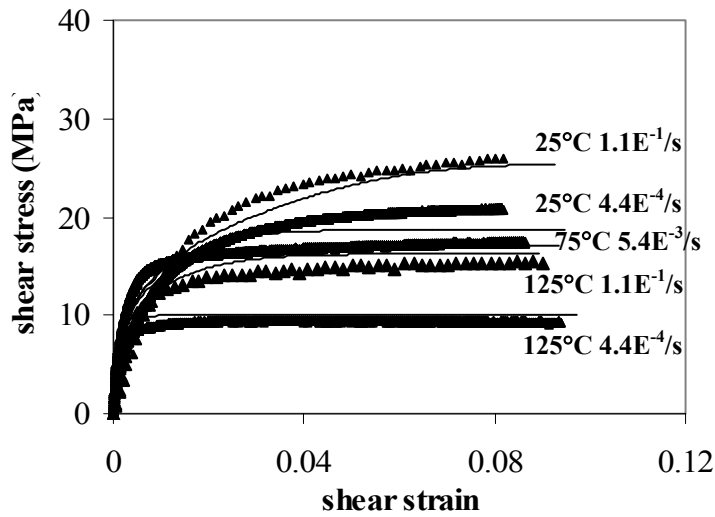


Figure 2.16: Comparison of model simulation to monotonic test data for Sn3.9Ag0.6Cu solder

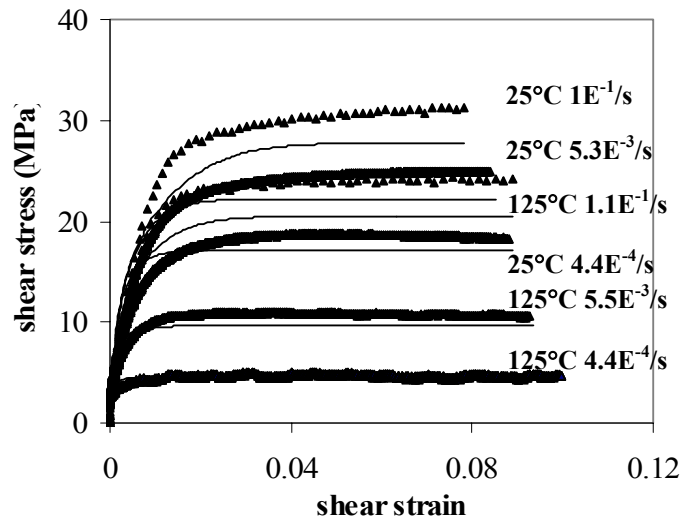


Figure 2.17: Comparison of model simulation to monotonic test data for Sn37Pb solder

2.2.5 Test Matrix

In order to obtain elastic, plastic, and creep constitutive properties, a number of monotonic and constant load creep tests were conducted in previous study [Haswell, 2001] and current study. Table 2.1 summarizes the test matrix for TMM monotonic and

creep tests of Sn37Pb and Sn3.9Ag0.6Cu solders. Both monotonic and creep tests were conducted at three temperatures in order to obtain the temperature dependence of constitutive properties. Strain rates of monotonic tests range from 10^{-4} to 10^{-1} /s. Creep tests were performed at constant loads from 1.05 to 18.8MPa. These test conditions cover most of environments found in electronic packaging.

Solder Alloy		Test Conditions		
		25°C	75°C	125°C
Sn37Pb	Mono. (strain rates)	3	4	3
	Creep (loads)	4	4	3
Sn3.9Ag0.6Cu	Mono. (strain rates)	4	3	4
	Creep (loads)	5	4	6

Table 2.1: Test matrix for TMM monotonic and creep tests.

2.2.6 Elastic Model

The Young's modulus E for two considered alloys is determined from the unloading slopes of the monotonic tests and the first reversing slopes of the cyclic tests. The temperature dependent Young's modulus of Sn37Pb and Sn3.9Ag0.6Cu solders is described by the following relationships (from data at the 10^{-1} /s strain rate):

$$\text{Sn37Pb: } E(\text{GPa}) = 18.9 - 0.044T(^{\circ}\text{C}) \quad (2.12a)$$

$$\text{Sn3.9Ag0.6Cu: } E(\text{GPa}) = 18.6 - 0.021T(^{\circ}\text{C}) \quad (2.12b)$$

It can be seen that the modulus of Sn3.9Ag0.6Cu has smaller temperature dependence than Sn37Pb. In addition, the modulus measured is smaller than the other published data. This is mainly due to the slow strain rates in most tests. Engelmaier [Engelmaier 1984] has reported that measured apparent elastic modulus can increase from about 12.4 to 17.3GPa, depending on the loading rate. Thus ultrasonic measurement techniques are

preferred, to minimize or eliminate the effects of inelastic deformation and obtain more accurate measurements of the Young's modulus.

2.2.7 Steady-state Creep Model

As the homologous temperature is higher than 0.5 in most applications, the creep deformation is significant and cannot be ignored. This is true for both SnPb and lead-free solders even at room temperature (the homologous temperature for Sn37Pb is 0.65 and for Sn3.9Ag0.6Cu is 0.61). Thus, an accurate creep model is very important for accurately predicting the total deformation of solder joints.

In constant-load creep tests, $\dot{\gamma}_{el}$ and $\dot{\gamma}_{pl}$ disappear. Steady-state creep is reached after the material has already passed through a primary (transient) phase of creep. The steady-state creep deformation kinetics of eutectic Sn37Pb solder alloys at high homologous temperature generally exhibits different characteristic behavior at different stress levels. Four distinct straight line segments can be observed if the steady-state shear creep strain rate $\dot{\gamma}_{scr}$ is plotted vs. shear stress τ on a log-log scale, as shown in Figure 2.18. Three of these segments occur at low and medium stresses. The dominant deformation mechanisms in these regions are: Nabarro-Herring matrix diffusion creep (region 1), superplasticity due to grain boundary sliding (region 2), and climb controlled dislocation creep (region 3) [Avery and Backofen 1965]. At high stresses, the steady-state creep rate $\dot{\gamma}_{scr}$ increases more rapidly with the shear stresses and the power law behavior breaks down. Therefore, this region is called *power law breakdown* creep (region 4). Generally, regions 1 and 2 are grain (phase) size controlled, whereas regions 3 and 4 are independent

of grain (phase) size. As discussed in eqn. (3.3), an Eyring relationship is often used to describe the power-law dependence on stress and Arrhenius (exponential) dependence on temperature. For convenience, this relationship is repeated below:

$$\frac{d\gamma_{scr}}{dt} = A \tau^{n'} \exp\left(-\frac{Q}{RT}\right) \quad (2.13)$$

where R is the universal gas constant ($= 8.31 \text{ m}^2 \text{ kg/s}^2\text{K mol}$), T is the absolute temperature in K, Q is an activation energy in J/mol, and A is a constant. The first three regions have stress exponents of about 3, 2, 3~7, respectively, when the following relation is used. Region 4 has an exponent larger than 10.

A complete creep model should include all four regions, representing distinct creep behavior for each region. However, most typical load levels in solder interconnects of electronic assemblies fall in regions 3 and 4, and a hyperbolic sine model is often used to model the steady-state creep in these two regions. This model is used for both Sn37Pb and Sn3.9Ag0.6Cu in this study. The steady-state shear creep strain rate is described by:

$$\frac{d\gamma_{scr}}{dt} = A' [\sinh(\alpha\tau)]^{n'} \exp\left(-\frac{Q}{RT}\right) \quad (2.14)$$

where α is related to the stress level at which the power law dependence breaks down and A' is a constant.

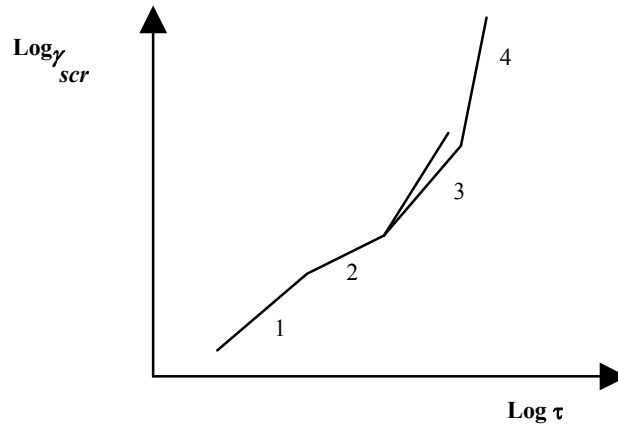


Figure 2.18: Schematic of a log-log plot of the shear secondary creep strain rate vs. the shear stress

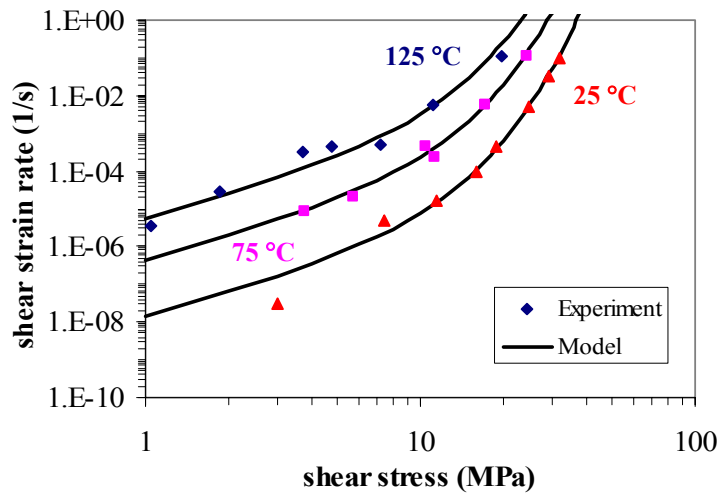


Figure 2.19: Steady-state creep data for Sn37Pb solder

To obtain the model constants, two sets of test data are used. One set of data is from monotonic tests and the measured average shear strain rate is plotted versus the flow onset stress (i.e. the stress beyond which the stress-strain relationship is nonlinear). The other set of data is from creep tests and the steady-state shear strain rate is plotted versus shear stress. Experimental results and model prediction are shown in Figure 2.19 for Sn37Pb and in Figure 2.20 for Sn3.9Ag0.6Cu. The normalized shear strain rate is plotted versus shear stress for Sn37Pb and Sn3.9Ag0.6Cu solders in Figure 2.21 and 22,

respectively. Based on normalized steady-state creep plots, the stress level at which the power law dependence breaks down and activation energy can be obtained.

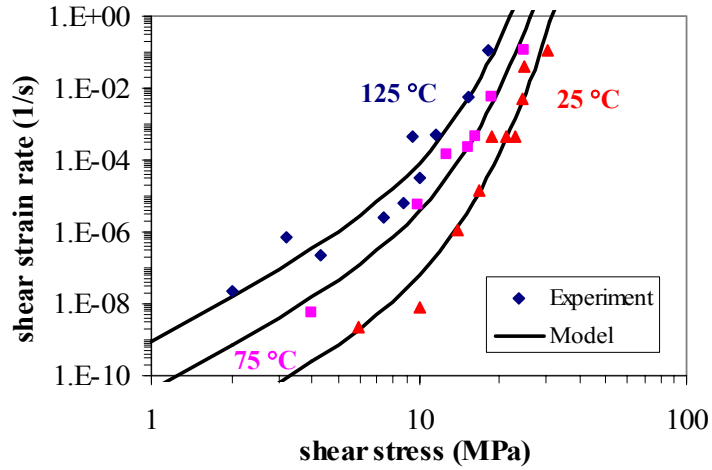


Figure 2.20: Steady-state creep data for Sn3.9Ag0.6Cu solder

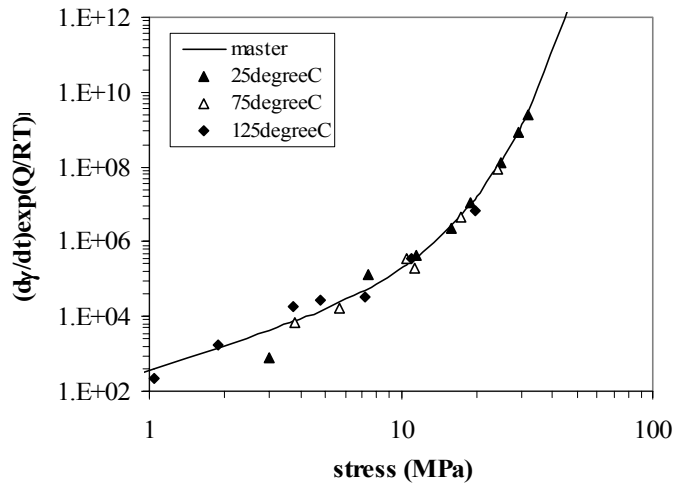


Figure 2.21: Normalized steady-state creep data for Sn37Pb solder

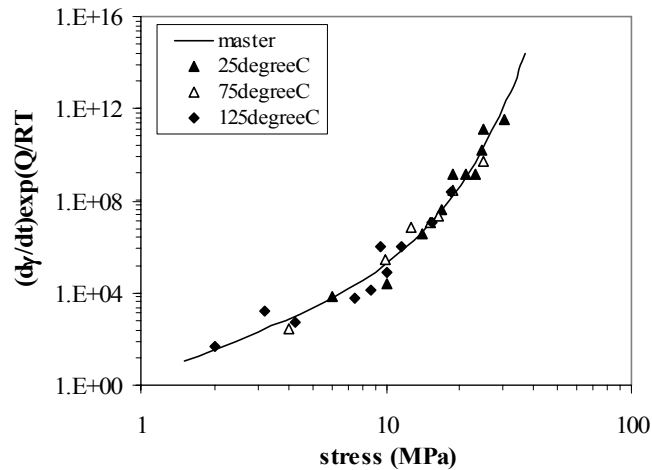


Figure 2.22: Normalized steady-state creep data for Sn3.9Ag0.6Cu solder

The model constants for these two solder alloys are presented in Table 2.2. Sn3.9Ag0.6Cu lead-free solder has larger stress exponent and activation energy. This is due to significant differences in the alloy composition and microstructure, which is discussed in the next paragraph. The same trend has been reported by Wiese [Wiese, et al., 2002]. In addition, the steady-state creep strain rates of these two solder alloys are plotted versus shear stresses at two temperatures in Figure 2.23. The lead-free solder is seen to have greater low-stress creep resistance (steady-state creep strain rate is two orders of magnitude lower at same temperature and stress level) at both room temperature and high temperature. However, as stress increases, the superiority of the Sn3.9Ag0.6Cu solder disappears gradually. Finally, above a stress level, Sn37Pb solder has better creep resistance than Sn3.9Ag0.6Cu solder. The cross-over stress level is dependent on the temperature.

Solder Alloy	A'	α	n'	Q (J/Mol)
Sn37Pb	1.15E4	0.20	2.2	5.93E4
Sn3.9Ag0.6Cu	1.50E3	0.19	4.0	7.13E4

Table 2.2: Comparison of the steady-state creep model constants between Sn37Pb and Sn3.9Ag0.6Cu solders

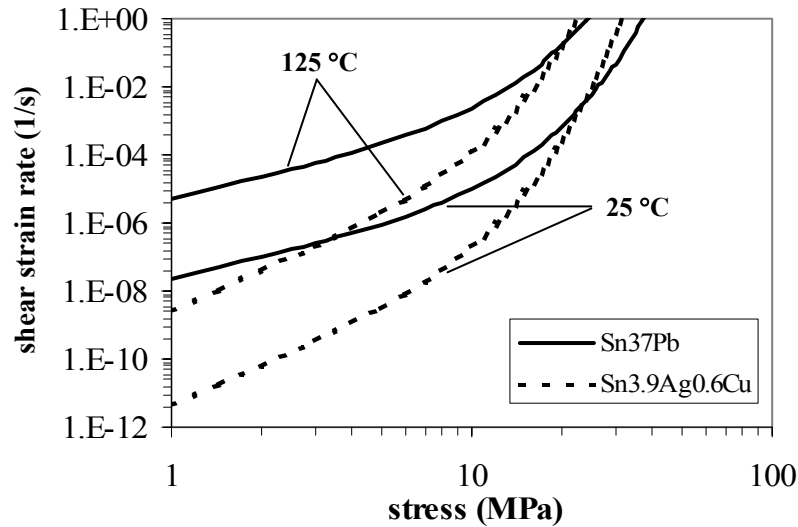


Figure 2.23: Comparison of the steady-state creep

As we discussed in section 2.1, the Sn37Pb solder is composed of two phases, the lead-rich soft particulates, in what can be essentially considered to be a tin-rich matrix. Sn3.9Ag0.6Cu solder consists of small (5-50nm diameter) intermetallic particles of Cu_6Sn_5 and Ag_3Sn embedded in the grain boundary and matrix of polycrystalline tin, as shown in Figure 2.1-2.3. The creep deformation of Sn37Pb solder is controlled by a grain boundary sliding process (superplasticity) and grain boundary diffusion at lower stresses, whereas the deformation is controlled by dislocation climb and glide and matrix diffusion at higher stress. At lower stress, soft lead-rich phases at Sn boundaries facilitate grain boundary sliding process in the Sn37Pb solder. In contrast, tiny rigid intermetallic

Ag_3Sn and Cu_6Sn_5 particles strengthen pure Sn grain boundaries and block grain boundary sliding in the SnAgCu solder. This microstructural difference results in the superior creep resistance of Sn3.9Ag0.6Cu solder alloy at low stress levels. At higher stresses, the influence of different microstructures disappears as matrix creep dominates in this region.

Considering the nature of the microstructure of the Sn3.9Ag0.6Cu solder, a dispersion strengthening creep mechanism is expected in steady-state creep behavior of Pb-free solders. Because dispersoids, e.g. intermetallic particles of Cu_6Sn_5 and Ag_3Sn , are extremely small, the interparticle spacing is such that direct interaction with dislocation results. A micromechanical model, based on thermally activated dislocation detachment mechanism, is explored as a possible source of the creep behavior. The micromechanical model is tested by fitting the model to the experimental data within the range of valid stress values. The details of the model and preliminary results are presented in Appendix C. The results from the micromechanical analysis lead to a proposition of steady-state creep mechanisms for Pb-free solders, as shown in Figure 2.24 in which the steady-state creep strain rate $\dot{\epsilon}_{scr}$ is plotted vs. stress σ on a log-log scale. Three regions cover the whole stress range. The dominant deformation mechanisms in these regions are: Nabarro-Herring matrix diffusion creep (region 1), dispersion strengthening creep (region 2), and climb controlled dislocation creep and athermal dislocation detachment creep (region 3). It is still not clear if superplasticity plays a role in the steady-state creep of Pb-free solders. Further study in this area has to be conducted.

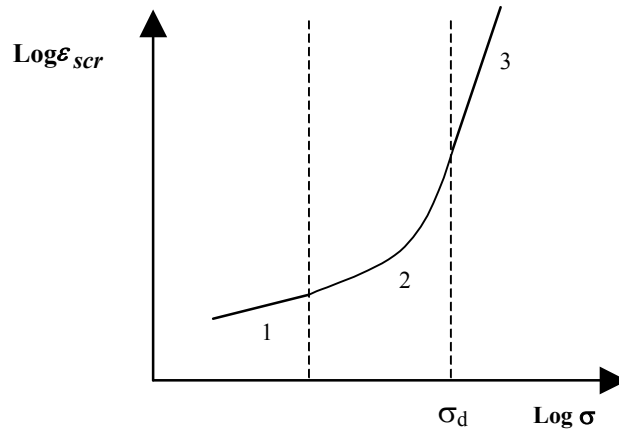


Figure 2.24: Schematic of proposed steady-state creep mechanisms of Pb-free solders

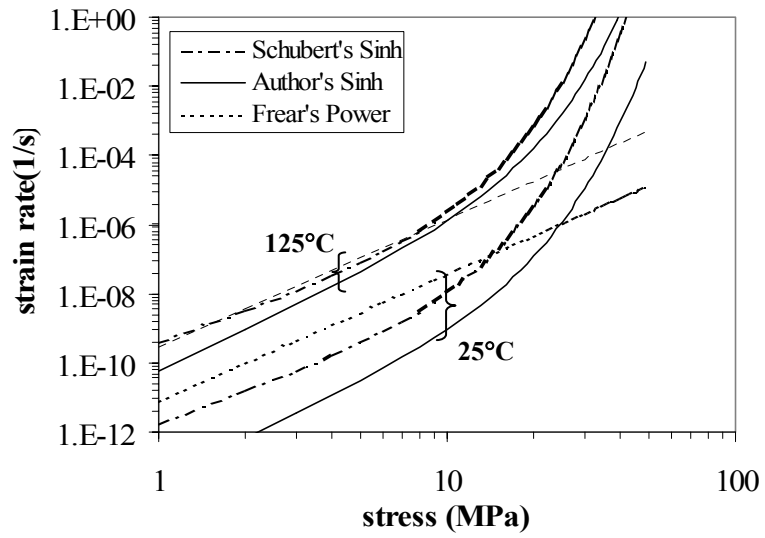


Figure 2.25: Comparison of three steady state creep models of SnAgCu solder

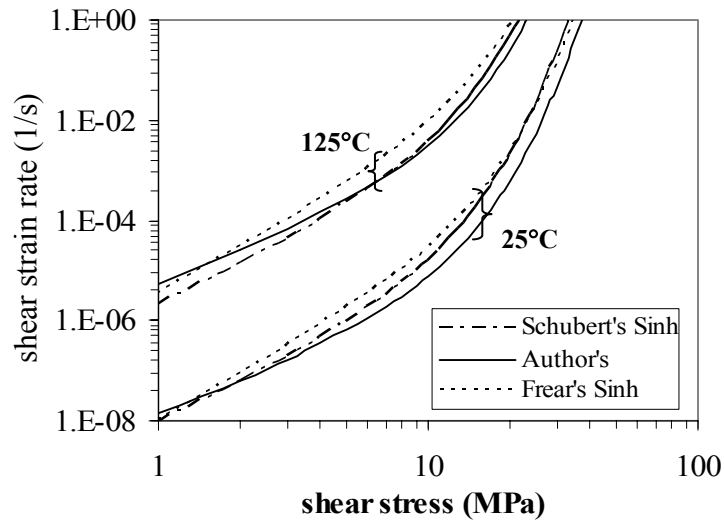


Figure 2.26: Comparison of three steady state creep models of SnPb solder

Finally, as shown in Figure 2.25, the obtained steady state creep model of Sn3.9Ag0.6Cu solder is compared with two creep models of similar Sn3.8Ag0.7Cu solder in the literature at 25°C and 125°C, respectively [Schubert, et. al., 2002a, Frear, et. al. 2001]. Our model shows a reasonable good agreement with other two models, considering the fact that reported creep models for eutectic Sn37Pb have a ten-order difference [Haswell 2001]. It is also found that the difference between models increases as temperature reduces. On the one hand, the difference is due to the different activation energies as our model has the largest activation energy. On the other hand, steady state creep models obtained from bulk solder specimens shows larger creep strain rate than those obtained from micro scale solder samples as Schubert's and Frear's models were obtained from bulk solder specimens [Wiese, et. al. 2001a]. A similar comparison for the Sn37Pb solder is showed in Figure 2.26 [Schubert, et. al., 2002a, Frear, et. al. 2001]. It is seen that the creep model obtained in this study has an excellent agreement with those models in the literature.

2.2.8 Transient Creep model

The total creep is composed of a transient (primary) part and steady-state (secondary) part if an acceleration to rupture (tertiary) part has not been reached. The transient creep strain can be obtained from constant-load creep test data by subtracting elastic strain and steady-state creep strain from total strain (provided there are no ‘plastic’ strains, i.e. the stress levels are below the yield stress at the test temperature). It is found that the transient creep strain reaches a saturated value when plotted versus time, as shown in Figure 2.27. The saturated transient creep strain shows power-law dependence on stress for two solders:

$$\text{Sn37Pb: } \gamma_{pcr-sat} = 0.0077\tau^{0.13} \quad (2.15a)$$

$$\text{Sn3.9Ag0.6Cu: } \gamma_{pcr-sat} = 0.0030\tau^{1.2} \quad (2.15b)$$

From the above two relationships, the saturated transient creep strain of Sn3.9Ag0.6Cu solder is seen to have much larger power-law dependence on stress, than that of Sn37Pb solder. At stresses below 7.6MPa, Sn37Pb solder has the larger saturated primary creep strain than Sn3.9Ag0.6Cu, and vice versa.

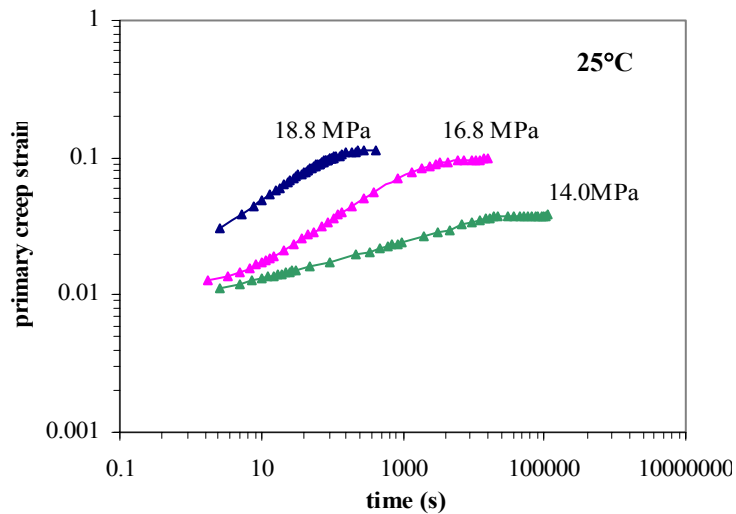


Figure 2.27: Transient creep shear strain vs. time for Sn3.9Ag0.6Cu solder

Based on the measured changes in the transient creep strain with time, the following general exponential model is postulated to simulate the transient creep behavior of solders:

$$\frac{\gamma_{pcr-sat} - \gamma_{pcr}}{\gamma_{pcr-sat}} = \exp(-A_{pcr}t) \quad (2.16a)$$

$$A_{pcr} = C_1 \tau^{n_1} \exp\left(-\frac{C_2}{T}\right) \quad (2.16b)$$

where A_{pcr} is dependent on the shear stress and temperature. All model constants for both Sn37Pb and Sn3.9Ag0.6Cu solders are summarized in Table 2.3.

Solder Alloy	C_1	n_1	C_2
Sn37Pb	7.08E3	3.3	6.95E3
Sn3.9Ag0.6Cu	0.072	3.3	4.39E3

Table 2.3: Model constants of the primary creep of Sn37Pb and Sn3.9Ag0.6Cu solders

2.2.9 Plastic Model

In order to obtain the plastic model for these two solders (Sn3.9Ag0.6Cu and Sn37Pb), the following approach is used. Monotonic stress-strain tests are first run at a relatively high strain. All monotonic tests at the highest strain rate are first simulated using a simple one-dimensional incremental analytic model to represent the test setup. The constitutive relationship in this model contains only the elastic and creep contributions discussed in Sections 2.3.6 through 2.3.8. The plastic strain is then estimated as the difference between the total experimentally measured strain and the total simulated strain predicted by the 1-D model. Finally, the model constants are determined by a least squares fit to the data at each temperature. The rate-independent plastic strain is formulated as:

$$\tau = C_{pl} \gamma_{pl}^n \quad (2.17)$$

where C_{pl} and n are temperature-dependent constants, which are summarized in Table 2.4. The plastic shear strain-stress curves at three temperatures are shown in Figure 2.28 for both solder alloys. Sn3.9Ag0.6Cu solder is seen to have larger plastic strain than Sn37Pb solder, at the same stress, for all three temperatures.

Solder Alloy	C_{pl} (MPa)	n
Sn37Pb	$76.8 - 0.28 * T(^{\circ}\text{C})$	$0.25 - 0.00028 * T(^{\circ}\text{C})$
Sn3.9Ag0.6Cu	$60.1 - 0.18 * T(^{\circ}\text{C})$	$0.29 - 0.00046 * T(^{\circ}\text{C})$

Table 2.4: Plastic model constants for Sn37Pb and Sn3.9Ag0.6Cu solders

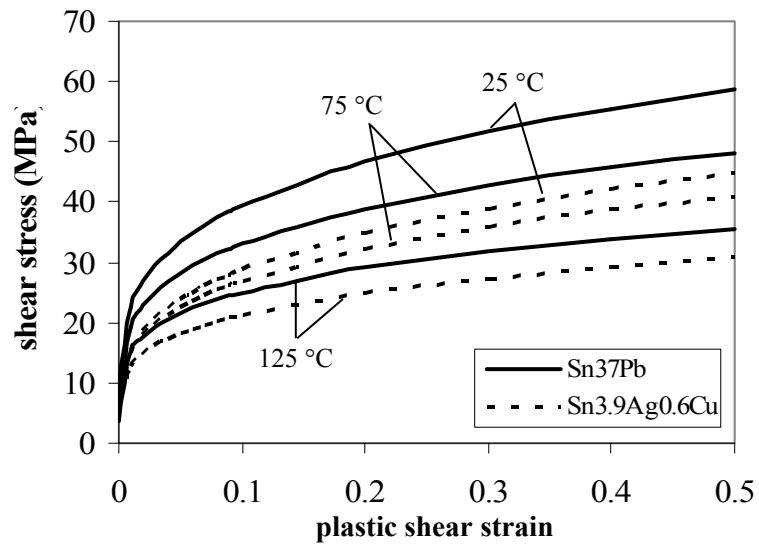


Figure 2.28: Plastic shear strain-stress curves for Sn37Pb and Sn3.9Ag0.6Cu solders

3 Isothermal Mechanical Durability

Isothermal mechanical durability of solder alloys is an important material property to measure the resistance of solder interconnects to cyclic mechanical loading at constant temperature. Examples of cyclic mechanical loading include cyclic bending, cyclic twisting, and cyclic shearing, in electronic packaging applications. While the isothermal mechanical durability of SnPb solders is well documented, Pb-free solder alloys still need to be characterized as the electronics industry is rapidly transferring to Pb-free soldering technologies.

Isothermal mechanical durability of three NEMI recommended Pb-free solders, Sn3.9Ag0.6Cu, Sn3.5Ag, and Sn0.7Cu, is now presented. The Thermo-Mechanical-Microstructural (TMM) test methodology, as discussed in Chapter 1, was used to characterize these leading Pb-free solder alloys. Experimental results in terms of power law durability curves for three solders at two different loading conditions are presented in Section 3.2.1, followed by damage propagation rate analysis of experimental results and microstructural observations of post-test specimens in Section 3.2.2 and 3.2.3, respectively. The comparison between Pb-free solders and eutectic Sn37Pb solder is also presented in Section 3.2. An approach for estimating model constants for the Energy-Partitioning (E-P) Damage Model of solder alloys from TMM test data is presented in the final section and the values of the E-P Damage Model constants for the examined Pb-free Solders are presented in the same section.

3.1 Characterization of Durability Properties

The characterization of durability properties is a very important and challenging issue in engineering application of materials. In this section, durability modeling is first reviewed to understand the previous study in the characterization of material durability. Second, the testing approach and testing matrices used in this study are presented.

3.1.1 Durability Modeling

The fatigue of various materials became a broad research topic since Wohler conducted the comprehensive reversed-stressing experiments on steels in the mid-nineteenth century. The earliest research examining fatigue phenomena dealt mostly with structural materials and often used stress-based approaches to determining cyclic fatigue life of materials. The fatigue phenomenon of these structural materials is often referred to as high cycle fatigue since the cyclic loading is in the elastic range. Solder material is subject to large plastic and creep deformations besides elastic deformation, in common application environments because of its rate-independent plastic behavior and its time and temperature dependent creep behavior. The fatigue phenomenon of materials, such as solders, is called low cycle fatigue as the inelastic deformation of materials plays a dominant role.

The Coffin-Manson empirical fatigue model [Coffin 1954, Manson 1965] is often used to express the low-cycle fatigue data, by relating total strain range experienced by the material to cycles-to-failure using a power law relationship, as follows:

$$\Delta\gamma = C \cdot N_f^n \quad (3.1)$$

where $\Delta\gamma$ is total strain range, N_f is the number of cycles-to-failure, and C and n are the fatigue coefficient and exponent, respectively. This model does not account for the material stress-strain history or mean temperature effects, but can be applied successfully under selected load histories. In order to account for the simultaneous interaction of creep and plasticity in visco-plastic materials, two empirical approaches were developed. The first approach, proposed by Coffin [1973], applies a correction factor to the fatigue coefficients and exponents in the Coffin-Manson relationship shown in Equation 3.1. The correction includes the effects of temperature and frequency in the low cycle fatigue model. In the second approach, Manson and Halford [Halford et al., 1973; Manson, 1971, 1973] moved to a strain-range partitioning approach, where the separate effects of plastic and creep strain ranges were correlated to cycles-to-failure, and the damage due to each mechanism combination (i.e. plastic-plastic, plastic-creep, creep-plastic and creep-creep) is superposed to express the aggregate damage condition. These two models have been used to characterize the creep fatigue life of solder due to cyclic loading. Examples of researchers using strain range approaches in the solder fatigue include Vaynman [1990], Enke et al. [1989] and Shine and Fox [1987].

A widely used variant of Coffin's approach for solder fatigue damage was proposed by Engelmaier [1984] on the basis of the Coffin-Manson model. The appropriate time and temperature dependent fatigue constants were obtained from Wild's experimental data [Wild 1975]. The model has been successfully applied to SnPb solders due to its simplicity and ease of implementation in solder fatigue design. Other approaches relate energy density to cycles-to-failure [Solomon 1989; Darveaux 1997; Popelar, 1997;

Vaynman 1990]. The Energy-Partitioning (E-P) damage model [Dasgupta et al., 1992] is an extension and combination of several of the above approaches. Damage due to elastic strain energy, plastic work and creep work are related individually to damage and then linearly superposed. The E-P model is discussed more extensively in Section 3.3.

Rather than attempting to predict the number of cycles to some pre-defined failure condition, several investigators model an effective macro damage propagation rate within the solder joint. The form of such models follows Paris' Law:

$$D = C_{cp} \left(\frac{da}{dN} \right)^{n_{cp}} \quad (3.2)$$

where $\frac{da}{dN}$ is the damage propagation rate, D is the damage metric, and C_{cp} and n_{cp} are the material constants. Damage metric used in such models can be continuum quantities such as energy [Guo and Conrad, 1993; Wiese et al., 1999] or fracture mechanics quantities such as stress intensity or J-integral [Guo and Conrad, 1993; Ju et al., 1996; Rafanelli, 1994;]. Other researchers explicitly model the number of cycles required to initiate a fatigue crack and the damage propagation rate separately, and then predict cycles-to-failure by adding these two quantities together [Darveaux, 1997; Dougherty et al., 1997; Lau, 1997].

Fatigue durability of solder is dependent on many factors, including temperature, cycling frequency [e.g. Grossman and Weber, 1997, Solomon and Tolksdorf, 1995] as well as the microstructures of the material itself [Frear, 1990; Frear et al., 1988, 1989; Frost, 1990]. The definition of failure used also plays a significant role [Cutiongco et al., 1990; Wilcox

et al., 1990]. Failure definitions vary according to the type of test being conducted, and the manner in which the damage is quantified and treated.

3.1.2 Durability Testing Approach and Test Matrices

TMM setup and cyclic load testing have been briefly discussed in last chapter. More details on TMM mechanical durability testing are presented in this section. First, test control algorithms have significant impact on durability testing. Four kinds of cyclic control modes are available in TMM testing: total displacement range, total strain range (TSR), inelastic strain range (ISR) and cyclic inelastic work (ΔW). The implementation of these control modes in TMM testing system and their effects on durability testing can be found in a previous study by Haswell [Haswell, 2001]. Based on his work, ISR control mode is used to characterize the isothermal mechanical durability of Pb-free solders. ISR is a very common control method for mechanical cycling tests, especially for low cycle fatigue. ISR testing is desirable since inelastic strain range is commonly used in solder durability modeling. Using same control mode also eliminates the effect of control modes and makes it easy to compare mechanical durability of various solders at different test conditions.

Since plastic and creep deformation mechanisms result in different types of material damage, as seen in various partitioned damage models (strain-range partitioning [Halford, et al., 1973] and energy partitioning [Dasgupta et al, 1992]), it is desirable to choose test conditions that isolate the effects of these mechanisms. In addition, creep deformation is time-temperature dependent and causes greater damage in solder materials as the homologous temperature increases. On the contrary, rate-independent plastic

deformation has greater influence on solder fatigue damage at low homologous temperature and high strain rate. Therefore, separate sets of cyclic durability tests are carried out at extreme conditions as allowed by the test setup. This results in two sets of test data, one in which TMM tests are performed at high strain rate and room temperature, and the other in which TMM tests are conducted at low strain rate and high temperature. In subsequent discussion, the first condition is referred as low creep condition or regime 1 as the solder material is subject to maximum creep deformation. The second condition is referred as high creep condition or regime 2, as the solder material is subject to maximum creep deformation. Separate load-damage relationships can be obtained for each set of conditions separately. The full cyclic durability test matrix is shown in Figure 3.1.

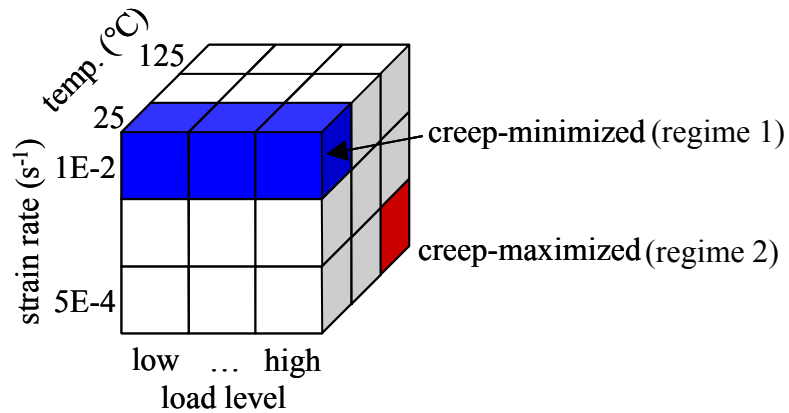


Figure 3.1: Cyclic durability test matrix

A number of TMM tests are conducted at multiple load levels under each test condition in order to obtain durability properties of Pb-free solders with high confidence.

In order to obtain the durability model of solder materials, an exact definition of cycles-to-failure should be determined. The choice of a definition for cycles-to-failure can vary

widely; a good choice should balance modeling accuracy and computational effort. For isothermal mechanical cycling tests, the most common failure criterion is a certain level of load drop, as follows:

$$\phi_N = \frac{P_{\max} - P_N}{P_{\max}} \quad (3.3)$$

where the load drop parameter ϕ_N at cycle N is determined by P_N , the load amplitude measured at cycle N , and P_{\max} , the maximum cyclic load amplitude, typically measured within the first few cycles of the test. The effect of percentage of load drop is determined by evaluating durability models with various load drop levels (50% to 80%) used as the failure criterion. The results are shown in Figure 3.2. It is found out that durability exponent is not affected by choice of failure criterion (50% to 80% load drop) but durability coefficient increases monotonically. Thus 50% load drop criterion, the most commonly used definition of cycles-to-failure for which $\phi_N = 50\%$ is attained, can capture the major characteristics of durability of solder materials and is an appropriate criterion.

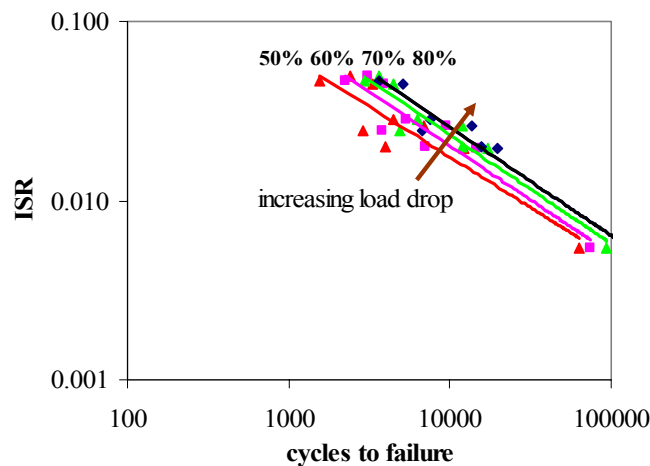


Figure 3.2: Effects of percentage of load drop on the durability model (Sn3.5Ag solder test results for regime 1)

Selecting this singular event as a failure criterion simplifies the required analysis and damage modeling greatly. However, this choice then consequently requires that the damage criterion (e.g. total strain range in Coffin-Manson relationship) be calculated based on parameters obtained from a single cycle during the test. Most commonly, experimental data or analysis of the first stabilized cycle is used to determine value of the durability criterion. This scheme can be used to obtain reasonable predictions of in-service durability provided that the method of analysis used for life prediction is similar to the one used to determine the model constants. However, as a typical solder interconnect is very different in shape and applied loading from that used to obtain the model constants, significant errors may occur in the durability estimate. The approach does not consider the contribution of the changing state of stress and strain beyond the initial cycle in the durability evaluation. In addition, no information is included concerning the rate of damage propagation through the interconnect. The effects of these disadvantages may be significant if parameters such as solder joint geometry, solder-pad metallization, and hydrostatic stress are significantly different from those used for the model calibration.

With the testing approach and testing matrices determined, TMM tests are conducted and time, displacement and force histories for the entire test are recorded as raw test data. Based on the specimen geometry information, a post processing program is used to calculate various parameters required to characterize the durability of Pb-free solders. The output of the post processing program includes all important parameters of solder

joints such as stress and strain histories, load drop statistics, total strain range (TSR) for each cycle, total inelastic strain range (ISR) for each cycle, and total work density (ΔW) for each cycle. The details of post processing methods and procedures can be found elsewhere [Haswell, 2001].

3.2 Experimental Results and Analysis

Experimental results of isothermal mechanical durability for the three selected Pb-free solders, Sn3.9Ag0.6Cu, Sn3.5Ag, and Sn0.7Cu, are presented in this section. First, the power law durability constants are discussed, followed by a comparison of the selective durability of the three Pb-free solders constants and baseline eutectic Sn37Pb solder. Second, the test data are analyzed to estimate damage propagation rate and the results are presented. Finally, post-test microstructural observations of three Pb-free solder test samples are presented.

3.2.1 Power Law Durability

Generally speaking, most damage models establish a power law relationship between a damage metric value (e.g. deformation range, inelastic strain range or cyclic work density) to the number of cycles required to meet a certain failure criterion. In this approach, a unique value of quantified damage and a specific failure definition are used to represent the full cyclic history of the solder material. As this approach is applied in mechanical durability tests, the most common example is to relate the strain range (total, inelastic, or partitioned) experienced by the solder material during the first stabilized cycle of the test to the number of cycles required to achieve 50% load drop by a power-

law, e.g. Coffin-Manson fatigue model. Many kinds of damage criteria are used in mechanical durability modeling. As discussed earlier in Section 3.1.2, the three cyclic damage criteria used in this work are: Total Strain Range (TSR); Inelastic Strain Range (ISR); Cyclic Work Dissipation Density (ΔW).

The results of the TMM experimental tests at the two test conditions shown in Figure 3.1, are used to determine the material parameters of the selected durability models. A power-law relationship between the chosen damage criterion and cycles-to-failure is established, which can be expressed both in terms of the damage criterion, D (TSR or ISR or ΔW):

$$D = C \cdot N_f^n \quad (3.4)$$

and the number of cycles-to-failure, N_f :

$$N_f = \left(\frac{D}{C} \right)^{\frac{1}{n}} \quad (3.5)$$

where C and n are material constants which may be dependent upon strain rate, temperature as well as other secondary parameters, such as material structure and aging history. While N_f data are purely experimental, the chosen damage criterion is a quantity either experimentally determined, or calculated through a combination of experimentation and numerical analysis. N_f data are statistical cycles-to-failure for which 50% load drop is reached in this study. Three damage criteria, TSR, ISR, and ΔW , are estimated by averaging corresponding values for first four stabilized cycles from post processing of TMM test data.

3.2.1.1 Sn3.9Ag0.6Cu Solder

Isothermal mechanical cyclic tests are extremely time-consuming, e.g. up to ten days in this study. It is necessary to strike a balance between the number of tests and load levels. TMM cyclic tests of Sn3.9Ag0.6Cu solder were conducted at multiple load levels under two extreme test conditions, as described in Figure 3.1. Summaries of the test statistics and load level for two regimes are presented in Table 3.1. The strain rate for each regime is average value of strain rates of all tests in that regime. The tests listed have included ones conducted in a previous study [Haswell 2001] and ones in current study. The numbers in bold indicate the tests conducted in this study. A total of 13 and 7 cyclic tests were performed at regime 1 and at regime 2, respectively. It is seen that a reasonable level of confidence can be attributed to these data.

Test Conditions		Load Levels and Test Statistics					
Regime 1 25°C, 3.3E-2 1/s	Deform. Range (µm)	-5.5~5.5	-7~7	-8~8	-9~9	-10~10	-11~11
	Test Statistics	1	2 (1)	2	4 (3)	1	3
Regime 2 125°C, 4.4E-4 1/s	Deform. Range (µm)	-3.8~3.8	-5.5~5.5	-6.8~6.8	-7.5~7.5	-9~9	
	Test Statistics	1	2	2	1	1	

Table 3.1: Summary of cyclic test statistics and load level for Sn3.9Ag0.6Cu solder

TMM test results of Sn3.9Ag0.6Cu solders under two test conditions are presented in Figure 3.3 and 3.4, respectively. The solid line indicates a least square fit. The dashed lines provide an estimate of the experimental scatter in the data. A power-law relationship as shown in Equation 3.4, is employed to correlate the three damage criteria to cycles-to-failure for 50% load drop. Least-square fits of material constants C and n for the three damage criteria are presented in Table 3.2. Variance of the test data (R^2) value for the least square fit are also shown in the same table.

		n	C	R^2
Regime 1	TSR	-0.16	0.25	0.40
	ISR	-0.49	2.4	0.92
	W	-0.57	201	0.96
Regime 2	TSR	-0.67	5.2	0.90
	ISR	-0.79	10.9	0.92
	W	-0.77	204	0.88

Table 3.2: Power-law durability parameters for Sn3.9Ag0.6Cu

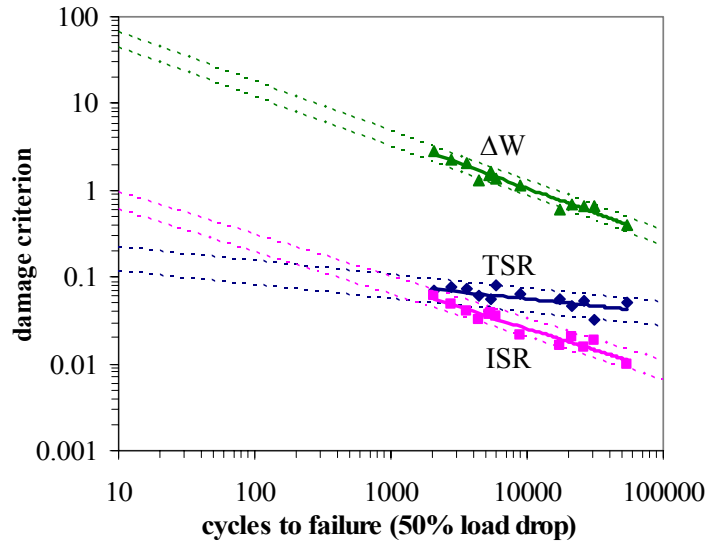


Figure 3.3: 25°C, 3.3E-2 1/s strain rate cyclic fatigue data, Sn3.9Ag0.6Cu solder

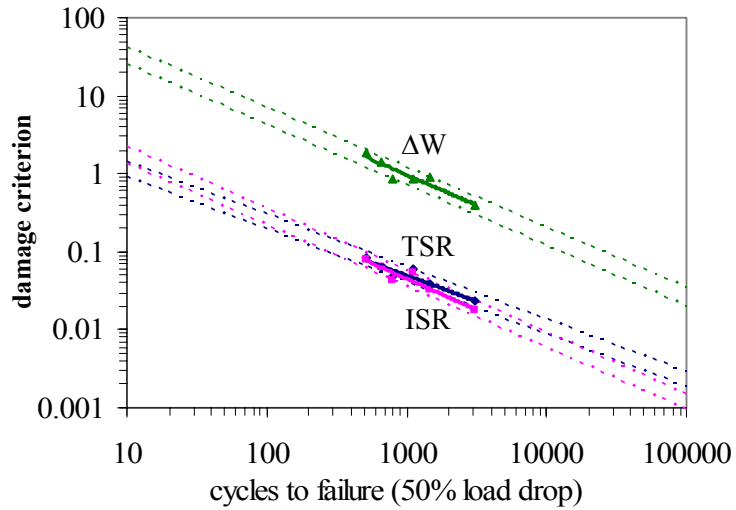


Figure 3.4: 125°C, 4.4E-4 1/s strain rate cyclic fatigue data, Sn3.9Ag0.6Cu solder

Table 3.2 indicates that variance from all data sets except TSR-based model for regime 1, are within accepted limits. Secondly, it is seen that the exponent n of the power law relation, i.e. the slopes of durability curves in Figure 3.3 and 3.4, for each of the three damage criteria, increases as the amount of creep increases. Of the three damage models, TSR-based model has the largest change in the power law exponent, suggesting that TSR is not a very stable damage criterion. Thus this model is not discussed further in this section. These obtained model parameters can be combined with Equation 3.4 or 3.5 to estimate isothermal mechanical cyclic life of Sn3.9Ag0.6Cu solder in use environments that are similar to or slightly beyond the test conditions.

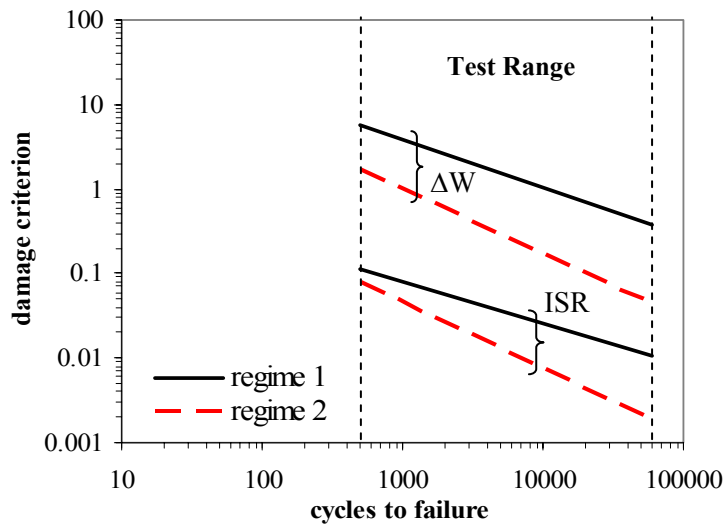


Figure 3.5: Comparison of regime 1 and regime 2 results: Sn3.9Ag0.6Cu solder, work-based (ΔW) and inelastic strain range-based (ISR) damage relation

A comparison between regime 1 and regime 2 tests in terms of work-based (ΔW) and inelastic strain range-based (ISR) damage models for Sn3.9Ag0.6Cu solder is presented in Figure 3.5. It is first noted that the durability of Sn3.9Ag0.6Cu solder for regime 1 is better than that for regime 2 in terms of Work-based durability model. According to ISR-

based damage model, however, there is a crossover point appears to be at around 200 cycles ($\Delta\varepsilon = 0.2$). The difference between the two damage criteria is the result of the fact that total cyclic work density (ΔW) includes the information of both stresses and strains but inelastic strain range (ISR) only has the strain contribution. Stresses of the tests in regime 1 are much higher than those in regime 2. Thus the effects of increased creep deformation in regime 2 are overestimated by ISR-based durability model.

As discussed before, the slope of the durability curve increases for both Work- and ISR-based damage models as the test condition changes from regime 1 to regime 2, thus indicating that the acceleration factor for accelerated testing will decrease as the amount of creep increases. This is consistent with prior findings for other solders in the literature.

3.2.1.2 Sn3.5Ag Solder

Similarly, TMM cyclic tests at multiple load levels under two selected test conditions were conducted to characterize the mechanical durability of Sn3.5Ag solder. Summaries of the test statistics and load level for the two regimes are given in Table 3.3. As creep deformation is directly related to the homologous temperature (i.e. the ratio of absolute temperature to absolute melting temperature), the test temperature of regime 2 is selected to be the same homologous temperature of 0.75 for all three Pb-free solders. For Sn3.5Ag solder, the high temperature tests were conducted at 128°C which represents the same homologous temperature of 0.75 as 125°C for Sn3.9Ag0.6Cu solder. A total of 9 and 11 cyclic tests were conducted at regime 1 and at regime 2, respectively.

Test Conditions		Load Levels and Test Statistics					
Regime 1 25°C, 2.9E-2 1/s	Deform. Range (μm)	-6~6	-7~7	-8~8	-9~9	-10~10	
	Test Statistics	1	2	2	2	2	
Regime 2 128°C, 4.5E-4 1/s	Deform. Range (μm)	-4~4	-5.6~5.6	-6.2~6.2	-7.2~7.2	-8.2~8.2	-9.2~9.2
	Test Statistics	2	1	2	1	2	3

Table 3.3: Summary of cyclic test statistics and load level for Sn3.5Ag solder

TMM test results of Sn3.5Ag solders at the two selected conditions are presented in Figure 3.6 and 3.7. A power-law relationship, as shown in Equation 3.4, is employed to correlate the three damage criteria and cycles-to-failure for 50% load drop. Least-square fits of material constants C and n for the three selected damage criteria are presented in Table 3.4. Variance of the test data (R^2) value for the least square fit are also shown in the same table.

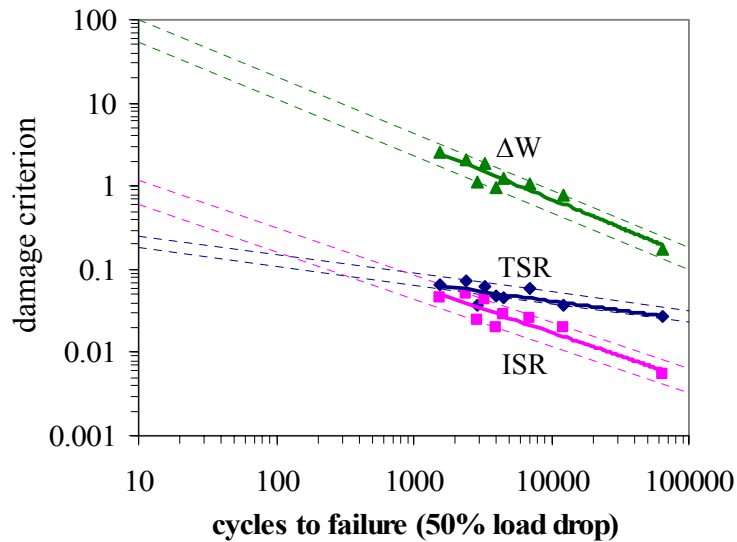


Figure 3.6: 25°C, 2.9E-2 1/s strain rate cyclic fatigue data, Sn3.5Ag solder

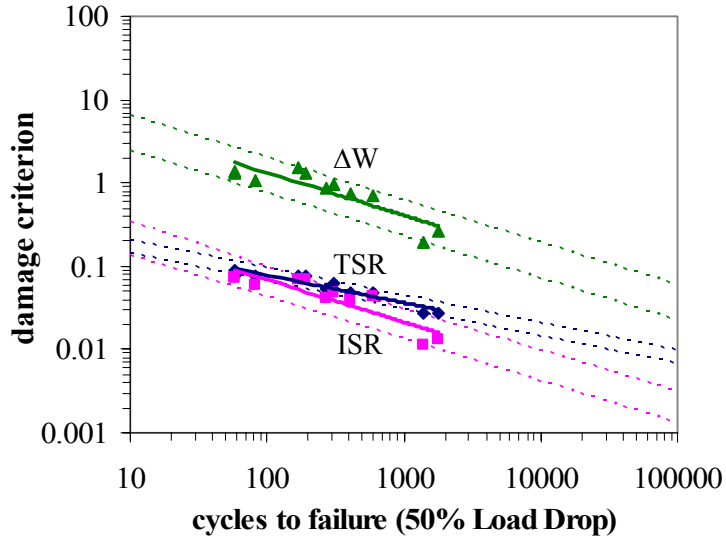


Figure 3.7: 128°C, 4.5E-4 1/s strain rate cyclic fatigue data, Sn3.5Ag solder

		n	C	R^2
Regime 1	TSR	-0.23	0.33	0.61
	ISR	-0.56	3.2	0.86
	W	-0.68	371	0.92
Regime 2	TSR	-0.33	0.36	0.89
	ISR	-0.51	0.71	0.81
	W	-0.51	14	0.77

Table 3.4: Power-law durability parameters for Sn3.5Ag

It is noted in Table 3.4 that the correlation coefficients of all data sets are reasonably good. It is also found that TSR-based durability model has the smallest slope among the three durability models while Work-based durability model has the largest slope for both regimes. When combined with Equation 3.4 or 3.5, the obtained durability parameters can be used to estimate isothermal mechanical cyclic life of Sn3.5Ag solder at these conditions.

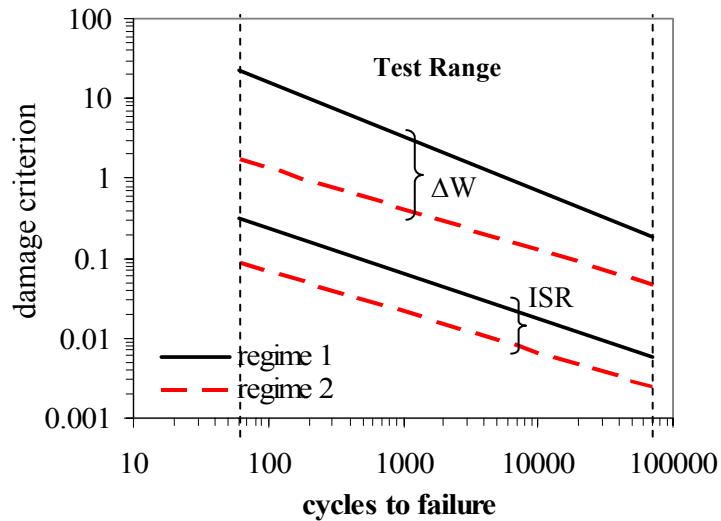


Figure 3.8: Comparison of regime 1 and regime 2 results: Sn3.5Ag solder, work-based (ΔW) and inelastic strain range-based (ISR) damage relation

Comparisons for Sn3.5Ag between regime 1 and regime 2 test conditions for work-based (ΔW) and inelastic strain range-based (ISR) damage metrics are presented in Figure 3.8. It can be seen graphically that the durability of Sn3.5Ag solder for regime 1 is better than that for regime 2 for both work- and ISR-based damage relation. It is also found that the slope of durability curve for ISR damage metrics slightly decreases across the two test environments while the slope for ΔW damage metrics drops relatively more. This is due to the different combination of creep and plastic deformation mechanisms for the two regimes.

3.2.1.3 Sn0.7Cu Solder

The repeatability of test results for Sn0.7Cu testing is improved because of improvement in TMM test calibration and installation procedures, as discussed in Section 2.1.2.1. The test statistics and load levels of cyclic tests for Sn0.7Cu solder are summarized in Table

3.5. High temperature (regime 2) tests were performed at 132°C, which represents the same homologous temperature of 0.75 as 128°C for Sn3.5Ag and 125°C for Sn3.9Ag0.6Cu. A total of 9 and 10 cyclic tests were conducted at regime 1 and at regime 2, respectively.

Test Conditions		Load Levels and Test Statistics		
Regime 1 25°C, 3.6E-2 1/s	Deform. Range (µm)	-5~5	-7~7	-9~9
	Test Statistics	3	3	3
Regime 2 132°C, 4.9E-4 1/s	Deform. Range (µm)	-4~4	-6.5~6.5	-9~9
	Test Statistics	3	4	3

Table 3.5: Summary of cyclic test statistics and load level for Sn0.7Cu solder

TMM test results of Sn0.7Cu solders for the two test regimes are presented in Figure 3.9 and 3.10, respectively. Similarly, a power-law relationship as shown in Equation 3.4, is employed to correlate the three selected damage criteria to cycles-to-failure for 50% load drop. Least-square fits of the material durability constants C and n and the correlation coefficients R^2 for all three selected damage criteria are presented in Table 3.6.

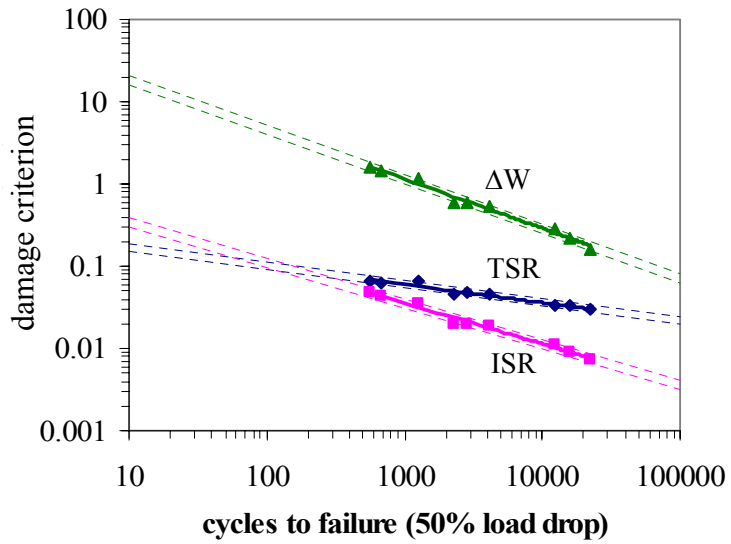


Figure 3.9: 25°C, 3.6E-2 1/s strain rate cyclic fatigue data, Sn0.7Cu solder

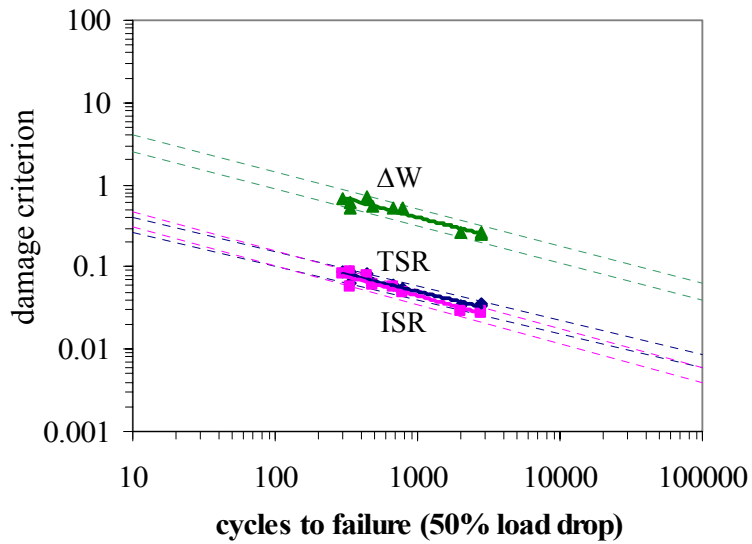


Figure 3.10: 132°C, 4.9E-4 1/s strain rate cyclic fatigue data, Sn0.7Cu solder

		n	C	R^2
Regime 1	TSR	-0.22	0.28	0.97
	ISR	-0.50	1.1	0.98
	W	-0.60	72.6	0.99
Regime 2	TSR	-0.41	0.88	0.90
	ISR	-0.47	1.2	0.91
	W	-0.45	9.1	0.90

Table 3.6: Power-law durability parameters for Sn0.7Cu

As seen in Figures 3.9 and 3.10 as well as in the R^2 values in Table 3.6, all data sets show very good correlation for all three damage criteria due to improved TMM testing approach. Similar to the cases of Sn3.9Ag0.6Cu and Sn3.5Ag solders, TSR-based durability model of Sn0.7Cu solder has the smallest slope among the three durability models for both regimes. Isothermal mechanical durability of Sn0.7Cu solder can be evaluated by employing durability parameters in Table 3.6 in Equation 3.4 or 3.5 for appropriate environments.

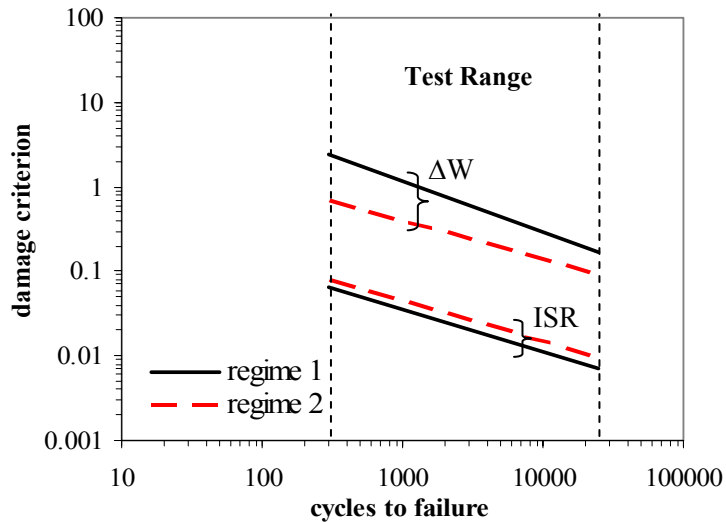


Figure 3.11: Comparison of regime 1 and regime 2 results: Sn3.5Ag solder, work-based (ΔW) and inelastic strain range-based (ISR) damage relation

Work- and ISR-based durability models for Sn0.7Cu solder under two test conditions are compared in Figure 3.11. It is seen that the durability of Sn0.7Cu solder for regime 1 is much better than that for regime 2 when Work-based durability model is used. But when ISR-based durability model is used, the durability for regime 1 is slightly worse than that for regime 2. This is due to the same reason as that presented for the Sn3.9Ag0.6Cu solder in Section 3.2.1.1. It is also noted that the overestimation of the effects of creep

deformation for Sn0.7Cu in regime 2 is greater than that for Sn3.9Ag0.6Cu because the Sn0.7Cu solder has larger creep deformation than the Sn3.9Ag0.6Cu solder under this test condition.

3.2.1.4 Comparison and Discussion

The three NEMI recommended Pb-free solders, Sn3.9Ag0.6Cu, Sn3.5Ag, and Sn0.7Cu solders are going to replace Pb-containing solders and be adapted by the electronics industry. Upon the completion of mechanical durability characterization of three solder alloys, comparing their relative durability performance with one another and with baseline eutectic Sn37Pb solder can provide the industry an insight to designing for solder durability. Three comparisons are presented in this section: (1) the comparison of isothermal mechanical durability of Sn3.9Ag0.6Cu, Sn3.5Ag, Sn0.7Cu, and Sn37Pb solders at room and high temperature; (2) the comparison of isothermal mechanical durability of four solders at same homologous temperature; (3) the comparison of durability parameters from this study with results from available literature.

Work-based and ISR-based durability relations are compared for three Pb-free Sn3.9Ag0.6Cu, Sn3.5Ag, and Sn0.7Cu solder alloys and eutectic Sn37Pb solder alloy at room temperature in Figure 3.12 and 3.13, respectively. Durability properties of Sn37Pb were obtained from previous TMM tests [Haswell 2001]. It is graphically seen that Sn0.7Cu solder has the worst durability of the three NEMI Pb-free solders at the low creep test condition (either by ISR-based damage model or W-based damage model). It is also found that the Pb-free Sn3.9Ag0.6Cu and Sn3.5Ag alloys do appear to have

superior durability to eutectic Sn37Pb alloy in the low creep test environment, with any potential crossover occurring well beyond the range of durability testing and most use environments. However, the Sn0.7Cu alloy only shows a comparable durability with Sn37Pb solder under this condition. Durability curves of the four solder alloys cross over at this test condition. The durability curve for the Sn3.5Ag solder alloy has the largest slope, followed by that for Sn3.9Ag0.6Cu, that for Sn0.7Cu and that for Sn37Pb. These trends result in crossovers of the Work-based durability curves, at 150 cycles ($\Delta W = 15 \text{ mJ/mm}^3$) between Sn3.5Ag and Sn3.9Ag0.6Cu; at 500 cycles ($\Delta W = 1.7 \text{ mJ/mm}^3$) between Sn0.7Cu and Sn37Pb; at 70,000 cycles ($\Delta W = 0.2 \text{ mJ/mm}^3$) between Sn3.5Ag and Sn37Pb. The corresponding cross-overs for ISR-based durability curves are at approximately 10 cycles ($\Delta \epsilon_{ie} = 0.85$) between Sn3.5Ag and Sn3.9Ag0.6Cu and 100,000 cycles ($\Delta \epsilon_{ie} = 0.004$) between Sn0.7Cu and 37Pb, respectively.

Work-based and ISR-based damage relations are also compared in Figures 3.15 and 3.16 for all alloys at similar high temperature, which represents 125°C for Sn37Pb solder, 128°C for Sn3.5Ag solder, 125°C for Sn3.9Ag0.6Cu solder and 132°C for Sn0.7Cu solder, respectively. The ranking of the four solders in terms of durability are different at different damage levels. For example, Sn3.9Ag0.6Cu shows the best durability among these four solders when work density per cycle is greater than 0.3 mJ/mm^3 , followed by Sn3.5Ag, by Sn0.7Cu and by Sn37Pb in descending order. But Sn3.9Ag0.6Cu shows the worst durability among the four solders for work density per cycle less than 0.07 mJ/mm^3 , behind Sn3.5Ag, Sn0.7Cu and Sn37Pb in ascending order. The durability curve for Sn3.9Ag0.6Cu solder has the largest slope, followed by that those for Sn3.5Ag, Sn0.7Cu,

and Sn37Pb in descending order. Similarly, crossovers of the Work-based durability curves exist at around 800 cycles ($\Delta W = 0.5 \text{ mJ/mm}^3$) among Sn3.5Ag, Sn0.7Cu and Sn37Pb; and at 6000 cycles ($\Delta W = 0.3 \text{ mJ/mm}^3$) between Sn3.9Ag0.6Cu and Sn37Pb; at 20,000 cycles ($\Delta W = 0.12 \text{ mJ/mm}^3$) between Sn3.9Ag0.6Cu and Sn0.7Cu; at 32,000 cycles ($\Delta W = 0.07 \text{ mJ/mm}^3$) between Sn3.9Ag0.6Cu and Sn3.5Ag. The corresponding crossovers for ISR-based durability curves are at approximately 120 cycles ($\Delta \epsilon_{ie} = 0.06$) between Sn3.5Ag and Sn37Pb; and at 1,500 cycles ($\Delta \epsilon_{ie} = 0.04$) among Sn3.9Ag0.6Cu, Sn0.7Cu, and 37Pb; at 25,000 cycles ($\Delta \epsilon_{ie} = 0.004 \text{ mJ/mm}^3$) between Sn3.9Ag0.6Cu and Sn3.5Ag.

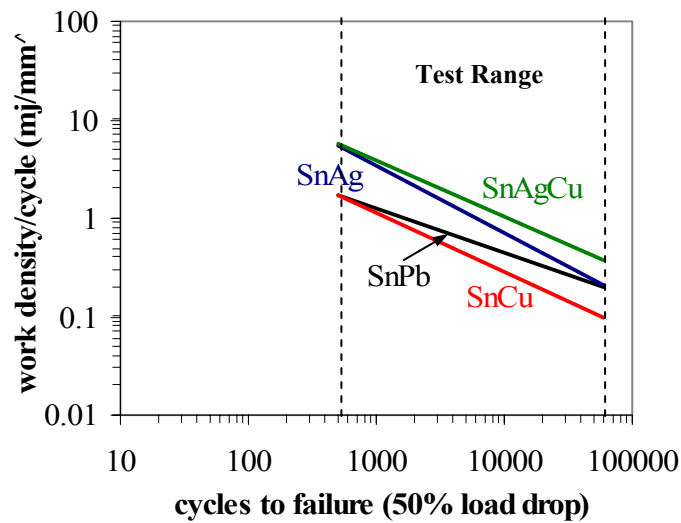


Figure 3.12: Work-based damage relation comparison of four solder alloys at room temperature

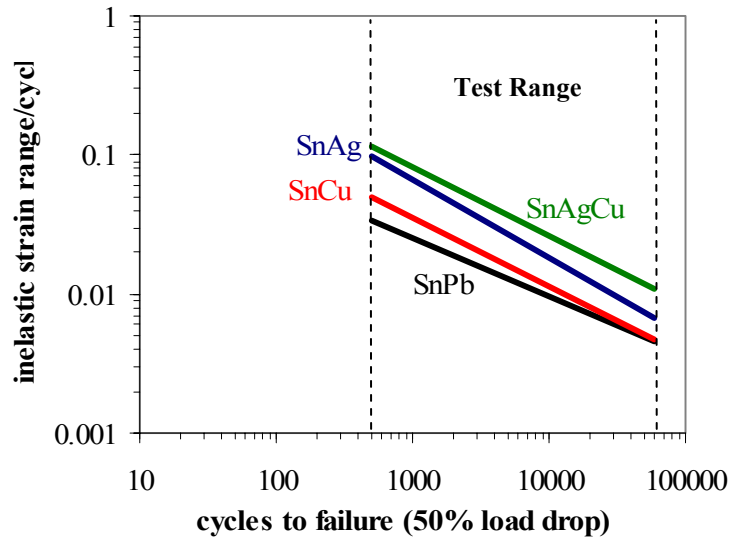


Figure 3.13: ISR-based damage relation comparison of four solder alloys at room temperature

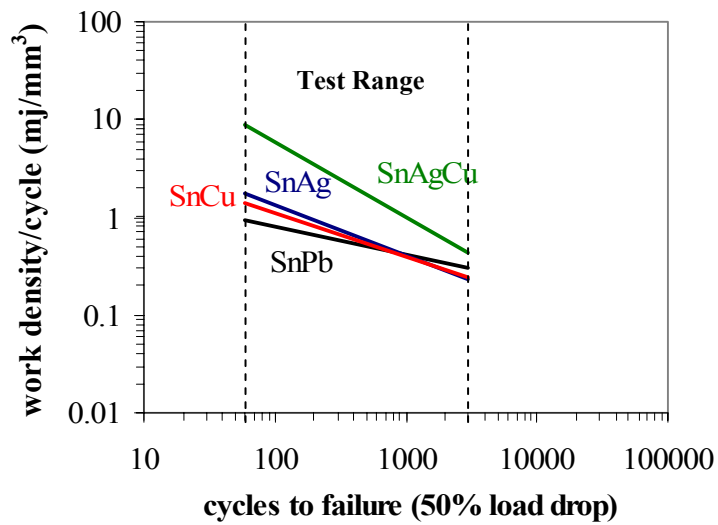


Figure 3.14: Work-based damage relation comparison of four solder alloys at high temperature

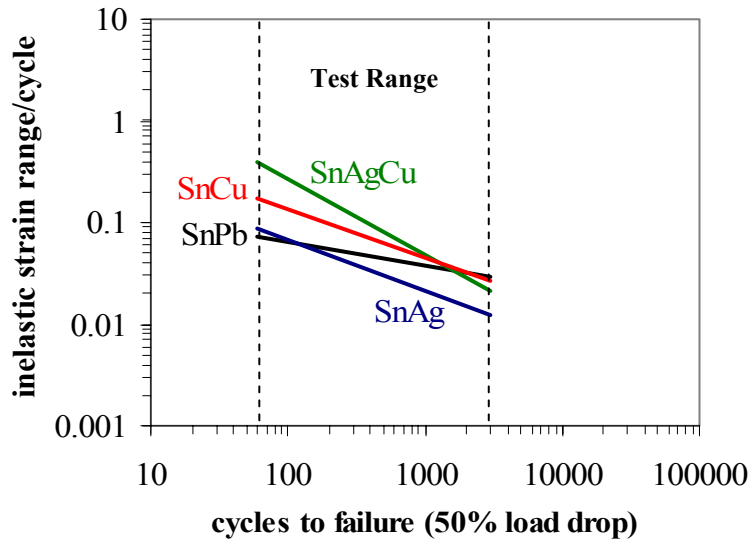


Figure 3.15: ISR-based damage relation comparison of four solder alloys at high temperature

In order to compare the mechanical durability of four solders at same homologous temperature of 0.75, a set of TMM cyclic tests of Sn37Pb solder were conducted at 98°C. The obtained durability parameters and test data are presented in Appendix D. Comparisons of Work and ISR-based durability models among four solders are presented in Figure 3.16 and 3.17. At same homologous temperature, Sn3.9Ag0.6Cu shows the best durability among the four selected solder alloys, while Sn3.5Ag, Sn0.7Cu and Sn37Pb have very similar durability performance according to Work-based damage relation. However, according to ISR-based damage relation, the durability ranking changes to Sn3.9Ag0.6Cu, followed by Sn0.7Cu, Sn37Pb, and Sn3.5Ag while the durability curve of Sn3.9Ag0.6Cu solder has crossovers with those of Sn0.7Cu, Sn37Pb, and Sn3.5Ag solders at 1200 cycles, 4000 cycles, and 25,000 cycles, respectively.

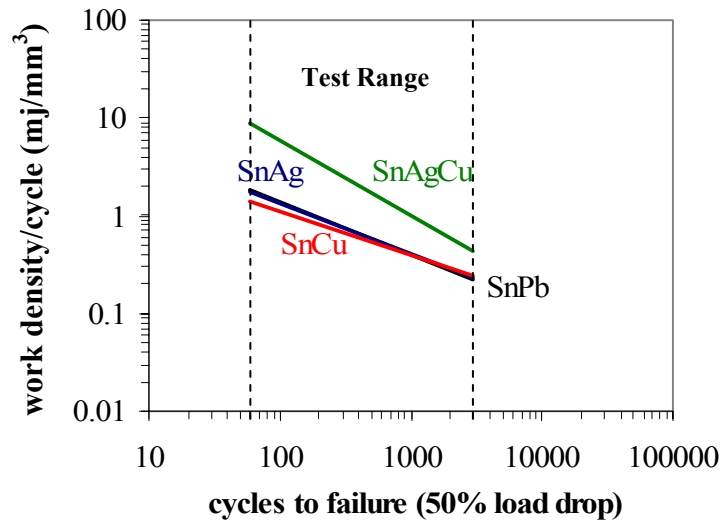


Figure 3.16: Work-based damage relation comparison of four solder alloys at same homologous temperature (0.75)

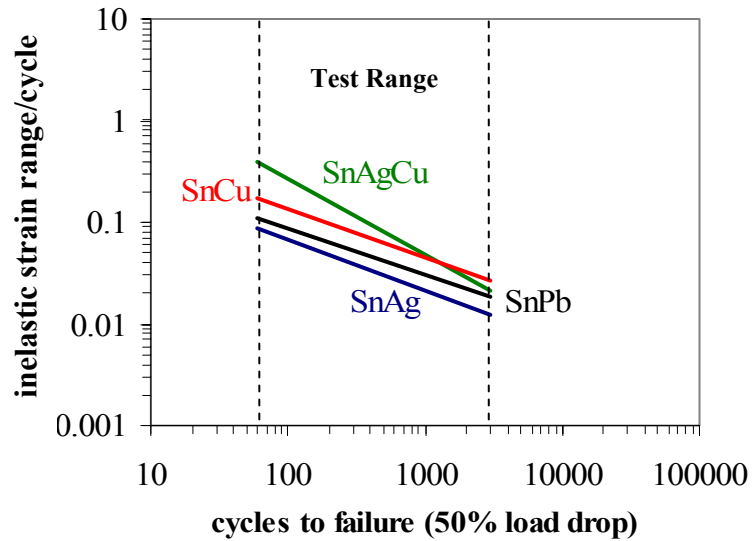


Figure 3.17: ISR-based damage relation comparison of four solder alloys at same homologous temperature (0.75)

Experimental data of the mechanical durability in the literature are sparse for Pb-free solders. Table 3.7 shows the comparison of power-law durability data at room temperature between this study and the work by Kariya [Kariya, et. al., 2001], which was

discussed in Chapter 1. Our results of Sn3.9Ag0.6Cu and Sn3.5Ag solders are in good agreement with data from the literature.

Author	Damage Metric	<i>n</i>	<i>C</i>
SnAgCu			
Kariya, et. al., 2001	ISR	-0.55	1.5
This Study	ISR	-0.49	2.4
Sn3.5Ag			
Kariya, et. al., 2001	ISR	-0.52	1.1
This Study	ISR	-0.56	3.2

Table 3.7: Power-law durability data from this study and the literature

3.2.2 Damage propagation Rate Analysis

An alternative approach to the previous power law durability analysis approach is now presented. Rather than defining failure at a specified load drop level, the rate of damage propagation through the interconnect is explicitly quantified. Several investigators have described the change in a crack length during the fatigue test [Ju et al., 1996; Guo and Conrad, 1993; Darveaux, 1997]. A relation between a chosen damage metric and the damage propagation rate can be established using a Paris' law similar to those presented previously:

$$D = C_{cp} \cdot \left(\frac{da}{dN}\right)^{n_{cp}} \quad (3.6)$$

where *D* is the chosen damage criteria (ISR, Δ*W*, TSR), *da/dN* is the damage propagation per cycle, and *C_{cp}* and *n_{cp}* are model constants. Ideally, *C_{cp}* and *n_{cp}* should be material constants. However, due to the proximity between the cracks and the boundary of the solder, the constants obtained from this test may also be a function of the test setup and specific geometry. The *da/dN* is estimated by multiplying the average load drop rate by

the original length of the solder joint. In most cases, a reasonably linear fit is obtained, as shown in Figure 3.18. This method is based on the assumption that the load drop can be represented by the propagation of one large equivalent macro crack (and a corresponding decrease in load-carrying area). However, in reality, there is extensive distributed micro cracking and significant branching of several macro-cracks, all of which contribute to average cyclic softening and loss of load carrying capacity. Thus, it should be clear that load loss as a metric for damage propagation is approximate at best, and the damage propagation constants must be viewed within this context.

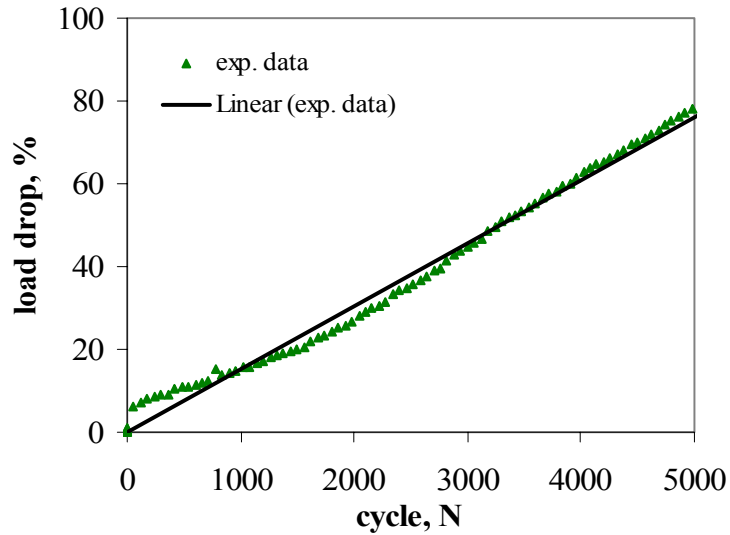


Figure 3.18: Load drop versus cycles from a TMM test of Sn3.5Ag solder

The results of this analysis for the three Pb-free solders are presented in Figure 3.21 to 3.24. Summaries of analysis results of constants C_{cp} and n_{cp} and correlation coefficients R^2 for the three solder alloys are presented in Table 3.8. The average damage propagation rate is found to correlate well with all three damage metrics: cyclic total work density (ΔW), cyclic total strain range (TSR) and cyclic inelastic strain range (ISR). It is also noted that the correlation coefficients for low creep tests are normally higher

than those for high creep tests. Results for Work and ISR damage relations appear more steady and consistent than those for TSR damage relation, suggesting that cyclic total work density and cyclic inelastic strain range are better damage criterion. Combined with Equation 3.6, these test results can be used to calculate the damage propagation rate in solder joints when this fracture mechanics approach is preferred.

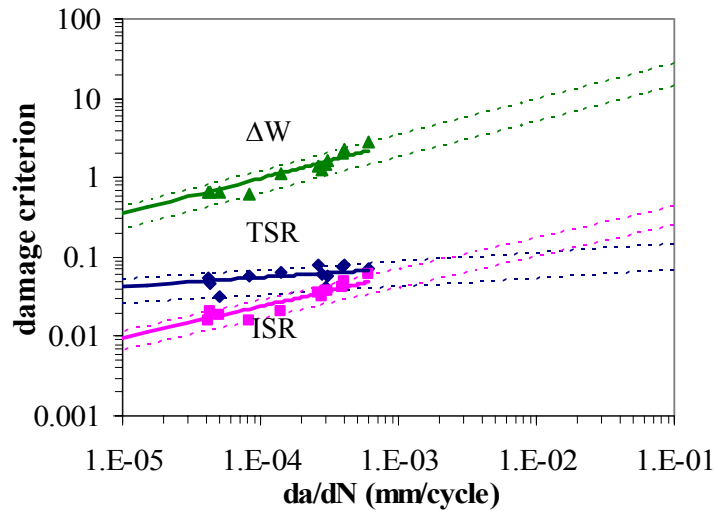


Figure 3.19: Damage propagation rate at 25°C, 3.3E-2 1/s strain rate: Sn3.9Ag0.6Cu

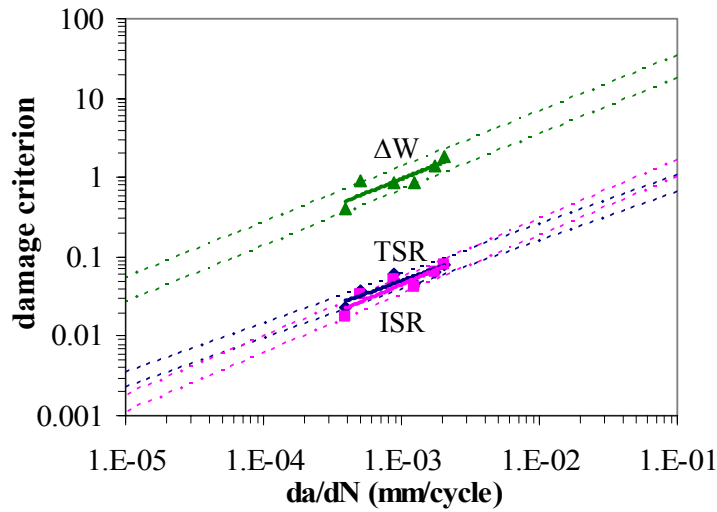


Figure 3.20: Damage propagation rate at 125°C, 4.4E-4 1/s strain rate: Sn3.9Ag0.6Cu

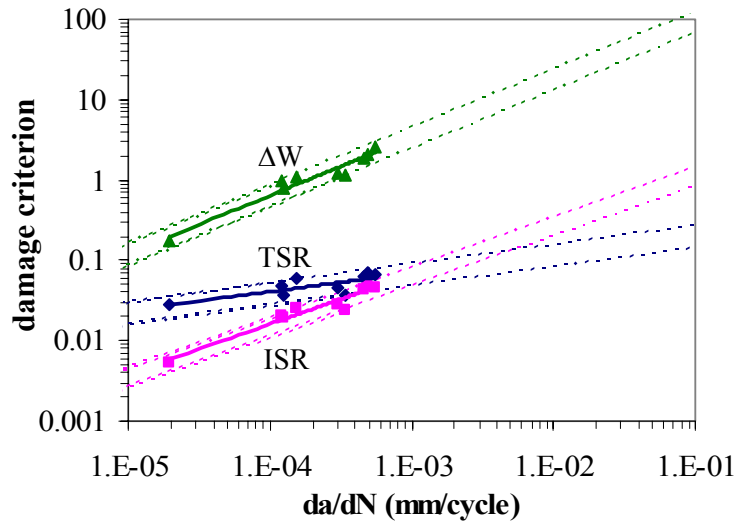


Figure 3.21: Damage propagation rate at 25°C, 2.9×10^{-2} 1/s strain rate: Sn3.5Ag

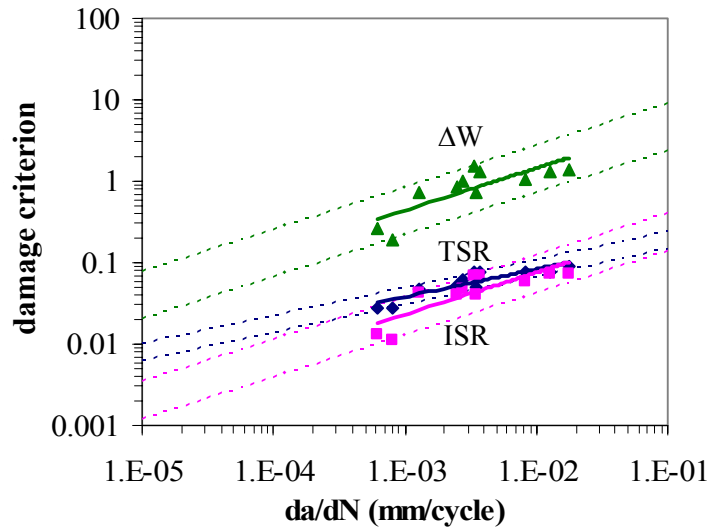


Figure 3.22: Damage propagation rate at 128°C, 4.5×10^{-4} 1/s strain rate: Sn3.5Ag

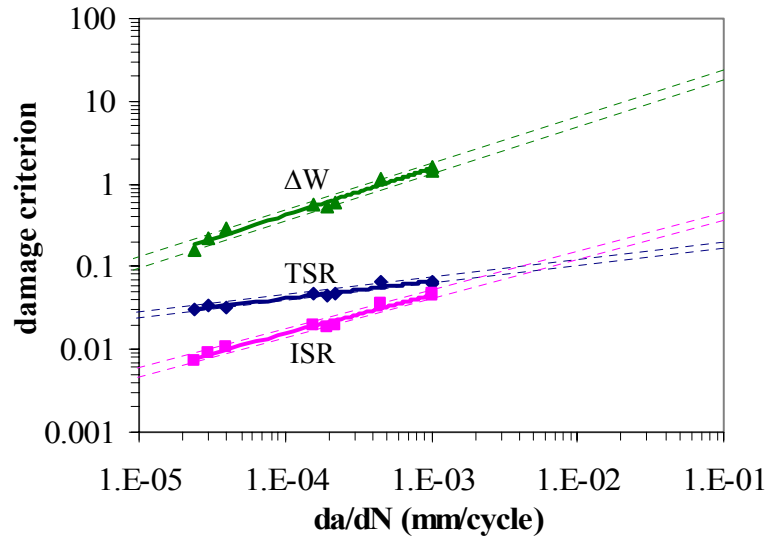


Figure 3.23: Damage propagation rate at 25°C, $3.6E-2$ 1/s strain rate: Sn0.7Cu

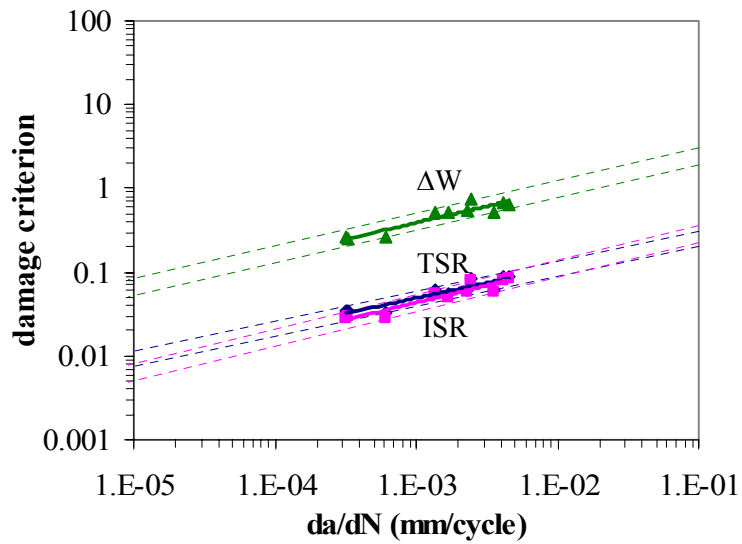


Figure 3.24: Damage propagation rate at 132°C, $4.9E-4$ 1/s strain rate: Sn0.7Cu

Solder		Regime 1			Regime 2		
		n_{cp}	C_{cp}	R^2	n_{cp}	C_{cp}	R^2
Sn3.9Ag0.6Cu	TSR	0.11	0.15	0.28	0.62	3.7	0.83
	ISR	0.39	0.90	0.90	0.74	7.3	0.85
	W	0.45	61.0	0.90	0.70	118	0.77
Sn3.5Ag	TSR	0.13	0.27	0.62	0.34	0.40	0.79
	ISR	0.62	4.9	0.94	0.52	0.82	0.70
	W	0.72	494	0.94	0.52	15.7	0.65
Sn0.7Cu	TSR	0.21	0.28	0.95	0.36	0.59	0.86
	ISR	0.47	1.2	0.98	0.41	0.75	0.89
	W	0.57	76.9	0.98	0.39	5.8	0.86

Table 3.8: Summary of damage propagation rate analysis for three Pb-free solder alloys

3.2.3 Post-test Microstructural Observations

As discussed in Chapter 2, TMM test specimens are well polished for measurement and microstructure observations prior to testing. After cyclic tests, it is still possible to make macro- and microscopic observations of the failed solder joint without further preparation. The main objectives of microstructural observations are to verify solder fatigue failure mode and to obtain qualitative knowledge of distribution and propagation of micro- and macro-cracks in Pb-free solder joints. The most desirable failure mode in cyclic mechanical tests is a macro-crack traversing through all or most of solder joint; an excellent example of such a failure can be seen in Figure 3.25. Failure mode found in the figure verifies that the TMM test is representative of the fatigue and damage accumulation characteristics of the bulk solder material. Distributed dense micro cracks are also apparent in this same figure, and are in fact present in almost all failed specimens.

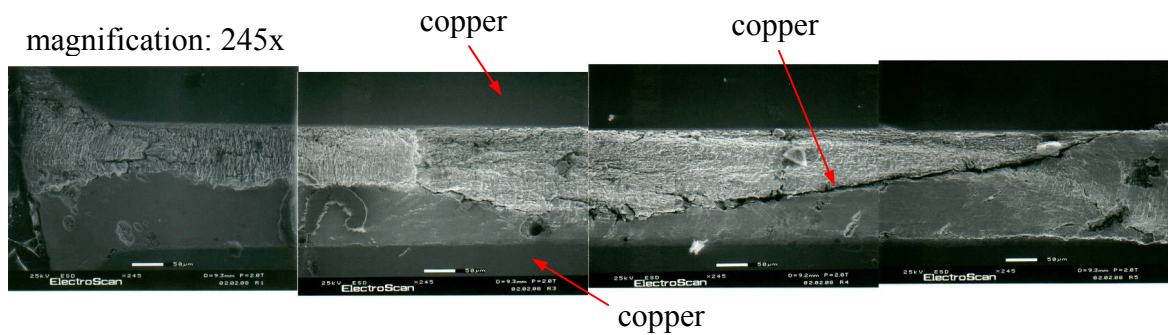


Figure 3.25: Post-test ESEM micrograph of Sn3.5Ag solder joint (low creep conditions, 25°C, 2.0% inelastic strain range control, 2.6E-2 1/s shear strain rate, 80% total load drop)

As mentioned earlier in Section 2.1, the microstructure of the Pb-free solders consists of essentially pure Sn matrix with elongated intermetallic Ag_3Sn and/or tiny round intermetallic Cu_6Sn_5 particles dispersed. With Sn phase dominant in the bulk solder, the active failure mechanisms take place mostly in the tin matrix, or at boundaries between tin grains. It is expected that rigid intermetallic particles interact with micro cracks at grain boundaries and play a role in solder fatigue failure mechanisms.

Failed specimens show different characteristic damage mechanisms under low creep and high creep test conditions due to different deformation mechanisms in two regimes. Figure 3.26 shows a detail of a Sn3.9Ag0.6Cu specimen after being subjected to loading under high creep conditions. Besides the macro-crack running in the middle of the solder joint, substantial distributed damage is observed around the crack. As seen under higher magnification (Figure 3.27), this damage appears to be concentrated at grain boundaries as grain boundary sliding. This is a major creep mechanism, known to dominate at high temperatures and low stresses. The same damage pattern is also found in the Sn3.5Ag and Sn0.7Cu solder joints under high creep conditions. Figure 3.28 and 3.29 show the similar damage patterns in Sn0.7Cu solders at low and high loading amplitudes. The Sn

grain size in Sn0.7Cu solder is observed to be much larger than that in Sn3.9Ag0.6Cu and Sn3.5Ag solders [Jang, et. al., 2001]. It is also noted that the damage density is inversely proportional to the distance from the macro crack, as shown in Figure 3.29.

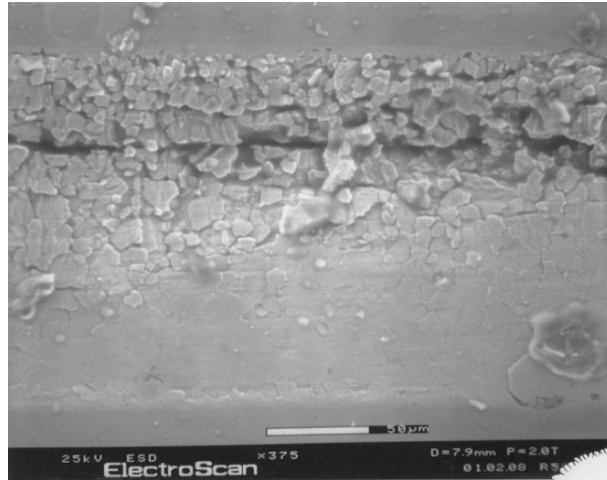


Figure 3.26: Post-test ESEM micrograph of Sn3.9Ag0.6Cu solder joint (high creep cyclic conditions, 125°C, 7.9% inelastic strain range control, $4.5E-4$ s⁻¹ shear strain rate, 55% total load drop)

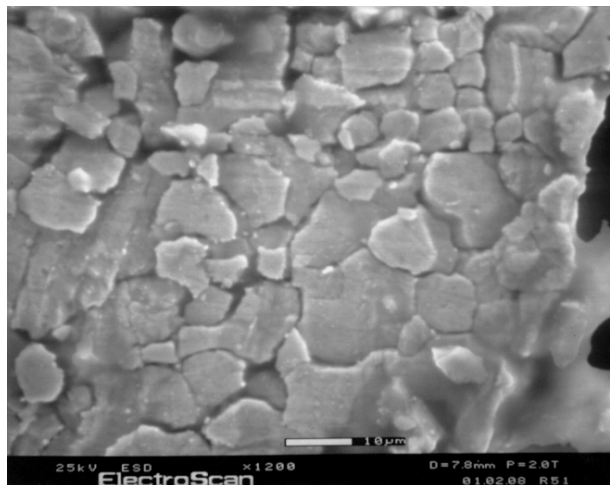


Figure 3.27: Post-test ESEM micrograph of Sn3.9Ag0.6Cu solder joint (high creep cyclic conditions, 125°C, 7.9% inelastic strain range control, $4.5E-4$ s⁻¹ shear strain rate, 55% total load drop)

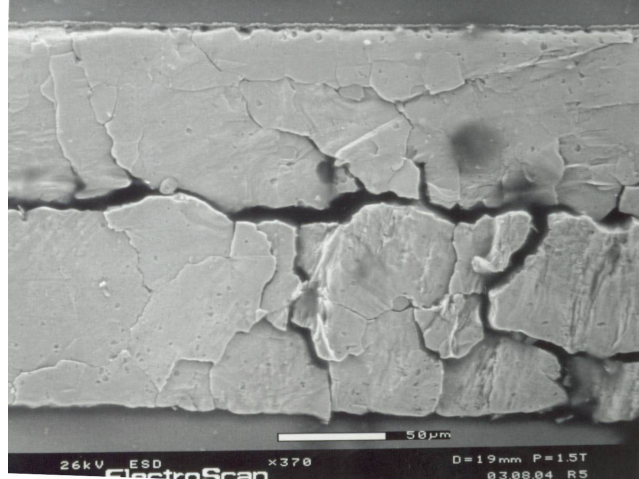


Figure 3.28: Post-test ESEM micrograph of Sn0.7Cu solder joint (high creep cyclic conditions, 132°C, 2.8% inelastic strain range control, 4.7E-4 1/s shear strain rate, 80% total load drop)



Figure 3.29: Post-test ESEM micrograph of Sn0.7Cu solder joint (high creep cyclic conditions, 132°C, 8.5% inelastic strain range control, 5.2E-4 1/s shear strain rate, 80% total load drop)

The characteristic damage in the low creep test specimens is expected to be quite different from that found in the high creep specimens because both plastic and creep deformation mechanisms are important in this regime. Rather than the significant grain boundary damage characteristic in the high creep specimens, damage evidence in the low creep specimens is localized and highly ordered. The parallel slip bands are very

common in all cases for all three Pb-free solders, with examples shown in Figure 3.30 to Figure 3.32. The orientations of the slip bands seem to be related the direction of the macro-damage propagation. The higher amplitude test specimen, shown in Figure 3.33, contains much denser and closely spaced distributed damage. It is observed that the slip bands are highly distorted at areas around the macro-crack while those far from the crack are still highly ordered. In addition, the macro-cracks in the high amplitude cases are wider and deeper than those in the low amplitude cases, as shown in Figure 3.32 and Figure 3.33. Thus, the macro-cracks have dominant effects on the final failure of the solder joint in the high amplitude cases.

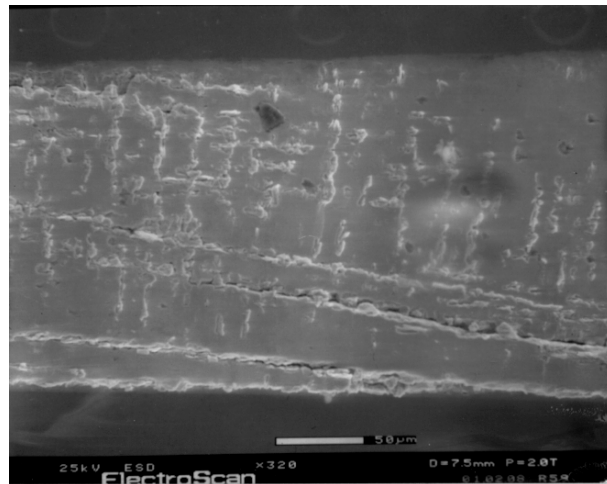


Figure 3.30: Post-test ESEM micrograph of Sn3.9Ag0.6Cu (low creep cyclic conditions, 25°C, 1.0% inelastic strain range control, $3.2E-2 \text{ s}^{-1}$ shear strain rate, 53% total load drop)



Figure 3.31: Post-test ESEM micrograph of Sn3.5Ag solder joint (low creep cyclic conditions, 25°C, 2.6% inelastic strain range control, $3.1\text{E-}2\text{ s}^{-1}$ shear strain rate, 80% total load drop)



Figure 3.32: Post-test ESEM micrograph of Sn0.7Cu solder joint (low creep cyclic conditions, 25°C, 4.7% inelastic strain range control, $3.9\text{E-}2\text{ s}^{-1}$ shear strain rate, 80% total load drop)

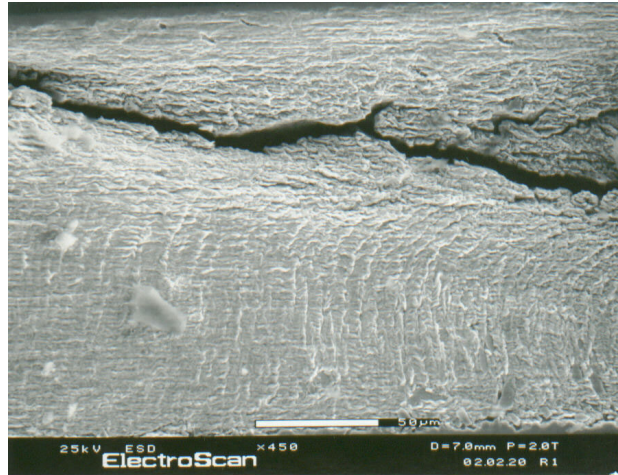


Figure 3.33: Post-test ESEM micrograph of Sn3.5Ag solder joint (low creep cyclic conditions, 25°C, 4.7% inelastic strain range control, $3.2\text{E-}2\text{ s}^{-1}$ shear strain rate, 80% total load drop)

3.3 Energy Partitioning Damage Model

The TMM test results presented in the last section are useful for predicting the mechanical durability of these solder alloys at two extreme conditions. They can also be employed to make a visual comparison of durability performance for those solder alloys. However, these durability parameters can only be used for the conditions similar to or same as the two test conditions because the damage mechanisms (creep and plastic damage) change as the test or use condition changes. An approach to derive a generic damage model (applicable to other test or use conditions) is the Energy Partitioning (E-P) Damage Model. E-P model constants for the three selected Pb-free solders are presented in this section, based on the TMM test data.

3.3.1 Approach

Low cycle fatigue, as observed in this study, is due to inelastic deformation occurring in the solder joints. There are multiple competing inelastic deformation mechanisms, each

with a different characteristic time scale. Some, like dislocation slip, occur over very short (almost instantaneous) time scales and result in plastic deformation. Plastic deformation is a function of applied stress and flow stress, which can vary with temperature. Others, like dislocation glide/climb, grain-boundary sliding, dislocation pipe diffusion (self diffusion along dislocation cores), grain-boundary diffusion, and intragranular diffusion, occur over much longer time scales and have an Arrhenius dependence on temperature. Deformation due to these mechanisms is termed creep deformation in this study. Creep deformation is the function of time, temperature, and stress. As test condition changes, specifically temperature, strain rate, and load magnitude, the ratio of plastic deformation to creep deformation changes. Different fatigue curves are thus expected for different test condition. In order to predict the mechanical durability of the Pb-free solder joints, a generic damage model has to be obtained from these test results. In other words, this model should be able to predict the durability of Pb-free solders under any test or use condition (any combination of plastic and creep deformation). One such damage model is the energy-partitioning model [Dasgupta et al., 1992].

The energy-partitioning (E-P) damage model assumes that cyclic fatigue damage is due to a combination of creep deformation mechanisms, plastic deformation mechanisms and elastic deformation mechanisms. This model predicts cyclic creep-fatigue damage based on the deviatoric energy densities: U_e (elastic), W_p (plastic) and W_c (creep) for a typical load cycle. The total damage is determined by using a power law equation and superposing the damage due to all these types of deformations:

$$\text{Total energy} = U_e + W_p + W_c = U_{e0} N_{fe}^b + W_{p0} N_{fp}^c + W_{c0} N_{fc}^d \quad (3.7a)$$

$$1/N_f = 1/N_{fe} + 1/N_{fp} + 1/N_{fc} \quad (3.7b)$$

where U_{e0} , W_{p0} , W_{c0} represent the intercepts of the elastic, plastic and creep energy density plots vs. cycles-to-failure, on a log-log plot; while the exponents b , c and d are their corresponding slopes. These constants are material properties. The variables N_{fe} , N_{fp} and N_{fc} represent the cycles-to-failure due to elastic, plastic and creep damage, respectively. The total number of cycles-to-failure N_f is then calculated from an Equation 3.7b. Elastic damage is typically very small and negligible, compared with plastic and creep damages in low cycle fatigue. So only plastic and creep terms in Equations (3.7a) and (3.7b) are considered in this study.

A systematic approach has been developed in this study to obtain E-P damage model constants for three Pb-free solders from their TMM test results. Figure 3.34 shows the whole approach employed in this study. In order to model the complex viscoplastic behavior of solder materials under mechanical cyclic loading, constitutive properties are needed as inputs in stress and damage analysis (box 1). Then a simplified one-dimensional analytic model is developed to simulate the TMM cyclic tests, as discussed in Section 2.3.1 (box 2). As shown in box 3, the analytic model provides stress-strain hysteresis for the TMM cyclic tests. Major outputs of this step are partitioned plastic and creep work densities which are needed to estimate damage based on models such as the E-P durability model of solders. In this study, this scheme is used in an inverse manner to estimate the model constants for the E-P model, for Pb-free solders. Combining partitioned work densities and cycles-to-failure data from mechanical cycling tests, the E-P durability model for solders can be obtained (box 4). Once the model

constants are known, the cycles-to-failure of Pb-free solder joints can be evaluated under any use/test condition by using the E-P damage superposition equation shown in box 5.

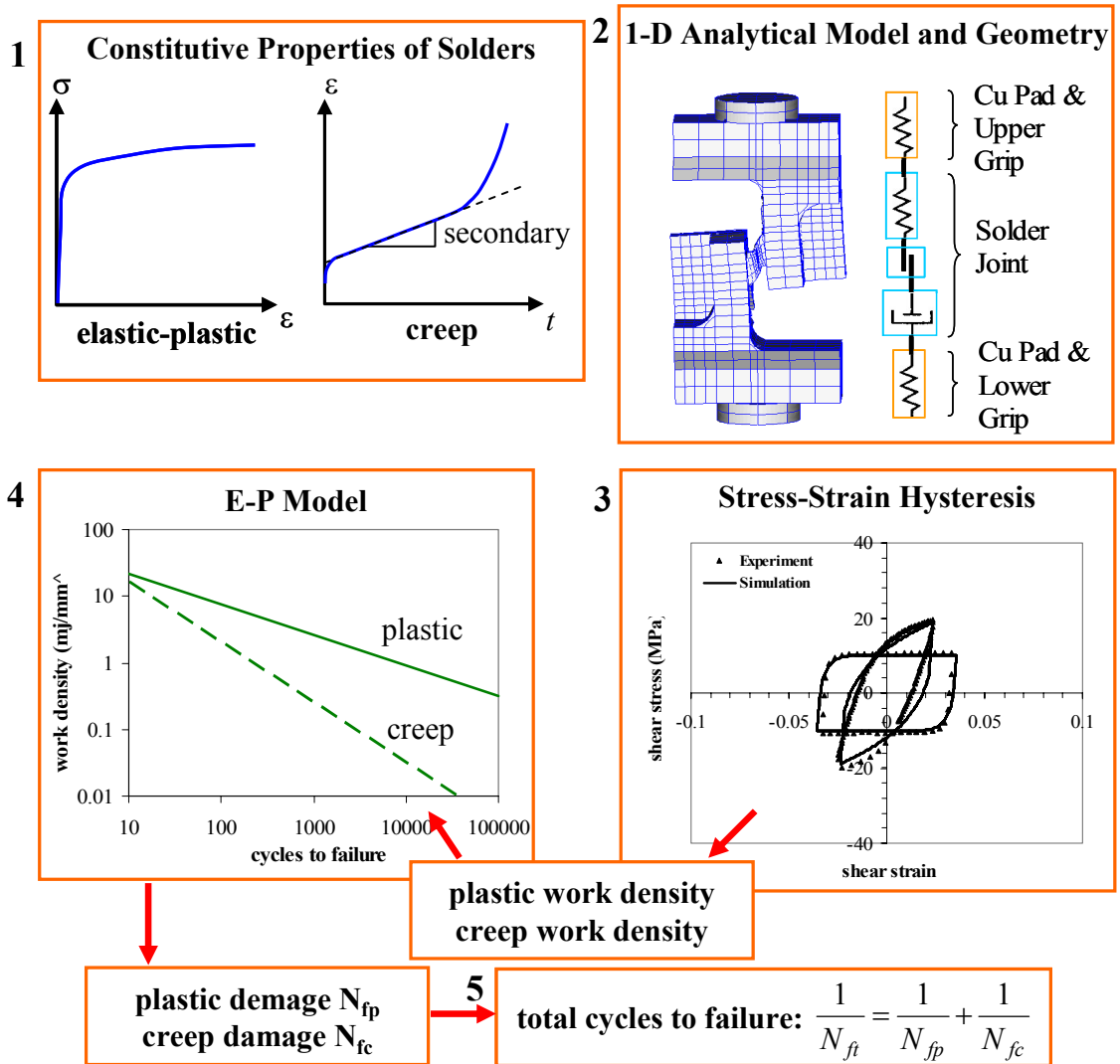


Figure 3.34: Overall approach for mechanical durability analysis

Implementation of the above approach to the TMM tests is now presented in this section. A partitioned constitutive model is adopted in this analysis. In this approach, the total shear strain of the solder joint, γ , is composed of rate-independent elastic strain, γ_{el} , rate-

independent plastic strain, γ_{pl} , rate-dependent primary creep strain, γ_{pcr} , and rate-dependent secondary creep strain, γ_{scr} :

$$\gamma = \gamma_{el} + \gamma_{pl} + \gamma_{pcr} + \gamma_{scr} \quad (3.8)$$

The shear modulus of the three Pb-free solders is summarized in Table 3.9. The model constants for Sn3.5Ag solder are obtained from the literature [Darveaux, et. Al., 1995]. Power law relationship is used for plasticity [Darveaux, et al., 1995], as shown in Equation (2.2):

$$\tau = C_{pl} \gamma_{pl}^{n_l} \quad (3.9)$$

where τ is the shear stress, γ_{pl} is the shear plastic strain, C_{pl} and n_l are the strength coefficient and the hardening exponent, respectively. C_{pl} and n_l used for the three Pb-free solder alloys are presented in Table 3.10. The model constants for Sn3.5Ag solder are obtained from the literature [Darveaux, et. Al., 1995].

Creep deformation of the solder joint is divided into primary and steady creep. Primary creep models for Sn3.9Ag0.6Cu and Sn3.5Ag are listed as follows:

$$\text{Sn3.9Ag0.6Cu solder: } \frac{\gamma_{pcr-sat} - \gamma_{pcr}}{\gamma_{pcr-sat}} = \exp(-A_{pcr}t) \quad (3.10a)$$

$$A_{pcr} = 0.0724\tau^{3.2688} \exp\left(-\frac{4393.6}{T}\right) \quad (3.10b)$$

$$\gamma_{pcr-sat} = 0.00298\tau^{1.1714} \quad (3.10c)$$

$$\text{Sn3.5Ag solder: } \frac{\gamma_{pcr-sat} - \gamma_{pcr}}{\gamma_{pcr-sat}} = \exp(-A_{pcr}t) \quad (3.11a)$$

$$A_{pcr} = 131 \frac{d\gamma_{scr}}{dt} \quad (3.11b)$$

$$\gamma_{pcr-sat} = 0.167 \quad (3.11c)$$

where γ_{pcr} is the primary creep strain, $\gamma_{pcr-sat}$ is the saturated primary creep strain, T is the temperature in K, t is the time in second, A_{pcr} is a model constant. No primary creep model is used for Sn0.7Cu solder in the analysis because none is available in the literature.

Steady-state creep of Sn3.9Ag0.6Cu and Sn3.5Ag solders is represented by the Garofalo, or sinh, creep model as shown here:

$$\frac{d\gamma_{scr}}{dt} = A_{scr} [\sinh(\alpha\tau)]^{n2} \exp\left(-\frac{Q}{RT}\right) \quad (3.12)$$

where R is the universal gas constant ($= 8.31451 \text{ m}^2 \text{ kg/s}^2\text{K mol}$), Q is an activation energy in J/mol, A_{scr} and $n2$ are model constants. Q , A_{scr} and $n2$ for two solders are listed in Table 3.11. The model constants for Sn3.5Ag solder was measured by Darveaux, et. Al. [Darveaux, et. Al., 1995]. A two-segment power law creep model is used to represent the steady-state creep deformation of Sn0.7Cu [Song, et. Al., 2002]. This relation is listed as follows:

$$\frac{d\gamma_{scr}}{dt} = 1.53E^4 \times [2.14E^{15} \times \tau^{3.5} \times \exp\left(-\frac{1.08E^4}{T}\right) + 3.33E^{37} \times \tau^{8.9} \times \exp\left(-\frac{1.02E^4}{T}\right)] \quad (3.13)$$

	Sn3.9Ag0.6Cu	Sn3.5Ag	Sn0.7Cu
Shear Modulus (GPa)	6.7-0.0080*T(°C)	4.7-0.0084*T(°C)	2.7

Table 3.9: Shear modulus for three Pb-free solders

	Sn3.9Ag0.6Cu	Sn3.5Ag	Sn0.7Cu
C_{pl} (MPa)	60.1-0.18*T(°C)	51.0-0.18*T(°C)	83.4
n_1	0.29-0.00046*T(°C)	0.23	0.39

Table 3.10: Plastic model constants for three Pb-free solders

	Sn3.9Ag0.6Cu	Sn3.5Ag
Q (J/mol)	7.13E4	7.24E4
A	1.50E3	2.46E5
α (1/MPa)	0.19	0.09
n_2	4.0	5.5

Table 3.11: Secondary creep model constants for Sn3.9Ag0.6Cu and Sn3.5Ag

Substituting the constitutive models presented here into the analytical model, the predicted stress-strain hysteresis loops for TMM cyclic tests at both test conditions can be obtained for the three Pb-free solders. The comparisons of the hysteresis loops from experiments and simulation are shown in Figure 3.35, Figure 3.36, and Figure 3.37 for Sn3.9Ag0.6Cu, Sn3.5Ag, and Sn0.7Cu, respectively. The experimental and predicted hysteresis loops are in good agreement for Sn3.9Ag0.6Cu solders under two selected test conditions (low creep and high creep conditions). It indicates that the analytical model is adequate for simulation of the stress-strain behavior of these two solders in TMM cyclic tests. However, for Sn3.5Ag solder, the analytical model underestimate the stress range for regime 1 and overestimates the strain range for regime 2. The differences are due to that the test specimens and conditions in which plastic and creep models were obtained in the literature are different from those in this study. As for Sn0.7Cu solder, the analytical model can predict a good hysteresis loop for regime 1 but not for regime 2. This is

probably due to absence of primary creep model and/or inappropriate secondary creep model in the analytical model. Then the creep and plastic deformations are calculated from the model analyses for all TMM tests of three solder alloys. Finally, the creep and plastic energy densities per cycle are obtained from the analytical model by integrating the individual stress-creep strain and stress-plastic strain hysteresis loops. Combining partitioned creep and plastic energy densities and tested cycles-to-failure into Equation 3.7a and 3.7b, two pairs of E-P model constants, W_{p0} and c for plastic damage, W_{c0} and d for creep damage, can be obtained.

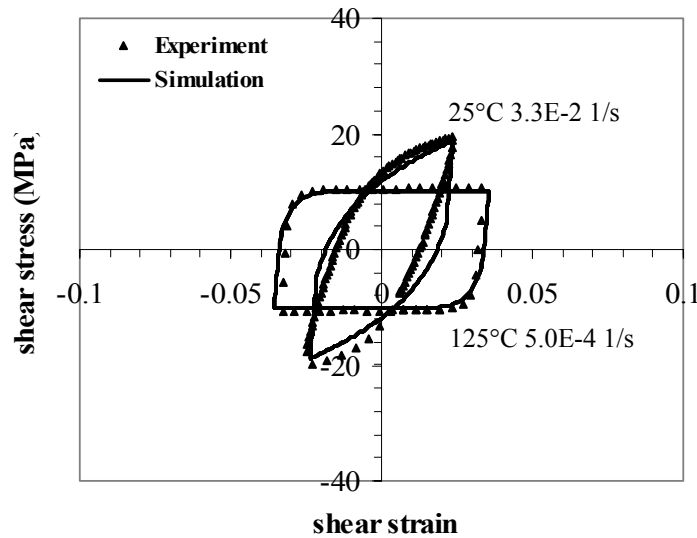


Figure 3.35: Comparison of the hysteresis loops from experiments and simulation for Sn3.9Ag0.6Cu solder

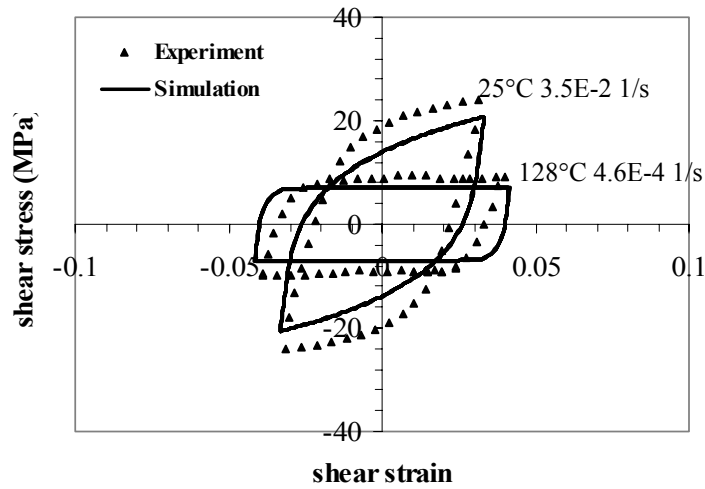


Figure 3.36: Comparison of the hysteresis loops from experiments and simulation for Sn3.5Ag solder

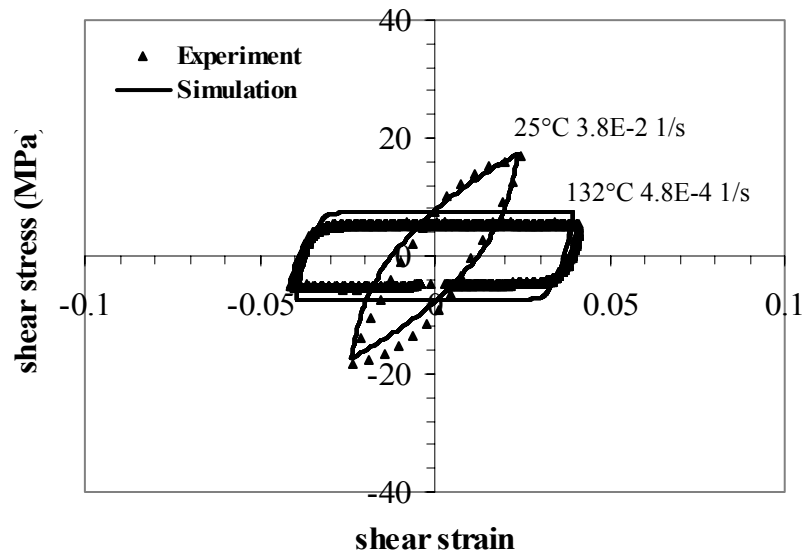


Figure 3.37: Comparison of the hysteresis loops from experiments and simulation for Sn0.7Cu solder

3.3.2 E-P Damage Models of Pb-free Solders

Using the least-square method to correlate the partitioned creep and plastic energy densities to corresponding cyclic test values, energy partitioning model constants can be obtained for three Pb-free solders. These constants are presented in Table 3.12. Using

these energy-partitioning model constants with Equation 3.7a and 3.7b, the isothermal mechanical durability of three Pb-free solders can be predicted for any test condition and use environment, in other words, any combination of plastic and creep damages. It is seen in the table that the values of W_{p0} and W_{c0} for Sn3.9Ag0.6Cu solders are larger than those for Sn3.5Ag and Sn0.7Cu solders. There are two possible reasons: (1) the Sn3.9Ag0.6Cu solder has the best durability in the three Pb-free solders for both regimes; (2) constitutive properties of Sn3.5Ag and Sn0.7Cu solders are obtained from the literature. Since the electronic packaging community usually uses only secondary creep model in the finite element analysis, the E-P model constants are also obtained for Sn3.9Ag0.6Cu solders without including primary creep model in the analytical model. These model constants are listed in Table 3.13. These E-P model constants are used to compare with that estimated from thermal cycling tests in Chapter 4.

The durability predicted by the estimated energy-partitioning damage model is compared to the test results for Sn3.9Ag0.6Cu, Sn3.5Ag and Sn0.7Cu solders in Figure 3.38. Of the fifty one tests for three Pb-free solders, most of the data points fall in the $\pm 100\%$ band. It indicates that the energy partitioning models can be used to evaluate the isothermal mechanical durability of three Pb-free solders for a broad range of creep and plastic damage.

	Sn3.9Ag0.6Cu	Sn3.5Ag	Sn0.7Cu
c	-0.46	-0.30	-0.35
W_{p0}	72.7	16.6	8.6
d	-0.77	-0.48	-0.55
W_{c0}	80.4	5.7	15.2

Table 3.12: Energy-partitioning model constants for three Pb-free solders

	With Primary Creep	Without Primary Creep
c	-0.46	-0.46
W_{p0}	72.7	72.7
d	-0.77	-0.90
W_{c0}	80.4	174.6

Table 3.13: Energy-partitioning model constants for Sn3.9Ag0.6Cu: with and without primary creep

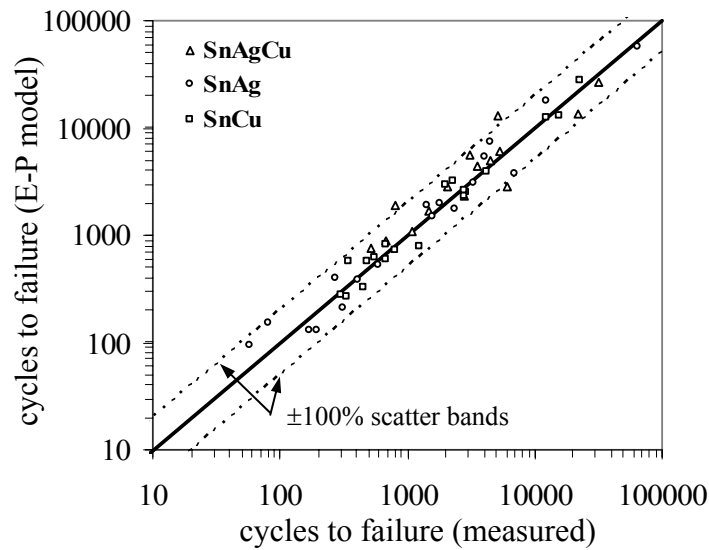


Figure 3.38: Comparison of the durability predicted by energy-partitioning model with measured test results for Sn3.9Ag0.6Cu, Sn3.5Ag and Sn0.7Cu solders

4 Thermo-Mechanical Durability

Solder materials are extensively used as interconnects in packaging technologies. In surface mount technologies the solder interconnect is required to act as not only an electronic and logical path but also a mechanical link between the silicon die and the substrate (flip chip), and between the component and the PWB in surface mount assemblies. These interconnects experience high mechanical stress, especially in advanced packaging technologies such as flip chip, BGA, PGA, and CSP. It is well-known that the principle cause of failures in solder interconnections can be attributed to the deformation that is caused by the mismatch in thermal expansion between a surface mounted device and the PWB, because of changes in the ambient temperature or temperature gradient during power cycling. In order to predict the durability of solder interconnections under field use condition, amplified thermal cycle loading is applied to surface mount assemblies during accelerated thermal cycling life test. The durability of solder joints subjected to thermal cycle loading is dependent on the thermo-mechanical durability of the solder material.

Thermo-Mechanical durability of solder is more complicated than isothermal mechanical durability of solder, and is affected by a lot of factors such as:

- loading parameters (cyclic temperature range, mean temperature, dwell times, dwell temperatures, and ramp rates)
- solder microstructure (e.g. grain size; dispersoid composition size, and distribution)

- solder joint geometry (e.g. solder balls, solder columns, solder joints for leaded packages)
- presence of complex intermetallics (e.g. Under Bump Metallurgy for flip chip)
- soldering defects (e.g. voids, misalignment)
- residual stresses due to processing

Due to complicated solder joint geometry and component geometry, the stress-strain distribution due to cyclic thermal loading is considerably different from that under mechanical cycling discussed in the last chapter. All of these factors play a role in thermo-mechanical durability of solder.

As mentioned before, there is an urgent need for thermo-mechanical durability tests and properties of Pb-free solders. Damage models for Pb-free solders need to be derived from the systematic post-processing of thermal cycling test data. In this chapter, thermal cycling test of a Circuit Card Assembly (CCA) test vehicle employing Sn3.8Ag0.7Cu solder, Sn37Pb solder, and mixed solder systems is discussed. The specimens were designed, fabricated and tested by CALCE sponsors. DPA for specimen characterization, for failure analysis was conducted as part of this dissertation. Detailed Finite element Analysis (FEA) was conducted as part of this dissertation, to estimate the damage metrics (Cyclic Work Density, ΔW , Inelastic Strain Range, ISR) in critical solder joints. Test results are analyzed and discussed in Section 4.2. A comprehensive failure analysis of failed specimens follows in Section 4.3. Finally, three-dimensional viscoplastic Finite element (FE) analysis of five thermal cycling tests is presented and E-P damage model for SnAgCu solders is obtained from thermal cycling test data and corresponding FE

analytical results. Applications of E-P damage models to predict the thermo-mechanical durability under field use conditions, and to evaluate the acceleration factor for the test (the ratio of durability under accelerated test condition to that under field use condition) are presented at the end.

4.1 Thermal Cycling Test

The main objectives of the thermal cycling tests in this study are to observe potential failure mechanisms in Pb-free soldered surface mount assemblies, to investigate the issue of Pb-free compatibility with SnPb technology, and to generate failure data to be used in the development of durability models for Pb-free solders. These goals were accomplished by accelerated temperature cycling durability tests.

Accelerated temperature cycling tests were conducted to investigate the effects of several design and assembly process variables when subjected to environmental extremes. CCA variables include solder paste type, solder bump type, component type, and use of underfill materials. Solder paste types include Sn37Pb and Sn3.8Ag0.7Cu solder alloys. Solder bumps are either Sn37Pb or Sn3.8Ag0.7Cu. Device types include area array components with pitches of 0.5, 0.75, 0.8 and 1.27 mm. Non-reworkable underfill materials are included under some components. Details of the test vehicle, board assembly, test vehicle characterization, and test profile are discussed below.

4.1.1 Test Vehicle

The test vehicle is depicted in Figure 4.1. The PWB was designed and supplied by the National Center for Manufacturing Sciences (NCMS) High Density Consortia effort. The PWB is a 152.4 x 101.6 x 1.6 mm, 6-layer, High-Tg FR4 substrate, with an electroless nickel, immersion gold (ENIG) surface finish and non-solder mask defined pads. Each PWB is populated with a total twenty one area array Surface Mount Technology (SMT) components. Five device styles, varying primarily in lead pitch include PBGA352 (one), fleXBGA144 (six), TABGA96 (two), μ BGA48 (six), and μ BGA46 (six). Two solder bump material and solder paste compositions are used: Sn37Pb (SnPb) and Sn3.8Ag0.7Cu (SAC) alloys. Table 4.1 and Table 4.2 contain detailed PWB and device characteristics. Table 4.3 describes the board assembly configuration.

PWB construction provides continuity through the solder joints interconnecting the PWB and daisy chained components. Monitoring net resistance during environmental stress testing enables detection of solder joint failures via an increase in electrical resistance caused by solder joint crack formation.

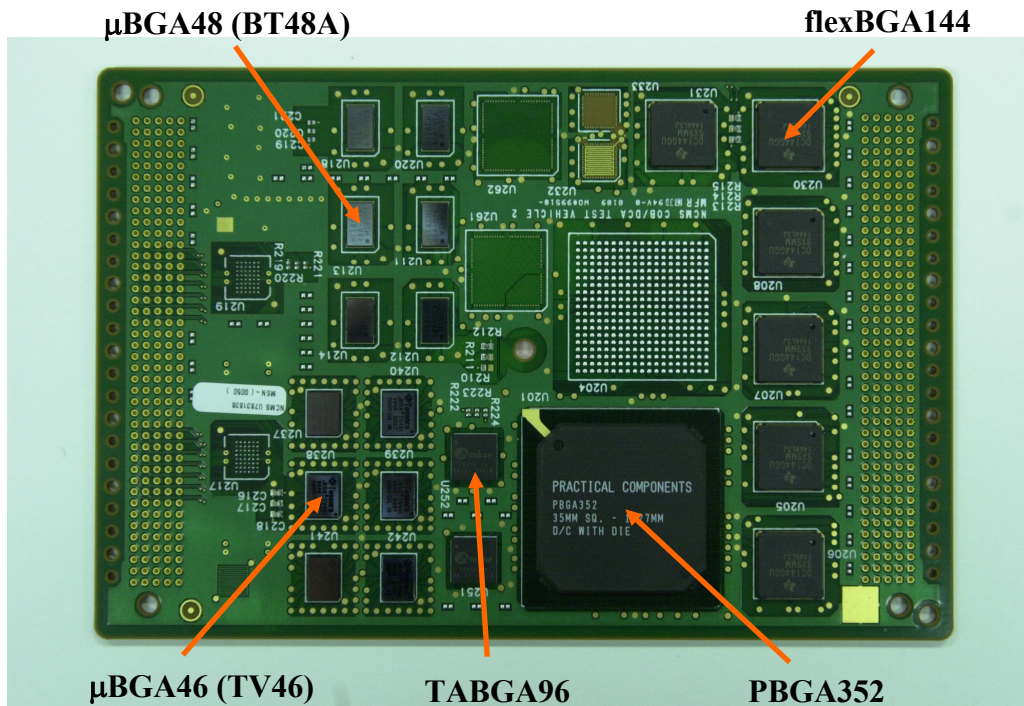


Figure 4.1: Test vehicle schematic

Characteristic	Device				
	PBGA352	flexBGA144	TABGA96	BT48A	TV46
Physical Dimension (mm)					
Length	35.00	12.00	8.00	8.23	7.87
Width	35.00	12.00	8.00	5.00	5.76
Height	2.29	1.09	0.97	0.76	0.83
Ball Dia.	0.76	0.46	0.30	0.30	0.30
Comp. Land	0.49	0.33	0.18	0.28	0.28
Package Details					
Pitch (mm)	1.27	0.80	0.50	0.75	0.75
Interposer Type	Rigid	Flex	Flex	Flex	Flex
I/O Count	352	144	96	48	46
Construction	Wire Bond			Lead Frame	
Pad Definition	Solder Mask Defined				
Die Dimension (mm)					
Length	12.3	8.95	5.14	7.49	7.47
Width	12.3	8.95	5.14	4.45	5.51
Thickness	0.30	0.27	0.31	0.27	0.43

Table 4.1: Device characteristics

Characteristic	Value
Material	High T _g FR-4 Epoxy
Layer Count	6
Surface Finish Thickness (μm)	
Gold	0.36~0.98
Nickel	0.84~1.26
Physical Dimension (mm)	
Length	152.4
Width	101.6
Thickness	1.6
Device Land Diameter (mm)	
PBGA352	0.69
FleXBGA144	0.36
TABGA96	0.28
BT48A	0.28
TV46	0.28
Pad Definition	Non-Solder Mask Defined

Table 4.2: PWB characteristics

QTY	Solder Alloy		Underfill
	Paste	Device	
4	SAC	SAC	No
4	SAC	SAC	Yes
4	SnPb	SAC	No
4	SAC	SnPb	No
4	SnPb	SnPb	No

Table 4.3: Board assembly configuration

4.1.2 Board Assembly

Test vehicles are assembled using standard SMT processes by a CALCE sponsor. Solder pastes are Type 3 with RO flux. Stencils are laser cut, electro-polished Alloy 42 with a base thickness of 0.152 mm and step-downs to 0.127 and 0.102 mm, to maintain acceptable area ratios. A seven zone, inert atmosphere, convection oven is used for reflow. The SnPb reflow profile has peak temperatures ranging from 206°C~221°C and time above 183°C averaging 74 seconds. The SAC reflow profile has peak temperatures

ranging from 236°C~250°C and time above 217°C averaging 72 seconds. Additionally, a set of SAC system assemblies, were underfilled.

X-ray laminography was the primary post assembly inspection tool. The data summarized in Table 4.4 provides comparison of defect calls for each paste alloy (reflow profile). Higher voiding levels were experienced on PWBs processed with Pb-free paste; consistent with the literature [Bath and Jasbir, 2003, Harrison, et. al., 2001, Kujala, et. al., 2003, Collier, et. al., 2002]. It should be noted that no process optimization activities were conducted. The reflow profile used was the paste formulator’s recommendation while the X-ray program, developed for SnPb systems, was used for all configurations.

Paste	Board Yield	Underfill				
		I	M	O	S	V
SAC	25%	0	0	0	16	352
SnPb	42%	0	0	1	0	31

I: Insufficient M: Misaligned O: Open
S: Short V: Void

Table 4.4: X-ray solder defect summary

4.1.3 Test Vehicle Characterization

All combinations of five component types and four solder joint configurations are characterized in detail during this dissertation, using DPA. The major objectives of the characterization were: a) to identify defects in CCAs after test vehicle assembly; b) to obtain the geometry of all assembled devices for finite element analysis; c) to collect and measure if needed, the coefficient of thermal expansion (CTE) and other material properties of components and PWB boards; d) to record the microstructures of solder joints (four combinations of SnPb solder ball/paste and SAC solder ball/paste). The first

two objectives were achieved through microsectioning, optical inspection and measurement. In order to more clearly reveal the solder microstructure, a solution of 5% HNO₃, 3% HCL, 92% CH₃OH was used to etch away solder for several seconds. Pb contamination is estimated by composition mapping using Scanning Electron Microscope.

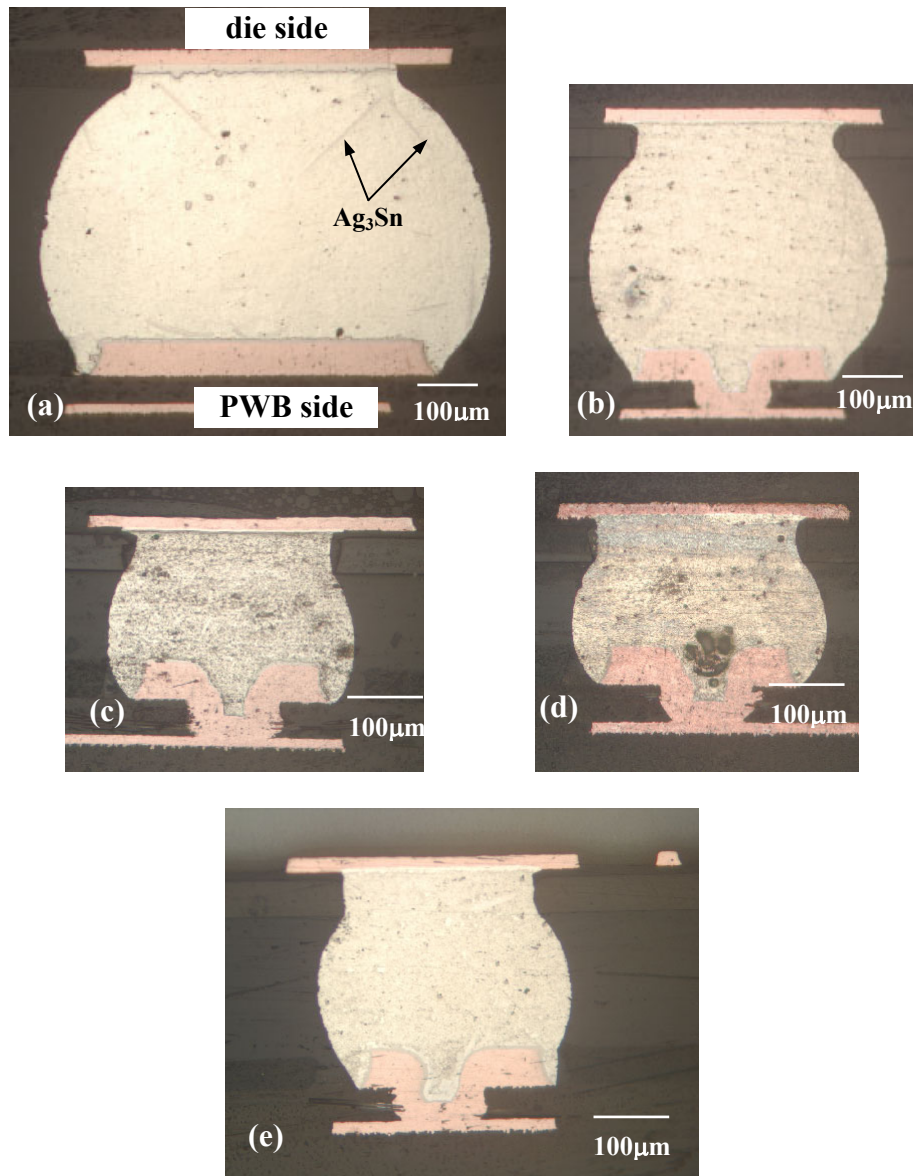


Figure 4.2: Optical micrographs of SnAgCu solder joints; (a) PBGA352, (b) fleXBGA144, (c) TABGA96, (d) μBGA46, (e) μBGA48

Figure 4.2 shows optical micrographs of typical Pb-free solder joints of five assembled BGA and CSP components. These joints use a combination of SnAgCu solder ball and paste. It is seen that all solder joints have fairly good appearance, except for a large void in μ BGA46 joints. Voids are also found in three other components with microvias (fleXBGA144, TABGA96, and μ BGA48). Microsectioning results show that voids are more common in small solder joints such as μ BGA46 and μ BGA48 than in large PBGA solder joints. It is because of the air trapped in microvias and because this air has a shorter time to escape during the reflow process as a shorter solidification time is expected for small solder joints. But these voids can be eliminated by optimizing reflow profile, solder flux and PWB surface finish. Besides voids, very slight misalignment exists in μ BGA48 packages for all solder joint configurations. It is also found that larger thin platelet Ag_3Sn intermetallic phases exist in PBGA solder joints but only small ones in other small joints. This is mostly due to short cooling time and small amount of silver. The last observation is that the intermetallic layer at the die side is much thicker than that at PWB side because it was subjected to two reflows.

Figure 4.3 shows optical micrographs of four combinations of solder ball/paste. Since over two thirds of the joint volume is made up of solder ball material, the solder joint microstructure is dominated by solder ball characteristics, resulting in darker appearance of SnPb components relative to SAC components. It should be noted that in all four cases, solder ball and paste are fused together very well. Even the worst case combination, Figure 4.3c, for which the solder ball has a much higher melting point than the paste and reflow temperatures match solder paste melting point, the micrograph

shows a good joint. Etching was performed to observe the microstructure of the solder joints. Figure 4.4 shows a typical microstructure of Pb-free solder that consists of essentially pure Sn matrix with intermetallic Ag_3Sn platelets and needles and tiny round intermetallic Cu_6Sn_5 particles dispersed at the grain boundaries. As seen in Figure 4.5, Ag_3Sn platelets and needles are revealed more clearly after etching. It is also seen that these platelets can be divided into two groups: one growing from the intermetallic layer to bulk solder and one growing from the center of solder joint to the peripheral area. Etching reveals the difference between two phases: SnAgCu solder ball and SnPb paste, as shown in Figure 4.6.

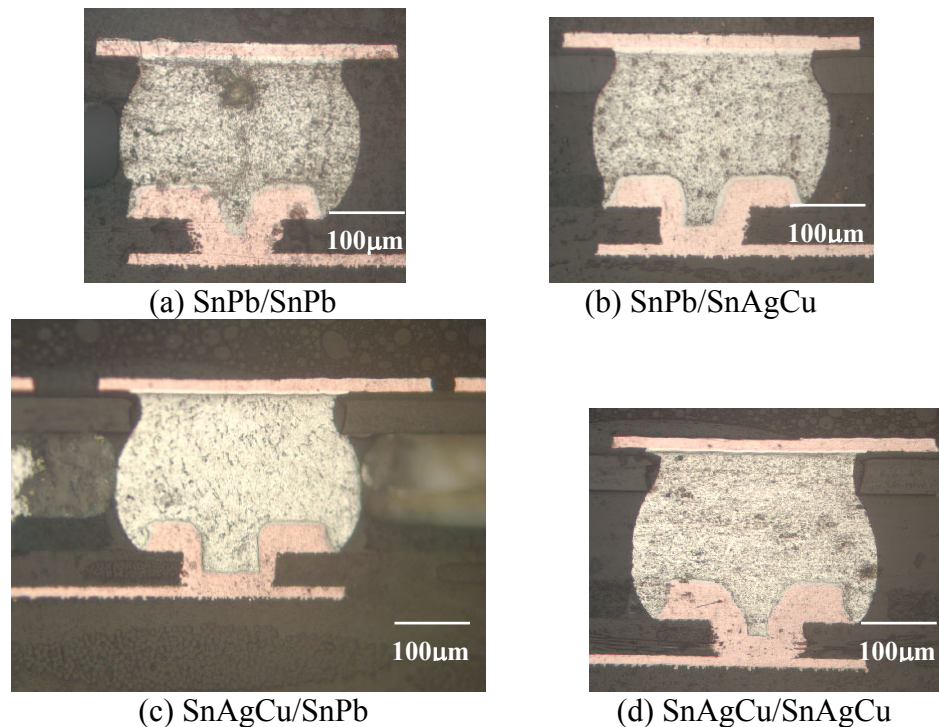


Figure 4.3: Optical micrographs of four solder systems of TABGA 96 component (label: Solder ball/paste)

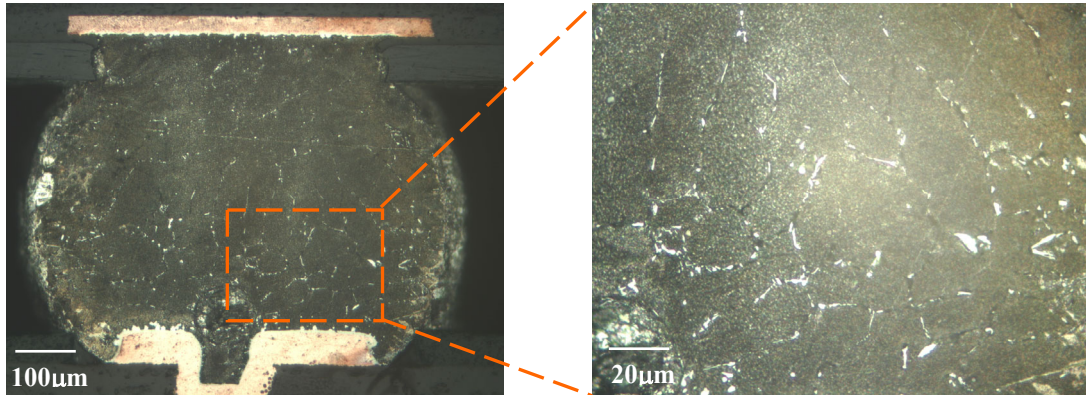


Figure 4.4: Optical micrograph of pure SnAgCu PBGA352 solder joint after etching

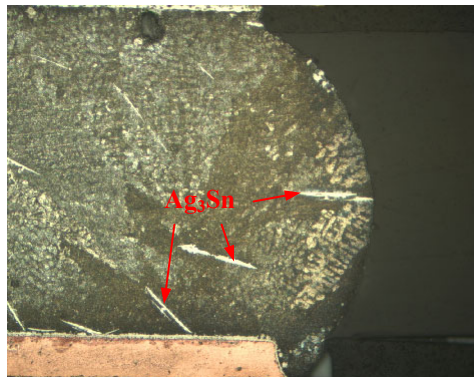


Figure 4.5: Optical micrograph of pure SnAgCu PBGA352 solder joint after etching

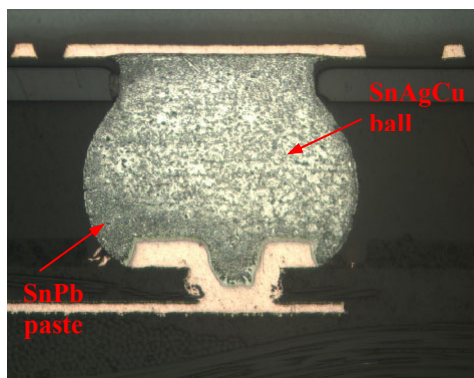


Figure 4.6: Optical micrograph of SnAgCu/SnPb solder joint of µBGA48 device after etching

The geometries of the solder joints in the assembled PBGA352, fleXBGA144, TABGA96, and µBGA46 components are measured by optical microscope after micro

cross sectioning. The geometry and corresponding dimensions of the PBGA352 solder joint are shown in Figure 4.7. The schematic geometry for the solder joints of the fleXBGA144, TABGA96, and μ BGA46 components includes microvia as shown in Figure 4.8. The measured geometry of three solder joints is summarized in Table 4.5. Other dimensions, such as die thickness, and substrate length, can be found in Table 4.1. The geometric information is used to build up the 3-D finite element models for these packages.

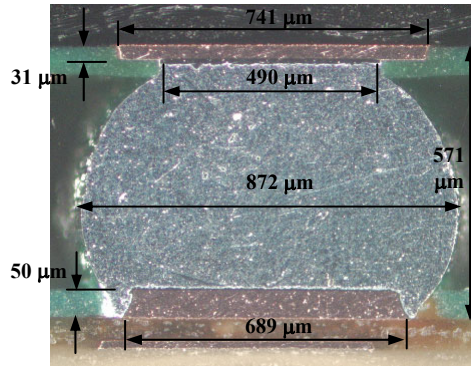


Figure 4.7: Dimensions of solder joint and copper pads for PBGA352 joint

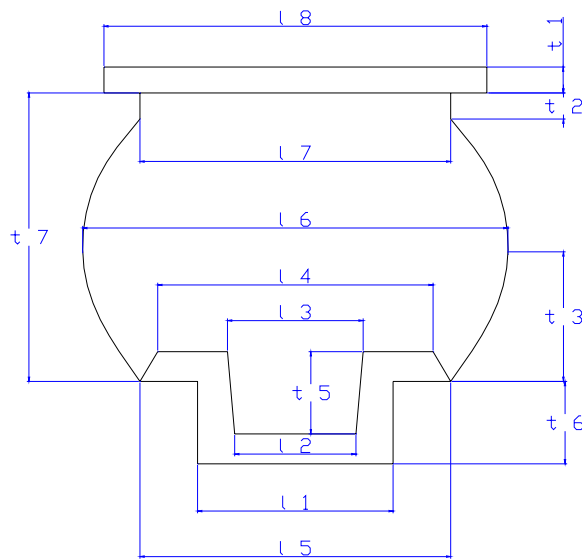


Figure 4.8: Schematic geometry for solder joints of the fleXBGA144, TABGA96, and μ BGA46

Component	t_1	t_2	t_3	t_4	t_5	t_6	t_7	
flexBGA144	26	61	212	47	72	49	449	
TABGA96	19	38	105	46	70	52	232	
μBGA46	20	54	99	38	64	49	239	
	l_1	l_2	l_3	l_4	l_5	l_6	l_7	l_8
flexBGA144	128	67	83	328	355	568	384	494
TABGA96	130	49	93	246	277	358	288	427
μBGA46	133	69	90	249	274	358	304	437

Table 4.5: Measured geometry for flexBGA144, TABGA96, and μ BGA46 joints

Most material properties of the die, molding compounds, substrate, die attach and FR-4 epoxy found in these packages are collected from component manufacturers and relevant literature. They are summarized in the following FEA section. The effective CTE of all four kinds of components and CTE of PWB are measured during this dissertation using a TMA. A step approach is used to measure the CTE. The specimen is first heated up at the rate of 6°C/min. from -50°C and held for 5 minutes after every 30°C increase until 125°C. This heating process is the same as that in thermal cycling tests. A typical TMA CTE test results for PBGA352 package is shown in Figure 4.9. The CTE is calculated for each segment in the figure. The average CTE of all segments is taken as the CTE value of this specimen. Two or three specimens are tested for each kind of component. The effective CTE of these components are obtained by averaging the test data of all specimens. The measured effective CTE of four components and PWB are listed in Table 4.6.

The effective CTE is critical for finite element analysis of thermal cycling because the stress-strain distribution in the solder joint directly results from the CTE mismatch

between the component and PWB. So the finite element model is built up for each component to simulate the CTE measurement process. The simulated effective CTE is compared with the test result to verify the accuracy of material properties used in the model. Material properties are fine tuned, where necessary, to match the simulated effective CTE of the component exactly to the tested CTE.

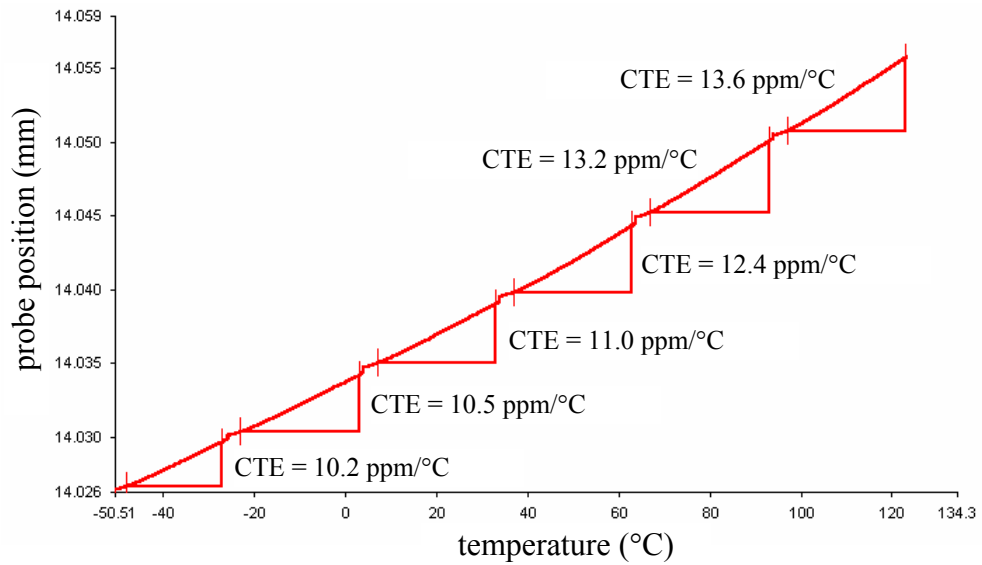


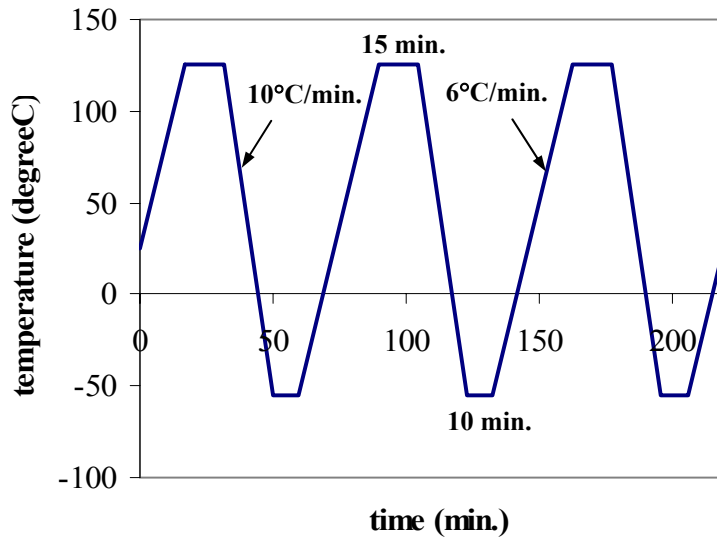
Figure 4.9: Typical TMA CTE test results for PBGA352 package

Device		CTE (ppm/°C)
PBGA352		12.0
fleXBGA144		5.9
TABGA96		6.8
μBGA46		26.1
PWB	Long Axis	17.8
	Short Axis	14.5

Table 4.6: Measured effective CTE of components and PWB

4.1.4 Reliability Testing

Thermal cycling was performed from -55°C to 125°C with a 10-minute dwell at cold and 15-minute dwell at hot extremes. Maximum ramp rate was 10°C per minute as measured on test vehicles. Thermal profile is shown in Figure 4.10. Data loggers were configured with event duration sensitivity of 0.2 microseconds. An event is defined as a net resistance increase exceeding 300 ohms. A failure is defined as 15 events to avoid the possibility of random false positive readings. Detected events were recorded every 164 seconds. Once a net was considered a failure, monitoring ceased.



Weibull reliability Function and the three-parameter Weibull Reliability Function included in Equations 4.1a and 4.1b.

$$\text{Two-parameter (2-P) Weibull: } R(t) = \exp\left(-\left(\frac{t}{\eta}\right)^\beta\right) \quad (4.1a)$$

$$\text{Three-parameter (3-P) Weibull: } R(t) = \exp\left(-\left(\frac{t-\gamma}{\eta}\right)^\beta\right) \quad (4.1b)$$

Where: β = shape parameter (a measure of the variance of the results); η = scale parameter (characteristic life for 2-P Weibull, when the 63.2% population fail); γ = location parameter (failure free period for 3-P Weibull).

The CALCE sponsors conducted thermal cycling tests up to 3431 cycles. 50% of the sample population failed on 20 out of 23 test configurations. Table 4.7 contains failure summary for each test configuration. Test configurations with less than 50% failure are indicated by bold numbers in the table. Table 4.8 contains Weibull Data for 18 test configurations of four component types. During the Weibull analysis, the value of 3431 cycles was used as censored test data for those nets, which did not fail at the end of the test. In Table 4.8, Weibull analysis results are represented in italic words when data points are removed as premature failures in that condition. Especially, for test condition 4 of TV46 component, data points for Weibull analysis are less than 50% available nets after premature failures are removed. In addition, test results of BT48A are not listed in Table 4.8 as all BT48A Components had only SnPb solder ball metallization.

Test Conditions			1	2	3	4	5
Solder System	Paste	SnPb	X	X			
		SAC			X	X	X
	Device	SnPb	X		X		
		SAC		X		X	X
Underfill							X
PBGA352	Failures		16	15	16	16	1
	Nets		16	16	16	16	16
fleXBGA144	Failures		24	24	23	24	19
	Nets		24	24	24	24	24
TABGA96	Failures		23	24	24	24	11
	Nets		24	24	24	24	24
BT48A*	Failures		15		25		16
	Nets		32		32		16
TV46	Failures		9	8	13	9	13
	Nets		15	16	16	15	16

*All BT48A Devices had SnPb solder ball metallization.

Table 4.7: Thermal cycling test results

Test Conditions	PBGA352			fleXBGA144			TABGA96			TV46						
	β	η	ρ	β	η	ρ	β	η	ρ	β	η	ρ				
2-P Weibull																
1	49.3	2046	0.96	8.2	902	0.99	6.2	1300	0.98	1.6	3466	0.97				
2	9.8	2858	0.94	7.0	1594	0.98	4.5	1163	0.96	1.8	3219	0.90				
3	9	2195	0.95	4.4	732	0.97	5	1540	0.94	1.5	2238	0.96				
4	4.1	2083	0.99	9.4	1370	0.97	4.4	1453	0.97	4.1	3737	0.99				
5				5.3	2368	0.96				2.5	2640	0.95				
3-P Weibull	β	η	γ	ρ	β	η	γ	ρ	β	η	γ	ρ	β	η	γ	ρ
1	2.5	154	1896	0.95	5.9	689	213	0.99	3.3	805	495	0.99	0.9	3946	497	0.99
2	1.2	645	2197	0.98	4.8	1195	401	0.98	1.5	558	581	0.98	0.5	6259	728	0.99
3	2.8	865	1324	0.96	3.2	588	146	0.97	1.6	667	833	0.99	0.9	2118	309	0.99
4	3.2	1762	317	0.99	2.4	450	908	0.99	1.9	814	617	0.99	1.6	2694	1463	0.99
5					2.9	586	2050	0.99					0.8	1974	942	0.98

Table 4.8: Weibull analysis results.

Weibull correlation coefficients are very close to one for both 2-P and 3-P Weibull analysis of all cases, which indicates that the life data do indeed follow Weibull distributions. For the shape parameter, β , the range for 2-P Weibull is from 1.5 to 9.8

(except extremely large value of 49.3 due to the removal of premature failures) with an average of 5.2. The β value for 3-P Weibull ranges from 1 to 5.9 with an average of 2.8, which is slightly larger than Clech et al.'s average value of 2.2 for SMT and very close to Darveaux et al.'s average value of 2.6 for PBGA. Four cases of TV46 component with β values of 0.5, 0.8, and 0.9 are excluded because the failure mechanism is not wearout as β is smaller than one.

Figure 4.11 shows the effects of mixed technology and component type on characteristic life, $\eta+\gamma$ for 3-P Weibull, of the solder joints. Corresponding Weibull plots are shown in Appendix F. Characteristic life, η for 2-P Weibull, is used for μ BGA46 packages as 4 out of 5 cases have the β values less than one. First, the results indicate that fleXBGA144 and TABGA96 packages have worse durability than PBGA352 and μ BGA46 packages for this thermal cycling condition. Second, for all four kinds of components, pure Pb-free solder joints have marginally better durability than pure SnPb solder joints. The improvement depends on the component type. For example, the characteristic life of pure Pb-free solder joints in fleXBGA144 component is 1.51 times longer than that of pure SnPb solder joints while the characteristic life of pure Pb-free solder joints in PBGA352 component is almost same as that of pure SnPb solder joints. This is due to the combined effects of different accumulated damage levels for different components and different damage mechanisms for Pb-free solders and SnPb solders.

Finally, the performance of mixed technology is complicated and contradictory. SnPb-paste mixed systems are expected to have lower reliability due to poor self alignment,

lack of ball collapse and grain growth associated with peak soldering temperatures that are lower than lead free solder ball melting point. Our results for PBGA352 and fleXBGA144 components, however, appear to show that the SnPb-paste mixed system has better reliability than pure Pb-free solder joints. One possible reason is that the solder joint behaves similarly to Column Grid Array (CGA) components, where the longer shape of the solder joint improves fatigue life of the interconnects.

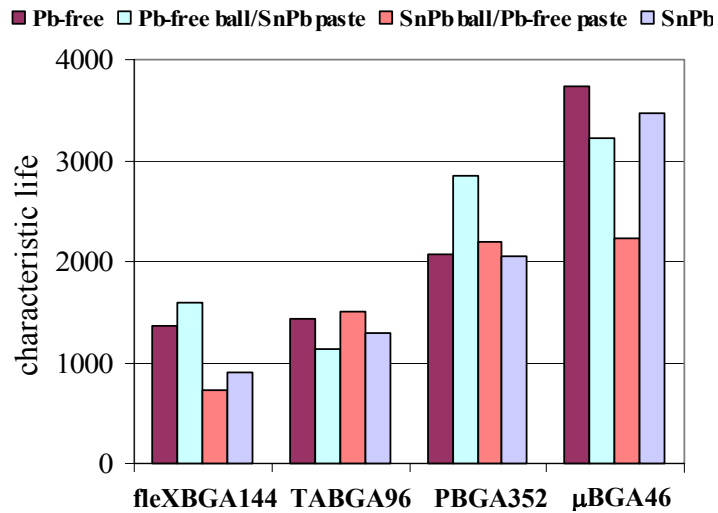


Figure 4.11: Effects of mixed technology and component type on characteristic life of the solder joints

Data for the PBGA352 components show that the reliability of SAC, SnPb, and SAC-paste mixed systems are comparable. SnPb-paste mixed system shows the best reliability of the four systems.

All Weibull graphs for fleXPBGA144 components seem to indicate two distinct populations, as shown in Figure 4.12 for the results of pure SnPb solder joints. It is found that the net design of two separate inner and outer loops of solder joints causes two

populations of the failures. So the final Weibull results for fleXBGA144 components are estimated only for failure data from outer loops. Weibull data for the fleXBGA144 components show that SAC and SnPb-paste mixed systems have better reliability than SnPb and SAC-paste mixed systems. Similarly, an unexpected result is that SnPb-paste mixed system yielded the best results. SAC-paste mixed system yielded inferior reliability results.

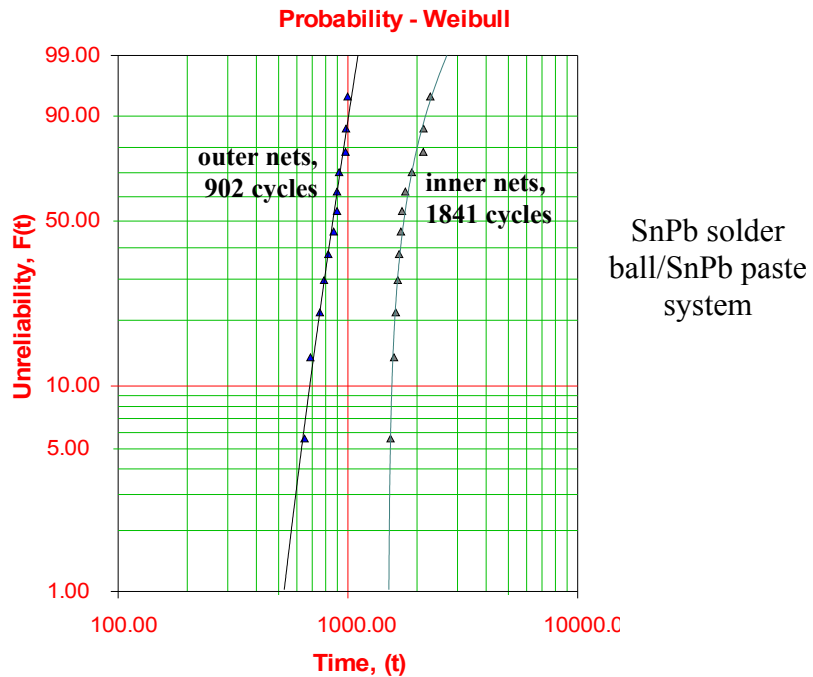


Figure 4.12: Weibull plot of fleXBGA144 components

Data for the TABGA96 components show that the reliability of SAC, SnPb and SAC-paste mixed systems were comparable. As expected, SnPb-paste mixed system yielded inferior reliability results.

Data for the μ BGA46 show that pure SAC system has the best reliability among SnPb, SAC, and mixed systems; although results for pure SAC system are based on failures of

less than 50% available nets. SAC-paste mixed system yielded the worst results of the four systems. In addition, the scale parameter β for SnPb and mixed systems is very small, which means large variance in test data.

The final data set that requires discussion is the SAC assembly for which all components were underfilled. It has been reported by many researchers that dramatic improvements in reliability can be achieved by underfilling PBGA and CSP components [e.g. Kirchner, et. al., 2002]. As expected, underfilling SAC solder joints almost doubles the reliability of fleXBGA144 components. But reliability of underfilled μ BGA46 components was degraded due to component design, which includes a flexible die-to-interposer bond.

4.3 Failure Analysis

Failure analysis is conducted as a part of this dissertation on tested boards and components. The main objectives are: to verify the failure modes, failure sites, and failure mechanisms of Circuit Card Assemblies; to find the effects of solder compositions and mixed technology on solder joint failures; and to identify the possible reason of premature failures in thermal cycling tests.

4.3.1 Pure SnAgCu System

Figure 4.13 shows optical micrographs of four kinds of components after micro sectioning. Solder joints in fleXBGA144, TABGA96, and PBGA352 components failed due to typical thermal cycling fatigue. The fatigue crack initiates at the corner of the solder joint, mostly at the interface between the intermetallic layer and bulk solder. Then

the crack propagates into the bulk solder area very close to the intermetallic layer until it reaches the opposite corner. It is also noted that the solder joint appears to undergo a very complicated loading during thermal cycling. As shown in Figure 4.13(a), as the shear force is expected on the solder joint due to CTE mismatch between the component and board, a curved solder pad implies a large normal force applied on the top of the solder joint during thermal cycling. No large crack was found in most of the solder joints in μ BGA46 components. Cracks were found in a μ BGA46 component with extremely early failure, as shown in Figure 4.14. Unlike the other components, the cracks can be only found at the cross section shown in Figure 4.14. The cracks disappear as the cross sectioning moves to the middle plane of the joints. This leads to suspicion that the failure mechanism may not be solder fatigue for μ BGA46 components.

As discussed in Section 4.1.3, the larger thin platelet Ag_3Sn intermetallic phases exist in the Pb-free solder joints. It is not clear if the presence of these intermetallic phases affects the solder fatigue. Our results show that the Ag_3Sn intermetallic phases may facilitate the crack propagation process if they are located along the route of the crack propagation and are parallel to the crack propagation direction. As shown in Figure 4.15, the crack propagates along Ag_3Sn intermetallic phases. But it is also possible that the Ag_3Sn intermetallic phases can block the crack propagation if they are vertical to the crack propagation direction.

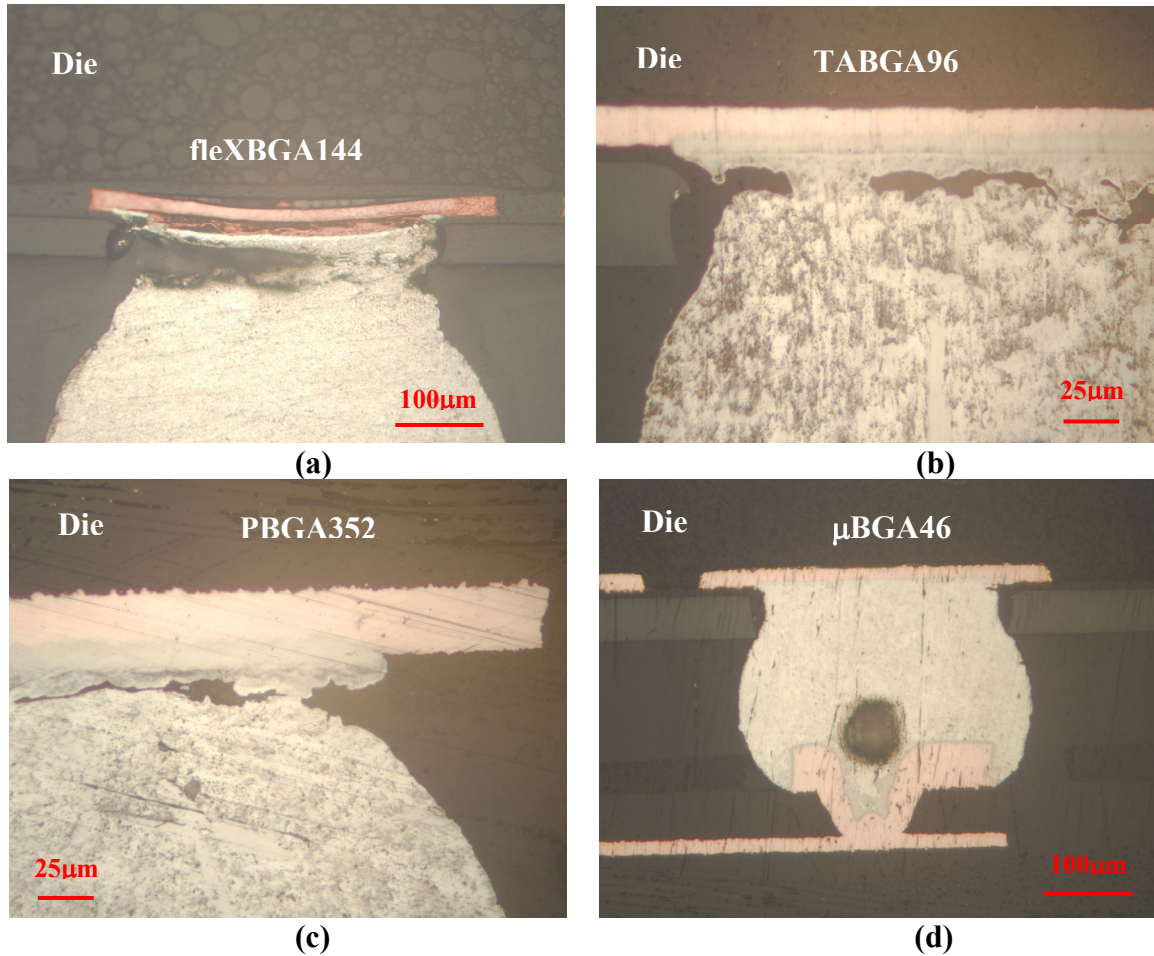


Figure 4.13: Optical micrographs of four kinds of components after micro sectioning.

The effect of voids on solder joint fatigue is another interesting topic. Figure 4.16 shows a crack propagating through a large void. Instead of propagating along a route parallel to the intermetallic layer (imaginary path shown in Figure 4.16), the cracks initiate at two corners and propagate downwards to the void. The presence of the void decreases the area and increases the stress in the solder joint. It accelerates the crack propagation and failure in this case.

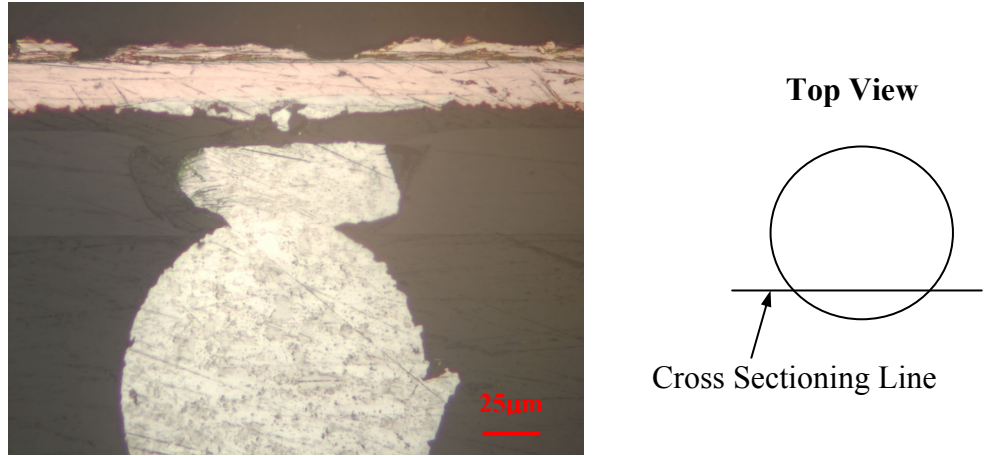


Figure 4.14: Optical micrographs of μ BGA46 with extremely early failure

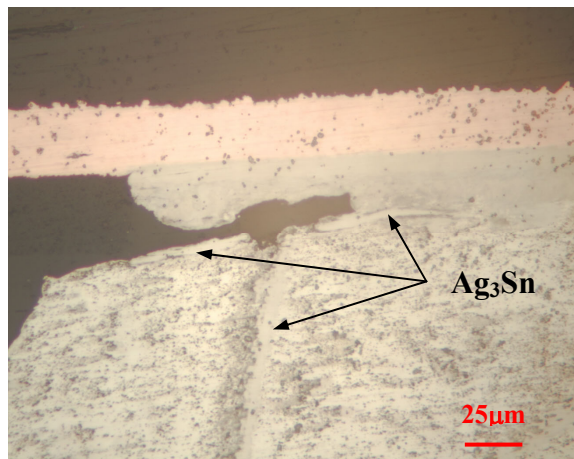


Figure 4.15: Optical micrographs of PBGA352 solder joint

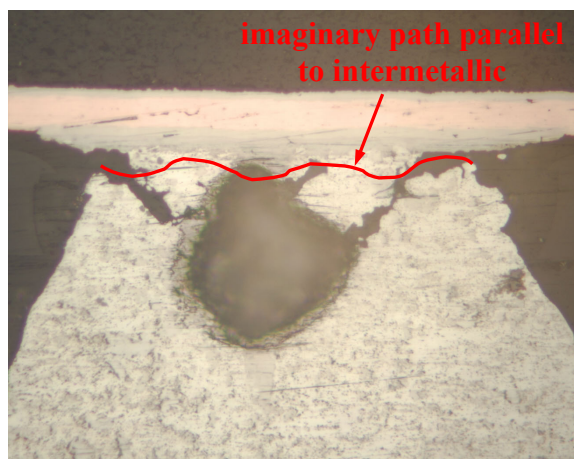


Figure 4.16: Optical micrographs of TABGA96 solder joint with voids

4.3.2 Pure SnPb System

Failed solder joints in fleXBGA144, TABGA96, and PBGA352 components show typical solder fatigue cracks, as seen in Figure 4.17. No crack was found in SnPb solder joints of μ BGA46 components. It is also found out that the cracks are closer to the intermetallic layer than those in Pb-free solder joints. Some studies have shown that a soft Pb-rich layer is formed near to the intermetallic layer as the tin continuously reacts with the copper to grow the intermetallic layer and finally is used up during thermal cycling process. This soft layer normally becomes the crack propagation path.

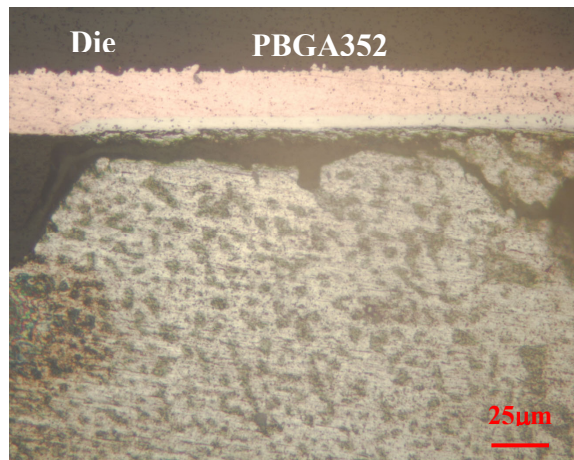


Figure 4.17: Optical micrographs of PBGA352 solder join

4.3.3 Mixed Technology

SnPb solder balls assembled with SAC paste show similar behavior to pure SnPb system, as shown in Figure 4.18. Solder fatigue cracks are located at areas close to the intermetallic layer of the die side. These cracks were found in fleXBGA144, TABGA96, and PBGA352 components, but not in μ BGA46 components.

Pb-free solder balls assembled with SnPb paste show slightly different behavior from pure Pb-free solder system. Fatigue cracks are not only found at the die side but also at the PWB side, as shown in Figure 4.19. As discussed in Section 4.2, SnPb paste mixed system has intrinsic disadvantages in terms of fatigue resistance. This mixed technology should be avoided in package assemblies because of the low fatigue resistance and the risk of increased voiding.

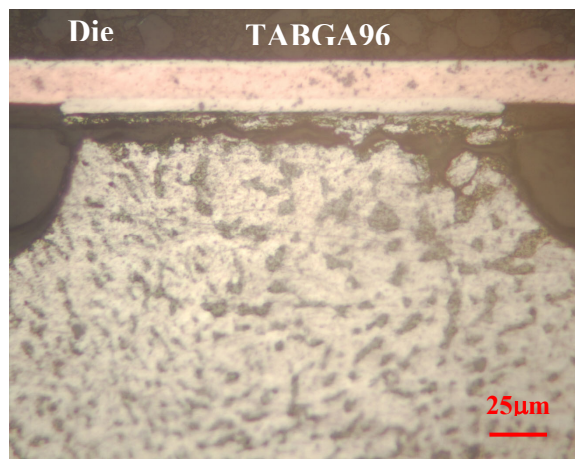


Figure 4.18: Optical micrographs of TABGA96 solder joint

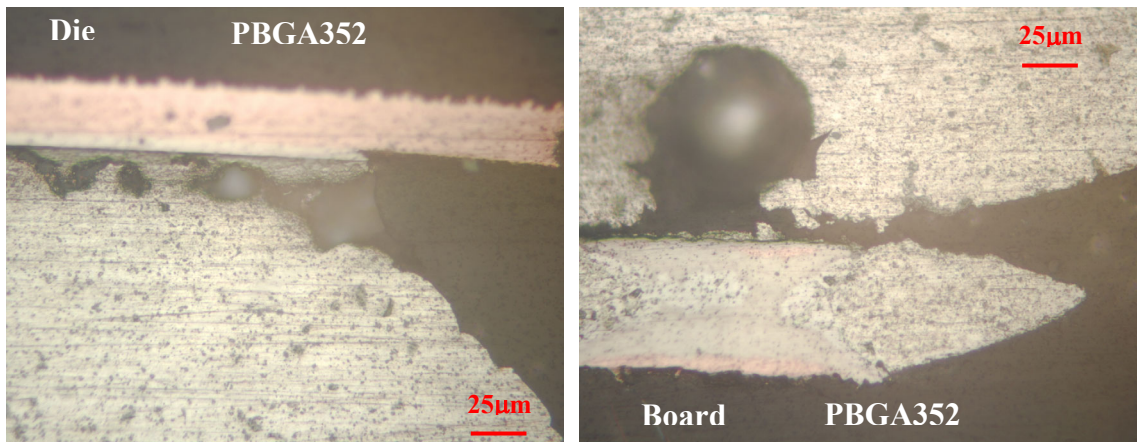


Figure 4.19: Optical micrographs of PBGA352 solder joints

4.4 Stress and Damage Modeling

One of the main objectives of this thesis is to develop a generic thermo-mechanical durability model for Pb-free solders. This is especially important for Pb-free solders because such a durability model is not currently available. Once the model is developed and correlated, it can be used to optimize the design of an assembly or component, and to predict field durability based on accelerated test results. It also reduces experimental costs and product development cycle time as fast and less expensive analytical approaches can be used and far fewer experiments need to be conducted during product design and development.

Figure 4.20 shows the whole approach employed in this study. In order to model the complex viscoplastic behavior of solder materials under thermal cycle loading, constitutive properties are needed as inputs in stress and damage analysis (box 1). Then a general purpose commercial FEA code (ANSYS 7.1 in this study) is used to build up different package geometries and to simulate the thermal cycling tests under investigation (box 2). As shown in box 3, the FE simulations provide stress-strain time history, thus identifying the critical solder ball and potential failure site based on maximum accumulated damage. Major outputs of this step are partitioned plastic and creep work densities which are needed to estimate damage based on models such as the E-P durability model of solders. In this study, this scheme is used in an inverse manner to estimate the model constants for the E-P model, for Pb-free solders. Combining partitioned work densities and cycles-to-failure data from thermal cycling tests, the E-P durability model for solders can be obtained (box 4). Similarly, model constants for other

thermo-mechanical durability models, e.g. Coffin-Manson model, can be obtained as well. Once the model constants are known, the cycles-to-failure of other SMT assemblies can be evaluated for any use/test environment by using the E-P damage superposition equation shown in box 5.

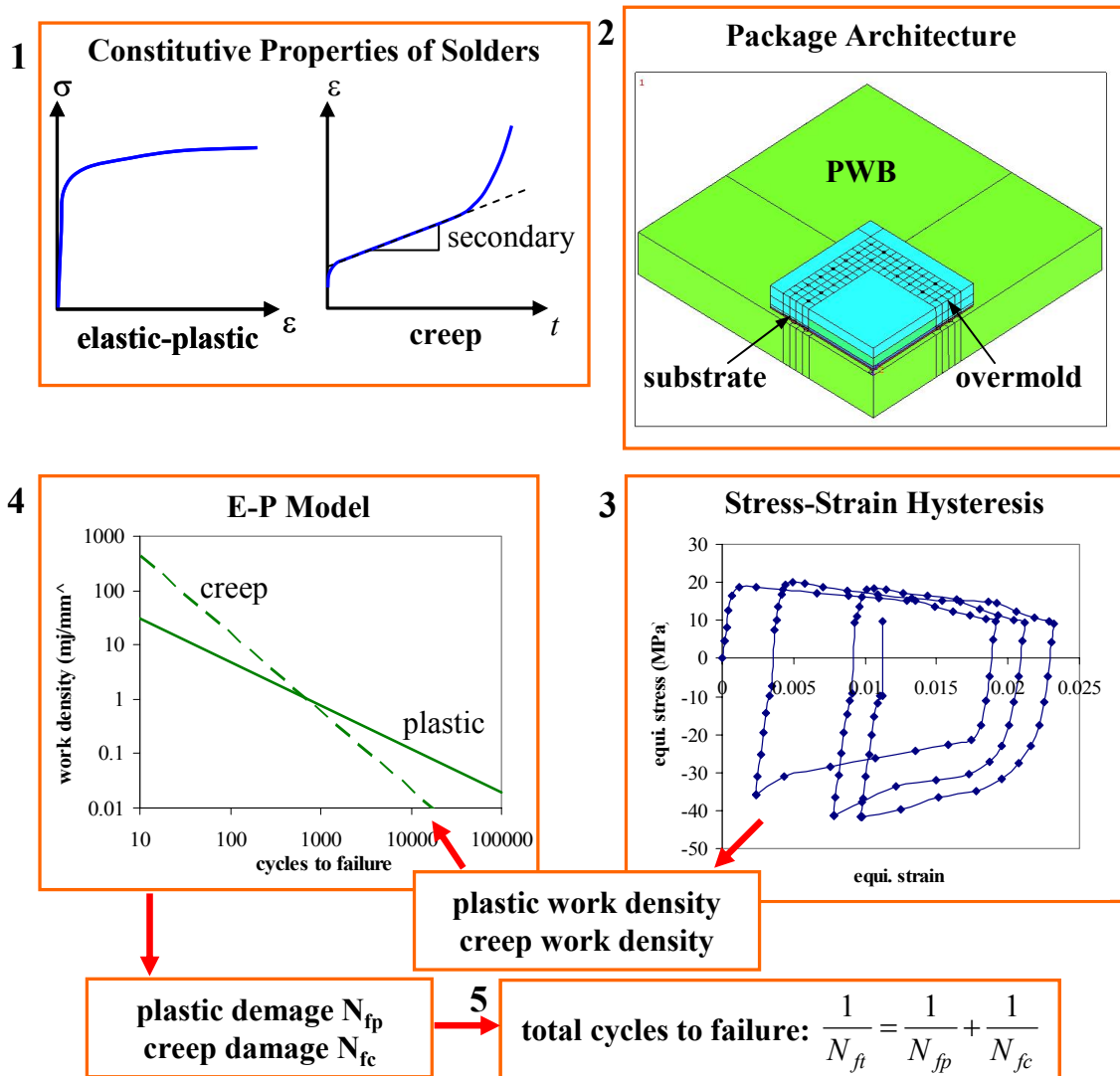


Figure 4.20: Overall approach for thermomechanical durability analysis

Implementation of the above approach to SMT assemblies of Pb-free solders is now presented in this section. First, three-dimensional finite element modeling and stress analysis of five thermal cycling tests for both SnPb and SnAgCu solders are presented

and then thermo-mechanical viscoplastic behavior of Pb-free solder joints is compared with that of eutectic Sn37Pb solder joints. Second, based on damage analysis and thermal cycling test results, the thermo-mechanical durability models (E-P model and Coffin-Manson models) for Pb-free solders, i.e. Sn3.8Ag0.7Cu in this chapter, are presented. At the end, the obtained durability models are employed to evaluate the acceleration factor (AF) for accelerated thermal cycling tests of Pb-free solders for field use applications.

4.4.1 Finite Element Modeling and Stress Analysis

In order to obtain the E-P damage model, thermal cycling test data from at least four different combinations of component types and thermal profiles are needed (due to four independent E-P model constants). Thermal cycling test data of μ BGA46 package were found in Section 4.2 to have very low confidence values, due to the inconclusive failure analysis. Thus test data of μ BGA46 were excluded from current stress and damage modeling. So additional thermal cycling test results are needed for the durability modeling. Another previous NCMS work, reported in the literature, is selected and their test data are included into this study [Syed, 2001]. Similar fleXBGA144 packages with different die size from ours were employed in their tests and the corresponding FE models are developed with minimal modifications. More importantly, test data under three different thermal profiles are available so that the effect of the thermal profile can be addressed in the obtained durability models. All five combinations of component type and thermal profiles are summarized in Table 4.9 and in Figure 4.21. It is seen that there are three component types, fleXBGA1, TABGA, fleXBGA2, subjected to four different

thermal cycle loading with temperature range varying from 100°C to 180°C (mean temperature from 35°C to 50°C), ramp rate from 6°C/min. to 90°C/min., and also dwell time from 5min. to 15 min..

Profile	Package	Temperature Range	Ramp Rate (°C/min.)	Dwell Time Hot/Cold (min.)	Cycles/Hour
Our TC	fleXBGA1	-55 to 125°C	6 (heating) /10 (cooling)	15/10	0.8
Our TC	TABGA	-55 to 125°C	6 (heating) /10 (cooling)	15/10	0.8
TC1	fleXBGA2	0 to 100°C	10	10/5	2
TC2	fleXBGA2	-40 to 125°C	11	15/15	1
TC3	fleXBGA2	-55 to 125°C	90	13/13	2

Table 4.9: Summary of temperature profiles

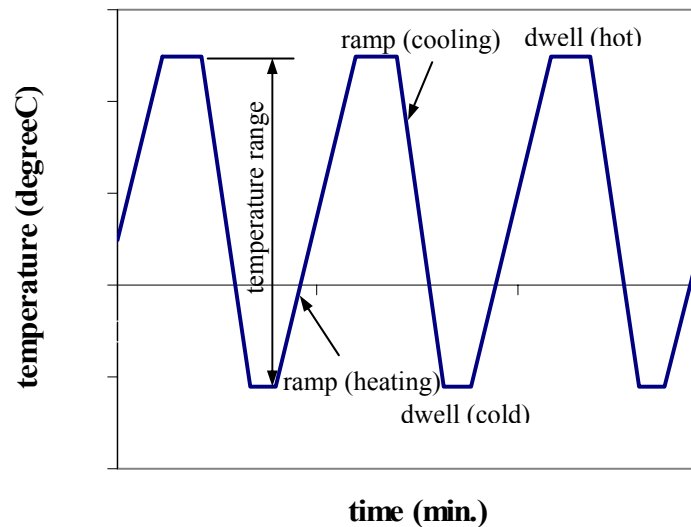


Figure 4.21: Schematic of thermal profile

The packages modeled include a 144-joint fleXBGA package and a 96-joint TABGA package on FR-4 board. The dimensions of packages and FR-4 PWB thickness are presented in Table 4.1 and Table 4.2. There are two models for fleXBGA144 packages

with different die size. One has the die size shown in Table 4.1 and the other one has a die size of 6.4mm x 6.4mm x 0.27mm. Other dimensions are the same for two fleXBGA144 packages. They are labeled as fleXBGA1 and fleXBGA2, respectively. The FR4 PWB length is much larger than the component and only a relevant part of the substrate is modeled in the analysis. The distance between the centers of two adjacent components is used as the length of the PWB in the FE models. Dimension of solder joints is obtained by averaging measurement of many solder joints after cross sectioning. These dimensions were reported in Table 4.5.

Nonlinear viscoplastic finite element analysis is conducted with ANSYS 7.1. Three-dimensional quarter models are built up for fleXBGA144 and TABGA96 packages in the FE analysis due to the symmetry in geometry. The FE models of fleXBGA144 and TABGA96 package are shown in Figure 4.22 and Figure 4.23, respectively. Solid element 185 is used in all FE models. The displacement boundary conditions are: 1) all nodes on the symmetric surfaces ($x=0$ and $z=0$) are fixed in the corresponding directions (x or z), and 2) the node at the origin ($x=y=z=0$) cannot move in any directions, as shown in Figure 4.24.

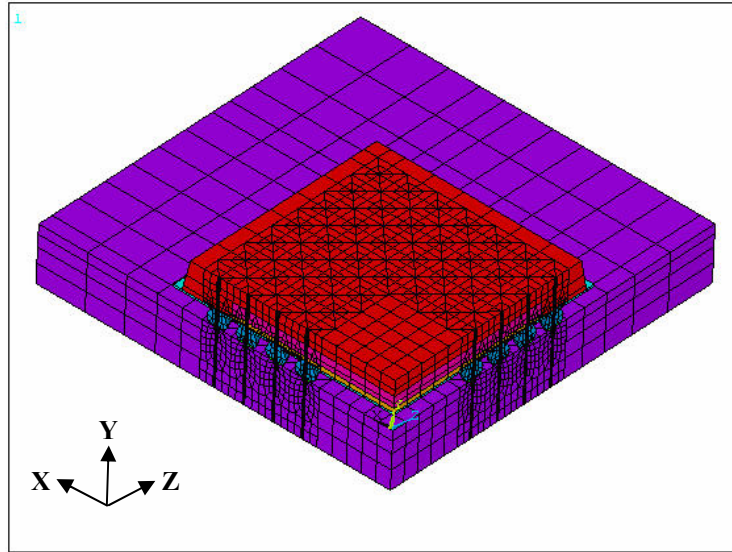


Figure 4.22: Finite element model of fleXBGA144 package

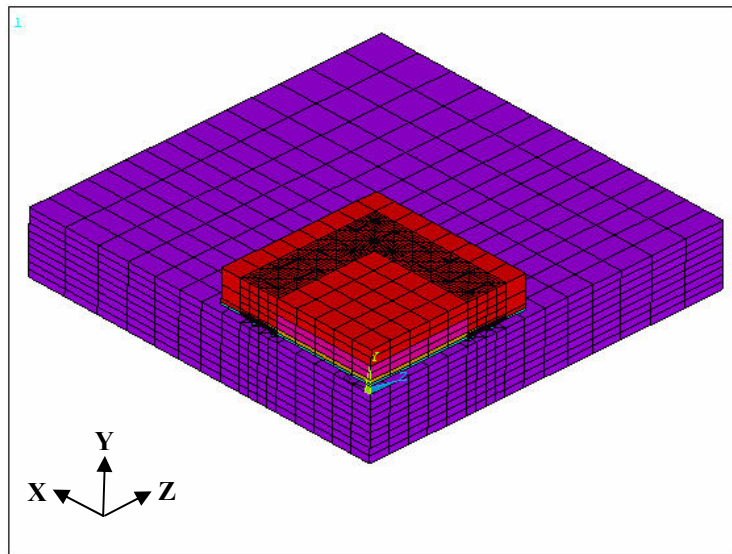


Figure 4.23: Finite element model of TABGA96 package

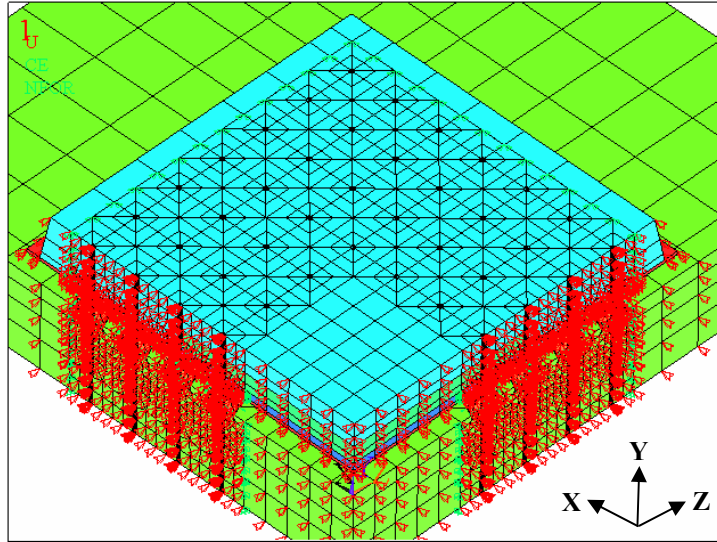


Figure 4.24: Finite element model showing boundary conditions

Mesh density sensitivity is studied on the FE model before final analysis is performed. The equivalent creep strain range per cycle is used to evaluate the mesh density sensitivity. The equivalent creep strain range per cycle is the average value of several elements, which enclose ten percent volume of the critical solder joint in the critical region. As shown in Figure 4.25, average equivalent creep strain range per cycle becomes stable as the number of elements increases from 40 to 112. Thus the corresponding mesh density for 112 elements is used for the critical solder joints for all FE models. A detailed finite element meshing of the solder ball array is shown in Figure 4.26. Fine meshing is employed for critical solder joints which normally are located at outer corner or in the die shadow. The rest of solder joints are meshed with far fewer elements in order to reduce the computation time. The total number of elements ranges from 20,000 to 30,000. Parametric modeling is used in the analysis and ANSYS input programs written by APDL (ANSYS Parametric Design Language) are listed in Appendix E.

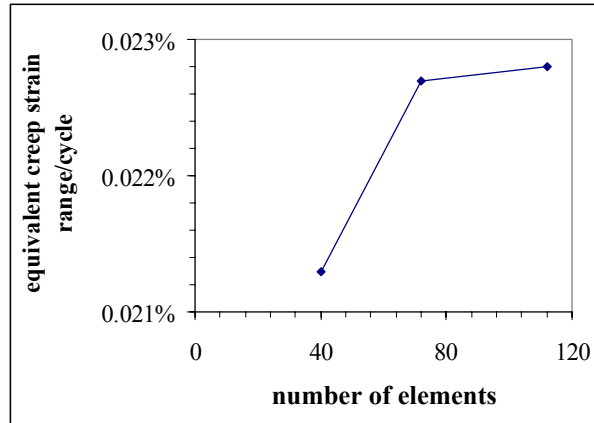


Figure 4.25: Variation of equivalent creep strain range per cycle with mesh density; creep strain is averaged in the local neighborhood of the critical region in the critical solder joint

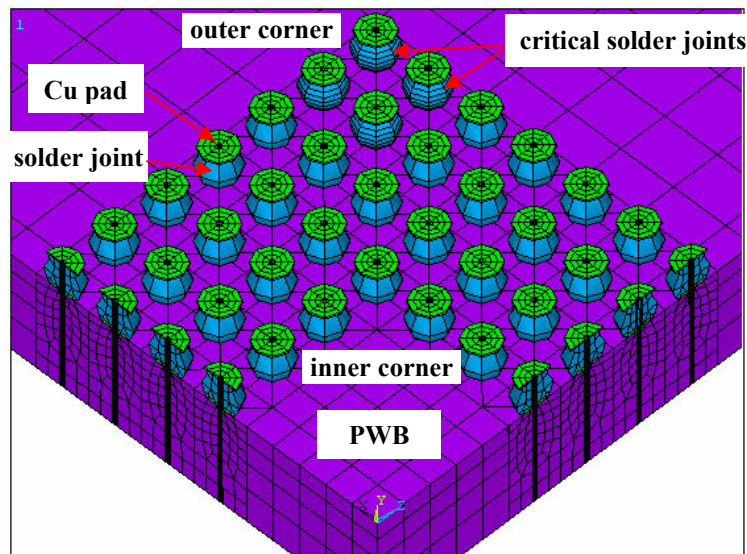


Figure 4.26: Finite element meshing of the solder ball array for fleXBGA144

Temperature profiles shown in Table 4.9 are applied to the assemblies as input loading. In each simulation, three complete thermal cycles are simulated as the hysteresis stabilizes in the third cycle, as shown in Figure 4.27. Automatic time stepping is used in the simulation, which results in total number of substeps ranging from 1,100 to 3,200.

The run time of the simulation varies from 16 to 48 hours. An example of APDL input file for one thermal profile is listed in Appendix E.

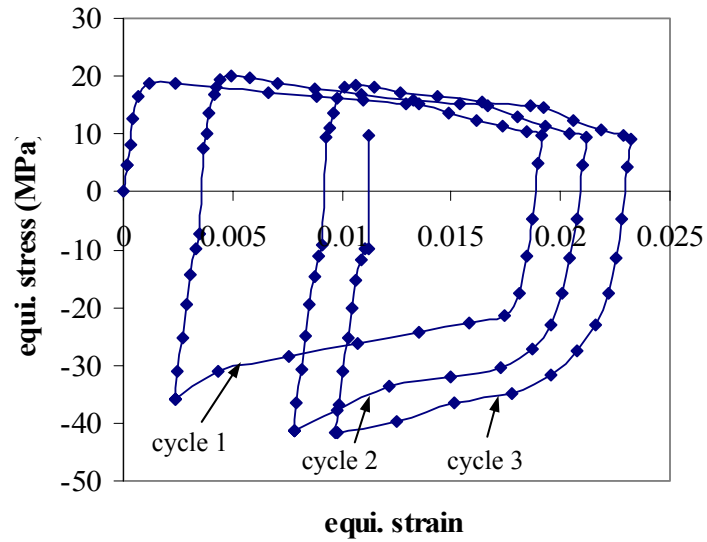


Figure 4.27: Equivalent stress-strain hysteresis loops for fleXBGA1 package subjected to our thermal cycling

All materials, except solder, are assumed to behave in a linear elastic manner. Their mechanical properties are shown in Table 4.10. All material properties except CTE values of PWB and overmold are obtained from Amkor Technology, Law, and Amagai, respectively [Amkor, 2003, Law and Pao, 1997, Amagai, 1999]. CTE of PWB is measured by TMA. CTE of overmold is obtained by matching FEA simulation of component TMA test to actual TMA test results.

Materials		Young's Modulus (MPa)	CTE (ppm/°C)	Poisson's Ratio
Copper		1.42E5-44.2T(K)	15.6-0.0041T(K)	0.35
PWB	In-plane	2.44E4-22.6T(K)	17.8/14.5	0.11
	Out-of-plane	1.06E4-9.6T(K)	64.1	0.39
Silicon		1.95E5-12.7T(K)	0.0095T(K)-0.5	0.28
Polyimide		5.65E3-6.2T(K)	13.8	0.3
Die Attach		1.20E3	110	0.42
Overmold		2.36E4-26.2T(K)	9	0.3
Solder	SAC	4.37E4-22.3T(K)	20.9	0.4
	SP	2.92E4-44.2T(K)	23.9	0.4

Table 4.10: Temperature-dependent elastic and plastic properties of the solder

The deformation of solder is much more complex and it deforms elastically, plastically, and viscoplastically under thermal cycling condition. A partitioned constitutive law is employed in the FE analysis, as shown below:

$$\varepsilon = \varepsilon_{el} + \varepsilon_{pl} + \varepsilon_{scr} \quad (4.2)$$

where ε is total strain; ε_{el} is elastic strain; ε_{pl} is rate-independent plastic strain; and ε_{scr} is rate-dependent secondary creep strain.

The partitioned temperature-dependent elastic, plastic and steady-state creep properties are used in order to be compatible with the E-P damage model for the Pb-free solder. The individual elastic, plastic and creep model constants have been presented in Chapter 2 in terms of shear strain and shear stress. In order to use these material properties in 3-D FE analysis, the following standard von Mises relations are employed to derive the model constants in terms of the effective strains and stresses:

$$\sigma = \sqrt{3}\tau \quad (4.3a)$$

$$\varepsilon = \frac{1}{\sqrt{3}}\gamma \quad (4.3b)$$

where σ and ε are effective stress and strain, respectively and τ and γ are shear stress and strain, respectively. Based on Equations (4.2a) and (4.2b), model constants for Sn3.9Ag0.6Cu and Sn37Pb solders are obtained. Elastic modulus E , CTE and Poisson's ratio ν are listed in Table 4.10. The rate-independent plastic strain is formulated as:

$$\varepsilon_{pl} = C_{pl}\sigma^n \quad (4.4)$$

where C_{pl} and n are temperature-dependent constants, which are summarized in Table 4.11. The steady-state creep strain rate is described by:

$$\frac{d\varepsilon_{scr}}{dt} = A'[\sinh(\alpha\sigma)]^n \exp\left(-\frac{Q}{RT}\right) \quad (4.5)$$

where α is related to the stress level at which the power law dependence breaks down; Q is the activation energy; A' and n are model constants. Primary creep is ignored in this study. All constants for two solders are summarized in Table 4.12. As the Sn3.8Ag0.7Cu solder, which is used to assemble the CCAs tested in thermal cycling, has very similar composition to the Sn3.9Ag0.6Cu solder, the material properties presented here for Sn3.9Ag0.6Cu are employed in the FE analysis of Sn3.8Ag0.7Cu solder.

Solder Alloy	C_{pl} (MPa)	n
Sn37Pb	152.5-0.6*T(°C)	0.25-0.00028*T(°C)
Sn3.9Ag0.6Cu	121.6-0.4*T(°C)	0.29-0.00046*T(°C)

Table 4.11: Plastic model constants for Sn37Pb and Sn3.9Ag0.6Cu solders

Solder Alloy	A'	α	n	Q (J/Mol)
Sn37Pb	1.15E4	0.20	2.2	5.93E4
Sn3.9Ag0.6Cu	1.50E3	0.19	4.0	7.13E4

Table 4.12: Steady-state creep model constants for Sn37Pb and Sn3.9Ag0.6Cu solders

4.4.2 FE Analysis Results and Discussion

FE analysis results of all five thermal cycling tests shown in Table 4.9 are now presented. In order to obtain damage models of Pb-free solders, damage criteria (e.g. ISR, total work, or partitioned plastic and creep work) have to be assessed for all tests. It is assumed that the accumulated damage at the potential failure site of critical solder joint is directly related to cycles-to-failure. So the potential failure site for each test case has to be identified. The contour plots at different time are checked for the critical solder balls in order to identify the potential failure site, which has the average accumulated maximum energy density. The averaging approach is discussed later in this section. The location of the potential failure site depends on the component type and the die size.

For the fleXBGA1 package, the critical solder joint is located in the shadow of the outer corner of the silicon die, as shown in Figure 4.28. The potential failure site is right below the top layer and located at inner side of the solder. As the die size decreases (from fleXBGA1 to fleXBGA2), the critical solder joint moves inward from the outmost (the fourth) row to the second row (counted from inside to outside of solder ball array). As shown in Figure 4.29, the critical solder joint is near the inner corner of the solder ball array. The potential failure site changes to the outer side of the top layer of the critical

solder joint. The potential failure site and critical solder joint are same for Sn37Pb and Sn3.8Ag0.7Cu solder. For TABGA packages, the solder joint at the outer corner of the substrate is stressed most severely for both SnPb and SnAgCu solders, as shown in Figure 4.30. The potential failure site is also at inner side of the critical solder and in the layer below the top layer.

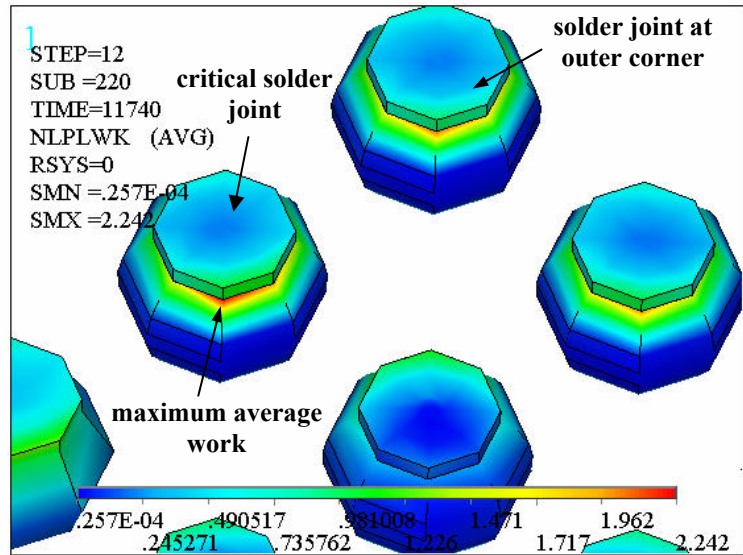


Figure 4.28: Total work density contour of fleXBGA1 package at -125°C before dwell: Sn3.8Ag0.7Cu solder

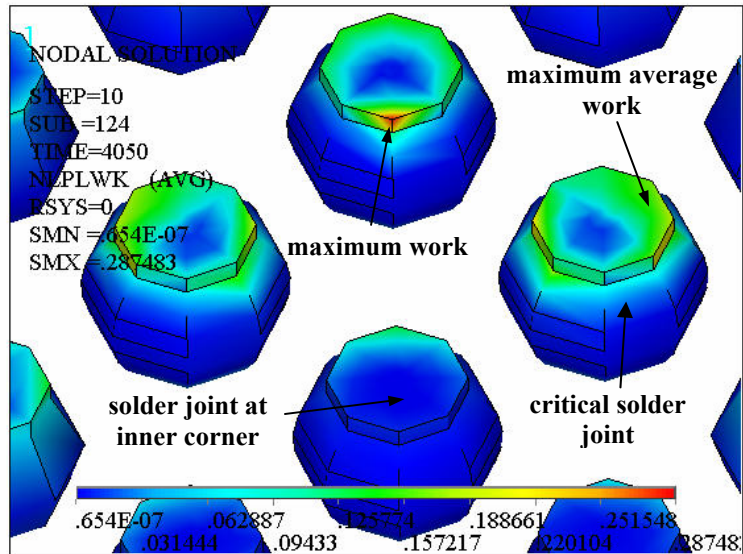


Figure 4.29: Total work density contours of fleXBGA2 package at 100°C before dwell: Sn3.8Ag0.7Cu solder

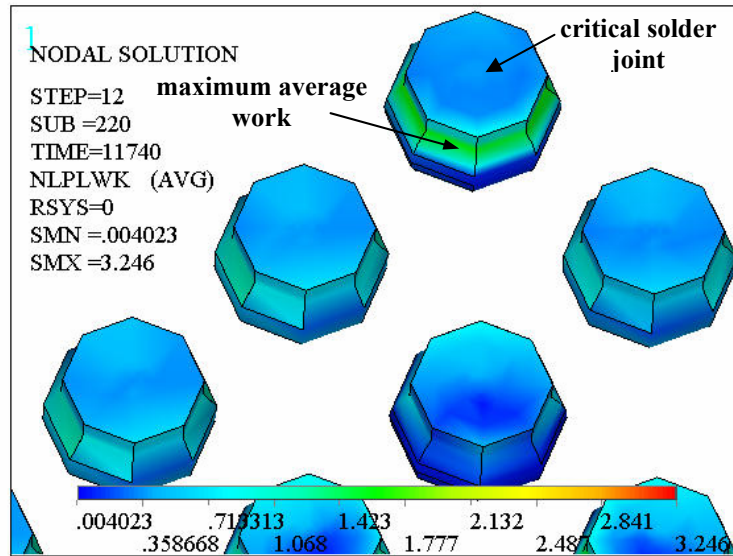


Figure 4.30: Total work density contours of TABGA package at -125°C before dwell: Sn3.8Ag0.7Cu solder

The failure analysis of failed specimens also verifies FE analysis results. Figure 4.31 shows a comparison between thermal cycle tests and FE simulation. The contour at the right shows the distribution of the total work density at same cross section of the solder joint as that in the picture on the left. There is good agreement between tests and simulation. The crack initiated at the site with maximum average work density predicted by FE analysis. It also propagated in the band of high work density. For TABGA96 packages, the comparison between thermal cycle tests and FE simulation, as shown in Figure 4.32, shows disagreement. It is noted that the crack initiation site has the relatively high energy density but maximum energy density occurs at areas close to the microvia of the board side. The possible reasons for this discrepancy are explained as follows. The areas with maximum work density are located at the interface between the solder and the copper via, which is inside the solder-via assembly. It needs a very large

energy to initiate a crack inside the solder joint. On the contrary, the areas close to the die side have large energy density and are on the solder surface. It is much easier to overcome the surface energy and initiate a surface crack.

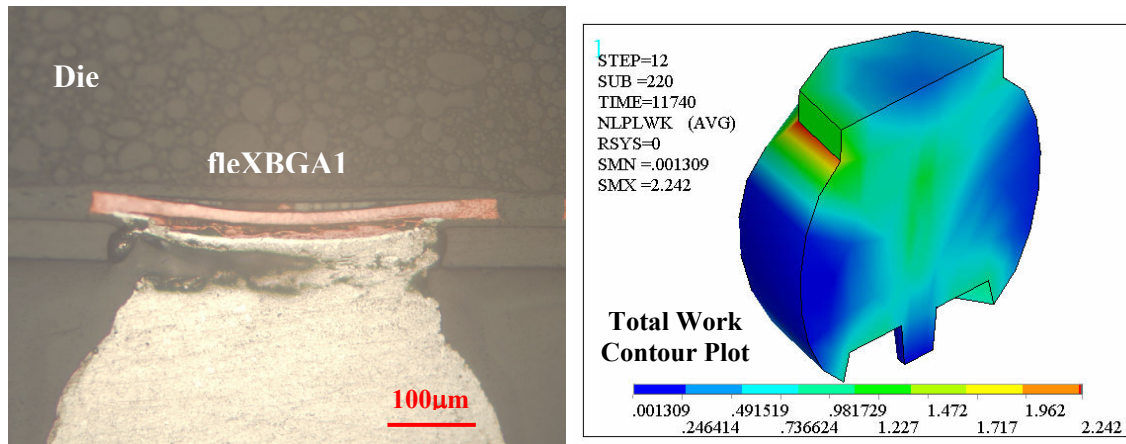


Figure 4.31: Comparison between thermal cycle tests and FE simulation of fleXBGA1: Sn3.8Ag0.7Cu solder

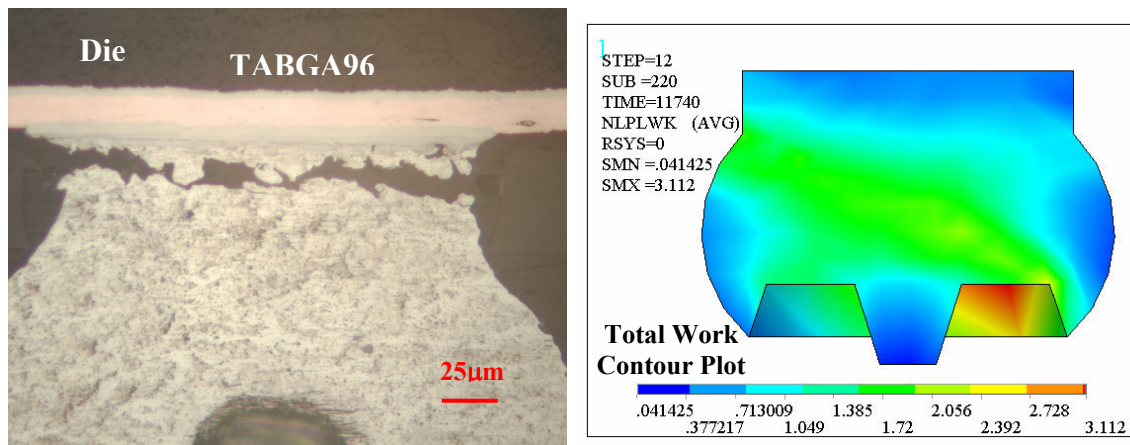


Figure 4.32: Comparison between thermal cycle tests and FE simulation of TABGA96: Sn3.8Ag0.7Cu solder

In order to minimize the effect of stress concentration, the stress, strain, and energy values at the potential failure site should be assessed by employing approximate averaging technologies. Actually, the averaging method is important because it directly determines the correlation equation (i.e. damage models) between the simulation results

and test data. In this study, we use a half layer of solder elements to calculate stress, strain and energy variables. Figure 4.33 shows an example of the half layer for fleXBGA1 package. Two reasons lead us to select this averaging technology. First, based on failure analysis, the fatigue cracks always initiate from one corner of the solder joint not from two corners or from the whole periphery. Second, in the whole layer with maximum energy density, the stress condition is normally asymmetric to the middle line, as shown in Figure 4.34 (the same layer as that in Figure 4.33). One side of the layer is in tension and the other side is in compression. So it is reasonable to use a half layer with same stress condition to average the variables. A post-processing APDL program has been written to implement this averaging technology, which can be found in Appendix E.

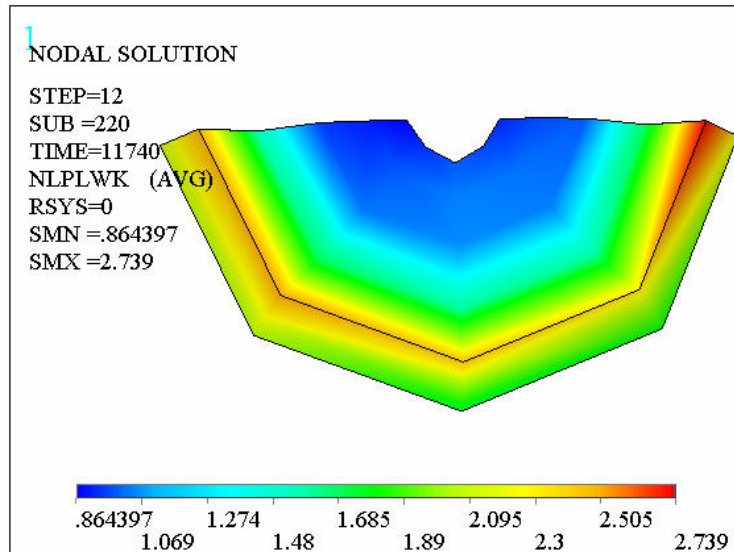


Figure 4.33: Half layer used to assess average stress, strain and energy: TABGA96, Sn3.8Ag0.7Cu, -125°C before dwell

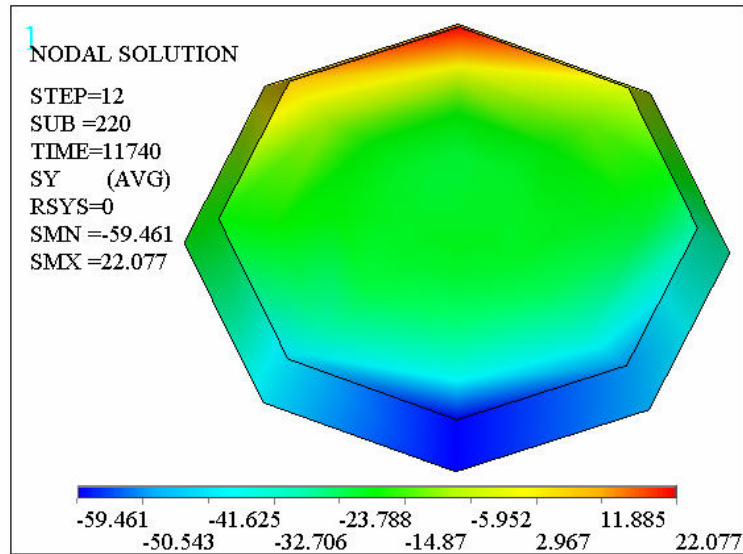


Figure 4.34: Normal stress contour plot of the whole layer of the critical solder joint: TABGA96, Sn3.8Ag0.7Cu, -125°C before dwell

The viscoplastic hysteretic response of Sn3.8Ag0.7Cu (SAC) and Sn37Pb (SP) to thermal cycling is compared for the third thermal cycle in Figure 4.35. The von-Mises stress is plotted against the equivalent strain. The temperature extremes and thermal profile segments are also shown in the figure. The sign of the von-Mises stress is arbitrarily assigned to be positive for increasing temperature and negative for decreasing temperature. The two hysteresis loops are different due to different plastic and creep properties of two solders. There is a larger increase in von-Mises stress for SAC than for SP when the temperature increases from 25°C to 125°C. During the same period, the increase in the equivalent strain of SP is larger than that of SAC. During the 125°C dwell period, SAC deforms less than SP due to the better creep resistance of Pb-free solders. The shape of the hysteresis loop is very different for two solders during the ramp down period from 125°C to -55°C because of the difference in creep resistance. SP experiences greater creep deformation and stress relaxation than SAC during the -55°C

dwell period. The difference in two loops results in different accumulated damage for Sn3.8Ag0.7Cu and Sn37Pb solders such as inelastic strain range (ISR) and total work density (ΔW). It is also noted that ramping up and down periods have larger effects on the strain range than dwell periods. This conclusion is dependent on the ramp rates used in this study.

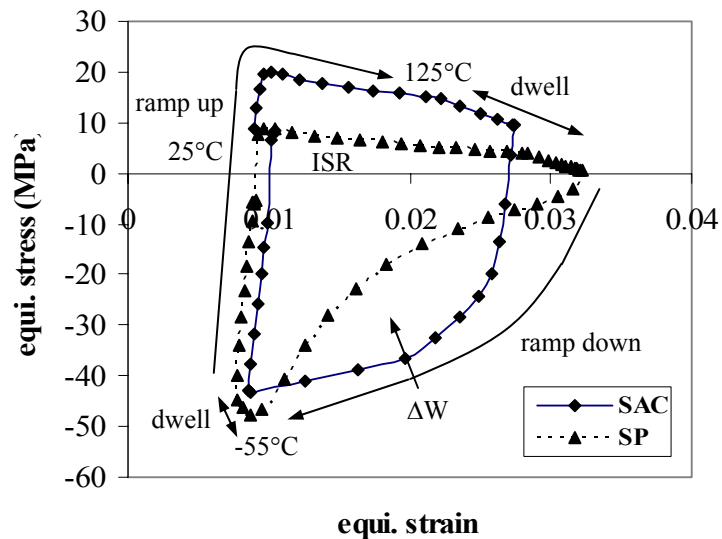


Figure 4.35: Hysteresis loops of Sn3.8Ag0.7Cu and Sn37Pb solders: TABGA96

Figure 4.36 compares the viscoplastic hysteresis of the Sn3.8Ag0.7Cu solder for the fleXBGA1 and TABGA96 package. Both packages are subjected to the same -55°C to 125°C thermal cycle loading (see details of our TC in Table 4.9). The von-Mises stress range is very similar for both packages but the inelastic strain range and total work density of TABGA96 are larger than those of fleXBGA1.

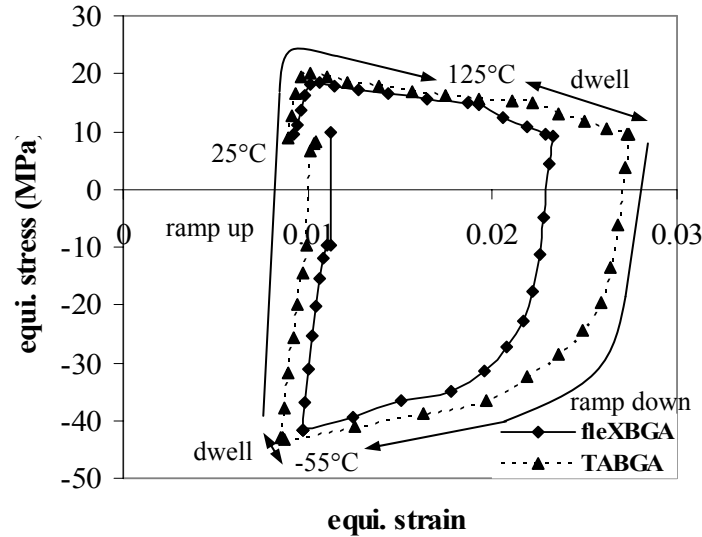


Figure 4.36: Comparison of hysteresis loops for fleXBGA1 and TABGA96 packages: Sn3.8Ag0.7Cu solder

The effect of different thermal profiles on the stress-strain hysteresis of Sn3.8Ag0.7Cu solder is shown in Figure 4.37 for fleXBGA2 package. TC1, TC2 and TC3 shown in Table 4.9 represent 0°C to 100°C, -40°C to 125°C, and -55°C to 125°C, respectively. It is obvious that there is a significant difference in the stress-strain range and the shape of the hysteresis loop. TC3 has the largest ISR and ΔW among three thermal profiles, followed by TC2 and then TC1. This trend agrees with the order of the measured characteristic life of these three cases (2809 cycles for TC3, 2967 cycles for TC2, and 9516 cycles for TC1, respectively). In addition, it is found that the maximum von-Mises stress for TC3 (22.9MPa) is much larger than those for TC2 (18.7MPa) and TC1 (13.2MPa), even that for fleXBGA1 (18.5MPa) shown in Figure 4.36. The reason is that TC3 has a very high ramp rate (90°C/min.). Since a short ramp period leads to insufficient stress relaxation, the solder balls have a large stress increase due to reduced creep deformation.

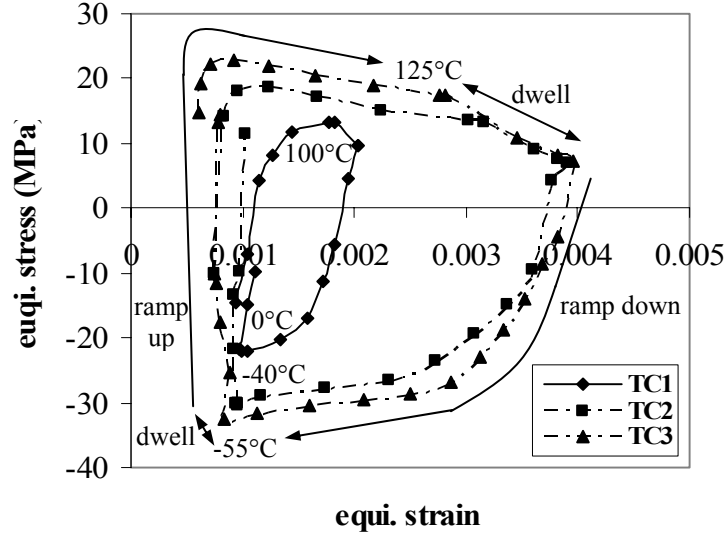


Figure 4.37: Effect of thermal profile on hysteresis loop of SAC for fleXBGA2

4.4.3 Thermo-Mechanical Durability Models

The electronic packaging community predicts thermo-mechanical durability of eutectic Sn37Pb solder joints using durability models similar to the ones discussed in Chapter 3. These models include the strain range type of Coffin-Manson model [Engelmaier, 1984, Enke, et al., 1989, Shine and Fox, 1987, Vaynman, 1990], the energy density type of Coffin-Manson model [Solomon 1989; Darveaux 1997; Popelar, 1997; Vaynman 1990], and Energy-Partitioning model [Dasgupta et al., 1992]. However, model constants for such thermo-mechanical durability models are almost non-existent for Pb-free solders. Schubert et al. presented the Coffin-Manson equations in terms of both equivalent creep strain (ε_{cr}^{acc}) and viscoplastic strain energy (ΔW_{cr}^{acc}) for Sn3.8Ag0.7Cu and Sn3.5Ag [Schubert, et al. 2002a], as shown below:

$$N_f = \Theta_1 (\varepsilon_{cr}^{acc})^{C_1} \quad \text{and} \quad N_f = \Theta_2 (\Delta W_{cr}^{acc})^{C_2} \quad (4.6)$$

where N_f is cycles-to-failure; Θ_1 , Θ_2 , C_1 , and C_2 are model constants. The exponents C_1 and C_2 in Equation 4.6 are -1.96 and -0.98, respectively. Their model constants were obtained by fitting to tests results of both SnPb and Pb-free solders as they assumed that the model parameters are the same for three solders: Sn37Pb, Sn3.5Ag, and Sn3.8Ag0.7Cu. But this assumption is not true because Pb-containing and Pb-free solders have different creep mechanisms as discussed in Chapter 2. In another study by Lee and Han [Lee and Han, 2003], Engelmaier Model constants were obtained for SnAgCu solders by fitting all published thermal cycling test data to Engelmaier Model, which is expressed as:

$$N_f = \frac{1}{2} \left(\frac{\Delta\gamma_p}{2\varepsilon_f} \right)^{\frac{1}{C}} \quad (4.7)$$

where $\Delta\gamma_p$ is inelastic strain range; ε_f is fatigue ductility coefficient; C is fatigue ductility exponent. They reported a C value of -0.62 for the SnAgCu solder from shear deformation dominated thermal cycling tests, which is steeper than -0.44 for the SnPb solder. The disadvantage of their approach is the inaccuracy of the $\Delta\gamma_p$ values, which were calculated by extremely simplified equations.

Thermo-mechanical durability models for the SnAgCu solder are presented now. The power law durability models in terms of both inelastic strain range and total work density are first presented, followed by the Energy-Partitioning (E-P) damage models for SnAgCu in next section. Then the difference of E-P damage models between mechanical cycling and thermal cycling is discussed. The applications of the obtained E-P durability model to field use conditions are presented in the end.

4.4.3.1 Power Law Durability Model

A power-law relationship between the chosen damage criteria and cycles-to-failure presented in Section 3.2.1 is used to characterize thermo-mechanical durability of Pb-free solders. Damage criteria used in this study are cyclic inelastic strain range (ISR) and total work density (ΔW) per cycle. The characteristic life, η , from 2-P Weibull analysis of thermal cycling data is used for cycles-to-failure because no 3-P Weibull data is available for three thermal cycling tests from the literature. ISR is evaluated from the von-Mises stress-equivalent strain hysteresis loop of the third cycle, as shown in Figure 4.35. ΔW is defined as the summation of the product between stress and inelastic strain increment vectors over the number of converged subsets in the third cycle.

Damage analysis results of Sn3.8Ag0.7Cu and Sn37Pb solders are presented Figure 4.38 and 4.39, respectively. Least-square fits of material constants C and n for two damage criteria (total cyclic work density, ΔW , and cyclic inelastic strain range, ISR) are presented in Table 4.13. Corresponding correlation coefficients are also shown in the same table.

From Figures 4.38 and 4.39 and Table 4.13, it is first noted that two damage criteria, ISR and ΔW , correlate well to thermo-mechanical durability of the Sn3.8Ag0.7Cu and Sn37Pb solder by power law relationship. It is also found that the correlation coefficients of work-based model are better than those of ISR-based model, suggesting that ΔW may be a more stable damage criterion for thermo-mechanical durability. As for the durability curve, ISR-based model has a steeper slope than ΔW -based model for both

Sn3.8Ag0.7Cu and Sn37Pb solders. This is the same as the results from mechanical cycling tests under high creep conditions. The power law model parameters obtained here can be employed to predict thermo-mechanical durability of Sn3.8Ag0.7Cu solder in thermal cycling conditions.

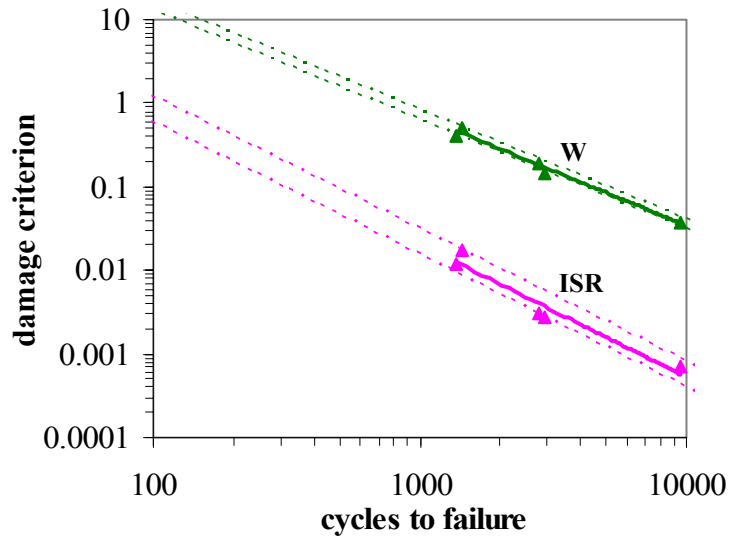


Figure 4.38: Power law durability model for Sn3.8Ag0.7Cu solder

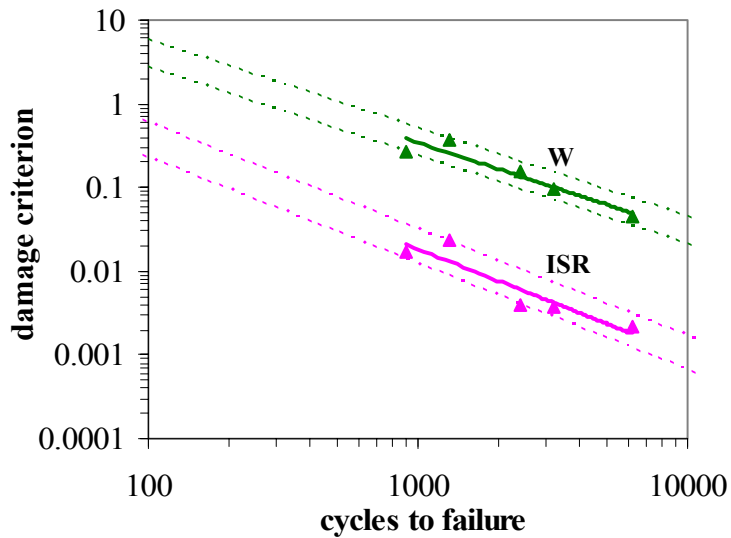


Figure 4.39: Power law durability model for Sn37Pb solder

Solder		n	C	R^2
SAC	ISR	-1.6	1.19E3	0.95
	W	-1.3	5.92E3	0.98
SP	ISR	-1.3	121	0.87
	W	-1.1	506	0.90

Table 4.13: Coffin-Manson type durability parameters for two solders

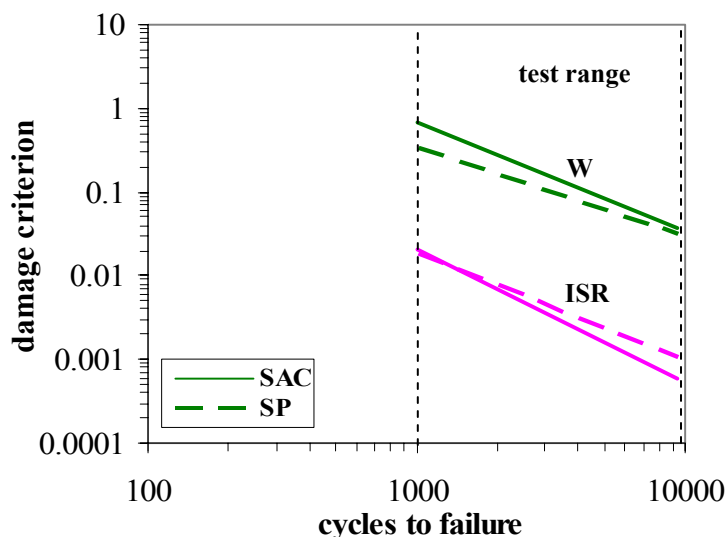


Figure 4.40: Comparison of Coffin-Manson type durability model between Sn3.8Ag0.7Cu solder and Sn37Pb solder

The comparison of the obtained thermo-mechanical durability model between two solders is shown in Figure 4.40. It is graphically seen that the Sn3.8Ag0.7Cu solder has better thermo-mechanical durability than the Sn37Pb solder if work-based model is used. However, the results are opposite when ISR-based model is employed in the test range. ISR-based results also show that a crossover point exists at around 1300 cycles ($\Delta\varepsilon \approx 0.015$). The results in terms of work-based model are consistent with the Weibull analysis results of thermal cycling test data discussed in Section 4.2, which show that the Pb-free solder outperforms the SnPb solder under the same thermal cycling condition. This is probably related to different stress-strain hysteresis loops for Sn3.8Ag0.7Cu and

Sn37Pb solders presented in Figure 4.35. In the figure, the SAC has larger stress range while the SP has much larger inelastic strain range under the same test condition. Thus the SAC has larger total work density (ΔW) but the SP has larger inelastic strain range (ISR) for the same condition.

4.4.3.2 Energy-Partitioning Durability Model

Partitioned plastic and creep deformation histories can be obtained from finite element analysis of thermal cycling tests. Consequently, plastic (W_p) and creep (W_c) work densities are partitioned from total work density. Based on thermal cycling life and partitioned plastic and creep work densities, the model constants are obtained for Energy-Partitioning (E-P) durability model as expressed in the following equations:

$$\text{Total energy} = W_p + W_c = W_{p0} N_{fp}^c + W_{c0} N_{fc}^d \quad (4.8a)$$

$$1/N_f = 1/N_{fp} + 1/N_{fc} \quad (4.9b)$$

where W_{p0} , W_{c0} represent the intercepts of the plastic and creep energy density plots vs. cycles-to-failure, respectively, on a log-log scale; while the exponents c and d are their corresponding slopes. The variables N_{fp} and N_{fc} represent the cycles-to-failure due to plastic and creep damage, respectively. The total number of cycles-to-failure N_f is then calculated from Equation 4.9b. Elastic terms in Equations (4.9a) and (4.9b) are ignored in this study because elastic energy has an insignificant effect on the thermo-mechanical durability of solders.

First, the comparison of the damage analysis in Table 4.14 shows that there is a significant difference in the ratio of plastic work density to creep work density between

the Pb-free solder and the SnPb solder. Accumulated plastic work density per cycle (ΔW_{pl}) is only a small part of creep work density per cycle (ΔW_{cr}) for the Sn37Pb solder while ΔW_{pl} for the Sn3.9Ag0.6Cu solder is comparable with the ΔW_{cr} . It suggests that plastic damage has an important effect on the thermo-mechanical durability of Pb-free solders, and hence, ΔW_{pl} should be included in the durability model of Pb-free solders. In addition, high ramp rate tests have higher ratio of ΔW_{pl} to ΔW_{cr} than low ramp rate tests as more plastic deformation is expected in these tests.

Profile	Package	Temperature Range	Ramp Rate (°C/min.)	$\Delta W_{pl}/\Delta W_{cr}/\text{Ratio}$	
				Sn37Pb	Sn3.8Ag0.7Cu
TC1	fleXBGA2	0 to 100°C	10	3.0E-4/0.045/0.01	0.016/0.021/0.75
TC2	fleXBGA2	-40 to 125°C	11	0.011/0.083/0.13	0.061/0.088/0.69
Our TC	fleXBGA1	-55 to 125°C	6 / 10	0.034/0.24/0.15	0.17/0.23/0.75
Our TC	TABGA	-55 to 125°C	6 / 10	0.038/0.34/0.11	0.21/0.31/0.67
TC3	fleXBGA2	-55 to 125°C	90	0.041/0.12/0.35	0.092/0.10/0.91

Table 4.14: Comparison of the ratio $\Delta W_{pl}/\Delta W_{cr}$ between Sn3.8Ag0.7Cu and Sn37Pb solders

Table 4.15 presents the obtained E-P model constants for both Sn3.8Ag0.7Cu and Sn37Pb solders. These model constants can be substituted into Equations 4.9a and 4.9b to predict the thermo-mechanical durability of two solders. Separate plastic energy density vs. cycles-to-failure due to plastic damage plot and creep energy density vs. cycles-to-failure due to creep damage plot are shown in Figure 4.41 for Sn3.8Ag0.7Cu (SAC) and Sn37Pb (SP) solders. Two important features are observed in the figure. First, plastic and creep curves for SAC have steeper slopes than the corresponding curves for SP, suggesting different plastic and creep damage mechanisms for the two solders. For example, comparing two creep curves at the left side of the crossover point, the curve

of SAC is at the right of that of SP. At the same creep work density, SAC has longer cycles-to-failure than SP. In other words, larger creep damage occurs in SP as the damage is defined as the reciprocal of cycles-to-failure. This is because SAC is more creep-resistant than SP. Furthermore, the crossover points between plastic and creep curves are different for Sn3.8Ag0.7Cu and Sn37Pb solders. The crossover for SAC is at approximately 800 cycles ($\Delta W_{cr} = 1 \text{ mJ/mm}^3$) while that for SP is at 12 cycles ($\Delta W = 25 \text{ mJ/mm}^3$). Therefore, in most of applied conditions, creep damage is dominant in the Sn37Pn solder. But for the Sn3.8Ag0.7Cu solder, two regions exist for normal use environments: creep damage dominant region when ΔW_{cr} is smaller than 1 mJ/mm^3 ; plastic damage dominant region when ΔW_{cr} is larger than 1 mJ/mm^3 .

	Sn3.8Ag0.7Cu	Sn37Pb
<i>c</i>	-0.80	-0.59
<i>W_{p0}</i>	198	103
<i>d</i>	-1.4	-1.0
<i>W_{c0}</i>	1.23E4	309

Table 4.15: Thermo-mechanical Energy-Partitioning model constants for Sn3.8Ag0.7Cu and Sn37Pb

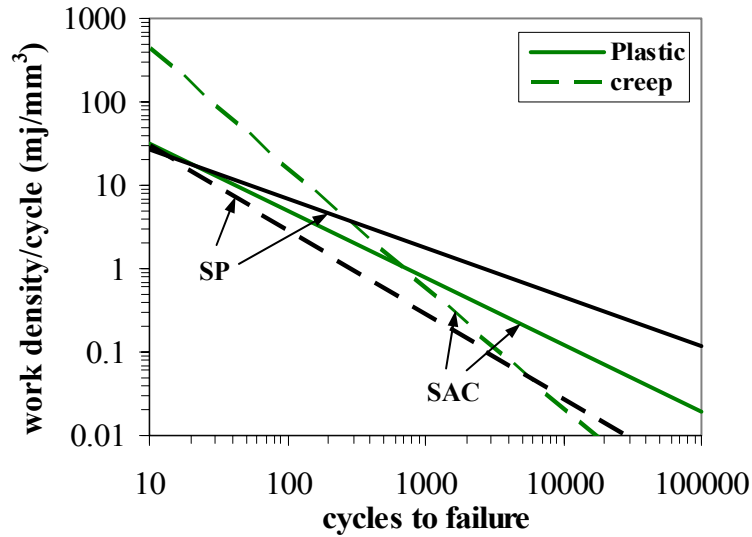


Figure 4.41: Comparison of Energy-Partitioning model between Sn3.8Ag0.7Cu and Sn37Pb solders

Since the E-P model constants are obtained by least square fit to several tests, the variance between the test results and E-P model predictions should be verified. The predicted thermo-mechanical durability by the energy-partitioning damage models for Sn3.8Ag0.7Cu and Sn37Pb is thus compared with thermal cycling test results in Figure 4.42. The experiment-model correlation is excellent. All data points from ten tests are located within a narrow scatter band of $\pm 35\%$. Five data points for Sn3.8Ag0.7Cu solders are located within a narrower scatter band (from -15% to +10%). This indicates that the E-P damage model works well for Sn3.8Ag0.7Cu Pb-free solder durability modeling.

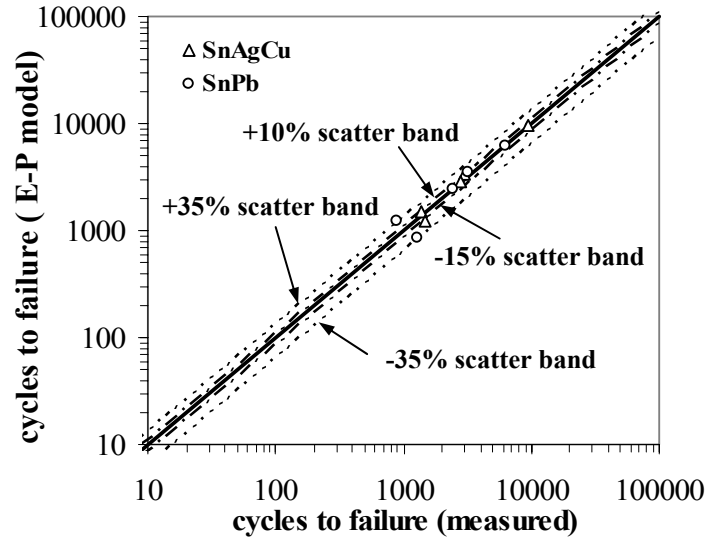


Figure 4.42: Comparison of the predicted thermo-mechanical durability by energy-partitioning model and thermal cycling test results for Sn3.8Ag0.7Cu and Sn37Pb

4.4.3.3 Comparison of E-P Durability Model for Thermal and Mechanical Cycling

The E-P durability model of SnPb solder presented in the literature [Okura, 2000] is employed to predict the thermo-mechanical durability for all five thermal cycling tests in Section 4.3. The results show that the predicted cycles-to-failure for the five tests are consistently smaller than the test results, by a factor ranging from 0.21 to 0.44. We assume that the E-P model constants are the same and the difference only results from the different definition of the cycles-to-failure N_f between this study and the literature. Therefore, an empirically-guided average scaling factor, 0.34, is introduced into the E-P damage model as follows:

$$\text{Total energy} = W_p + W_c = W_{p0} N_{fp}^c + W_{c0} N_{fc}^d \quad (4.9a)$$

$$1/N_f = SF(1/N_{fp} + 1/N_{fc}) \quad (4.10b)$$

where SF is the scaling factor; other model constants are obtained from elsewhere [Okura, 2000]. The prediction results of the E-P damage model with the scaling factor

and without the scaling factor are shown in Figure 4.43. It is seen that the adjusted E-P damage model works pretty well in predicting thermo-mechanical durability of the SnPb solder.

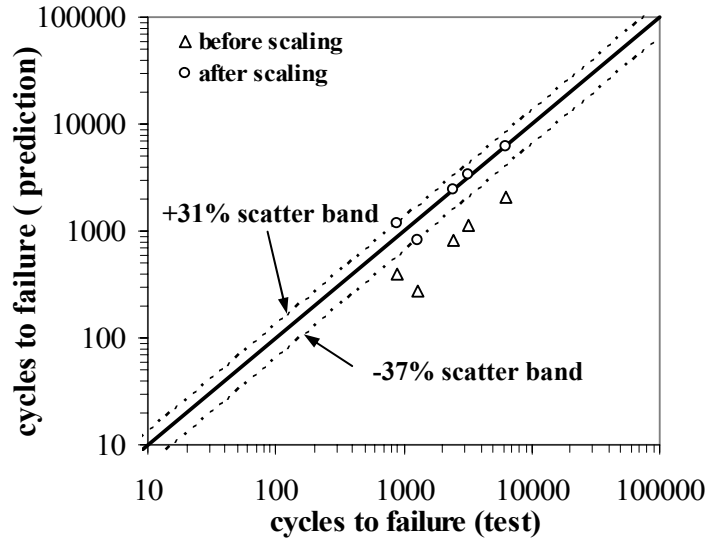


Figure 4.43: Comparison of the prediction results of previous E-P durability model for Sn37Pb: before scaling and after scaling

One of the major objectives of this study is to compare the energy-partitioning damage models of the Pb-free solder obtained from isothermal mechanical cyclic tests and from thermal cycling tests. Figure 4.44 shows the comparison between two E-P damage models. It is evident that the plastic and creep curves for thermal cycling are steeper than the corresponding curves for mechanical cycling. The crossover between plastic and creep curves is also different for thermal cycling and mechanical cycling. The reasons for these differences are grouped under two main categories. First, the definition of N_f and second, the evaluation of partitioned plastic and creep energies are different in the two tests.

The cycles when the 50% load drop is reached are defined as cycles-to-failure N_f in mechanical cycling. But in thermal cycling, cycles-to-failure N_f is defined as the cycles when electrical opens repeat for a certain number of times. There is no simple relationship between failure criterion of mechanical cycling and that of thermal cycling because mechanical cycling test includes partial damage propagation while thermal cycling includes complete damage propagation. Furthermore, because of the differences in specimen geometry and loading configuration, the ratio of cycles for damage initiation to damage propagation and their relationship to load magnitude are very different.

As for the evaluation of partitioned plastic and creep energies, different methods are used for mechanical cycling and thermal cycling. In mechanical cycling, nominally pure shear condition is assumed and only uniform shear stress and shear strain are considered in the simple incremental analytical model. In thermal cycling, although more accurate finite element method is used, the geometry and loading condition are much more complex as well. First, the stress-strain distribution is not pure shear but very complicated as there are more factors such as solder joint shape, complex package geometry, the number of solder balls, intermetallic layer and local CTE mismatch. As shown in Figure 4.45, peeling stress component σ_y has much larger range than shear stress component σ_{yz} (106MPa vs. 14 MPa). Thus the thermal cycling test has more mixed mode damage than the mechanical cycling test. Second, current finite element models do not include the intermetallic layer, which has a significant effect on thermo-mechanical durability of the Pb-free solder. The change of the solder composition near the intermetallic layer due to metallization is also not considered in the current finite element model. These effects

should be included in future work. Finally, the plastic and creep work densities are evaluated on the critical half layer of solder in the finite element analysis while average values across the whole solder joint are calculated in mechanical cycling. In summary, separate energy-partitioning damage constants should be used for mechanical cycling and thermal cycling of Pb-free solder joints unless the abovementioned issues are addressed.

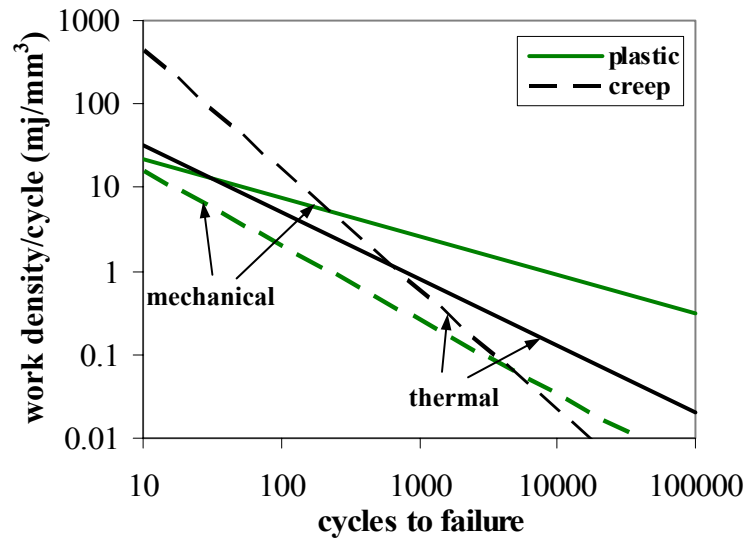


Figure 4.44: Comparison of Energy-Partitioning damage model of SnAgCu solder between mechanical cycling and thermal cycling

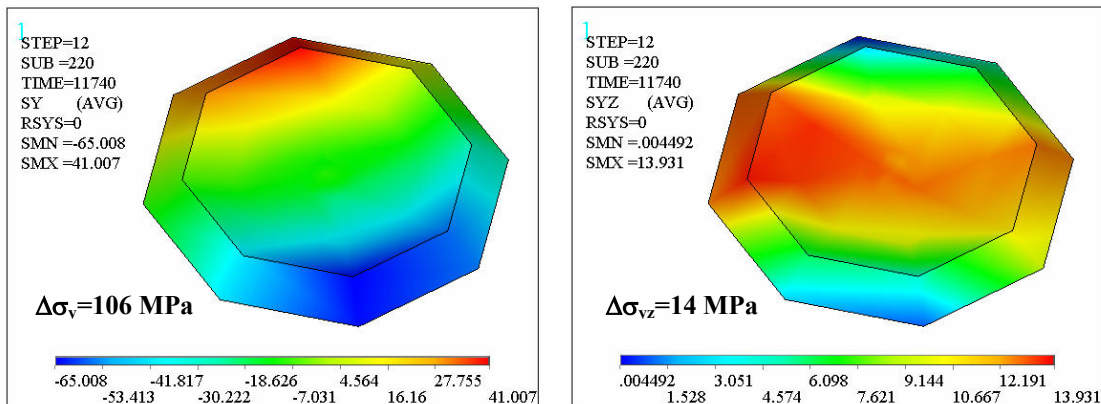


Figure 4.45: Stress contour plots of flexBGA1 package at -55°C before dwell

The scaling approach presented earlier in this section is used for the Pb-free solder, as shown in Figure 4.46. There is no previous E-P damage model available for the Pb-free solder so that the model from mechanical cycling tests in Chapter 3 is employed. It is noted that the adjusted E-P damage model with a scaling factor of 1.4 yields a reasonably good prediction of thermo-mechanical durability of the SnAgCu solder.

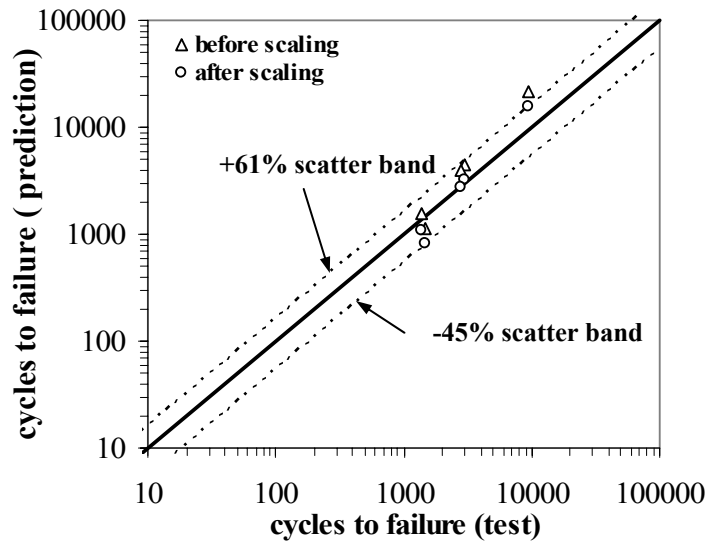


Figure 4.46: Comparison of the prediction results of the E-P durability model from mechanical cycling tests of Sn3.9Ag0.6Cu: before scaling and after scaling

4.4.3.4 Life Cycle Durability Assessment

The major application of thermo-mechanical durability modeling is to assess the life cycle durability of solder joints. As an illustration, the life cycle durability of the fleXBGA1 package subjected to a typical laptop environmental condition is evaluated by using the E-P damage models discussed in the last section. The acceleration factor (the ratio of the cycles-to-failure under life cycle environment to the accelerated test condition) is also assessed for this environment.

A typical thermal profile for a laptop life cycle environment is shown in Figure 4.47 [Darveaux, et al., 1995]. The finite element stress and damage analysis of the fleXBGA1 subjected to this profile are conducted for the Sn3.8Ag0.7Cu and Sn37Pb solders. The obtained characteristic life and the acceleration factor are listed in Table 4.16. The cycles to 1% failure is more useful than characteristic life in product design. If the same shape parameter is assumed for the life cycle environment and the accelerated test condition, the cycles to 1% failure can be calculated by the Weibull distribution. The results of the cycles to 1% failure are also listed in Table 4.16. It is seen in the table that the Sn3.8Ag0.7Cu solder has much longer thermo-mechanical durability in this life cycle environment than the Sn37Pb solder. If the product is designed for 1% failure and 750 cycles per year, the Sn3.8Ag0.7Cu solder can last for 21 years but the Sn37Pb solder only has 6 year life. The acceleration factor of the Sn3.8Ag0.7Cu solder is also much larger than that of the Sn37Pb solder. This agrees with the results in the literature [Syed, 2001b]. Under the field use environment, accumulated creep damage in the Sn3.8Ag0.7Cu solder joint is much less than that in the Sn37Pb solder joint (0.005 mJ/mm^3 vs. 0.037 mJ/mm^3) because of the better creep resistance of Pb-free solders. Thus the estimated life of the Sn3.8Ag0.7Cu solder by the E-P damage model is much longer than that of the Sn37Pb solder, and the acceleration factor for SAC is larger than that for SP.

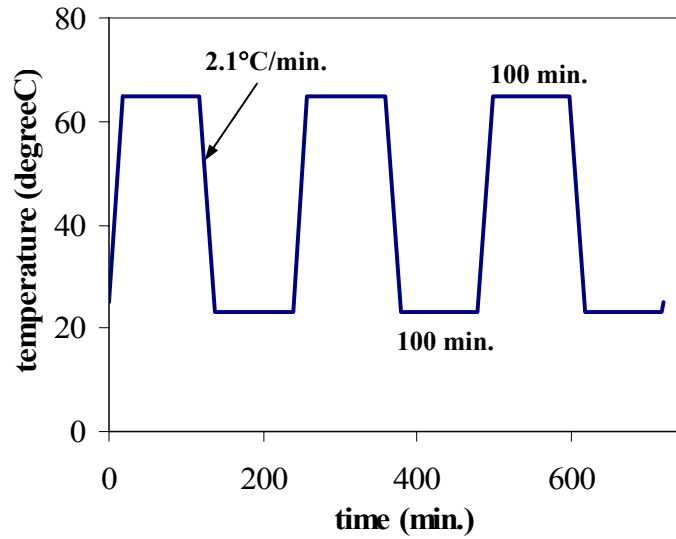


Figure 4.47: Thermal profile of typical laptop life cycle environment [Darveaux, et al., 1995]

	Sn3.8Ag0.7Cu	Sn37Pb
Acceleration Factor	20	9
Characteristic Life	27621	7697
Cycles to 1% failure	16026	4466

Table 4.16: Summary of characteristic life, acceleration factor and life cycle durability under the laptop use environment

5 Summary, Contributions and Suggestions for Future Work

This study is motivated by the urgent need in the electronics industry for constitutive properties, mechanical durability, and thermo-mechanical durability of Pb-free solders because the use of Pb will be banned in EU by July 1, 2006. Systematic research of these mechanical properties by employing both experimental and numerical tools is crucial to understand the differences in reliability characteristics between Pb-free technologies and SnPb technologies. The results of this study will be crucial for virtual qualification of Pb-free electronics during design and development of electronics for complex use environments that contain combined thermal and mechanical loading.

5.1 Summary of Results

A partitioned constitutive model consisting of elastic, plastic, primary creep and secondary creep models is obtained for the Sn_{3.9}Ag_{0.6}Cu solder and the baseline Sn₃₇Pb solder from comprehensive monotonic and creep tests conducted on Thermo-Mechanical-Microscale (TMM) setup. These results include some from a previous study [Haswell, 2001] and more from this study. The results are compared between two solders and with the available test data from the literature. An incremental analytical model has been developed in this study to simulate the monotonic, creep, and cyclic tests on the TMM setup.

The isothermal mechanical durability of three NEMI recommended Pb-free solders, Sn_{3.9}Ag_{0.6}Cu, Sn_{3.5}Ag, Sn_{0.7}Cu, is tested on the TMM setup under two test

conditions: room temperature and relatively high strain rate which results in very low creep deformation; high temperature and low strain rate which results in relatively high creep deformation. The major outputs of these tests are power law durability model constants and Energy-Partitioning model constants, which can be used to assess the mechanical cycling durability of three Pb-free solders. The damage propagation rate is also analyzed from the test data. The obtained mechanical durability models of three Pb-free solders are compared with those of the eutectic Sn37Pb solder at the two selected test conditions and at the same homologous temperature of 0.75. The generic energy-partitioning durability model is obtained for three Pb-free solders with the aid of the incremental analytical model of TMM cyclic tests. The scatter of the test results from the mean value predicted by these E-P durability model constants is small. Comprehensive microstructural observations before and after TMM tests are performed for all three Pb-free solder and the results are addressed in the dissertation.

The thermo-mechanical durability of the Pb-free Sn3.8Ag0.7Cu solder is investigated by a systematic approach combining comprehensive thermal cycling tests and finite element modeling. This task is conducted in cooperation with the sponsor. Assembly of the test boards and the thermal cycling tests were conducted by the sponsor. Test vehicle characterization, failure data analysis, failure analysis and FE analysis are conducted as part of this dissertation. The effects of mixed solder systems, device types, and underfill are addressed in the thermal cycling tests. Three-dimensional viscoplastic finite element analysis is conducted for five different thermal cycling tests of both Sn3.8Ag0.7Cu and Sn3Pb solders. Power law type thermo-mechanical durability models of Sn3.8Ag0.7Cu

and Sn3Pb solders are obtained from thermal cycling test data and stress and damage analysis. The energy-partitioning durability models of Sn3.8Ag0.7Cu and Sn3Pb solders are also obtained. The comparison of energy-partitioning durability model of the Pb-free solder from mechanical cycling tests and from thermal cycling tests is performed and the results are discussed.

The major contributions of this dissertation and suggestions for future work in experimental and numerical research of the Pb-free solders are summarized in the following sections.

5.2 Contributions of the Dissertation

The main contributions of this dissertation concentrate on the comprehensive experimental and numerical study of constitutive properties, mechanical cycling durability and thermo-mechanical durability of the Pb-free solders. These include:

1. A complete set of partitioned constitutive model constants is obtained for the Sn3.9Ag0.6Cu solder. The Pb-free Sn3.9Ag0.6Cu solder shows much better creep resistance than the eutectic Sn37Pb solder at the low and medium stresses. But the superiority of the Pb-free solder disappears as the stress increases. The Pb-free solder is even worse than the Sn37Pb solder beyond certain stress levels. The same trend has been reported by Wiese [Wiese, et. al., 2002]. The time-dependent primary creep and power law plastic models are also obtained for the Sn3.9Ag0.6Cu solder. These properties have not been reported for this Pb-free solder in the literature.
2. Mechanical durability data are obtained for the Sn3.9Ag0.6Cu, Sn3.5Ag, and Sn0.7Cu solders at room and high temperatures. This is the first study which reports

the high temperature mechanical durability of the three selected Pb-free solders. At room temperature, the Sn3.9Ag0.6Cu and Sn3.5Ag solders show much better mechanical durability than the SnPb solder while the Sn0.7Cu solder does not have this superiority. At high temperature, all durability curves of four solders cross over together, suggesting a complicated situation. Power law durability models obtained in this study provide insights into the mechanical durability of the Pb-free solders and also make it possible for packaging engineers to design Pb-free electronics for mechanical cycling environments. The comparison of power law durability between the Pb-free solders and the SnPb solder shows that the durability curves of the Pb-free solders have steeper slopes than those of the SnPb solder under the two selected extreme test conditions, no matter what damage criterion is used (inelastic strain range or total work density).

3. A systematic approach has been developed to obtain the energy-partitioning damage models for the mechanical durability of the three selected Pb-free solders. The approach is composed of two parts: (1) using an incremental analytical model to simulate the TMM cyclic tests and partition the plastic and creep deformations; (2) obtaining the E-P model constants from the partitioned plastic and creep energies and the mechanical durability data. At this time, the energy-partitioning damage model constants are obtained for the Sn3.9Ag0.6Cu, Sn3.5Ag, and Sn0.7Cu solders.
4. The thermo-mechanical durability data of the Sn3.8Ag0.7Cu solder has been obtained by systematic thermal cycling tests of the circuit card assemblies with five types of SMT components populated on. Testing has been conducted by CALCE sponsors, but test vehicle characterization, failure data analysis, failure analysis and

FE analysis have been conducted as part of this dissertation. Thermal cycling results show that the Sn_{3.8}Ag_{0.7}Cu solder system outperforms the SnPb solder system for four different components under the studied accelerated test condition. The results for mixed solder systems (Pb-free ball/SnPb paste and SnPb ball/Pb-free paste) are complex, suggesting package and process dependence. Extensive failure analyses of tested boards verify that the failure mode for several of the Pb-free solder joints is fatigue crack initiation and propagation. Failure analysis also shows that the existence of long thin plate-shaped Ag₃Sn intermetallic compounds facilitates the crack initiation and propagation. The effects of voids and Pb contamination are also addressed in the study.

5. This study investigates the viscoplastic deformation behavior of the Sn_{3.8}Ag_{0.7}Cu solder under thermal cycling loading through extensive detailed three-dimensional viscoplastic finite element stress and damage analyses. Compared with the SnPb solder, the Pb-free solder bears with larger stress range and smaller inelastic strain range due to different plastic and creep properties. The damage analysis results also show that cyclic plastic work is a considerably large portion of the total inelastic work and can not be ignored in the thermo-mechanical durability model for the Pb-free solder. Based on the damage analysis and thermal cycling test results, the major outputs of this study, thermo-mechanical durability model of the Pb-free solders, are obtained. Both the power law durability model and the energy-partitioning damage model are presented in the dissertation. The E-P damage model of the Pb-free solder has the value of -1.4 for the constant d , the slope of the plot of creep energy density vs. life due to creep damage, which is different from the corresponding value for the

SnPb solder. The value for the SnPb solder obtained in this study is -1.0, which is the same as the value reported by Dasgupta [Dasgupta, 1992]. It is also found that the slopes of the plastic and creep curves in the E-P damage model for thermal cycling are steeper than those for mechanical cycling. The discrepancy is due to different failure criteria and damage estimation methods.

6. The design and production of new TMM apparatus holder make it possible to install the specimens and run the TMM tests in the horizontal orientation. In this way, the consistence of TMM test data has been improved. It also makes it easy to integrate a microscope in TMM setup to *in situ* observe the microstructural evolution of the solder during the test.

5.3 Suggestions for Future Work

Based on the insights from this study, possible future work is suggested in this section. These suggestions include improvements in both experimental and analytical tasks which may lead to potential improvements and developments in TMM testing, thermal cycling tests, finite element analysis, and durability models of the Pb-free solders.

1. A general optical microscope can be easily integrated into the TMM setup in the horizontal direction. It is possible to conduct *in situ* measurement of solder fatigue crack length during the TMM tests. The crack initiation and propagation in Pb-free solders can be studied on the TMM setup. In addition, as we discussed before, the discrepancy between mechanical durability model and thermo-mechanical durability model is partially due to different failure criteria. But the crack initiation and propagation can be used as the failure criterion for both

mechanical and thermal cycling tests. It can also be measured in two kinds of tests. If the test data from both mechanical and thermal cycling tests are available, the durability model for two tests may be related and even unified.

2. As shown in Chapter 4, large normal stresses exist in the critical layer under thermal cycling conditions. It is expected that the stress conditions in real mechanical cycling environments are not pure shear either. It is also known that the hydrostatic stress has a significant effect on solder durability. So it is desirable to develop the capability of the TMM setup to characterize the hydrostatic stress. One possible solution is to design a loading system, which can maintain a constant normal stress on both ends of the TMM specimen. By conducting TMM cyclic tests under different applied normal stresses, the effects of the hydrostatic stress on the mechanical durability of solder alloys can be investigated.
3. A preliminary attempt has been made to develop a micro-mechanical creep model for Pb-free Solders (Appendix C). Future work can be extended to both plastic and creep models. In order to develop such a micro-mechanical model, some material properties have to be measured. They include both macro-scale properties such as elastic, plastic and creep properties of pure tin and micro-scale properties such as intermetallic particle size, dislocation density of tin matrix, volume diffusivity. Macro-scale properties can be measured on the TMM setup. Measuring the micro-scale properties needs other testing technologies.
4. An incremental viscoplastic analytical model has been developed on the basis of the Maxwell model, in this study. This model can be improved by using more

complex viscoplastic models to represent the mechanical behavior of the solder. Some examples of such models are the three-parameter standard model and the four-parameter Burger's model [Skrzypek, 1993].

5. Thermal cycling tests of the Pb-free solder interconnects in various packages are still important tools to understand the effects of a number of process and geometric parameters on the solder failures. It is suggested to conduct the thermal cycling tests under more benign and more severe conditions. These test data can be used to verify the obtained E-P damage model and also can be integrated to improve the damage model. Another important issue is the effect of the mixed solder system. A more benign test condition is suggested to address this issue because there is a larger difference between thermo-mechanical durability of pure Pb-free solder and pure SnPb solder. In addition, accurate control of the solder joint height is critical to obtain good test results for this issue.
6. It is known that the intermetallic layer, the change of solder composition in the area close to the intermetallic layer and voids have effects on the thermo-mechanical durability of the Pb-free solder. This study also shows that they may affect the results of stress analysis and damage analysis, consequently, the thermo-mechanical durability model. So future finite element analysis should include the effects of the intermetallic layer.
7. Effects of defects (voids, excessive intermetallics in the bulk solder, large grain size, etc.) on thermal cycling reliability are very important for Pb-free solder joints because of different microstructure and processing of Pb-free solders from

eutectic SnPb solders. These effects should be studied experimentally and numerically in the future work.

6 Appendices

Appendix A: TMM Modification Drawings

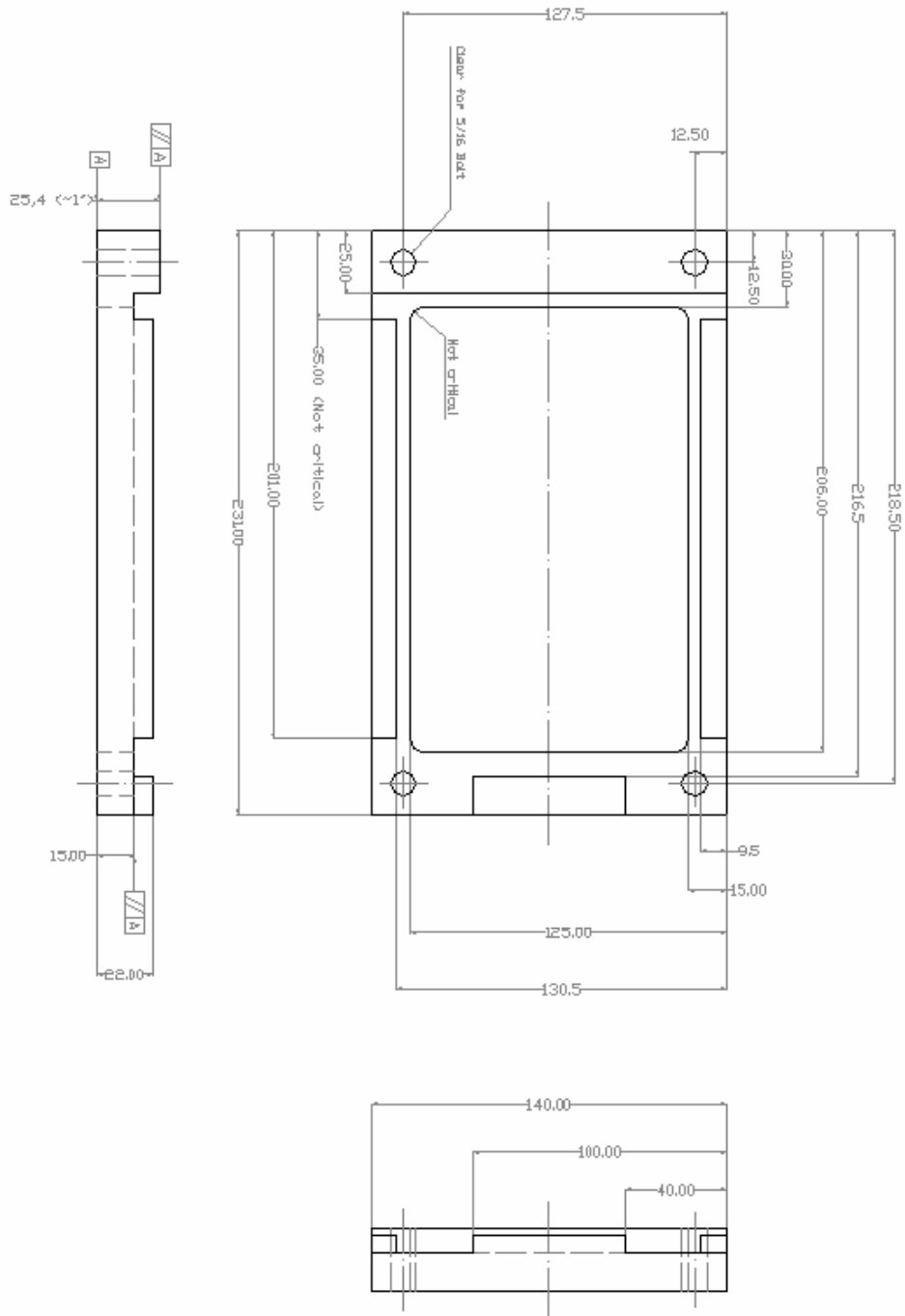


Figure 6.1: Mechanical drawing of fixture frame

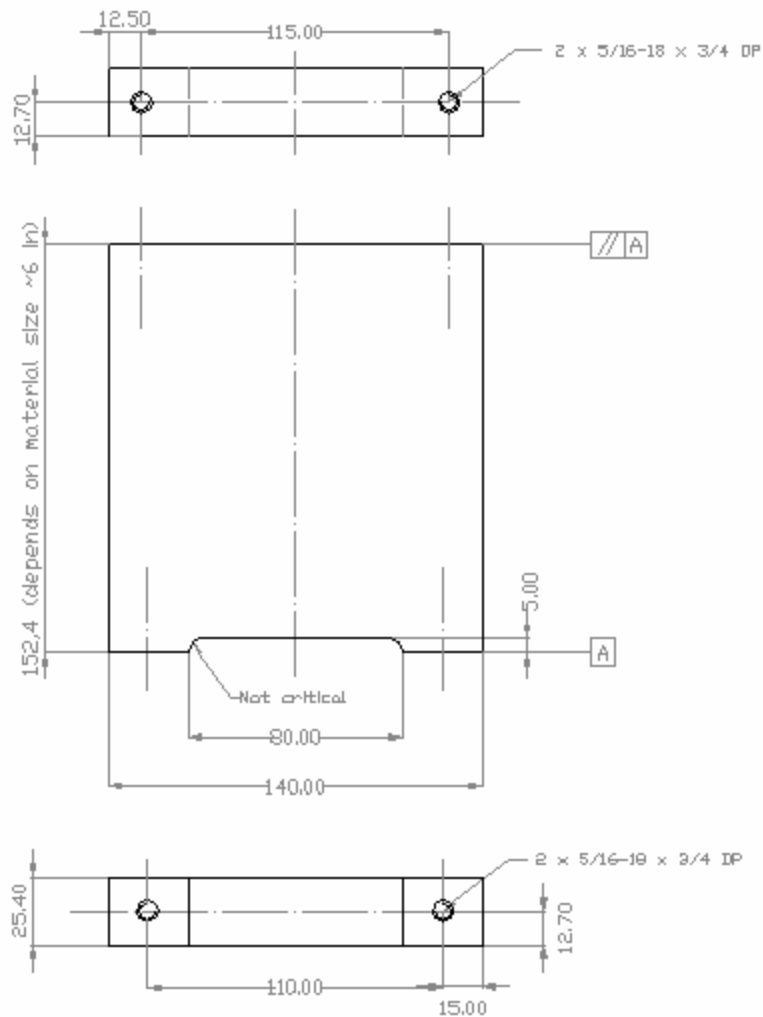


Figure 6.2: Mechanical drawing of frame foot

Appendix B: VB Program of Incremental analytic model of TMM Tests

This is an example of VB program for Sn3.9Ag0.6Cu Solder.

```
Public pos_start As Double, pos_max As Double, pos_min As Double, ramp As Double
Public t_cycle As Double, dt As Double, out_interval As Double
```

```
Public num_cycles As Integer, N As Integer, direction As Integer
Public stats_begin As Integer, stats_end As Integer, outcount As Integer
```

```
Public Gsol As Double, m As Double, C As Double, np As Double
Public C_LT As Double, h As Double, Asol As Double, A As Double, Astress As Double
Public DHOR As Double, nc As Double, temp As Double, t As Double, t_out As Double
Public pos As Double, load_0 As Double, load_1 As Double, stress As Double, true_stress As Double
```

```
Public strain_tot As Double, strain_crp As Double, strain_el As Double
```

```
Public strain_crp2 As Double, strain_crp_tot2 As Double
Public strain_crp1 As Double, strain_crp_tot1 As Double, crp1_tot As Double
Public crp1_sat As Double, crp1_b As Double, Maxstress As Double, Minstress As Double
```

```
Public crpstrn_tot As Double, crpstrn_tot1 As Double, crpstrn_tot2 As Double
Public plstrn_tot As Double, elstrn_tot As Double, Stress_0 As Double, Strain_sol0 As Double
Public plstrn_in As Double, elstrn_in As Double, intI As Integer, EnergyEls As Double
```

```
Dim EnergyCrp(9) As Double, EnergyPls(9) As Double
```

```
Public out As Integer
```

```
Sub Elastic_Plastic_Creep()
```

```
Worksheets("output").Range("A3:G10000").ClearContents
Worksheets("cycle stats").Range("A3:G10000").ClearContents
Worksheets("output").Range("L5:L8").ClearContents
```

```
test_type = Worksheets("inputs").Cells(7, 2)
pos_start = Worksheets("inputs").Cells(9, 2)
pos_max = Worksheets("inputs").Cells(10, 2)
pos_min = Worksheets("inputs").Cells(11, 2)
ramp = Worksheets("inputs").Cells(12, 2)
t_cycle = Worksheets("inputs").Cells(16, 2)
dt = Worksheets("inputs").Cells(17, 2)
out_interval = t_cycle / Worksheets("inputs").Cells(18, 2)
num_cycles = Worksheets("inputs").Cells(19, 2)
```

```
C_LT = Worksheets("inputs").Cells(20, 2)
h = Worksheets("inputs").Cells(3, 2)
Asol = Worksheets("inputs").Cells(4, 2)
A = Worksheets("inputs").Cells(5, 6)
DHOR = Worksheets("inputs").Cells(6, 6)
nc = Worksheets("inputs").Cells(4, 6)
```

```
temp = Worksheets("inputs").Cells(8, 2)
m = Worksheets("inputs").Cells(10, 6)
C = Worksheets("inputs").Cells(11, 6)
Gsol = Worksheets("inputs").Cells(3, 6)
```

```
N = 1
t = 0
Astress = 0
pos = 0
load_0 = 0
load_1 = 0
stress = 0
Stress_0 = 0
true_stress = 0
strain_sol = 0
Strain_sol0 = 0
strain_tot = 0
strain_tot1 = 0
strain_tot2 = 0
strain_crp = 0
strain_crp1 = 0
```

```

strain_crp2 = 0
strain_el = 0
TauRange = 0

For intI = 0 To 9
    EnergyCrp(intI) = 0
    EnergyPls(intI) = 0
Next

crpstrn_tot = 0
crpstrn_tot1 = 0
crpstrn_tot2 = 0
plstrn_tot = 0
elstrn_tot = 0
plstrn_in = 0
elstrn_in = 0

out = 3
out3 = 2
stats_begin = 2
outcount = 2

Maxstress = 0
Minstress = 0

t_out = out_interval

If test_type = 3 Then
    'Cyclic test profile
    Do
        direction = -1
        Call IncrCalcS
        Loop While pos > pos_min / 1000
        If stress > Maxstress Then
            Maxstress = stress
        End If
        If stress < Minstress Then
            Minstress = stress
        End If
    Do
        direction = 1
        Do
            Call IncrCalc2
            Loop While pos < pos_max / 1000
            If stress > Maxstress Then
                Maxstress = stress
            End If
            If stress < Minstress Then
                Minstress = stress
            End If
        direction = -1
    Do
        Call IncrCalc1
        Loop While pos > pos_min / 1000
        If stress > Maxstress Then
            Maxstress = stress

```

```

End If
If stress < Minstress Then
    Minstress = stress
End If
stats_end = out
Call maxmin

N = N + 1
Asol = Asol * 1
Worksheets("output").Cells(5, 12) = N

Loop While N < num_cycles + 1
ElseIf test_type = 1 Then
'Monotonic test profile
Do
direction = 1
Do
    Call IncrCalcS
    Loop While pos < pos_max / 1000

direction = -1

Do
    Call IncrCalcS
    Loop While load_1 > 0
    pos_max = pos * 1000 + Worksheets("inputs").Cells(10, 2)
Loop While pos_max < Worksheets("inputs").Cells(11, 2)

ElseIf test_type = 2 Then
'Constant-load test profile
Do
    load_0 = Worksheets("inputs").Cells(13, 2)
    t = t + dt
    G = Gsol
    d_el = load_0 * (h / Asol / G)
    xxx = Worksheets("inputs").Cells(23, 2)
'creep strain calculation
    If Worksheets("inputs").Cells(21, 2) = 2 Then
        'Wiese secondary creep
        Astress = 0.192 * Abs(load_0) / Asol
        strain_crpr = Sgn(load_0) * A * xxx * ((Exp(Astress) - Exp(-1 * Astress)) / 2) ^ nc * Exp(-DHOR /
temp)
        strain_crp = strain_crpr * dt
    ElseIf Worksheets("inputs").Cells(21, 2) = 1 Then
        'transient + steady state [Wiese, 2001]
        Astress = 0.192 * Abs(load_0) / Asol
        strain_crpr = Sgn(load_0) * A * xxx * ((Exp(Astress) - Exp(-1 * Astress)) / 2) ^ nc * Exp(-DHOR /
temp)
        crp1_sat = 0.00298 * (Abs(load_0) / Asol) ^ 1.1714
        PrimC = 0.0724 * (Abs(load_0) / Asol) ^ 3.2688 * Exp(-4393.6 / temp)
        strain_crp2 = Sgn(load_0) * strain_crpr * dt
        strain_crp1 = Sgn(load_0) * crp1_sat * (1 - Exp(-PrimC * dt))
        strain_crp = strain_crp2 + strain_crp1
    Else
        'no creep
        strain_crp = 0

```

```

End If
strain_crp_tot1 = strain_crp_tot1 + strain_crp1
strain_crp_tot2 = strain_crp_tot2 + strain_crp2
strain_crp_tot = strain_crp_tot + strain_crp
strain_sol = d_el / h + strain_crp_tot
stress = load_0 / Asol

If (strain_sol - Worksheets("output").Cells(out - 1, 4)) > 0.0002 Then
    Worksheets("output").Cells(out, 1) = N
    Worksheets("output").Cells(out, 2) = t
    Worksheets("output").Cells(out, 3) = strain_sol * h * 1000
    Worksheets("output").Cells(out, 4) = strain_sol
    Worksheets("output").Cells(out, 5) = stress
    Worksheets("output").Cells(out, 6) = stress
    Worksheets("output").Cells(out, 7) = strain_crp_tot
    Worksheets("output").Cells(out, 8) = strain_crp_tot1
    Worksheets("output").Cells(out, 9) = strain_crp_tot2
    out = out + 1
End If

'Check solution rate
If strain_crp < 0.001 Then
    dt = dt * 2
ElseIf strain_crp > 0.01 Then
    dt = dt / 2
End If

Worksheets("output").Cells(6, 20) = t
Worksheets("output").Cells(7, 20) = strain_sol * h * 1000
Worksheets("output").Cells(8, 20) = dt

    Loop While (strain_sol * h * 1000) < pos_min
End If

Call AutoChart

End Sub

Sub IncrCalcS()

    t = t + dt
    pos = pos + direction * ramp * dt / 1000

    'no plasticity
    If Worksheets("inputs").Cells(22, 2) = 0 Then
        G = Gsol
    'plasticity
    ElseIf Worksheets("inputs").Cells(22, 2) = 1 And Abs(stress) <= 6.986 Then
        G = Gsol
    ElseIf Worksheets("inputs").Cells(22, 2) = 1 And Abs(stress) > 6.986 Then
        G = 1 / (1 / Gsol + (1 / m) * (1 / C) ^ (1 / m) * Abs(stress) ^ (1 / m - 1))
    End If
    load_0 = load_1 + (direction * ramp * dt / 1000) / (h / Asol / G + C_LT / 1000)

    xxx = Worksheets("inputs").Cells(23, 2)
'creep strain calculation

```

```

If Worksheets("inputs").Cells(21, 2) = 2 Then
'Wiese secondary creep
Astress = 0.192 * Abs(load_0) / Asol
strain_crpr = A * xxx * ((Exp(Astress) - Exp(-1 * Astress)) / 2) ^ nc * Exp(-DHOR / temp)
strain_crp = strain_crpr * dt
ElseIf Worksheets("inputs").Cells(21, 2) = 1 Then
'transient + steady state [Wiese, 2001]
Astress = 0.192 * Abs(load_0) / Asol
strain_crpr = A * xxx * ((Exp(Astress) - Exp(-1 * Astress)) / 2) ^ nc * Exp(-DHOR / temp)
crp1_sat = 0.00298 * (Abs(load_0) / Asol) ^ 1.1714
PrimC = 0.0724 * (Abs(load_0) / Asol) ^ 3.2688 * Exp(-4393.6 / temp)
strain_crp2 = Sgn(load_0) * strain_crpr * dt
strain_crp1 = Sgn(load_0) * crp1_sat * (1 - Exp(-PrimC * dt))
strain_crp = strain_crp2 + strain_crp1
Else
'no creep
strain_crp = 0
End If
crpstrn_tot1 = crpstrn_tot1 + Abs(strain_crp1)
crpstrn_tot2 = crpstrn_tot2 + Abs(strain_crp2)
crpstrn_tot = crpstrn_tot + Abs(strain_crp)

load_1 = load_0 - (strain_crp * h) / (h / Asol / Gsol + C_LT / 1000)
strain_sol = (pos - load_1 * C_LT / 1000) / h
stress = load_1 / Worksheets("inputs").Cells(4, 2)
true_stress = load_1 / Asol
elstrn_in = (stress - Stress_0) / Gsol
plstrn_in = (strain_sol - Strain_sol0) - strain_crp - elstrn_in
elstrn_tot = stress / Gsol
plstrn_tot = plstrn_tot + Abs(plstrn_in)
EnergyCrp(0) = EnergyCrp(0) + strain_crp * 0.5 * (stress + Stress_0)
EnergyPls(0) = EnergyPls(0) + plstrn_in * 0.5 * (stress + Stress_0)
Stress_0 = stress
Strain_sol0 = strain_sol

If t >= t_out Then
Worksheets("output").Cells(out, 1) = N
Worksheets("output").Cells(out, 2) = t
Worksheets("output").Cells(out, 3) = pos * 1000
Worksheets("output").Cells(out, 4) = strain_sol
Worksheets("output").Cells(out, 5) = stress
Worksheets("output").Cells(out, 6) = true_stress
Worksheets("output").Cells(out, 7) = crpstrn_tot
Worksheets("output").Cells(out, 8) = crpstrn_tot1
Worksheets("output").Cells(out, 9) = crpstrn_tot2
Worksheets("output").Cells(out, 10) = elstrn_tot
Worksheets("output").Cells(out, 11) = plstrn_tot
Worksheets("output").Cells(out, 12) = strain_crpr
t_out = t_out + out_interval
out = out + 1

Worksheets("output").Cells(6, 20) = t
Worksheets("output").Cells(7, 20) = pos * 1000
Worksheets("output").Cells(8, 20) = dt
End If
End Sub

```

Sub IncrCalc1()

```
t = t + dt
pos = pos + direction * ramp * dt / 1000

'no plasticity
If Worksheets("inputs").Cells(22, 2) = 0 Then
G = Gsol
'plasticity
ElseIf Worksheets("inputs").Cells(22, 2) = 1 And Abs((Maxstress - stress) / 2) <= 6.986 Then
G = Gsol
ElseIf Worksheets("inputs").Cells(22, 2) = 1 And Abs((Maxstress - stress) / 2) > 6.986 Then
G = 1 / (1 / Gsol + (1 / m) * (1 / C) ^ (1 / m) * Abs((Maxstress - stress) / 2) ^ (1 / m - 1))
End If
load_0 = load_1 + (direction * ramp * dt / 1000) / (h / Asol / G + C_LT / 1000)

xxx = Worksheets("inputs").Cells(23, 2)
'creep strain calculation
If Worksheets("inputs").Cells(21, 2) = 2 Then
'Wiese secondary creep
Astress = 0.192 * Abs(load_0) / Asol
strain_crpr = A * xxx * ((Exp(Astress) - Exp(-1 * Astress)) / 2) ^ nc * Exp(-DHOR / temp)
strain_crp = strain_crpr * dt
ElseIf Worksheets("inputs").Cells(21, 2) = 1 Then
'transient + steady state [Wiese, 2001]
Astress = 0.192 * Abs(load_0) / Asol
strain_crpr = A * xxx * ((Exp(Astress) - Exp(-1 * Astress)) / 2) ^ nc * Exp(-DHOR / temp)
crp1_sat = 0.00298 * (Abs(load_0) / Asol) ^ 1.1714
PrimC = 0.0724 * (Abs(load_0) / Asol) ^ 3.2688 * Exp(-4393.6 / temp)
strain_crp2 = Sgn(load_0) * strain_crpr * dt
strain_crp1 = Sgn(load_0) * crp1_sat * (1 - Exp(-PrimC * dt))
strain_crp = strain_crp2 + strain_crp1
Else
'no creep
strain_crp = 0
End If
crpstrn_tot1 = crpstrn_tot1 + Abs(strain_crp1)
crpstrn_tot2 = crpstrn_tot2 + Abs(strain_crp2)
crpstrn_tot = crpstrn_tot + Abs(strain_crp)

load_1 = load_0 - (strain_crp * h) / (h / Asol / Gsol + C_LT / 1000)
strain_sol = (pos - load_1 * C_LT / 1000) / h
stress = load_1 / Worksheets("inputs").Cells(4, 2)
true_stress = load_1 / Asol
elstrn_in = (stress - Stress_0) / Gsol
plstrn_in = (strain_sol - Strain_sol0) - strain_crp - elstrn_in
elstrn_tot = stress / Gsol
plstrn_tot = plstrn_tot + Abs(plstrn_in)
EnergyCrp(N - 1) = EnergyCrp(N - 1) + strain_crp * 0.5 * (stress + Stress_0)
EnergyPls(N - 1) = EnergyPls(N - 1) + plstrn_in * 0.5 * (stress + Stress_0)
Stress_0 = stress
Strain_sol0 = strain_sol

If t >= t_out Then
Worksheets("output").Cells(out, 1) = N
Worksheets("output").Cells(out, 2) = t
```

```

Worksheets("output").Cells(out, 3) = pos * 1000
Worksheets("output").Cells(out, 4) = strain_sol
Worksheets("output").Cells(out, 5) = stress
Worksheets("output").Cells(out, 6) = true_stress
Worksheets("output").Cells(out, 7) = crpstrn_tot
Worksheets("output").Cells(out, 8) = crpstrn_tot1
Worksheets("output").Cells(out, 9) = crpstrn_tot2
Worksheets("output").Cells(out, 10) = elstrn_tot
Worksheets("output").Cells(out, 11) = plstrn_tot
Worksheets("output").Cells(out, 12) = strain_crpr
t_out = t_out + out_interval
out = out + 1

Worksheets("output").Cells(6, 20) = t
Worksheets("output").Cells(7, 20) = pos * 1000
Worksheets("output").Cells(8, 20) = dt
End If
End Sub
Sub IncrCalc2()

t = t + dt
pos = pos + direction * ramp * dt / 1000

'no plasticity
If Worksheets("inputs").Cells(22, 2) = 0 Then
G = Gsol
'plasticity
ElseIf Worksheets("inputs").Cells(22, 2) = 1 And Abs((stress - Minstress) / 2) <= 6.986 Then
G = Gsol
ElseIf Worksheets("inputs").Cells(22, 2) = 1 And Abs((stress - Minstress) / 2) > 6.986 Then
G = 1 / (1 / Gsol + (1 / m) * (1 / C) ^ (1 / m) * Abs((stress - Minstress) / 2) ^ (1 / m - 1))
End If
load_0 = load_1 + (direction * ramp * dt / 1000) / (h / Asol / G + C_LT / 1000)

xxx = Worksheets("inputs").Cells(23, 2)
'creep strain calculation
If Worksheets("inputs").Cells(21, 2) = 2 Then
'Wiese secondary creep
Astress = 0.192 * Abs(load_0) / Asol
strain_crpr = A * xxx * ((Exp(Astress) - Exp(-1 * Astress)) / 2) ^ nc * Exp(-DHOR / temp)
strain_crp = strain_crpr * dt
ElseIf Worksheets("inputs").Cells(21, 2) = 1 Then
'transient + steady state [Wiese, 2001]
Astress = 0.192 * Abs(load_0) / Asol
strain_crpr = A * xxx * ((Exp(Astress) - Exp(-1 * Astress)) / 2) ^ nc * Exp(-DHOR / temp)
crp1_sat = 0.00298 * (Abs(load_0) / Asol) ^ 1.1714
PrimC = 0.0724 * (Abs(load_0) / Asol) ^ 3.2688 * Exp(-4393.6 / temp)
strain_crp2 = Sgn(load_0) * strain_crpr * dt
strain_crp1 = Sgn(load_0) * crp1_sat * (1 - Exp(-PrimC * dt))
strain_crp = strain_crp2 + strain_crp1
Else
'no creep
strain_crp = 0
End If
crpstrn_tot1 = crpstrn_tot1 + Abs(strain_crp1)
crpstrn_tot2 = crpstrn_tot2 + Abs(strain_crp2)

```

```

crpstrn_tot = crpstrn_tot + Abs(strain_crp)

load_1 = load_0 - (strain_crp * h) / (h / Asol / Gsol + C_LT / 1000)
strain_sol = (pos - load_1 * C_LT / 1000) / h
stress = load_1 / Worksheets("inputs").Cells(4, 2)
true_stress = load_1 / Asol
elstrn_in = (stress - Stress_0) / Gsol
plstrn_in = (strain_sol - Strain_sol0) - strain_crp - elstrn_in
elstrn_tot = stress / Gsol
plstrn_tot = plstrn_tot + Abs(plstrn_in)
EnergyCrp(N - 1) = EnergyCrp(N - 1) + strain_crp * 0.5 * (stress + Stress_0)
EnergyPls(N - 1) = EnergyPls(N - 1) + plstrn_in * 0.5 * (stress + Stress_0)
Stress_0 = stress
Strain_sol0 = strain_sol

If t >= t_out Then
    Worksheets("output").Cells(out, 1) = N
    Worksheets("output").Cells(out, 2) = t
    Worksheets("output").Cells(out, 3) = pos * 1000
    Worksheets("output").Cells(out, 4) = strain_sol
    Worksheets("output").Cells(out, 5) = stress
    Worksheets("output").Cells(out, 6) = true_stress
    Worksheets("output").Cells(out, 7) = crpstrn_tot
    Worksheets("output").Cells(out, 8) = crpstrn_tot1
    Worksheets("output").Cells(out, 9) = crpstrn_tot2
    Worksheets("output").Cells(out, 10) = elstrn_tot
    Worksheets("output").Cells(out, 11) = plstrn_tot
    Worksheets("output").Cells(out, 12) = strain_crp
    t_out = t_out + out_interval
    out = out + 1

    Worksheets("output").Cells(6, 20) = t
    Worksheets("output").Cells(7, 20) = pos * 1000
    Worksheets("output").Cells(8, 20) = dt
End If
End Sub

Sub maxmin()
BaseCycle = 2
RawCount = 0
Milestone = 0.05
Cur = 0

Worksheets("cycle stats").Cells(outcount, 1) = Worksheets("output").Cells(stats_begin, 1)

For x = 3 To 5
    Min = 0
    Max = 0
    For RawCount = stats_begin To stats_end
        Cur = Worksheets("output").Cells(RawCount, x).Value
        If Cur > Max Then
            Max = Cur
        ElseIf Cur < Min Then
            Min = Cur
        End If
    End For
    If x = 3 Then

```

```

        norm = h
    Else: norm = 1
    End If
    Worksheets("cycle stats").Cells(outcount, x - 1) = (Max - Min) / norm
Next RowCount
Next x

'Calculate hysteresis area and ISR
RowCount = stats_begin
FirstTauEng = Worksheets("output").Cells(RawCount, 5).Value
FirstTauTrue = Worksheets("output").Cells(RawCount, 6).Value
FirstGamma = Worksheets("output").Cells(RawCount, 4).Value
time_start = Worksheets("output").Cells(RawCount, 2).Value

gamma1 = 0
gamma2 = 0

For RowCount = stats_begin To stats_end - 2
    CurTauEng = Worksheets("output").Cells(RawCount, 5).Value
    CurTauTrue = Worksheets("output").Cells(RawCount, 6).Value
    CurGamma = Worksheets("output").Cells(RawCount, 4).Value
    NextTauEng = Worksheets("output").Cells(RawCount + 1, 5).Value
    NextTauTrue = Worksheets("output").Cells(RawCount + 1, 6).Value
    NextGamma = Worksheets("output").Cells(RawCount + 1, 4).Value

    If NextTauEng * CurTauEng > 0 Then
        EnerIncrEng = (NextGamma - CurGamma) * 0.5 * (NextTauEng + CurTauEng)
        EnerIncrTrue = (NextGamma - CurGamma) * 0.5 * (NextTauTrue + CurTauTrue)
    Else
        EnerIncrEng = -0.5 * (NextGamma - CurGamma) * (NextTauEng ^ 2 + CurTauEng ^ 2) / _
            (CurTauEng - NextTauEng)
        EnerIncrTrue = -0.5 * (NextGamma - CurGamma) * (NextTauTrue ^ 2 + CurTauTrue ^ 2) / _
            (CurTauTrue - NextTauTrue)

        'Interpolate crossover strain for ISR calculation
        If gamma1 = 0 Then
            gamma1 = NextGamma - NextTauEng / (NextTauEng - CurTauEng) * (NextGamma -
CurGamma)
        Else
            gamma2 = NextGamma - NextTauEng / (NextTauEng - CurTauEng) * (NextGamma -
CurGamma)
        End If

        End If
        EnerTotEng = EnerTotEng + EnerIncrEng
        EnerTotTrue = EnerTotTrue + EnerIncrTrue
    Next RowCount

LastTauEng = Worksheets("output").Cells(RawCount - 1, 5).Value
LastTauTrue = Worksheets("output").Cells(RawCount - 1, 6).Value
LastGamma = Worksheets("output").Cells(RawCount - 1, 4).Value
time_end = Worksheets("output").Cells(RawCount, 2).Value

CloseIncrEng = (FirstGamma - LastGamma) * 0.5 * (FirstTauEng + LastTauEng)
EnerTotEng = EnerTotEng + CloseIncrEng

```

```

CloseIncrTrue = (FirstGamma - LastGamma) * 0.5 * (FirstTauTrue + LastTauTrue)
EnerTotTrue = EnerTotTrue + CloseIncrTrue
TauRange = Worksheets("cycle stats").Cells(outcount, 4)
EnergyEls = 0.5 * TauRange ^ 2 / Gsol
Worksheets("cycle stats").Cells(outcount, 5) = gamma1 - gamma2
Worksheets("cycle stats").Cells(outcount, 6) = EnerTotEng
Worksheets("cycle stats").Cells(outcount, 7) = EnerTotTrue
Worksheets("cycle stats").Cells(outcount, 9) = EnergyCrp(outcount - 2)
Worksheets("cycle stats").Cells(outcount, 10) = EnergyPls(outcount - 2)
Worksheets("cycle stats").Cells(outcount, 11) = EnergyEls
outcount = outcount + 1
stats_begin = out + 1

End Sub

Sub AutoChart()

'Autoscale charts
displ_min = 0
displ_max = 0
displ_unit = 0
strain_min = 0
strain_max = 0
strain_unit = 0
stress_min = 0
stress_max = 0
stress_unit = 0

time_min = 0
time_max = Worksheets("output").Cells(out - 1, 2) * 1.1

For x = 2 To out - 1
    If Worksheets("output").Cells(x, 3) < displ_min Then displ_min = Worksheets("output").Cells(x, 3)
    If Worksheets("output").Cells(x, 3) > displ_max Then displ_max = Worksheets("output").Cells(x, 3)

    If Worksheets("output").Cells(x, 4) < strain_min Then strain_min = Worksheets("output").Cells(x, 4)
    If Worksheets("output").Cells(x, 4) > strain_max Then strain_max = Worksheets("output").Cells(x, 4)

    If Worksheets("output").Cells(x, 6) < stress_min Then stress_min = Worksheets("output").Cells(x, 6)
    If Worksheets("output").Cells(x, 6) > stress_max Then stress_max = Worksheets("output").Cells(x, 6)
Next x

raw = (stress_max - stress_min) / 6
If raw >= 1 Then
    f = 10
    c_dir = 1
Else
    f = 0.1
    c_dir = -1
End If
test = raw
powCount = 0
If (test < 1 Or test >= 10) Then
    Do
        test = test / f

```

```

    powCount = powCount + c_dir
    Loop Until (test >= 1 And test < 10)
End If
stress_unit = Round(raw / 10 ^ powCount) * 10 ^ powCount

raw = (strain_max - strain_min) / 6
If raw >= 1 Then
    f = 10
    c_dir = 1
Else
    f = 0.1
    c_dir = -1
End If
test = raw
powCount = 0
If (test < 1 Or test >= 10) Then
    Do
        test = test / f
        powCount = powCount + c_dir
        Loop Until (test >= 1 And test < 10)
    End If
strain_unit = Round(raw / 10 ^ powCount) * 10 ^ powCount
raw = (displ_max - displ_min) / 6
If raw >= 1 Then
    f = 10
    c_dir = 1
Else
    f = 0.1
    c_dir = -1
End If
test = raw
powCount = 0
If (test < 1 Or test >= 10) Then
    Do
        test = test / f
        powCount = powCount + c_dir
        Loop Until (test >= 1 And test < 10)
    End If
displ_unit = Round(raw / 10 ^ powCount) * 10 ^ powCount

'Check for monotonic/creep or cyclic test
If displ_min = 0 Then
    displ_max = (Round((displ_max / displ_unit)) + 1) * displ_unit
Else
    displ_max = (Round((displ_max / displ_unit)) + 1) * displ_unit
    displ_min = -displ_max
End If

If Abs(strain_min) < 0.01 Then
    strain_min = 0
    strain_max = (Round((strain_max / strain_unit)) + 1) * strain_unit
Else
    strain_max = (Round((strain_max / strain_unit)) + 1) * strain_unit
    strain_min = -strain_max
End If

```

```

If Abs(stress_min) < 1 Then
    stress_min = 0
    stress_max = (Round((stress_max / stress_unit)) + 1) * stress_unit
Else
    stress_max = (Round((stress_max / stress_unit)) + 1) * stress_unit
    stress_min = -stress_max
End If

```

```

'Update charts
With Charts("stress-time").Axes(xlValue)
    .MinimumScale = stress_min
    .MaximumScale = stress_max
    .MajorUnit = stress_unit
End With
With Charts("stress-time").Axes(xlCategory)
    .MinimumScale = time_min
    .MaximumScale = time_max
    .MajorUnitIsAuto = True
End With

```

```

With Charts("strain-time").Axes(xlValue)
    .MinimumScale = strain_min
    .MaximumScale = strain_max
    .MajorUnit = strain_unit
End With
With Charts("strain-time").Axes(xlCategory)
    .MinimumScale = time_min
    .MaximumScale = time_max
    .MajorUnitIsAuto = True
End With

```

```

With Charts("stress-strain").Axes(xlValue)
    .MinimumScale = stress_min
    .MaximumScale = stress_max
    .MajorUnit = stress_unit
End With

```

```

With Charts("stress-strain").Axes(xlCategory)
    .MinimumScale = strain_min
    .MaximumScale = strain_max
    .MajorUnit = strain_unit
End With

```

```

With Charts("displ-time").Axes(xlValue)
    .MinimumScale = displ_min
    .MaximumScale = displ_max
    .MajorUnit = displ_unit
End With
With Charts("displ-time").Axes(xlCategory)
    .MinimumScale = time_min
    .MaximumScale = time_max
    .MajorUnitIsAuto = True
End With

```

```

'cycle statistics chart
cycle_min = 0

```

```

cycle_max = 0
cycle_unit = 0
energy_min = 0
energy_max = 6
energy_unit = 1

cycle_max = Round(Worksheets("cycle stats").Cells(outcount - 1, 1) * 1.1)

raw = cycle_max / 6
If raw >= 1 Then
    f = 10
    c_dir = 1
Else
    f = 0.1
    c_dir = -1
End If
test = raw
powCount = 0
If (test < 1 Or test >= 10) Then
    Do
        test = test / f
        powCount = powCount + c_dir
    Loop Until (test >= 1 And test < 10)
End If
cycle_unit = Round(raw / 10 ^ powCount) * 10 ^ powCount

With Charts("cycle statistics").Axes(xlValue)
    .MinimumScale = 0
    .MaximumScale = strain_max * 2
    .MajorUnit = strain_unit
End With

With Charts("cycle statistics").Axes(xlCategory)
    .MinimumScale = 0
    .MaximumScale = cycle_max
    .MajorUnit = cycle_unit
End With

End Sub

```

Appendix C: A Microstructural Steady-State Creep Model for Pb-free Solders

Sn3.9Ag0.6Cu solder has much higher creep resistance than Sn37Pb solder below certain stresses at high temperature (in terms of homologous temperature), as discussed in Section 2.3.6. Considering the nature of the microstructure of Sn3.9Ag0.6Cu solder, a dispersion strengthening creep mechanism is expected in steady-state creep behavior of Pb-free solders. Because dispersoids, e.g. intermetallic particles of Cu_6Sn_5 and Ag_3Sn ,

are extremely small, the interparticle spacing is such that direct interaction with dislocation results. In this section a micromechanical model, based on thermally activated dislocation detachment mechanism, is explored as a possible source of the creep behavior. This material system is treated as a tin matrix, which has been dispersion-hardened with Cu_6Sn_5 and Ag_3Sn intermetallic particles. The assumption is that the dominant mechanism (within the stress range of interest) is thermally assisted dislocation pinning and detachment at the intermetallic particles. This mechanism is expected to dominate at intermediate stress levels. At very high stress, athermal detachment is expected to dominate, while diffusion is expected to play an important role at low stress levels.

The model for thermally assisted detachment has been presented elsewhere in the literature [Rosler and Arzt, 1990, Rosler and Baker, 2000] and is only summarized here for completeness. According to this model, the net creep rate ε is a combination of the matrix creep rate ε_m and the dispersion hardening creep rate ε_d , as follows:

$$\frac{1}{\dot{\varepsilon}} = \frac{1}{\dot{\varepsilon}_m} + \frac{1}{\dot{\varepsilon}_d} \quad (1a)$$

Where ε_d is given by:

$$\frac{\dot{\varepsilon}_d}{\dot{\varepsilon}_0} = \exp\left(-\frac{Gb^2 r [(1-k)(1-\sigma/\sigma_d)]^{3/2}}{k_B T}\right) \quad (1b)$$

in which the athermal detachment stress σ_d is:

$$\sigma_d = M \frac{Gb}{2\lambda} \sqrt{1-k^2} \quad (1c)$$

and the critical relaxation factor $k = k_{cr} = 0.94(1 - \frac{r}{\lambda})^{0.073}$

where: $\dot{\epsilon}_0$ is a normalization constant, G is the shear modulus, b is the burger's vector for tin, r is the average dispersoid diameter (assumed to be 10 nm in this example), λ is the interparticle spacing (estimated from square packing and the stoichiometric volume fraction), M is the Taylor factor ($=3$), k_B is Boltzman's constant, and T is the absolute temperature. In this study, $\dot{\epsilon}$ is obtained from the test data in Figure 2.20 and $\dot{\epsilon}_m$ is obtained from the literature [Adeva, et. al., 1995]. Both sets of data are summarized in Figure 6.3, for convenience. The normalization constant is then estimated by fitting Equations 1a-1c to the experimental data within the range of valid stress values. The model constant values are summarized in Table 6.1. However, we find that to obtain a reasonable fit (as shown in Figure 6.4), the normalization 'constant' has to be a function of stress (as shown in Figure 6.5). This raises questions about the validity of this model for the rate-governing deformation mechanisms in Sn3.9Ag0.6Cu solder, and further studies are required, to explore this issue. Some of the reasons for this disagreement could be due to: (i) the fact that there are particles of many different sizes in the solder, but the model is assuming a uniform size distribution; (ii) inaccuracies in the assumed values for G , b , and k ; (iii) differences in test methods between our SnAgCu creep data and the pure tin creep data obtained from the literature [Adeva, et. al., 1995]; and (iv) other competing creep mechanisms (such as matrix diffusion, grain boundary diffusion, dislocation climb, and athermal dislocation detachment) have been ignored.

Matrix	
Shear modulus, G	8.84-8.0T, GPa [Adeva 1995]
Burger's vector, b	4.12×10^{-10} , m
Taylor factor, M	3 [Rosler 2000]
Volume diffusivity, D_v	$1 \times 10^{-4} \exp(-46000/RT)$, m ² /s [Adeva 1995]
Dislocation density, ρ	1×10^{14} , 1/m ² [Rosler 2000]
Dispersoids	
Particle radius, r	25, nm [Wiese 2001a]
Interparticle spacing, 2λ	142, nm

Table 6.1: Material parameters in the micromechanical model of a Tin matrix containing both Ag₃Sn and Cu₅Sn₆ dispersoids

It is also noted in Figure 6.4 that the model prediction is moving away from our test results at high stresses because the model is not applicable beyond athermal detachment stress σ_d . In addition, the rapidly decreasing reference strain rate at low stresses in Figure 6.5 implies that the dispersion strengthening mechanism is not dominant in low stress region. These observations lead to a proposition of steady-state creep mechanisms for Pb-free solders, as shown in Figure 6.6 in which the steady-state creep strain rate $\dot{\epsilon}_{scr}$ is plotted vs. stress σ on a log-log scale. Three regions cover the whole stress range. The dominant deformation mechanisms in these regions are: Nabarro-Herring matrix diffusion creep (region 1), dispersion strengthening creep (region 2), and climb controlled dislocation creep and athermal dislocation detachment creep (region 3). It is still not clear if superplasticity plays a role in the steady-state creep of Pb-free solders. Further study in this area has to be conducted.

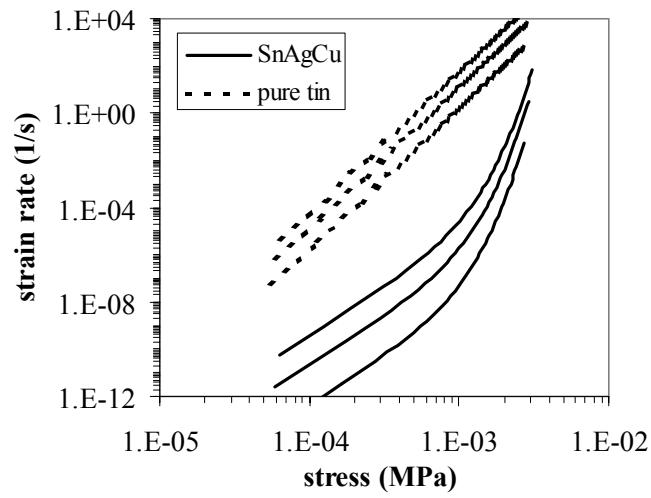


Figure 6.3: Comparison of the steady-state creep strain rate between pure tin and Sn3.9Ag0.6Cu solder

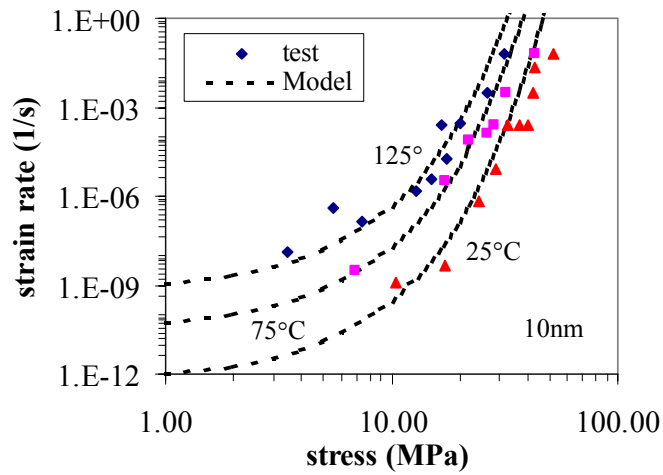


Figure 6.4: Comparison of the steady-state creep strain rate between test data and results from the micromechanical model

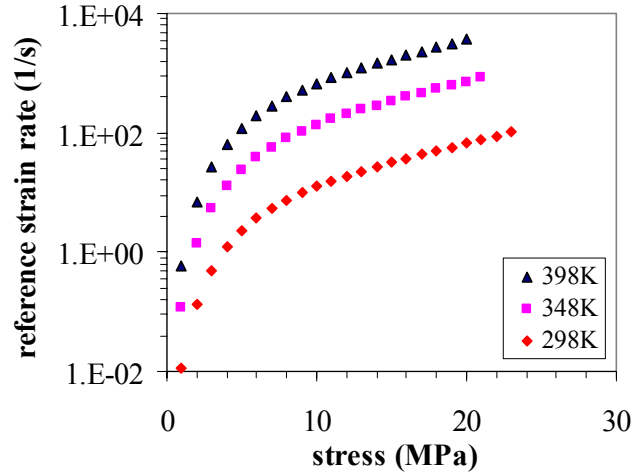


Figure 6.5: The reference strain rate $\dot{\epsilon}_0$ used in the micromechanical model

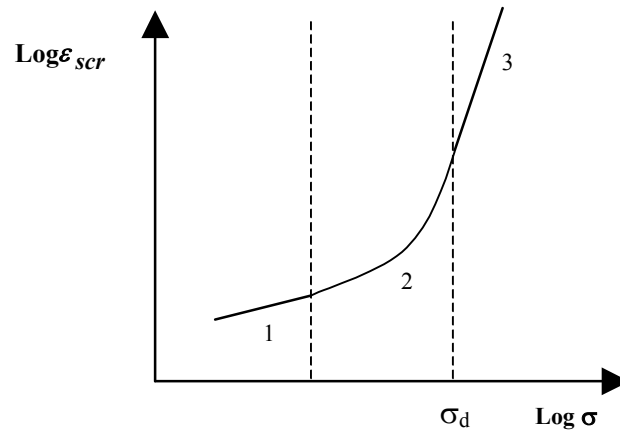


Figure 6.6: Schematic of proposed steady-state creep mechanisms of Pb-free solders

Appendix D: Test Data and Durability Parameters of Sn37Pb at 98°C

In order to compare mechanical durability with Pb-free solders at the same homologous temperature of 0.75, TMM cyclic tests at multiple load levels at 98°C were conducted on Sn37Pb solder specimens. Summaries of the test count and load level are given in Table 6.2. TMM test results of Sn37Pb solders at 98°C are presented in Figure 6.7. A power-law relationship as shown in Equation (3.4) is employed to correlate three damage criterion and cycles to failure for 50% load drop. Least-square fits of material constants

C and n for three load criteria: total cyclic inelastic work density (ΔW), total cyclic strain range (TSR) and cyclic inelastic strain range (ISR), are presented in Table 6.3. Corresponding test data variations are also shown in the same table.

Test Conditions		Load Levels and Test Count			
98°C, 4.6E-4 1/s	Deform. Range (μm)	-4~4	-4.8~4.8	-8.6~8.6	-10~10
	Test Count	3	1	1	3

Table 6.2: Summary of cyclic test count and load level for Sn37Pb solder

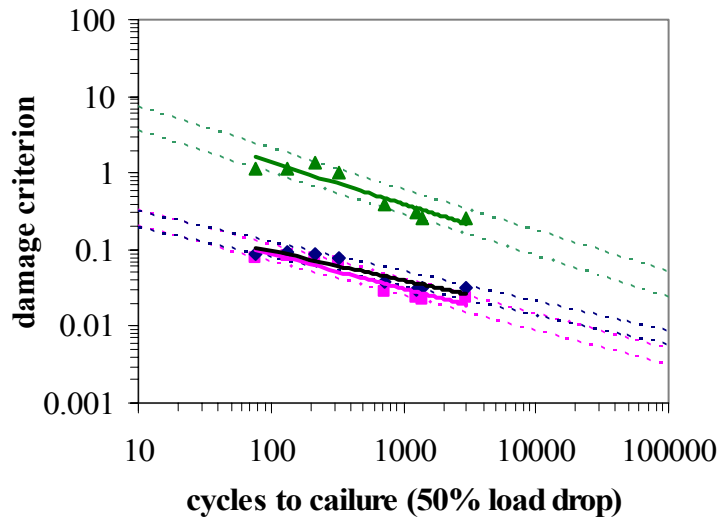


Figure 6.7: 98°C, 4.6E-4 1/s strain rate cyclic fatigue data, Sn37Pb solder

		n	C	R^2
98°C	TSR	-0.38	0.57	0.86
	ISR	-0.45	0.69	0.87
	W	-0.54	16.5	0.86

Table 6.3: Power-law durability parameters for Sn37Pb

Appendix E: Ansys Input Files

Ansys input files used in this study are presented in this Appendix.

Appendix E1: Ansys Input File for Parametric Modeling

This is an example input file for creating a TABGA package model.

```
<001.inp>
/prep7
bopt,numb,off
!-----< start of defining >-----
!define PBC parameters-----< step 1 >----pbcl1=6
pbcl2=6
pbch=1.51
!define substrate parameters-----< step 2 >----sbsl1=4
sbsl2=4
sbsl3=0.055
!define overmode parameters-----< step 3 >----ovmbottoml1=4
ovmbottoml2=4
ovmtop1=4
ovmtop2=4
ovmh=0.747
!define dieattach-----< step 4 >----diabottoml1=2.81
diabottoml2=2.81
diatop1=2.7577
diatop2=2.7577
diah=0.087
!define die-----< step 5 >----diel1=2.5775
diel2=2.5775
dieh=0.3
!define solderball crosssection parameters-----< step 6 >----t1=0.019
t2=0.038
t3=0.105
t4=0.046
t5=0.070
t6=0.052
t7=0.232
l1=0.130
l2=0.049
l3=0.093
l4=0.246
l5=0.277
l6=0.358
l7=0.288
l8=0.427
!-----< end of defining >-----
numstr,kp,20000
numstr,line,20000
numstr,area,20000
! basic PBC shape
numstr,volu,2010
k,,,-pbch
k,,pbcl1,-pbch
k,,pbcl1,-pbch,pbcl2
k,,,-pbch,pbcl2
k,,
k,,pbcl1
k,,pbcl1,,pbcl2
k,,,,pbcl2
```

```

v,20000,20001,20002,20003,20004,20005,20006,20007
! basic substrate shape
numstr,volu,2020
dist1=t7-sbsh
dist2=dist1+sbsh
k,,dist1
k,,sbsl1,dist1
k,,sbsl1,dist1,sbsl2
k,,dist1,sbsl2
k,,dist2
k,,sbsl1,dist2
k,,sbsl1,dist2,sbsl2
k,,dist2,sbsl2
v,20008,20009,20010,20011,20012,20013,20014,20015
! basic overmold shape
numstr,volu,2030
dist3=dist2+ovmh
k,,ovmbottom1,dist2
k,,ovmbottom1,dist2,ovmbottoml2
k,,dist2,ovmbottoml2
k,,dist3
k,,ovmtop1,dist3
k,,ovmtop1,dist3,ovmtopl2
k,,dist3,ovmtopl2
v,20012,20016,20017,20018,20019,20020,20021,20022
! die attach shape
numstr,volu,2040
dist4=dist2+diah
k,,diabottom1,dist2
k,,diabottom1,dist2,diabottoml2
k,,dist2,diabottoml2
k,,dist4
k,,diatop1,dist4
k,,diatop1,dist4,diatopl2
k,,dist4,diatopl2
v,20012,20023,20024,20025,20026,20027,20028,20029
numstr,volu,2050
! die shape
dist5=dist4+dieh
k,,diel1,dist4
k,,diel1,dist4,diel2
k,,dist4,diel2
k,,dist5
k,,diel1,dist5
k,,diel1,dist5,diel2
k,,dist5,diel2
v,20026,20030,20031,20032,20033,20034,20035,20036
numstr,volu,2060
vsbv,2030,2050,sepo,delete,keep
numstr,volu,2070
vsbv,2060,2040,sepo,delete,keep

```

<002.inp>
/prep7

```

bopt,numb,off
!-----< start of defining >-----!define location of first solderball----
-----< step 8 >-----
startl1=0.25
startl2=0.25
!defien ball pitch-----< step 9 >----ballpitch=0.5
!define the number of columns and rows-----< step 10 >---column=7
raw=7
!----- *dim,grid,array,row,column!-----
----- *dim,lol,array,column,row!-----
!-----
!define no solderballs (for instance: grid(1,1)=1)< step 11 >---
lol(1,1)=1,1,1,1,1,0,0
lol(1,2)=1,1,1,1,1,0,0
lol(1,3)=1,1,1,1,1,0,0
lol(1,4)=1,1,1,1,1,0,0
lol(1,5)=1,1,1,1,1,0,0
lol(1,6)=0,0,0,0,0,0,0
lol(1,7)=0,0,0,0,0,0,0
!-----< end of defining >-----

*do,j,1,column
  *do,i,1,row
    grid(i,j)=lol(j,i)
  *enddo
*enddo
numstr,kp,1
numstr,line,1
numstr,area,1
numstr,volu,1
dist3=t7+ovmh
! pcb
k,,-pbch
k,,ballpitch/2,-pbch
k,,ballpitch/2,-pbch,ballpitch/2,
k,,-pbch,ballpitch/2
k,,dist3
k,,ballpitch/2,dist3,,
k,,ballpitch/2,dist3,ballpitch/2
k,,dist3,ballpitch/2
numstr,volu,10
v,1,2,3,4,5,6,7,8
numstr,volu,10
vsymm,x,10,10,1
vsymm,z,10,11,1
vadd,10,11
numstr,volu,11
vadd,12,13
numstr,volu,10
vadd,11,14
numstr,kp,30000
numstr,line,30000
numstr,area,30000
numstr,volu,30000
counter=0
*do,j,1,column

```

```

*do,i,1,raw
*if,grid(i,j),eq,0,then
  counter=counter+1
  vgen,2,10,10,1,startl1+ballpitch*(j-1),,startl2+ballpitch*(i-1),,,
*endif
*enddo
*enddo
vdele,10,10,1,1
*if,counter,gt,1,then
  z=0
  FLST,2,counter,4
  *do,k,1,counter
    z=z+1
    FITEM,2,29999+z
  *enddo
  numstr,volu,80
  VADD,P51X
  FLST,2,5,4
  FITEM,2,2010
  FITEM,2,2020
  FITEM,2,2040
  FITEM,2,2050
  FITEM,2,2070
  vsbv,P51X,80,sepo,delete,delete
*else
  FLST,2,5,4
  FITEM,2,2010
  FITEM,2,2020
  FITEM,2,2040
  FITEM,2,2050
  FITEM,2,2070
  vsbv,P51X,30000,sepo,delete,delete
*endif

```

<003.txt>

```

/prep7
bopt,numb,off
numstr,kp,1
numstr,line,1
numstr,area,1
numstr,volu,1
! pcb
k,,,-pbch
k,,ballpitch/2,-pbch
k,,ballpitch/2,-pbch,ballpitch/2,
k,,,-pbch,ballpitch/2
k,,,
k,,ballpitch/2,,,
k,,ballpitch/2,,ballpitch/2
k,,,ballpitch/2
numstr,volu,10
v,1,2,3,4,5,6,7,8
! substrate
dist1=t7-sbsh
dist2=dist1+sbsh

```

```

k,,dist1
k,,ballpitch/2,dist1
k,,ballpitch/2,dist1,ballpitch/2
k,,dist1,ballpitch/2
k,,dist2
k,,ballpitch/2,dist2
k,,ballpitch/2,dist2,ballpitch/2
k,,dist2,ballpitch/2
numstr,volu,20
v,9,10,11,12,13,14,15,16
! die attach
dist4=dist2+diah
dist5=dist2+t1
k,,dist5
k,,ballpitch/2,dist5
k,,ballpitch/2,dist5,ballpitch/2
k,,dist5,ballpitch/2
numstr,volu,30
v,13,14,15,16,17,18,19,20
! die shape
dist5=dist4+dieh
k,,dist5
k,,ballpitch/2,dist5
k,,ballpitch/2,dist5,ballpitch/2
k,,dist5,ballpitch/2
numstr,volu,39
v,17,18,19,20,21,22,23,24
! overmold
dist3=dist2+ovmh
k,,dist3
k,,ballpitch/2,dist3
k,,ballpitch/2,dist3,ballpitch/2
k,,dist3,ballpitch/2
numstr,volu,50
v,21,22,23,24,25,26,27,28
! die attach 2
k,,dist4
k,,ballpitch/2,dist4
k,,ballpitch/2,dist4,ballpitch/2
k,,dist4,ballpitch/2
numstr,volu,60
v,17,18,19,20,29,30,31,32
numstr,volu,40
vsbv,39,60,sepo,delete,keep
! solderballshape
numstr,kp,1000
numstr,line,1000
numstr,area,1000
numstr,volu,100
k,,t4-t5
k,,l2/2,t4-t5
k,,l3/2,t4
k,,l4/2,t4
k,,l5/2
k,,l1/2,
k,,l1/2,-t6

```

k,,,t6
k,,,t7
k,,l7/2,t7
k,,l7/2,t7-t2
k,,l6/2,t3
k,,l8/2,t7
k,,l8/2,t7+t1
k,,,t7+t1
lstr,1000,1001
lstr,1001,1002
lstr,1002,1003
lstr,1003,1004
lstr,1004,1005
lstr,1005,1006
lstr,1006,1007
lstr,1007,1000
lstr,1000,1008
lstr,1008,1014
lstr,1014,1013
lstr,1013,1012
lstr,1012,1009
lstr,1009,1008
lstr,1009,1010
bsplin,1004,1011,1010,,,,-2,-1,-2,1,,
lang,1008,1002,90,,
al,1000,1001,1002,1003,1004,1005,1006,1007
al,1000,1001,1017,1008
al,1017,1002,1003,1014,1015,1013,1016
al,1013,1012,1011,1010,1009
vrotat,1000,1001,1002,1003,,,1007,1000,360,4
vdele,100,111,1,1
numstr,volu,10
vsbv,10,113,sepo,delete,keep
numstr,volu,11
vsbv,11,112,sepo,delete,keep
numstr,volu,20
vsbv,20,114,sepo,delete,keep
numstr,volu,30
vsbv,30,115,sepo,delete,keep
numstr,volu,200
vdrag,1065,,,,,1016,,,,
vdrag,1024,,,,,1009,,,,
vdrag,1028,,,,,51,,,,
vdrag,1032,,,,,57,,,,
vdrag,1036,,,,,43,,,,
vdrag,1058,,,,,1007,,,,
vdrag,1044,,,,,1038,,,,
numstr,volu,106
vsbv,12,206,sepo,delete,keep
numstr,volu,105
vsbv,112,205,sepo,delete,keep
numstr,volu,100
vsbv,114,200,sepo,delete,keep
vsbv,115,201,sepo,delete,keep
vsbv,60,202,sepo,delete,keep
vsbv,40,203,sepo,delete,keep

```

vsbv,50,204,sepo,delete,keep
numstr,volu,300
vsymm,x,200,206,1
vsymm,x,100,106,1
vsymm,x,113,113,1
vsymm,x,21,21,1
vsymm,x,31,31,1
vdele,200,206,1,1
vdele,100,106,1,1
vdele,113,113,1,1
vdele,21,21,1,1
vdele,31,31,1,1
numstr,volu,200
counter=0
*do,1,1,17
counter=counter+1
vsymm,x,299+counter,299+counter,1
vdele,299+counter,299+counter,1,1
*enddo
numstr,volu,100
counter=0
*do,1,1,17
counter=counter+1
vgen,2,199+counter,199+counter,1,-1,-1,,
vdele,199+counter,199+counter,1,1
*enddo

```

Appendix E2: Ansys Input File for Thermal Profile

This is input file for our thermal profile.

```

resume,flexbga144-SAC1m,db
/prep7
allsel,all
tref,298
toffst,0
finish

/solu
outres,erase
antype,static,new      !specifies new static analysis
rescontrol,,all,,     !specifies restart files
solcontrol,on         !turn on the optimized nonlinear solver
nlgeom,on             !turn on the large deformation effect
lnsrch,auto          !Auto line search
timint,off
autots,on            !automated time stepping
rate,1               !Turn on creep
crplim,0.25         !creep criterion
cutcontrol,crplimit,0.25,1 !specifies cutcontrol of creep
bfunif,temp,298      !specifies initial condition
lswrite,init        !reset load step file number

! step 1             !temperature up 10 degree in 100
time,100            !time at the end of step 1

```

```

nsubst,,100      !specifies the maximum number of substeps
deltim,1e-2,5e-16,5,on  !time increment
kbc,0           !ramped load
bfunif,temp,308    !apply temperature load
outres,all,none
outres,esol,20,solderball !specifies the results file
lswrite         !write the load step file fcoc50-1.S3

! step 2         !temperature up 100 degree in 1000
time,1000       !time at the end of step 1
nsubst,,100     !specifies the maximum number of substeps
deltim,,5e-16,5,on  !time increment
kbc,0          !ramped load
bfunif,temp,398   !apply temperature load
outres,all,none
outres,esol,20,solderball !specifies the results file
lswrite         !write the load step file fcoc50-1.S3

!step 3         !temperature dwell for 900 seconds
time,1900       !time at the end of step
nsubst,,100     !specifies the maximum number of substeps
deltim,,5e-16,20,on  !time increment
kbc,1          !stepped load
outres,all,none
outres,esol,20,solderball !specifies the results file
lswrite         !write the load step file fcoc50-1.S6

! step 4         !temperature down 180 degree in 1080
time,2980       !time at the end of step 1
nsubst,,100     !specifies the maximum number of substeps
deltim,,5e-16,5,on  !time increment
kbc,0          !ramped load
bfunif,temp,218   !apply temperature load
outres,all,none
outres,esol,20,solderball !specifies the results file
lswrite         !write the load step file fcoc50-1.S3

!step 5         !temperature dwell for 600 seconds
time,3580       !time at the end of step
nsubst,,100     !specifies the maximum number of substeps
deltim,,5e-16,20,on  !time increment
kbc,1          !stepped load
outres,all,none
outres,esol,20,solderball !specifies the results file
lswrite         !write the load step file fcoc50-1.S12

! step 6         !temperature up 180 degree in 1800
time,5380       !time at the end of step 1
nsubst,,100     !specifies the maximum number of substeps
deltim,,5e-16,5,on  !time increment
kbc,0          !ramped load
bfunif,temp,398   !apply temperature load
outres,all,none
outres,esol,20,solderball !specifies the results file
lswrite         !write the load step file fcoc50-1.S3

```

```

!step 7          !temperature dwell for 900 seconds
time,6280       !time at the end of step
nsubst,,100     !specifies the maximum number of substeps
deltim,,5e-16,20,on  !time increment
kbc,1          !stepped load
outres,all,none
outres,esol,20,solderball !specifies the results file
lswrite        !write the load step file fcoc50-1.S6

! step 8        !temperature down 180 degree in 1080
time,7360       !time at the end of step 1
nsubst,,100     !specifies the maximum number of substeps
deltim,,5e-16,5,on  !time increment
kbc,0          !ramped load
bfunif,temp,218  !apply temperature load
outres,all,none
outres,esol,20,solderball !specifies the results file
lswrite        !write the load step file fcoc50-1.S3

!step 9          !temperature dwell for 600 seconds
time,7960       !time at the end of step
nsubst,,100     !specifies the maximum number of substeps
deltim,,5e-16,20,on  !time increment
kbc,1          !stepped load
outres,all,none
outres,esol,20,solderball !specifies the results file
lswrite        !write the load step file fcoc50-1.S12

! step 10       !temperature up 180 degree in 1800
time,9760       !time at the end of step 1
nsubst,,100     !specifies the maximum number of substeps
deltim,,5e-16,5,on  !time increment
kbc,0          !ramped load
bfunif,temp,398  !apply temperature load
outres,all,none
outres,esol,20,solderball !specifies the results file
lswrite        !write the load step file fcoc50-1.S3

!step 11        !temperature dwell for 900 seconds
time,10660      !time at the end of step
nsubst,,100     !specifies the maximum number of substeps
deltim,,5e-16,20,on  !time increment
kbc,1          !stepped load
outres,all,none
outres,esol,20,solderball !specifies the results file
lswrite        !write the load step file fcoc50-1.S6

! step 12       !temperature down 180 degree in 1080
time,11740      !time at the end of step 1
nsubst,,100     !specifies the maximum number of substeps
deltim,,5e-16,5,on  !time increment
kbc,0          !ramped load
bfunif,temp,218  !apply temperature load
outres,all,none
outres,esol,20,solderball !specifies the results file
lswrite        !write the load step file fcoc50-1.S3

```

```

!step 13          !temperature dwell for 600 seconds
time,12340       !time at the end of step
nsubst,,100     !specifies the maximum number of substeps
deltim,,5e-16,20,on !time increment
kbc,1           !stepped load
outres,all,none
outres,esol,20,solderball !specifies the results file
lswrite         !write the load step file fcoc50-1.S12

! step 14        !temperature up 2 degree in one second
time,13140      !time at the end of step 1
nsubst,,100     !specifies the maximum number of substeps
deltim,,5e-16,5,on !time increment
kbc,0           !ramped load
bfunif,temp,298 !apply temperature load
outres,all,none
outres,esol,20,solderball !specifies the results file
lswrite         !write the load step file fcoc50-1.S3

!solve,1,14     !solve load steps
finish
/exit,nosav

```

Appendix E3: Ansys Input File for Post Processing

This is an example input file for post processing the SnAgCu solder results of the fleXBGA1 package subjected to our thermal profile.

```

/post26
reset
numvar,13
allsel,all

*dim,elemlist,array,13
*set,elemlist(1),13,35781,35889,35901,36165,36175,36180,36282,36283,36294
*set,elemlist(11),36295,36411,36423

*dim,ENPL,array,214,13
*dim,ENCR,array,214,13
*dim,ENPLWK,array,214,13
*dim,ENAVE,array,214,4
vget,ENAVE(1,1),1

*dim,volu,array,13
*set,volu(1),13
Svolu=0
*do,i,2,volu(1)
*get,volu(i),ELEM,elemlist(i),volu
Svolu=Svolu+volu(i)
*enddo

*do,i,2,elemlist(1)

```

```
esol,i,elemelist(i),,send,plastic,ENPL
store,merge
vget,ENPL(1,i),i
*enddo
```

```
*do,i,1,214
SUM=0
*do,j,2,volu(1)
SUM=SUM+ENPL(i,j)*volu(j)
*enddo
SUM=SUM/Svolu
ENAVE(i,2)=SUM
*enddo
```

```
*do,i,2,elemelist(1)
esol,i,elemelist(i),,send,creep,ENCR
store,merge
vget,ENCR(1,i),i
*enddo
```

```
*do,i,1,214
SUM=0
*do,j,2,volu(1)
SUM=SUM+ENCR(i,j)*volu(j)
*enddo
SUM=SUM/Svolu
ENAVE(i,3)=SUM
*enddo
```

```
*do,i,2,elemelist(1)
esol,i,elemelist(i),,nl,plwk,ENPLWK
store,merge
vget,ENPLWK(1,i),i
*enddo
```

```
*do,i,1,214
SUM=0
*do,j,2,volu(1)
SUM=SUM+ENPLWK(i,j)*volu(j)
*enddo
SUM=SUM/Svolu
ENAVE(i,4)=SUM
*enddo
```

```
*cfoopen,ENAVE,dat
*vwrite,ENAVE(1,1),ENAVE(1,2),ENAVE(1,3),ENAVE(1,4)
(4(6x,f12.6))
*cfclose
finish
```

Appendix F: Weibull Plots

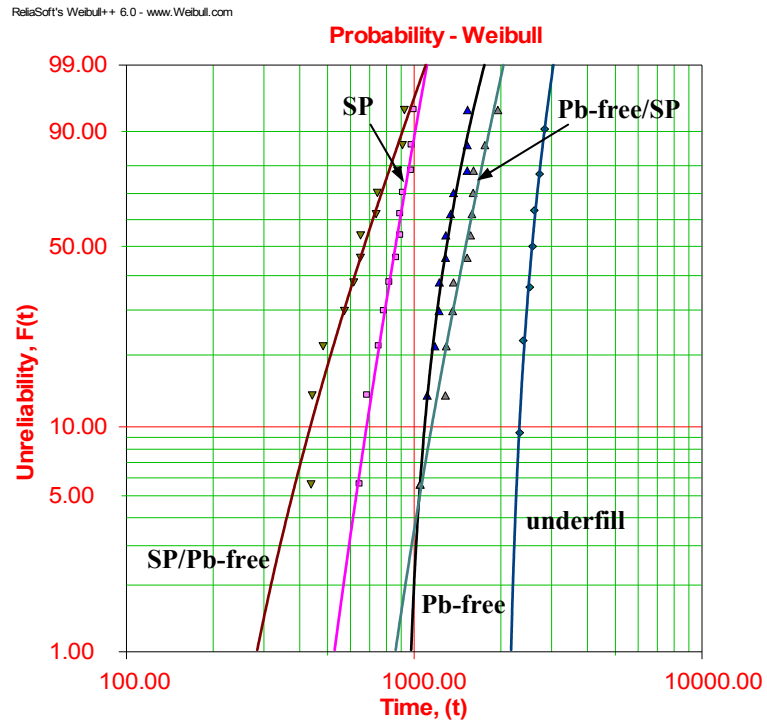


Figure 6.8: 3-P Weibull plots for fleXBGA144 package

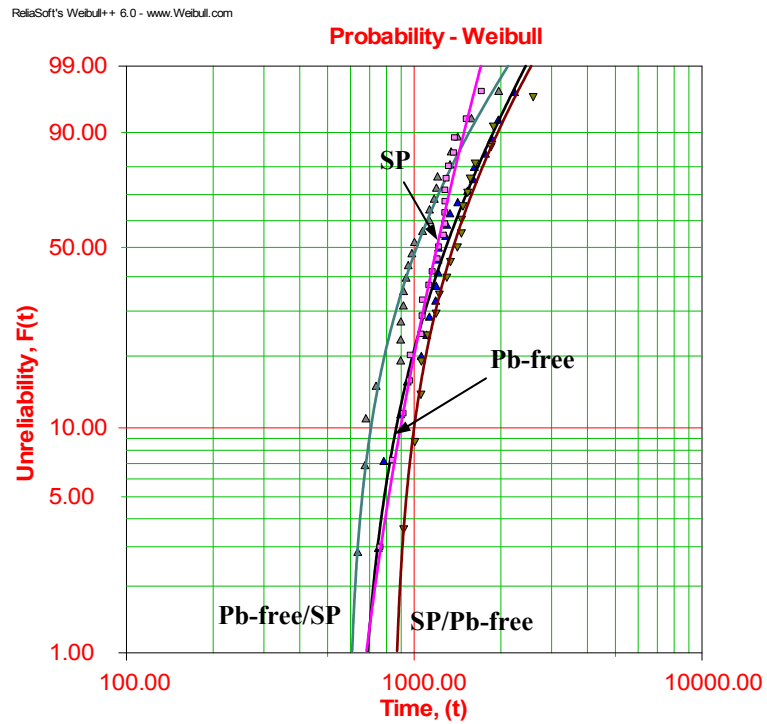


Figure 6.9: 3-P Weibull plots for TABGA96 package

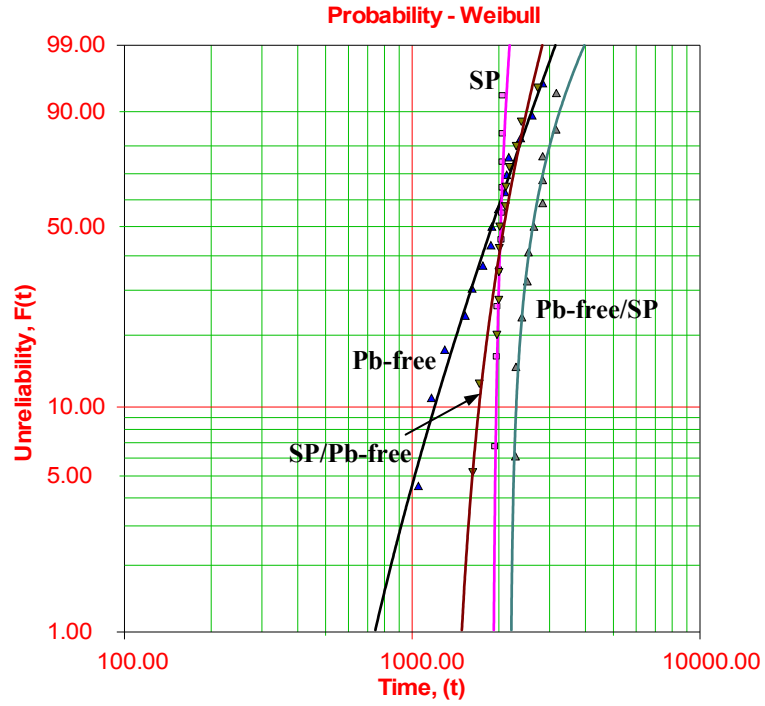


Figure 6.10: 3-P Weibull plots for PBGA352 package

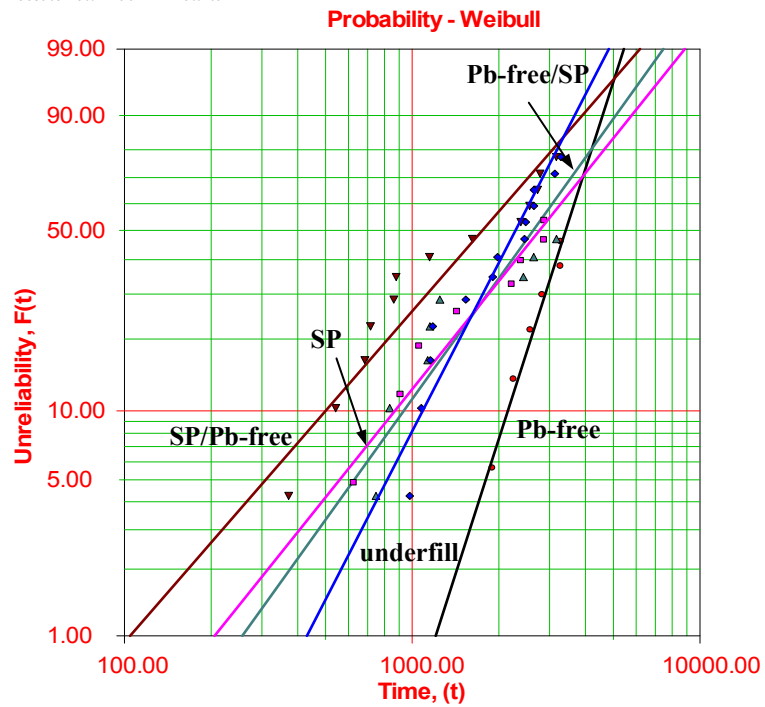


Figure 6.11: 2-P Weibull plots for μ BGA46 package

7 Reference

1. Adeva, P., Caruana, G., Ruano, O.A., Torralba, M., 1995, "Microstructure and High Temperature Mechanical Properties of Tin," *Materials Science and Engineering A*, Vol. 194, pp. 17-23.
2. Amagai, M., 1999, "Chip Scale Package (CSP) Solder Joint Reliability and Modeling," *Microelectronics Reliability*, Vol. 39, pp. 463-477.
3. Amagai, M., Watanabe, M., Omiya, M., Kishimoto, K., Shibuya, T., 2002, "Mechanical Characterization of Sn-Ag-based Lead-free Solders," *Microelectronics Reliability*, Vol. 42, pp. 951-966.
4. Amkor Technology, Personal Communications, 2003.
5. Anand, L., 1982, "Constitutive Equations for the Rate-Dependent Deformation of Metals at Elevated Temperatures," *ASME Journal of Engineering Materials and Technology*, Vol. 104, pp. 12-17.
6. Avery, D. H., Backofen, W. A., 1965, *Transactions of the American Society of Metals*, Vol. 58, pp. 551.
7. Bath, Jasbir, 2003, "A Manufacturable Lead-free Surface-Mount Process?" *Circuits Assembly*, Vol. 14, no. 1, January 2003, pp. 26-30.
8. Boeing Tech Notes, 2002, "Lead Elimination from Printed Wiring Assemblies (Get the Lead Out)," www.boeing.com.
9. Brandenburg, S. and S. Yeh, 1998, "Electromigration Study of Flip Chip Bump Solder Joint," *Surface Mount International Conference and Exposition*, p. 327.

10. Cheng, Z.N., Wang, G.Z., Chen, L., Wilde, J., Becker, K., 2000, "Viscoplastic Anand Model for Solder Alloys and its Application," *Soldering and Surface Mount Technology*, Vol. 12(2), pp.31-36.
11. Coffin, L.F., 1954, *Transactions of the ASME*, Vol. 76, pp. 931-950.
12. Coffin, L.F., 1973, "Fatigue at High Temperature," *ASTM STP 520*, PA.
13. Collier, P., Sunappan, V., Periannan, A., 2002, "Lead-free Solder Process Implementation for PCB Assembly." *Soldering and Surface Mount Technology*, Vol. 14, no. 3, pp. 12-18.
14. Commission of the European Communities, "Proposal for a Directive of the European Parliament and of the Council on Waste Electrical and Electronic Equipment, Document No. 500PC0347(01)," June 13, 2000, <http://europa.eu.int/eur-lex/en/com/dat/2000/en_500PC0347_01> accessed March 16, 2001.
15. Cunningham, K. and Donahue, M., 1990, "Tin Whiskers: Mechanisms of Growth and Prevention," *Proceedings of the 4th International SAMPE Electronics Conference*, pp. 569-575.
16. Cutiongco, E. C., Vaynman, S., Fine, M. E., Jeannotte, D. A., 1990, "Isothermal Fatigue of 63Sn-37Pb Solder," *ASME Trans., Journal of Electronic Packaging*, Vol. 112, No. 2, pp. 110-114.
17. Darveaux, R., Banerji, K., 1992, "Constitutive Relations for Tin-Based Solder Joints," *IEEE Transactions on Components, Hybrids, and Manufacturing Technology*, Vol. 15 (6), pp. 1013-1024.

18. Darveaux, R., Banerji, K., Mawer, A., Dody, G., 1995, "Durability of Plastic Ball Grid Array Assembly," *Ball Grid Array Technology*, Lau, J., Editor, McGraw-Hill, Inc., New York.
19. Darveaux, R., 1997, "Solder Joint Fatigue Life Model," in *Design and Reliability of Solders and Solder Interconnections*, The Minerals, Metals and Materials Society, pp. 213-218.
20. Darveaux, R., 2000, "Effect of Simulation Methodology on Solder Joint Crack Growth Correlation," *IEEE ECTC 2000*.
21. Dasgupta, A., Oyan, C., Barker, D., and Pecht, M., 1992, "Solder Creep-Fatigue Analysis by an Energy-Partitioning Approach," *ASME Journal of Electronic Packaging*, Vol. 114, No. 2, pp. 152-160.
22. Dougherty, D. J., Fusaro, J. M., Culbertson, D., 1997, "Reliability Model for Micro-Miniature Electronic Packages," *Proceedings of ISHM 1997*, Philadelphia, PA.
23. Engelmaier W., 1984, "Test Method Considerations for SMT Solder Joint Durability," *IEPS*, pp. 360-369.
24. Enke, N.F., Kilinski, T.J., Schroeder, S.A., and Lesniak, J.R., 1989, "Mechanical Behaviors of 60/40 Tin-lead Solder Lap Joints," *IEEE Trans. CHMT*, Vol. 12, No. 4, pp.459-468.
25. Environmental Concepts Inc., "A History of Lead," March 12, 1997, <<http://www.gate.net/~verstraa/history.htm>> accessed May 3, 2001.
26. Frear, D. R., 1990, "Microstructural Evolution During Thermomechanical Fatigue of 62Sn-36Pb-2Ag and 60Sn-40Pb Solder Joints," *IEEE Transactions on Components, Hybrids and Manufacturing Technology*, Vol. 13, No. 4, pp. 718-726.

27. Frear, D. R., Jang, J. W., Lin, J. K., and Zhang, C., 2001, "lead-Free Solders for Flip-Chip Interconnects," *JOM*, Vol. 53, No. 6, pp. 28-32.
28. Frost, H. J., Howard, R. T., 1990, "Creep Fatigue Modeling for Solder Joint Reliability Predictions Including the Microstructural Evolution of the Solder," *IEEE Transactions on Components, Hybrids and Manufacturing Technology*, Vol. 13, No. 4, pp. 727-735.
29. Gan, H., Xu, G., and Tu, K. N., 2003, "Unique Phase Changes Induced by Electromigration (EM) in Solder Joints," *ECTC 2003*, pp. 71-76, New Orleans, LA.
30. Gayle, F. W., et. al., 2001, "High Temperature Lead-free Solder for Microelectronics," *JOM*, pp. 17-21.
31. Guo, Y., Lin, J.-K., and Silva, A.D., 2002, "Durability Evaluation of Chip Interconnect in Lead-Free Solder Systems," *ECTC 2002*, pp. 1275-1280.
32. Guo, Z. and Conrad, H., 1993, "Fatigue Crack Growth Rate in 63Sn37Pb Solder Joints," *ASME Trans. J. Electronic Packaging*, Vol. 115, No. 2, pp. 159-164.
33. Halford, G. R., Hirschberg, M. H., and Manson, S. S., 1973, "Temperature Effects on the Strain-Range Partitioning Approach for Creep Fatigue Analysis," *ASTM STP 520*, pp. 658-667, PA.
34. Harrison, M.R., Vincent, J.H., Steen, H.A.H., 2001, "Lead-Free Reflow Soldering for Electronics Assembly." *Soldering and Surface Mount Technology*, Vol. 13, no. 3, pp. 21-38.
35. Haswell, P. and Dasgupta, A., 1999, "Viscoplastic Characterization of Constitutive Behavior of Two Solder Alloys," *ASME International Mechanical Engineering Congress and Exposition*, November 14-19, 1999, Nashville, Tennessee.

36. Haswell, P. and Dasgupta, A., 2000, "Durability Properties Characterization of Sn₆₂Pb₃₆Ag₂ Solder Alloy," *Proceedings ASME IMECE*, EEP-Vol. 28, pp. 181-187, Orlando, FL.
37. Haswell, P. and Dasgupta, A., 2001a, "Viscoplastic Constitutive Properties of Lead-Free Sn-3.9Ag-0.6Cu Alloy," *MRS Proceedings*, San Francisco, CA.
38. Haswell, P., 2001b, Durability Assessment and Microstructural Observations of Selected Solder Alloys, Ph.D. Dissertation, University of Maryland, College Park, MD.
39. Hayward, J., 2000, "Lead (Pb)-Free Packaging Strategy 2000–2003," <www.amd.com>.
40. Hwang, J., 1994, "Overview of Lead-free Solders for Electronics and Microelectronics", *Surface Mount International Conference and Exposition*, Surface Mount Int., Edina, MN, USA, pp. 405-21.
41. Hwang, J., 2002, "Anatomy of Sn/Ag/Cu in SMT Applications", *Surface Mount Technology*, August 2002, pp. 14-18.
42. IDEALS Presentation, 1999a, <<http://www.lead-free.org/download/files/pdf/IDEALS%20Report1.pdf>>.
43. IDEALS Report, 1999b, <<http://www.lead-free.org/download/files/pdf/IDEALS%20Report2.pdf>>.
44. IDEALS Synthesis Report, 1999c, <http://www.alphametals.com/products/lead_free/PDF/synthesis.pdf>.
45. Igoshev, V.I., Kleiman, J.I., 2000, "Creep Phenomena in Lead-Free Solders," *Journal of Electronic Materials*, 29 (2), pp. 244-250.

46. Jonnalagadda, K., Bai, T., and Olson, B., 2001, "Thermal and Bending Fatigue of PBGA Assemblies with Lead-Free Solder Pastes," *2001 International Symposium on Microelectronics*, pp.553-558.
47. JEDEC Solid State Technology Association, "JEDEC Announces Lead-free Definition," <<http://www.jedec.org/Home/press/leadfreePR.pdf>>, accessed September 2002.
48. Jang, J. W., De Silva, A. P., Lee, T. Y., Lin J. K., and Frear, D. R., "Direct Correlation between Microstructure and Mechanical Tensile Properties in Pb-free Solders and Eutectic SnPb Solder for Flip Chip Technology," *Applied Physics Letters*, Vol. 79, No. 4, pp. 482-484, 2001.
49. Ju, S. H., Sandor, B. I., Plesha, M. E., Dec. 1996, "Life Prediction of Solder Joints by Damage and Fracture Mechanics," *ASME Trans., Journal of Electronic Packaging*, Vol. 118, pp. 193-200.
50. Kariya, Y. and Otsuka, M., 1998, "Effect of Bismuth on the Isothermal Fatigue Properties of Sn-3.5mass%Ag Solder Alloy," *Journal of Electronic Materials*, Vol. 27(7), pp. 866-870.
51. Kariya, Y., Morihata, T., Hazawa, E., and Otsuka, M., 2001, "Assessment of Low-Cycle Fatigue Life of Sn-3.5mass%Ag-X (X=Bi or Cu) Alloy by Strain Range Partitioning Approach," *Journal of Electronic Materials*, Vol. 30(9), pp. 1184-1189.
52. Kirchner, K., Nelson, D., 2002, "Manufacturing and Reliability of Chip Scale Area Array packaging in Avionics Environments." *Proceedings of the 2002 SMTA International Conference*, Rosemont, IL, September 22-26, pp. 437-444.

53. Kujala, A., Reinikainen, T., Ren, W., 2002, "Transition to Pb-free Manufacturing Using Land Grid Array Packaging Technology." *52nd Electronic Components and Technology Conference*, San Diego, CA, May 28-31 2002, pp. 359-364.
54. Lau, J. H., and Pao, Y. H., 1996, *Solder Joint Reliability of BGA, Flip Chip, CSP, and Fine Pitch SMT Assemblies*, McGraw-Hill, New York.
55. Lau, J. H., 1997, "Solder Joint Reliability of a Low Cost Chip Scale Package - NuCSP," *Proceedings of ISHM 1997*, Philadelphia, PA.
56. Lee, Y., Han, B.T., 2002, "Constitutive Relationships of Binary Lead-Free Solders," *CALCE Internal Report*.
57. Lee, Y., Han, B.T., 2003, "Calibration of Virtual Qualification Model for Leaded Packages with Pb-free Solder," *CALCE Internal Report*.
58. Levine, B., 2002, "Will 'Tin Whiskers' Grow When You Get the Lead Out?" *Electronic News*.
59. Levis, K.-M., and Mawer, A., 2000, "Assembly and Solder Joint Durability of Plastic Ball Grid Array with Lead-Free Versus Lead-Tin Interconnect," *ECTC 2000*, pp. 1198-1204.
60. Liang, J., et al., 1997, "Creep Study for Fatigue Life Assessment of Two Pb-Free High Temperature Solder Alloys," *Mater. Res. Soc. Symp. Proc.*, Vol. 445, pp. 307-312.
61. Lin, J.-K., Silva, A.D., Frear, D., Guo, Y., Jang, J.-W., Mitchell, D., Yeung, B., Zhang, C., 2001, "Characterization of Lead-Free Solders and Under Bump Metallurgies for Flip-Chip Package," *ECTC 2001*.
62. Manson, S. S., 1965, *Experimental Mechanics*, Vol. 5, No. 7, pp. 193-226.

63. Manson, S. S., Halford, G. R., and Hirschberg, M. H., 1971, "Creep-Fatigue Analysis by Strain-Range Partitioning," *ASME Symposium on "Design for Elevated Temperature Environment"*, San Francisco, CA.
64. Manson, S. S., "The Challenge to Unify Treatment of High Temperature Fatigue-A Partisan Proposal Based on Strain Range Partitioning," *ASTM STP 520*, PA.
65. Mavoori, H., Chin, J., Vaynman, S., Moran, B., Keer L. and Fine, M., 1997, "Creep, Stress Relaxation, and Plastic Deformation in Sn-Ag and Sn-Zn Eutectic Solders," *J. Electronic Materials*, Vol. 26(7), pp. 783-790.
66. McDowell, D. L., 1992, "A Nonlinear Kinematic Hardening Theory for Cyclic Thermoplasticity and Thermoviscoplasticity," *Int. J. Plast.*, Vol. 8, pp. 695-728.
67. Mei, Z. and Morris, J.W., 1992, "Characterization of Eutectic Sn-Bi Solder Joints," *J. Electron. Mater.*, Vol. 21, pp. 599-607.
68. Meyers, M.A., Chawla, K.K., 1984, *Mechanical Metallurgy, Principles and Applications*, Englewood Cliffs, NJ: Prentice-Hall.
69. CALCE NCMS Internal Report, 1997, "Life Prediction Model Development for Lead-free Solder Alloys,"
70. National Center for Manufacturing Sciences (NCMS), 1998, Final Report on Lead-free Alternatives Project.
71. National Electronics Manufacturing Initiative (NEMI) Press Release, Jan. 24 2000, <http://www.nemi.org/newsroom/PR/2000/PR012400.html>
72. NEMI Newsroom, February 15, 2001, http://www.nemi.org/newsroom/Presentations/lf_workshop.html

73. National Electronics Manufacturing Initiative (NEMI), "NEMI's Lead-free Assembly Project Reports Latest Results at APEX 2002,"
<<http://www.nemi.org/Newsroom/PR/PR012102b.html>> accessed September 12, 2002.
74. Neu, R.W., Scott, D.T., Woodmansee, M.W., 2001, "Thermomechanical Behavior of 96Sn-4Ag and Castin Alloy," *ASME Journal of Electronic Packaging*, Vol. 123, pp. 238-246.
75. Nurmi, S.T., Ristolainen, E. O., 2002, "Durability of Tin-Lead Balled BGAs Soldered with Lead-Free Solder Paste," *Soldering and Surface Mount Technology*, 14(2), pp. 35-39.
76. Okura, J.H., 2000, Effects of Temperature and Moisture on Durability of Low Cost Flip Chip on Board (FCOB) Assemblies, Ph.D. Dissertation, University of Maryland, College Park, MD.
77. Park, T.-S., and Lee, S.-B., 2002, "Isothermal Low Cycle Fatigue Tests of Sn/3.5Ag/0.75Cu and 63Sn/37Pb Solder Joints under Mixed-mode Loading Cases," *ECTC 2002*, pp. 979-984, Las Vegas, NV.
78. Patwardhan, V., Kelkar, N., and Nguyen, L., 2002, "Lead-Free Wafer Level-Chip Scale Package: Assembly and Durability," *ECTC 2002*, pp. 1355-1358.
79. Prasad, S., Carson, F., Kim, G. S., Lee, J. S., Roubaud, P., Henshall, G., Kamath, S., Garcia, A., Herber, R., and Bulwith, R., 2000, "Board Level Durability of Lead-Free Packages," *SMTAI 2000*.
80. Raeder, C.H., et al., 1994, "Isothermal Creep of Eutectic SnBi and SnAg Solder and Solder Joints," *International Electronics Manufacturing Technology Symposium*, Sept. 12-14, La Jolla, CA, USA.

81. Rafanelli, A. J., 1994, "The Validation and Evaluation of the J-Integral for 63-37 Tin Lead Solder," *ASME Mechanics and Materials for Electronic Packaging: Volume 2-thermal and Mechanical Behavior and Modeling*, AMD Vol. 187, pp. 91-99.
82. Reinkainen, T., Poech, M., Krumm, M., Kivilahti, J., 1997, "A finite-element and experimental analysis of stress distribution in various shear tests for solder joints."
83. Robins, M., "The History of Lead Free," *Electronic Packaging and Production Supplement*, Vol. 40, No. 6, pp. 7-10, June 2000.
84. Rosler, J., Artz, E., 1990, "A New Model-Based Creep Equation for Dispersion Strengthened Materials," *Acta Materials*, Vol. 38, pp. 671-683.
85. Rosler, J., Baker, M., 2000, "A Theoretical Concept for the Design of High-Temperature Materials by Dual-Scale Particle Strengthening," *Acta Materials*, Vol. 48, pp. 3553-3567.
86. Roubaud, P., Henshall, G., Bulwith, R., Prasad, S., Carson, F., Kamath S. and O'Keeffe, E., 2001, "Thermal Fatigue Resistance of Pb-free Second Level Interconnect," *SMTAI 2001*.
87. Schubert, A., et. al., 2002a, "Lead-free Flip-Chip Solder Interconnects – Materials Mechanics and Durability Issues," *Micromaterials and Nanomaterials*, Issue 1, pp. 12-24.
88. Schubert, A., Dudek, R., Doring, R., Walter, H., Auerswald, E., Gollhardt, A., Schuch, B., Sitzmann, H. and Michel, B., 2002b, "Lead-free Solder Interconnects: Characterization, Testing, and Durability," *3rd Int. Conf. On Benefiting from Thermal and Mechanical Simulation in Micro- Electronics, EuroSIME2002*, pp. 74-84, Paris, France.

89. Seelig, K. and Suraski, D., 2001, "Lead-Contamination in Lead-free Electronics Assembly," www.aimsolder.com.
90. Shine, M.C. and Fox, L.R., 1988, "Fatigue of Solder Joints in Surface Mount Devices," *Low Cycle Fatigue*, Solomon, Halford, Kaisand, and Leis eds., ASTM STP 942.
91. Skrzypek, J.J., 1993, *Plasticity and Creep: Theory, Examples, and Problems*, Begell House: CRC Press.
92. SOLDERTEC, 1999, "Lead-Free Alloys - The Way forward", <www.lead-free.org>.
93. Solomon, H.D. and Tolksdorf, E.D., 1995, "Energy Approach to the Fatigue of 60/40 Solder: Part I—Influence of Temperature and Cycle Frequency," *ASME Trans. J. Electronic Packaging*, Vol. 117, pp 130-135.
94. Solomon, H.K., 1989, "Low Cycle Fatigue of Surface Mounted Chip Carrier/Printed Wiring Board Joints," *Proceedings IEEE 39th ECC*, pp. 277-292.
95. Stam, F.A. and Davitt, E., 2001, "Effects of Thermomechanical Cycling on Lead and Lead-free (SnPb and SnAgCu) Surface Mount Solder Joints," *Microelectronics Durability*, 41, pp. 1815-1822.
96. Suhling, J., Islam, N., Johnson, R. W., Lall, P., 2003, "Thermal Cycling Reliability of Chip Resistor Lead Free Solder Joints," *ASME IMECE 2003*, Washington, D.C., USA.
97. Syed, A., 2001a, "Durability and Au Embrittlement of Lead Free Solders for BGA Applications," *2001 International Symposium on Advanced Packaging Materials*, pp. 143-147.

98. Syed, A., 2001b, "Durability of Lead-Free Solder Connections for Area-Array Packages," *IPC SMTA Council APEX 2001*, LF2-7.
99. Tribula, D., Morris, J. W. Jr., 1990, "Creep in Shear of Experimental Solder Joints," *ASME Trans., Journal of Electronic Packaging*, Vol. 112, No. 2, pp. 87-93.
100. Vaynman, S., 1990, "Effect of Temperature on Isothermal Fatigue of Solders," *IEEE Transactions on Components, Hybrids and Manufacturing Technology*, Vol. 13, No. 4, pp. 909-913.
101. Vaynman, S., McKeown, S. A., 1993, "Energy-Based Methodology for the Fatigue Life Prediction of Solder Materials," *IEEE Transactions on Components, Hybrids and Manufacturing Technology*, Vol. 16, No. 3, pp. 317-323.
102. Wang, G.Z., Cheng, Z.N., Becker, K., Wilde, J., 2001, "Applying Anand Model to Represent the Viscoplastic Deformation Behavior of Solder Alloys," *Journal of Electronic Packaging*, Vol. 123, pp. 247-253.
103. Whitten, G., "Lead-free Solder Implementation for Automotive Electronics," *ECTC 2000*, pp. 1410-1415.
104. Wiese, S., Schubert, A., Walter, H., Dudek, R., Feustel, F., 2001a, "Constitutive Behavior of Lead-free Solders vs. Lead-containing Solders – Experiments on Bulk Specimens and Flip-Chip Joints," *ECTC 2001*, pp. 890-902, Las Vegas, NV.
105. Wiese, S., Jakschik, S., Feustel, F., Meusel, E., 2001b, "Fracture Behavior of Flip Chip Solder Joints," *ECTC 2001*, pp. 1299-1306, Las Vegas, NV.
106. Wiese, S., Rzepka, E., Meusel, E., 2002, "Time-independent elastic-plastic behavior of solder materials," *3rd Int. Conf. On Benefiting from Thermal and*

- Mechanical Simulation in Micro- Electronics, EuroSIME2002*, pp. 91-97, Paris, France.
107. Wilcox, J. R., Subrahmanyam, R., Li, C.-Y., 1990, "Assembly Stiffness and Failure Criterion Considerations in Solder Joint Fatigue," *ASME Trans., Journal of Electronic Packaging*, Vol. 112, No. 2, pp. 115-122.
 108. Wild, R. N., 1975, "Some Fatigue Properties of Solder and Solder Joints," *IBM Rep. No. 74Z000481*, also INTERNEPSON, Brighton, England.
 109. Wilde, J., Becker, K., Thoben, M., Blum, W., Jupitz, T., Wang, G., Cheng, Z.N., 2000, "Rate-Dependent Constitutive Relations Based on Anand Model for 92.5Pb5Sn2.5Ag Solder," *IEEE Transaction on Advanced Packaging*, Vol. 23(3), pp. 408-414.
 110. Woodrow, T. A., 2002, "Durability and Leachate Testing of Lead-free Solder Joints," *International Conference on Lead-Free Electronic Components and Assemblies*, San Jose, CA, pp.116-125, May 1-2.
 111. Zeng, K., Tu, K.N., 2002, "Six Cases of Reliability Study of Pb-free Solder Joints in Electronic Packaging Technology," *Materials Science and Engineering R*, Vol. 273, pp. 1-51.
 112. Zhang, C., Lin, J.-K., and Li, L., 2001, "Thermal Fatigue Properties of Lead-free Solders on Cu and NiP Under Bump Metallurgies," *ECTC 2001*.
 113. Zhang, Q., Dasgupta, A., Haswell, P., 2002, "Cyclic Mechanical Durability of Sn3.9Ag0.6Cu and Sn3.5Ag Lead-free Solder Alloys", *Proceedings of IMECE'02: 2002 ASME International Mechanical Engineering Congress and Exposition*, New Orleans, LA.

114. Zhang, Q., Dasgupta, A., Haswell, P., Osterman, M., 2003a, “Isothermal Mechanical Fatigue of Pb-free Solders: Damage Propagation & Time to Failure,” *34th International SAMPE Technical Conference*, Baltimore, MD.
115. Zhang, Q., Dasgupta, A., Haswell, P., 2003b, “Viscoplastic Constitutive Properties and Energy-Partitioning Model of Lead-Free Sn3.9Ag0.6Cu Solder Alloy”, *ECTC 2003*, New Orleans, Louisiana, USA.